



I. R. IRAN

ISSN: 2423-7167

e-ISSN: 1735-9244



International Journal of Engineering

Journal Homepage: www.ije.ir



TRANSACTIONS C: ASPECTS

Volume 36, Number 09, September 2023

Materials and Energy Research Center

INTERNATIONAL JOURNAL OF ENGINEERING

Transactions C: Aspects

DIRECTOR-IN-CHARGE

H. Omidvar

EDITOR IN CHIEF

G. D. Najafpour

ASSOCIATE EDITOR

A. Haerian

EDITORIAL BOARD

- | | | | |
|------|--|-------|--|
| S.B. | Adeloju, Charles Sturt University, Wagga, Australia | A. | Mahmoudi, Bu-Ali Sina University, Hamedan, Iran |
| K. | Badie, Iran Telecomm. Research Center, Tehran, Iran | O.P. | Malik, University of Calgary, Alberta, Canada |
| M. | Balaban, Massachusetts Ins. of Technology (MIT), USA | G.D. | Najafpour, Babol Noshirvani Univ. of Tech., Babol, Iran |
| M. | Bodaghi, Nottingham Trent University, Nottingham, UK | F. | Nateghi-A, Int. Ins. Earthquake Eng. Seis., Tehran, Iran |
| E. | Clausen, Univ. of Arkansas, North Carolina, USA | S. E. | Oh, Kangwon National University, Korea |
| W.R. | Daud, University Kebangsaan Malaysia, Selangor, Malaysia | M. | Osanloo, Amirkabir Univ. of Tech., Tehran, Iran |
| M. | Ehsan, Sharif University of Technology, Tehran, Iran | M. | Pazouki, MERC, Karaj, Iran |
| J. | Faiz, Univ. of Tehran, Tehran, Iran | J. | Rashed-Mohassel, Univ. of Tehran, Tehran, Iran |
| H. | Farrahi, Sharif University of Technology, Tehran, Iran | S. K. | Sadrnezhaad, Sharif Univ. of Tech, Tehran, Iran |
| K. | Firoozbakhsh, Sharif Univ. of Technology, Tehran, Iran | R. | Sahraeian, Shahed University, Tehran, Iran |
| A. | Haerian, Sajad Univ., Mashhad, Iran | A. | Shokuhfar, K. N. Toosi Univ. of Tech., Tehran, Iran |
| H. | Hassanpour, Shahrood Univ. of Tech., Shahrood, Iran | R. | Tavakkoli-Moghaddam, Univ. of Tehran, Tehran, Iran |
| W. | Hogland, Linnaeus Univ, Kalmar Sweden | T. | Teng, Univ. Sains Malaysia, Gelugor, Malaysia |
| A.F. | Ismail, Univ. Tech. Malaysia, Skudai, Malaysia | P. | Tiong, Nanyang Technological University, Singapore |
| M. | Jain, University of Nebraska Medical Center, Omaha, USA | X. | Wang, Deakin University, Geelong VIC 3217, Australia |
| M. | Keyanpour rad, Materials and Energy Research Center, Karaj, Iran | H. | Omidvar, Amirkabir Univ. of Tech., Tehran, Iran |

EDITORIAL ADVISORY BOARD

- | | | | |
|-------|--|-------|---|
| S. T. | Akhavan-Niaki, Sharif Univ. of Tech., Tehran, Iran | A. | Kheyroddin, Semnan Univ., Semnan, Iran |
| M. | Amidpour, K. N. Toosi Univ of Tech., Tehran, Iran | N. | Latifi, Mississippi State Univ., Mississippi State, USA |
| M. | Azadi, Semnan university, Semnan, Iran | H. | Oraee, Sharif Univ. of Tech., Tehran, Iran |
| M. | Azadi, Semnan University, Semnan, Iran | S. M. | Seyed-Hosseini, Iran Univ. of Sc. & Tech., Tehran, Iran |
| F. | Behnamfar, Isfahan University of Technology, Isfahan | M. T. | Shervani-Tabar, Tabriz Univ., Tabriz, Iran |
| R. | Dutta, Sharda University, India | E. | Shirani, Isfahan Univ. of Tech., Isfahan, Iran |
| M. | Eslami, Amirkabir Univ. of Technology, Tehran, Iran | A. | Siadat, Arts et Métiers, France |
| H. | Hamidi, K.N.Toosi Univ. of Technology, Tehran, Iran | C. | Triki, Hamad Bin Khalifa Univ., Doha, Qatar |
| S. | Jafarmadar, Urmia Univ., Urmia, Iran | | |

TECHNICAL STAFF

M. Khavarpour; M. Mohammadi; V. H. Bazzaz, R. Esfandiar; T. Ebadi

DISCLAIMER

The publication of papers in International Journal of Engineering does not imply that the editorial board, reviewers or publisher accept, approve or endorse the data and conclusions of authors.

CONTENTS

Transactions C: Aspects

I. E. Luc, E. D. Jean-François, M. Jacques, Y. S. Joe	New Approach of Deployment of the Multi-static Radars Based on an Aperture Angle and the Probability of False Alarm	1589-1596
A. R. Joshi, S. Patel	Application of Class C Fly Ash and Quarry Dust Mix for Utilization as Subbase Material in Flexible Pavement	1597-1604
D. G. Petrakov, A. V. Loseva, N. T. Alikhanov, H. Jafarpour	Standards for Selection of Surfactant Compositions used in Completion and Stimulation Fluids	1605-1610
B. Asghari Beirami, M. Mokhtarzade	Land Covers Classification from LiDAR-DSM Data Based on Local Kernel Matrix Features of Morphological Profiles	1611-1617
F. Fouladinia, M. Gholami	Decimal to Excess-3 and Excess-3 to Decimal Code Converters in QCA Nanotechnology	1618-1625
B. Hazrati Dorigh, E. Khakzadeh, I. Ahadzadeh, R. Salamat-Ahanghari	Non-destructive Corrosion Monitoring of Reinforced Concrete Steel Rebars in Chloride Media by Smartphone Magnetic and Analog Hall-Effect Sensors	1626-1635
A. Hatif Obaid, A. A. Jaafar, E. Noroozinejad Farsangi	Experimental Investigation of Brick-Slabs: Evaluation of the Performance and Ductility of Various Brick Materials	1636-1644
A. W. Al-Bayati, M. A. AL-Neami, F. H. Rahil	Experimental Work on the Effect of Under-reamed Pile Geometry on the Pullout Capacity of Sand	1645-1651
E. Radhamma, D. Vemana Chary, A. Krishnamurthy, D. Venkatarami Reddy, D. Sreenivasa Rao, Y. Gowthami, B. Balaji	Performance Analysis of High-K Dielectric Heterojunction High Electron Mobility Transistor for RF Applications	1652-1658
B. Patel, U. K. Dewangan	Mode Shape Change Based System Identification: An Improvement using Distribute Computing and Roving Technique	1659-1666
I. E. K. Mekki, A. Kessar, R. Mouaz	Design of a Printed Circuit Board for Real-time Monitoring and Control of Pipeline's Cathodic Protection System via IoT and a Cloud Platform	1667-1676

A. Amrullah, O. Farobie, W. Fatriasari	Catalytic Upgrading of Bio-oil from <i>Ulva lactuca</i> using Amberlyst-15 Catalyst: Experimental and Kinetic Model	1677-1685
S. Lamultree, M. Phalla, P. Kunkritthanachai, C. Phongcharoenpanich	Design of a Circular Patch Antenna with Parasitic Elements for 5G Applications	1686-1694
S. Honarmandnia, H. Shahrajabian	Effect of nGO on Morphology, Mechanical Properties and Thermal Behavior of PLA/nGO Sheets Before and After Thermoforming: An Experimental Study	1695-1703
M. Sadeghian Kerdabadi, R. Ghazizadeh, H. Farrokhi, M. Najimi	Joint Sensing Times Detection Thresholds and Users Association Optimization in Multi-Channel Multi-Antenna Cognitive Radio Networks	1704-1719



New Approach of Deployment of the Multi-static Radars Based on an Aperture Angle and the Probability of False Alarm

I. E. Luc^{*a}, E. D. Jean-François^{a,b,c}, M. Jacques^b, Y. S. Joe^d

^a *Technology and Applied Sciences Laboratory, University Institute of Technology of Douala, University of Douala, Douala, Cameroon*

^b *Laboratory of Energy, Materials, Modeling and Methods, National Higher Polytechnic School of Douala, University of Douala, Douala, Cameroon*

^c *Department of Electrical Engineering, Advanced Teachers' Training College for Technical Education, University of Douala, Douala, Cameroon*

^d *Department of Physics and Astronomy, Ball State University, Muncie, IN 47306, USA*

PAPER INFO

Paper history:

Received 31 March 2023

Received in revised form 09 May 2023:

Accepted 24 May 2023

Keywords:

Aperture Angle

Probability of False Alarm

Multi-static Radar

Sensor Spacing

Tomographic Resolution

ABSTRACT

This article proposes a new engineering approach to detect targets using multi-static radars. It considers the aperture angle and the probability of false alarm of detection which allow to improve the performances of the radar system deployment. This proposed method is tested on three tomographic modes of multi-static radars: Single Input Multiple Output (SIMO), Multiple Input Multiple Output (MIMO), and Synthetic Aperture Radar (SAR). In this work, a calculation and estimation method for the parameters (spacing sensor and tilt angle of baseline) are developed using the deployment of the radar system based on geometrical arrangements. Employing these parameters, estimated by the proposed approach, and using them for the calculation of the tomographic resolution, the nearest ambiguity location, and the scan loss which are radar deployment performances. The results show that the spacing between sensors varies from 40 to 70% with an increment of aperture angle from 15° to 30° and the step of 10⁻³ variation in the false alarm probability of detection. The length of the radar system deployment is also reduced by 6.66%. This approach improves the capabilities of distinction of the targets in a multi-static radar system and allows a reduction in deployment costs.

doi: 10.5829/ije.2023.36.09c.01

1. INTRODUCTION

The range resolution can be enhanced by decreasing the bandwidth, which depends on the transmit array geometry. The achievable resolution of the estimation direction depends on the receive array geometry [1]. Multi-static radars studies formed into array created several works based on the estimation methods of the arrived angles of signals (by coupling them with the types of the sensor's radars) [2-6], the geometrical form of deployment of these sensors [7, 8], and the slope angle of the radiation pattern [9, 10]. It is the case introduced by Shen and Wang [7], which they have used planar geometry in order to solve the problem of extraction of poles in 2-D. The circular geometry coupled with the Bayesian method [8] and a linear geometry formed of monostatic radars [2, 3] are used in considering the arrived angles of signals.

Nowadays, the improvement of the performance of a radar system is based on the algorithms for the targets detection and on the deployment environments [11-13]. There are several parameters which allow to evaluate the performances emanating from the radar equation [14]. The performance can also be analyzed according to technologies which are characteristic of the nature of the used signals for the transmitters [15]. Thus, criteria such as resolution can be used to determine the ability of a radar to identify several distinct targets [16] and the location of the nearest ambiguity can be used to determine how far away the radar can detect the next ambiguity or replica [17]. In addition to these parameters, we also have the probability of detection which is the possibility that a radar receives the echo of a target compared to the noise [18, 19]. All the multi-static radar systems have parameters of deployment such as spacing between the sensors, the physical angle of slope, the slope

*Corresponding Author Email: eyembeluc@yahoo.fr (I. E. Luc)

compared to the base line, and the number of sensor's radars for the formation of the array [17]. Multi-static radars is primarily formed of phased antenna arrays [20-23] and spacing between them is estimated in wavelength [24]. This method works well for small-scale deployments at large frequencies, requiring small antennas [19, 25, 26]. However, for large-scale deployments, such as satellite radar platforms, it is difficult to determine the wavelength spacing [27]. Moreover, development of consumer loyalty of the sensors decreases the fidelity of the simulated scene as well as the complexity of the formation geometry, which is a problem.

This paper aims to target detection in multi-static radars which mainly focus on the specific interesting area. The approach used consider the aperture angle and the probability of false alarm detection in order to improve the performance of the radar system such as tomographic resolution, location of the nearest ambiguity, and scanning losses.

This article is organised as follows: The first section is based on the introduction. Second section explains the problem, materials technique, along with some working assumptions, and a suggested solution is offered. Section 3 presents the findings and related discussion. Conclusions are provided in section 4.

2. MATERIALS METHOD

2. 1. Problem Description

Let us consider an imagery tomographic system for multi-static radar represented in Figure 1. The system is placed in space up to altitude H and is composed of N identical sensors radars having a regular spacing d and deployed on the $N \times d$ distance. θ represents the angle of sight compared to the ground, Ω is the aperture angle of the sensor radar, ε is the tilt angle compared to the base line and D is the range of the radar following the r direction. The geometry of deployment in Figure 1 admits a symmetry at the level of the placement of the sensor's radars. The radar's sensors are assumed to be distributed along a line in the across-track plane and can transmit and receive or be received-only depending on the tomographic mode (SIMO, SAR and MIMO). The quality of 2-D tomographic images on the ground-range (vertical and horizontal) plane depends on the tomographic performance along the look direction r and along n (perpendicular to look direction), which are coupled via the angle of sight and the local terrain slope μ . Therefore, in addition to resolution and ambiguity along n , ambiguity along r and range resolution were also included. The resolution in distance is a function of the bandwidth of transmission and it is expressed in Equation (1):

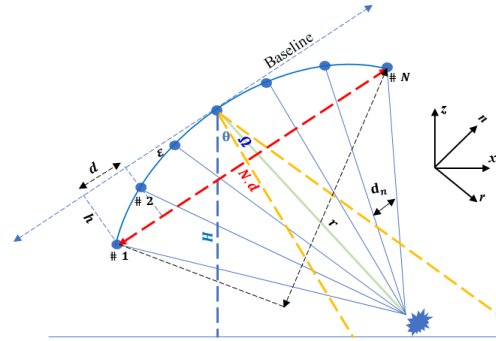


Figure 1. Multi-static observation geometry, relevant parameters, and spatial directions

$$\delta_r = \omega_r \frac{c}{2B} \quad (1)$$

where c is the speed of the light in the vacuum, B is the bandwidth of the transmitted signal, and ω_r is the coefficient of expansion applied to reduce the side lobes by considering the effects of fenestration.

The performances of the multi-static radars depend on two parameters: the spacing between the sensors and the tomographic resolution along the normal direction (n) in the plane, which depends on the maximum length of the basic deployment. Its equation is similar to the equation of resolution of the SAR, the synthetic aperture length replaced by the basic tomographic deployment length δ_n :

$$\delta_n = \omega_n \frac{\lambda D}{\rho_n L_n} \quad (2)$$

where λ is the wavelength, $D = \frac{H}{\cos \theta}$ is the range of the sensor radars which is the center of symmetry of the architecture, $L_n = N \cdot d \cdot \cos(|\theta - \omega|)$ is the perpendicular maximum length of the base line $\omega_n = \omega_r$.

While replacing L_n in the expression (2), we obtained:

$$\delta_n = \frac{\omega_n}{p_\delta} \frac{\lambda H}{N \cdot d \cdot \cos(|\theta - \omega|) \cos \theta} \quad (3)$$

where p_δ is the coefficient of resolution depending on the multi-static mode.

Platform spacing that is periodic leads to ambiguous returns, often known as target replicas [28, 29]. The closest (relative to the real target) ambiguity's position is crucial since it helps define how much of the target may be photographed without copies overlapping. It should be noted that ambiguous copies of targets outside the scene of interest might nonetheless fall within the scene of interest, even if the scene of interest is smaller than the position of the nearest ambiguity. The closest ambiguity for a flat surface, according to Seker and Lavalle [17], is at:

$$A_n^1 = \pm \frac{\lambda H}{p_a d_n \cos \theta} \quad (4)$$

where p_a is the coefficient of localization of an ambiguity and $d_n = d \cos(|\theta - \omega|)$.

Here, the spacing d between sensor's radars is generally determined by deployments requiring large spacings such as satellites by:

$$dx = \frac{2 \cdot v \cdot PRI}{\psi} \quad (5)$$

where v is the orbital velocity, PRI is the pulse repetition interval and ψ is a factor to reduce the pulse repetition rate. The systems, which use Equation (5) to make the deployment, encounter the problem of radar fidelity on the area of interest involving noise due to the signals of the replicas.

2.2. Proposed Solution To solve the radar retention problem in the target area, the probability of false detection alarm and the aperture angle on radar system were used. The probability α of false alarm is defined as the probability that a sample of the signal $r(t)$ will exceed the threshold of tension V_T when the noise alone is present in the radar:

$$\alpha = \int_{V_T}^{\infty} \frac{r}{\sigma^2} \exp\left(-\frac{r^2}{2\sigma^2}\right) dr = \exp\left(-\frac{V_T^2}{2\sigma^2}\right) \quad (6)$$

where $V_T = \sqrt{2\sigma^2 \ln\left(\frac{1}{\alpha}\right)}$ and σ is the variance.

Figure 2 shows the evolution of the probability of detection according to the signal to noise ratio (SNR) under several values of the probability of false alarm. We observe that the probability of false alarm influences the capacity of a receiver radar in the sense that as α becomes small, the ratio signal to noise increases. This also effected on the parameters of deployment and the performances.

In the case of antennae having only one beam, the aperture angle of the beam represents the solid angle through which all the power radiated by the antenna is concentrated. This aperture angle of the beam, Ω_a , is given by:

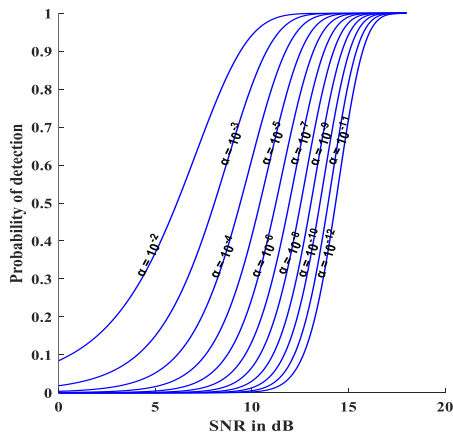


Figure 2. Probability of detection

$$\Omega_a = \oint K_n(\theta, \phi) d\Omega. \quad (7)$$

The probability of false alarm detection and the aperture angle of a radar are used to determine the spacing between the radars as follows.

Let us consider a multi-static system formed of N aligned sensors radars and the aperture angle Ω as illustrated in Figure 3. By considering the triangles (OEB) and (OAB) , we can express $\cos(\Omega/2)$ in the form as $\cos(\Omega/2) = OB/OE$ and $\cos(\Omega/2) = OA/OB$, respectively.

By multiplying the two values, we obtained:

$$\cos^2\left(\frac{\Omega}{2}\right) = \frac{OA}{OE} \quad (8)$$

where $OA = OE \cos^2\left(\frac{\Omega}{2}\right)$ and $OE = \alpha D$. In the triangle (OAB) , we have $d = OA \tan\left(\frac{\Omega}{2}\right)$ with $AB = d$. Now, we obtained a regular spacing d between the sensors as follows:

$$d = \alpha D \cos\left(\frac{\Omega}{2}\right) \sin\left(\frac{\Omega}{2}\right) \quad (9)$$

In our case, we proposed to use an elliptic architecture (Figure 1) having the length of the semi-major and semi-minor axes a and b : $a = \frac{N \cdot d}{2}$ and $b = h$, where $h < \frac{N \cdot d}{2}$.

In this architecture, we have an angle of the curve ε which is formed between the baseline and symmetrical elliptic architecture. This angle can be expressed in the form:

$$\varepsilon = \tan^{-1}\left(\frac{2h}{d(N-1)}\right) \quad (10)$$

By replacing d by its equation (10), we have:

$$\varepsilon = \tan^{-1}\left(\frac{2h}{(N-1)\alpha D \cos\left(\frac{\Omega}{2}\right) \sin\left(\frac{\Omega}{2}\right)}\right) \quad (11)$$

Here, ε represents necessary calibration to better deploy a satellite radar system on the basis of the principle that the ground has an elliptic form. For primarily reasons related to the practice, it is necessary that $h \leq \alpha D$. In the tomographic radars the formation of

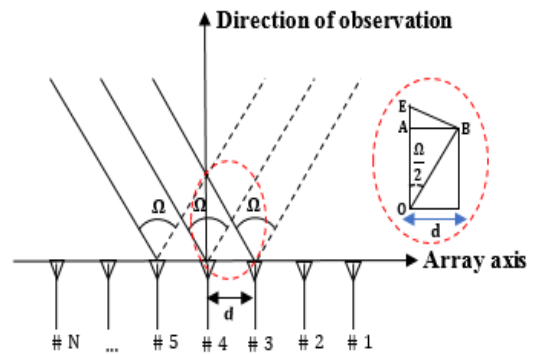


Figure 3. Geometry for calculation of spacing

the spotlight is very significant; this is why the designers find the compromise between the adequate spacing of the sensors radars in term of the value of d and the angle slope compared to the normal of the direction of observation φ . We can thus determine φ by the following relation:

$$\varphi = \frac{\pi}{N-1} \tag{12}$$

Equation (3) presents the parameters entering the determination of the tomographic resolution without considering the probability of a false alarm and the aperture angle. Thus, we propose to insert d of Equation (9) into Equation (3), we obtained then:

$$\delta_n = \frac{\omega_n}{p_\delta} \frac{\lambda}{\alpha \cos(\frac{\Omega}{2}) \sin(\frac{\Omega}{2}) N \cos(|\theta - \omega|)} \tag{13}$$

Equation (13) allows to focus on the zone delimited by the aperture angle of the sensor radar to avoid having information about the not targeted zones which are sources of perturbations.

Equation (4) does not integrate the aperture angle and the probability of false alarm and the probability of having replicas which are not in the zone of interest. While substituting Equation (9) into Equation (4), the nearest ambiguity with the aperture angle and the probability of false alarm is obtained by:

$$A_n^1 = \pm \frac{\lambda}{p_\alpha \alpha \cos(\frac{\Omega}{2}) \sin(\frac{\Omega}{2}) \cos(|\theta - \omega|)} \tag{14}$$

3. RESULTS AND DISCUSSION

Figure 4 represents the evolution of spacing between the sensors as a function of the range of the radar (up to 800 km) for four values of the probability of false alarm of the detection of order 10^{-3} under three different apertures angles. The numerical results show that the spacing between the sensors varies when both the probability of false alarm detection and the apertures angle changes.

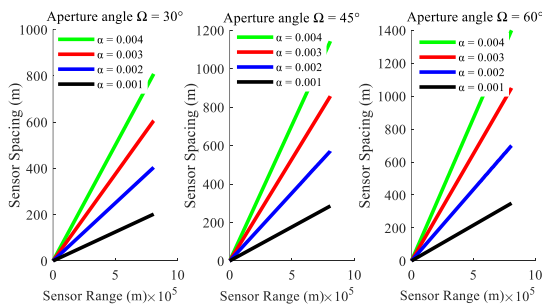


Figure 4. Evolution of spacing between the sensor’s vs radar sensor range for four values of the probability of false alarm detection under three different apertures angles

Note that variations of spacing between the probabilities of false alarm are 200 m for $\Omega = 30^\circ$, 285 m for $\Omega = 45^\circ$, and 350 m for $\Omega = 60^\circ$, respectively.

When the probability of false alarm detection becomes extremely small for a fixed apertures angle, this variability of spacing is decreasing. The percentage in the increase of spacing radar sensor vs. the probability of false alarm detection under three apertures angles is shown in Figure 5. When the aperture angle of reference is taken as $\Omega = 30^\circ$, an increase in average distance for the tested values of α is about 41% as Ω varies from 30° to 60° and 73% as Ω varies from 30° to 60° .

The tilted angle of the base line as a function of the spacing of the sensor’s radars is presented in Figure 6 for four different probabilities of false alarm (detection of order 10^{-3} under three different apertures angles). This angle, used in Equation (12), is the angular variation of the normal (r direction) towards the base line.

Note that the angle of inclination of the baseline decreases when the aperture angle increases and the probability of false alarm increases. We find that the variations in angle between the probabilities of false alarm is 7° for $\Omega = 30^\circ$, 9° for $\Omega = 45^\circ$, and 10° for $\Omega = 60^\circ$. Figure 7 presents the percentage decrease in the tilted baseline angle vs the probability of false alarm using the same parameters Figure 6. Percentage of

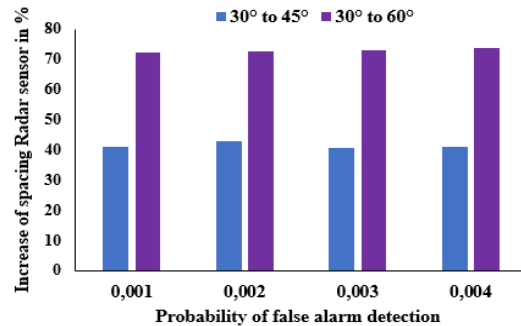


Figure 5. Percentage in the increase of spacing radar sensor vs. the probability of false alarm detection under three apertures angles

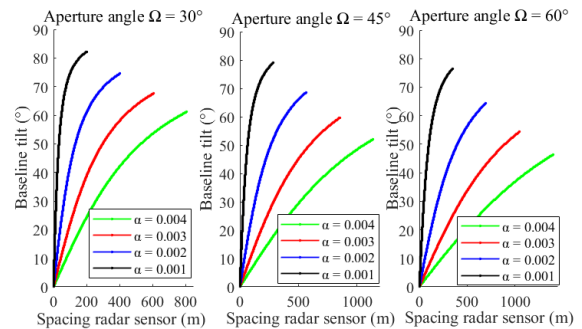


Figure 6. Evolution of the tilted angle of the baseline vs. the spacing of the sensor’s radars

increase in spacing radar sensor vs. the probability of false alarm detection under three apertures angles in Figure 7. Observe that with a reference of the aperture angle $\Omega = 30^\circ$, the percentage in the angle of inclination of the base line decreases according to the decrease of α and the growth of Ω .

Figure 8 presents the tomographic resolution with a bilateral resolution of 4 dB under various multi-static modes of radars. In the two left figures of Figure 8, three dashed lines are obtained with parameter values of $\theta = 30^\circ, \epsilon = 30^\circ$ (Figure 8(a)) and $\theta = 60^\circ, \epsilon = 60^\circ$ (Figure 8(b)) [17].

In the meantime, we add the aperture angle $\Omega = 30^\circ$ (Figure 8(a)) and $\Omega = 60^\circ$ (Figure 8(b)) and obtain the tomographic resolution for three multi-static modes (three solid lines). In the two right figures of Figure 9, it is exactly the same situation as the two left ones of Figure 9 except that we have different values of the tilted angle of the baseline, $\epsilon = 60^\circ$ (Figure 8(a)) and $\epsilon = 45^\circ$ (Figure 8(b)).

We obtained a spacing between radars $d=1400$ m using our approach, whereas $d=1500$ m is used by Seker and Lavalle [17]. We note here that when $\theta = 30^\circ, \epsilon = 30^\circ$ or $\theta = 60^\circ, \epsilon = 60^\circ$, the resolution is the same even if we include the aperture angle in our calculation (two

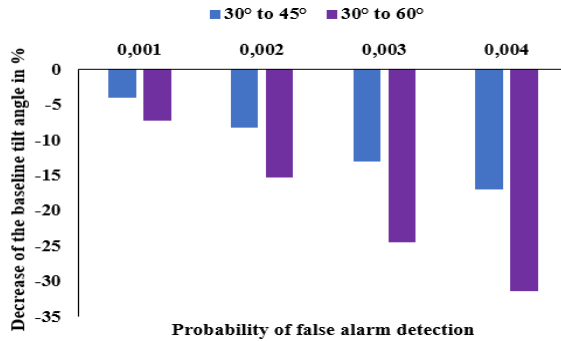
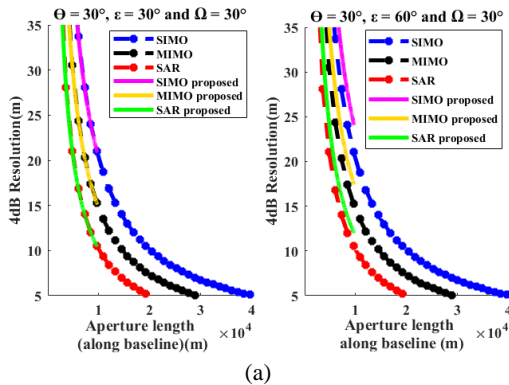
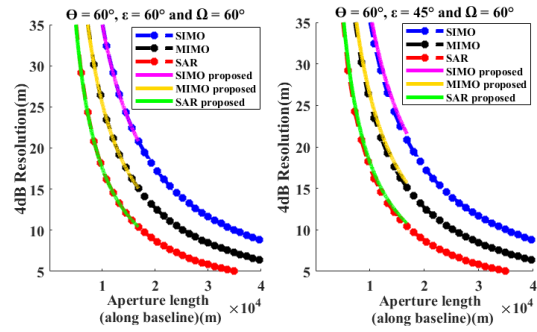


Figure 7. Percentage in the tilted angle of the baseline vs. the probability of false alarm of detection under three apertures angles



(a)



(b)

Figure 8. Tomographic resolution vs. aperture length for look angle: (a) $\theta = 30^\circ$ and (b) $\theta = 60^\circ$

left figures of Figure 9). When we consider $\epsilon = 60^\circ$ the aperture angle $\Omega = 60^\circ$ with $\theta = 60^\circ, \epsilon = 45^\circ$, however, we obtained a resolution increase of 1.84 m in mode SIMO, of 1.6 m in mode MIMO, and of 1.05 m in mode SAR for an aperture length of 10 km. (right figure of Figure 9(b)). In the case of $\Omega = 30^\circ$ with $\theta = 30^\circ$, we have a resolution increase of 5.14 m in mode SIMO, of 3.52m in mode MIMO, and of 2.58 m in mode SAR when a length of aperture is 10 km (right figure of Figure 8 (a)).

The localization of the nearest ambiguity as a function of the spacing to sensor's radars for a probability of false alarm of detection $\alpha = 4 \times 10^{-3}$ is shown in Figure 10. Here, Figure 9(a) is obtained with the same parameters as reported by Seker and Lavalle [17] and Figure 9(b) presents the localization of nearest ambiguity while applying Equations (3) and (14). It is interesting to note that we have the same results when we changed the basic angle of slope. We obtained a better localization of the zone of interest by taking into account the aperture angle and the probability of false alarm detection in the determination of the localization of the nearest ambiguity corresponding to the selected spacing. This allows to fight against the problem of the replicas that we meet out of tomographic radars.

Figure 10 represents the amplitude of the power reflected by the target and received by the receivers for the SIMO, MIMO, and SAR modes. Observe that the amplitude peaks reproduce in a specific distance to the SIMO, MIMO and SAR corresponding to the resolution estimated in left-side of Figure 8(b). The system in SIMO mode detects two separate targets at 10 m and 20 m while the two others are at 15 m and 21 m, respectively.

We noted a maximum level of sidelobe is -15 dB in the MIMO and SAR system and -10 dB in the SIMO system. The effects of the aperture angle and the probability of false alarm of detection allow to improve the precision of the parameter values in the multi-static radar system.

Table 1 compares the values for Theoretical Resolution 4dB (TR4dB), Theoretical Ambiguity

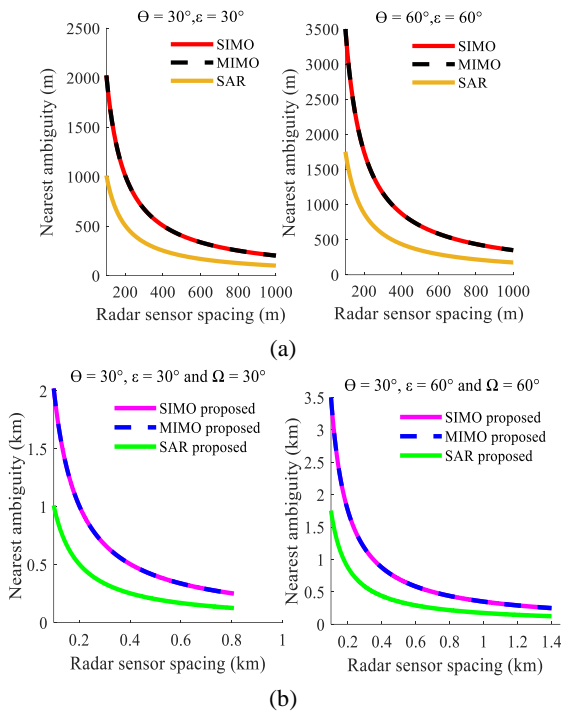


Figure 9. Nearest ambiguity location vs. platform spacing for two different cases, (a) as per [17] and (b) as per Equation (14)

Location (TAL), and Maximum Sidelobe Level (MLS). This comparison is done between the suggested approach and that presented in the literature [17]. The suggested method is less effective in the 4dB resolution than [17], and this is also true for the sidelobe level.

This approach improves the literature in terms of ambiguity location and enables, through the introduction of the false alarm probability and the aperture angle, to have a spacing that allows for the achievement of a high signal-to-noise ratio, thereby limiting the impact of the replicas that raise the noise level and lower the detection capability of two targets when they are close to one another.

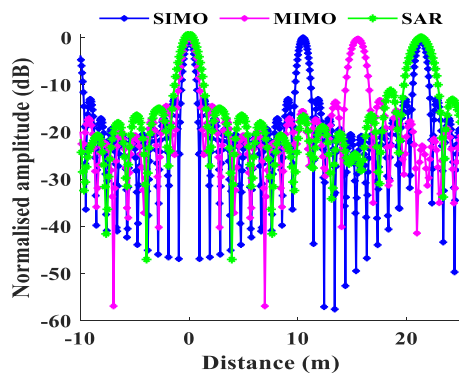


Figure 10. Tomographic “images” in 1-D for the SAR, SIMO, and MIMO modes

TABLE 1. Comparison of results

	Ref. [17]		Proposed approach			
	Spacing = 1500 m			Spacing = 1400		
	SAR	SIMO	MIMO	SAR	SIMO	MIMO
TR 4dB	4.9 m	9.7 m	7.0 m	6.5 m	13 m	9.5 m
TAL	58 m	117 m	117 m	10 m	15 m	21 m
MLS	-13 dB	-13 dB	-26 dB	-13 dB	-13 dB	-15 dB

4. CONCLUSION

In conclusion, we have considered the aperture angle and the probability of false alarm detection in the estimation of the parameters of deployment in order to improve the multi-static performances of the radars. This new approach has allowed to develop an estimation method for the spacing between the sensor’s radars for deployments on a large scale and the angle of slope of the baseline. The performance evaluations with the aperture angle and the probability of false alarm of detection such as the resolution, the ambiguity and the scan loss have been examined. We also determined the physical angle of slope allowing the sensor’s radars to form a spotlight. Our approach was tested under three multi-static modes of radars. The results showed that the multi-static performances of the radars, like their deployment, were improved. In addition, it solves the problems related to the complexity of the deployment geometries in the multi-static radar systems. In particular, the SAR, which has realistic values of resolution, locates on the area covered by the spotlight formed by several sensors in order to avoid noise due to areas of no interest.

Future research on the optimal estimation of the tilt angle of the baseline and the aperture angle to make a better compromise to reduce the losses of scanning and to make an experimental study by applying our approach will be necessary.

5. REFERENCES

- Hyder, M.M., Mahata, K. and Hasan, S.M., "A new target localization method for bistatic fda radar", *Digital Signal Processing*, Vol. 108, (2021), 102902. doi: 10.1016/j.dsp.2020.102902.
- Li, Z. and Zhang, X., "Monostatic mimo radar with nested l-shaped array: Configuration design, dof and doa estimation", *Digital Signal Processing*, Vol. 108, (2021), 102883. doi: 10.1016/j.dsp.2020.102883.
- Wen, F., Mao, C. and Zhang, G., "Direction finding in mimo radar with large antenna arrays and nonorthogonal waveforms", *Digital Signal Processing*, Vol. 94, (2019), 75-83. doi: 10.1016/j.dsp.2019.06.008.
- Jia, Y., Chen, C., Zhong, X., Yan, C., Duo, B. and Guo, Y., "Doa estimation of coherent and incoherent targets based on monostatic co-prime mimo array", *Digital Signal Processing*, Vol. 94, (2019), 56-66. doi: 10.1016/j.dsp.2019.06.004.

5. Tian, Y., Lian, Q. and Xu, H., "Mixed near-field and far-field source localization utilizing symmetric nested array", *Digital Signal Processing*, Vol. 73, (2018), 16-23. doi: 10.1016/j.dsp.2017.10.021.
6. Huang, Y., Liao, G., Li, J., Li, J. and Wang, H., "Sum and difference coarray based mimo radar array optimization with its application for doa estimation", *Multidimensional Systems and Signal Processing*, Vol. 28, (2017), 1183-1202. doi: 10.1007/s11045-016-0387-2.
7. Shen, H. and Wang, B., "Two-dimensional unitary matrix pencil method for synthesizing sparse planar arrays", *Digital Signal Processing*, Vol. 73, (2018), 40-46. doi: 10.1016/j.dsp.2017.10.019.
8. Behmandpoor, P. and Haddadi, F., "Circular array design based on bayesian cramer-rao bound", *Multidimensional Systems and Signal Processing*, Vol. 31, (2020), 317-328. doi: 10.1007/s11045-019-00668-1.
9. Wang, W., Ren, S. and Chen, Z., "Unified coprime array with multi-period subarrays for direction-of-arrival estimation", *Digital Signal Processing*, Vol. 74, (2018), 30-42. doi: 10.1016/j.dsp.2017.11.015.
10. Wang, W., Zhang, Q., Tan, W., Shi, W. and Pang, F., "Direction finding via acoustic vector sensor array with non-orthogonal factors", *Digital Signal Processing*, Vol. 108, (2021), 102910. doi: 10.1016/j.dsp.2020.102910.
11. Ahmad, F. and Amin, M.G., "A noncoherent approach to radar localization through unknown walls", in 2006 IEEE Conference on Radar, IEEE. (2006).
12. Rabe, H., Denicke, E., Armbrrecht, G., Musch, T. and Rolfes, I., "Considerations on radar localization in multi-target environments", *Advances in Radio Science*, Vol. 7, (2009), 5-10. doi: 10.5194/ars-7-5-2009.
13. Schreiber, R. and Bajer, J., "Time difference measurement algorithm for tdoa positioning system using rtl-sdr", in 2017 International Conference on Military Technologies (ICMT), IEEE. (2017), 608-612.
14. George, B.A., Obot, A.B. and Udofia, K.M., "Modelling and performance evaluation of ground based monostatic radar surveillance system", *Communications*, Vol. 7, (2019), 17-21.
15. Yang, J., Qiu, Z.-K., Li, X. and Zhuang, Z.-W., "Uncertain chaotic behaviours of chaotic-based frequency-and phase-modulated signals", *IET Signal Processing*, Vol. 5, No. 8, (2011), 748-756. doi: 10.1049/iet-spr.2010.0096.
16. Grasso, M., Renga, A., Fasano, G., Graziano, M., Grassi, M. and Moccia, A., "Design of an end-to-end demonstration mission of a formation-flying synthetic aperture radar (ff-sar) based on microsattelites", *Advances in Space Research*, Vol. 67, No. 11, (2021), 3909-3923. doi: 10.1016/j.asr.2020.05.051.
17. Seker, I. and Lavalle, M., "Tomographic performance of multi-static radar formations: Theory and simulations", *Remote Sensing*, Vol. 13, No. 4, (2021), 737. doi: 10.3390/rs13040737.
18. Zaimbashi, A. and Li, J., "Tunable adaptive target detection with kernels in colocated mimo radar", *IEEE Transactions on Signal Processing*, Vol. 68, (2020), 1500-1514. doi: 10.1109/TSP.2020.2975371.
19. Golbon-Haghighi, M.-H., Mirmozafari, M., Saeidi-Manesh, H. and Zhang, G., "Design of a cylindrical crossed dipole phased array antenna for weather surveillance radars", *IEEE Open Journal of Antennas and Propagation*, Vol. 2, (2021), 402-411. doi: 10.1109/OJAP.2021.3059471.
20. Fenn, A.J., Temme, D.H., Delaney, W.P. and Courtney, W.E., "The development of phased-array radar technology", *Lincoln Laboratory Journal*, Vol. 12, No. 2, (2000), 321-340.
21. Basit, A., Khan, W., Khan, S. and Qureshi, I.M., "Development of frequency diverse array radar technology: A review", *IET Radar, Sonar & Navigation*, Vol. 12, No. 2, (2018), 165-175. doi: 10.1049/iet-rsn.2017.0207.
22. Jeon, S.-I., Kim, Y.-W. and Oh, D.-G., "A new active phased array antenna for mobile direct broadcasting satellite reception", *IEEE Transactions on Broadcasting*, Vol. 46, No. 1, (2000), 34-40. doi: 10.1109/11.845863.
23. Wei, Y., Zhang, X., Bai, Y. and Tang, L., "A novel range alignment method for isar based on linear t/r array model", *Multidimensional Systems and Signal Processing*, Vol. 25, No. 4, (2014), 759-773. doi: 10.1007/s11045-013-0229-4.
24. Mahafza, B.R., "Radar signal analysis and processing using matlab, CRC Press, (2016).
25. Sridher, T., Sarma, A. and Naveen Kumar, P., "Performance evaluation of onboard wi-fi module antennas in terms of orientation and position for iot applications", *International Journal of Engineering, Transactions A: Basics*, Vol. 35, No. 10, (2022), 1918-1928. doi: 10.5829/IJE.2022.35.10A.11.
26. Kadam, V., Deshmukh, A. and Bhosale, S., "Hybrid beamforming for dual functioning multi-input multi-output radar using dimension reduced-baseband piecewise successive approximation", *International Journal of Engineering, Transactions A: Basics*, Vol. 36, No. 1, (2023), 182-190. doi: 10.5829/IJE.2023.36.01A.20.
27. Madhu Krishna, K. and Naveen Kumar, P., "Improving the position accuracy of rover receiver using differential positioning in indian regional navigation satellite system", *International Journal of Engineering, Transactions C: Aspects*, Vol. 36, No. 3, (2023), 497-504. doi: 0.5829/IJE.2023.36.03C.09.
28. Reigber, A. and Moreira, A., "First demonstration of airborne sar tomography using multibaseline l-band data", *IEEE Transactions on Geoscience and Remote Sensing*, Vol. 38, No. 5, (2000), 2142-2152.
29. Moreira, A., Prats-Iraola, P., Younis, M., Krieger, G., Hajnsek, I. and Papathanassiou, K.P., "A tutorial on synthetic aperture radar", *IEEE Geoscience and Remote Sensing Magazine*, Vol. 1, No. 1, (2013), 6-43. doi: 10.1109/MGRS.2013.2248301.

COPYRIGHTS

©2023 The author(s). This is an open access article distributed under the terms of the Creative Commons Attribution (CC BY 4.0), which permits unrestricted use, distribution, and reproduction in any medium, as long as the original authors and source are cited. No permission is required from the authors or the publishers.



Persian Abstract

چکیده

این مقاله یک رویکرد مهندسی جدید برای شناسایی اهداف با استفاده از رادارهای چند استاتیکی پیشنهاد می‌کند. زاویه دیافراگم و احتمال هشدار کاذب تشخیص را در نظر می‌گیرد که امکان بهبود عملکرد استقرار سیستم رادار را فراهم می‌کند. این روش پیشنهادی بر روی سه حالت توموگرافی رادارهای چند استاتیکی آزمایش می‌شود: خروجی چندگانه ورودی (SIMO)، خروجی چندگانه ورودی (MIMO)، و رادار دیافراگم مصنوعی (SAR) در این کار، یک روش محاسبه و تخمین برای پارامترها (حسگر فاصله و زاویه شیب خط مبنا) با استفاده از استقرار سیستم رادار بر اساس آرایش‌های هندسی توسعه داده شده است. استفاده از این پارامترها، برآورد شده توسط روش پیشنهادی، و استفاده از آنها برای محاسبه وضوح توموگرافی، نزدیکترین محل ابهام، و از دست دادن اسکن که عملکرد استقرار رادار است. نتایج نشان می‌دهد که فاصله بین سنسورها از ۴۰ تا ۷۰ درصد با افزایش زاویه دیافراگم از ۱۵ درجه به ۳۰ درجه و گام تغییرات $[[10^{-3}]]$ در احتمال تشخیص کاذب تغییر می‌کند. طول استقرار سیستم راداری نیز ۶.۶۶ درصد کاهش یافته است. این رویکرد قابلیت‌های تمایز اهداف را در یک سیستم رادار چند استاتیکی بهبود می‌بخشد و امکان کاهش هزینه‌های استقرار را فراهم می‌کند.



Application of Class C Fly Ash and Quarry Dust Mix for Utilization as Subbase Material in Flexible Pavement

A. R. Joshi*, S. Patel

Department of Civil Engineering, Sardar Vallabhbhai National Institute of Technology, Surat, Gujarat, India

PAPER INFO

Paper history:

Received 01 May 2023

Received in revised form 08 June 2023

Accepted 09 June 2023

Keywords:

Fly Ash

Sustainable Material

Subbase

Resilient Modulus

Microstructure

KENLAYER

ABSTRACT

Depleting good quality natural aggregates and soils call for the need of use of industrial by-products and waste materials in road construction. Use of wastes and by-products in road construction consume large quantities and resolve issue of their safe disposal. Class C fly ash is the by-product from thermal power plants while quarry dust is waste left behind during quarrying processes. This study investigated the application of class C fly ash and quarry dust mix for utilization in subbase layer of flexible pavement. The class C fly ash and quarry dust mixed were studied with the help of unconfined compressive strength test, repeated load triaxial test, durability test and microstructural analysis. The mixture of 90% fly ash plus 10% quarry dust was found to be suitable with respect to strength and durability criteria to be used as subbase material in flexible pavement. Owing to the formation of cementitious phases during pozzolanic reaction, proposed mix demonstrated significantly higher resilient modulus than conventional granular subbase material. The service life ratio for pavement with proposed mix is 1.2 and 1.26 in fatigue and rutting respectively compared to conventional pavement. The use of quarry dust and fly ash in large quantities in flexible pavement is an economical as well as sustainable solution for road construction.

doi: 10.5829/ije.2023.36.09c.02

1. INTRODUCTION

Rapid infrastructure development is crucial economic driver and responsible for overall growth of nation. Construction of roads network is one of the prime components of infrastructure sector. The Bharatmala project designed by Government of India aims at vigorous construction of roads, highways, and expressways. The construction of road pavements demands good quality natural aggregates in large quantities. Nowadays, it is difficult to obtain good quality aggregates for road construction due to depleting natural resources [1]. Hence, it is utmost important to use industrial wastes and by products for road construction to minimize requirement of natural resources. Industrial wastes and by-products such as fly ash [2, 3], steel slag [4], copper slag [5], silica fume, ground granulated blast furnace slag (GGBS) [6, 7] are widely used in construction. By-products such as Fly ash, silica fume,

GGBS and rice husk ash are also used as supplementary cementitious materials in construction materials [8,9,10]. Apart from industrial waste, recycled aggregates along with polymers [11] as well as recycled asphalt pavement materials [12] are identified as eco-friendly and feasible materials for replacing conventional natural aggregates in road construction.

Fly ash is one of the industrial by-products which possess pozzolanic properties due to the presence of calcium oxide, silica and alumina which can enhance the properties of soils when used for stabilization purpose [13]. Based on oxide content, fly ashes are classified as classes 'C' and 'F'[14].

Class C fly ashes are self-cementitious and do not require activator for initiation of hydration process. Many researchers have contributed towards utilization of fly ash along with natural aggregates and soils as road embankment, base, subbase, and subgrade materials.

*Corresponding Author Email: joshiamruta89@gmail.com
(A. Ram Joshi)

Class C fly ashes are previously studied for used in embankments, subgrade, base, and subbase of flexible pavement as additive for strength improvement and reduction in expansive properties of soils [15,16]. Class C fly ash was used along with copper slag as pavement base material and the suitability of mix was demonstrated through comparative study of full-scale pavement sections made using conventional material as well as proposed mix in field [17]. The dredged sediments were stabilized using class C fly ash and cement for pavement application. It was found that the strength, resilient modulus and CBR value of sediments were improved in order that the mix was suitable as pavement material [12]. Utilization of reclaimed asphalt pavement material along with class C fly ash was investigated for base application in flexible pavement and was found to be suitable in accordance with the design standards [18]. Use of class C fly ash for stabilization and reuse of reclaimed asphalt pavement materials and recycled concrete aggregates is investigated through freezing and thawing for highway base construction [19]. Addition of class C fly ash to conventional materials used in base and subbase layers cause significant strength improvement and consequently reduction in layer thicknesses. Hence, using class C fly ash in pavement in bulk quantities is economical and sustainable [2].

The quarry dust is coarse material that is generated as a by-product of the crushing process is a material that can be utilized as aggregates, particularly as fine aggregates. The rock is broken down into fragments of varying sizes before it is used in the quarrying process. Quarry dust is a type of waste that is produced as a byproduct of this operation and is referred to as the dust. Therefore, it becomes a material that is of no use and contributes to the pollution of the air. As a result, quarry dust if used in construction projects; can potentially bring about a reduction in the cost of construction, as well as the saving of construction material and the optimal utilization of natural resources. In recent years, many studies are conducted based on utilization of quarry dust for construction purpose [20]. The ferrochrome slag was used along with quarry dust as alternative to conventionally used aggregates in pavement, it was found that the ferrochrome slag and quarry dust mix can be effectively used base and subbase of flexible pavement [21]. Stabilization of soft subgrade was attempted using quarry dust and it was observed that addition of quarry dust to soft soil yielded in higher CBR compared to untreated soil [22]. Quarry dust used for treating expansive clay for road foundation was found to inhibit the swelling properties of clay and an economical for natural soil stabilization for road construction [23].

Class C fly ash is the by-product from thermal power plants and quarry dust is waste produces in aggregate crushing plants. Conventionally used natural aggregates and soil for subbase construction in road is limited and

non-renewable resource. It is the need of the hour to use the waste materials in pavement construction on large scale to cut down the use of depleting natural resources. IRC 37 [24] permits provision of cemented subbase in flexible pavement along with crack relief layer. This study aims to assess the feasibility of use of class C fly ash along with quarry dust as subbase material in flexible pavement.

2. METHODOLOGY

2. 1. Materials As per ASTM D618 [14], fly ash used in this study classifies as class 'C' fly ash. The chemical composition of fly ash is stated in Table 1. The quarry dust used in this study was collected from local aggregate crushing plant in Surat, Gujarat. The quarry dust had particle passing through 1.18mm sieve.

2. 2. Experimental Program For trial mixes, the fly ash was replaced with different percentage of quarry dust equal to 10%, 20%, 40% and 60%. The modified proctor test as per IS 2720-Part 8 [25] was performed on all trial mixed to find out the maximum dry density (MDD) and optimum moisture content (OMC). The mix designations along with description are given in Table 2. Further, cylindrical samples measuring 100mm height and 50mm diameter were cast using the MDD and OMC value for each mix. Such cylindrical specimens were used to perform the unconfined compressive strength (UCS) test on specimens in accordance with IS 2720-Part 10 [26]. Similar cylindrical samples were cast to obtain

TABLE1. Chemical composition of fly ash used in the study

Parameter	Content (%)
SiO ₂	36.8
Al ₂ O ₃	3.82
Fe ₂ O ₃	14.78
CaO	25.12
MgO	0.895
Na ₂ O	0.55
SO ₃	10.03

TABLE 2. Description of mixes used in the study

Mix description	Designation
90% fly ash + 10% quarry dust	C10QD
80% fly ash + 20% quarry dust	C20QD
60% fly ash + 40% quarry dust	C40QD
40% fly ash + 60% quarry dust	C60QD

weight loss upon subjecting to alternate wetting and drying as per ASTM D559 [27]. Based on results of UCS and weight loss, the mix qualifying IRC criteria was chosen for obtaining the resilient modulus (MR) values as per AASHTO T307 [28], which is key parameter for designing the flexible pavement. MR value indicates the response of pavement materials to actual loads imposed on layers due to movement of traffic [29]. The microstructural development of phases within the mix was analyzed using the X-ray Diffraction (XRD) and Scanning electron microscopy (SEM) methods.

3. RESULTS AND DISCUSSION

3.1. Standard Proctor Test Figure 1 shows that as the percentage addition of quarry dust in fly ash increases, the MDD of mix increases. This is due to addition of quarry dust particles which have higher specific gravity than fly ash particles. It can be observed from Figure 1 that the OMC value goes on decreasing with the percentage substitution of fly ash with quarry dust. This is because as soon as water is added to class C fly ash, the pozzolanic reaction initiates. For the pozzolanic reaction to take place, fly ash consumes water. When quarry dust which has non-cohesive fine particles, does not take up water during strength gain. Also, the specific surface of fly ash particles is greater than that of quarry dust particles, hence for achieving maximum dry density, more the fly ash in mix, more will be the amount of water consumed.

3.2. Unconfined Compressive Strength (UCS) Test

Figure 2 shows variation of UCS value for various fly ash – quarry dust mixes obtained after curing for 3, 7 and 28 days. The strength gain within the mixes containing fly ash is attributed to the presence of silica and alumina [30]. It was observed that as the percentage of quarry dust

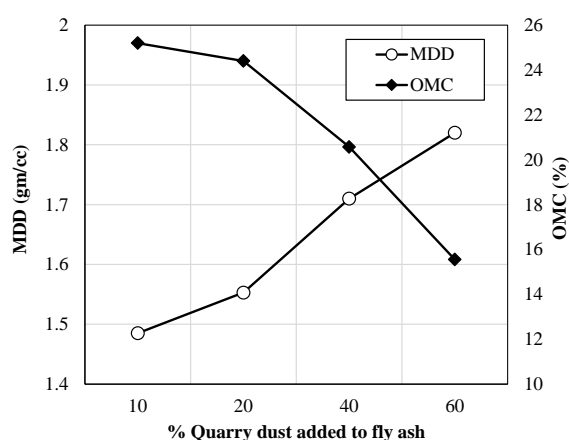


Figure 1. Maximum dry density and optimum moisture content with varying quarry dust addition to fly ash

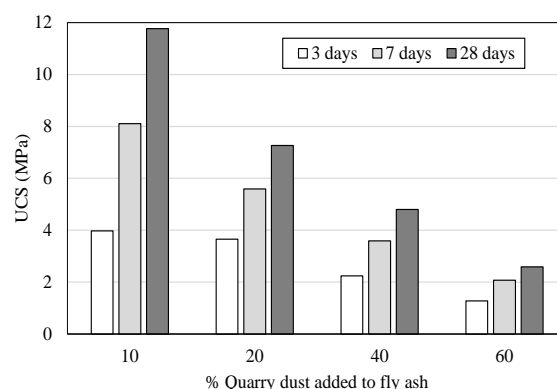


Figure 2. Variation of unconfined compressive strength with varying quarry dust addition to fly ash

addition to fly ash increased, the strength of the mix decreased. This is due to addition of quarry dust increasing the amount of coarser non-cohesive particles in the mix. As the amount of quarry dust increases, the formation of binding gels formed during cementation process in the class C fly ash decreases. Hence, for the C10QD mix, the UCS values are higher at 3, 7 and 28 days than other that for C20QD, C30QD, C40QD mixes. According to IRC 37 [24], the subbase material for flexible pavements must have a minimum UCS of 7 MPa after 7 days of curing. Therefore, the mix containing C10QD mix meets the requirements specified by IRC 37 [24] for the use in subbase.

3.3. Durability Test

The weight loss after 12 alternate wetting and drying cycles as per ASTM D559 [27], the % weights lost for all mixes are shown in Table 3. Weight loss during a durability test for material intended for the use as subbase of flexible pavement should not exceed 14%, following IRC 37 [24]. For its part, C10QD not only outperforms C20QD, C30QD AND C40QD in terms of durability but also meets the requirements set forth by IRC 37 [24]. C40QD does not meet the durability criteria for subbase application.

3.4. Repeated Load Triaxial Test

The C10QD mix satisfied both strength and durability criteria to be used as subbase material in flexible pavement, hence the repeated triaxial load test was performed on this mix after initial 7 days of curing and the results were compared to conventional GSB. For the subbase of typical flexible pavement, confining pressure of 34.5 kPa and deviator stress of 103.5 kPa were estimated [31]. For this reason, the resilient moduli of C10QD and GSB have been compared (see Figure 3) using the stress combination of confining pressure 34.5 kPa and deviator stress 93.1 kPa which is one of the stress combination in the testing sequence for subbase material as per AASHTO T307 [28]. The resilient modulus values were found to be

TABLE 3. Weight loss (%) for all mixes

Mix	Weight loss, %
C10QD	9.74
C20QD	11.90
C40QD	13.67
C60QD	15.83

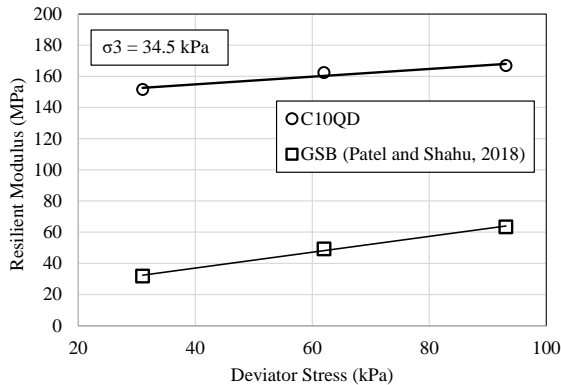


Figure 3. Comparison of resilient moduli of C10QD with conventional GSB

increasing with increment in deviator stress. This increment in MR is observed due to strain hardening phenomenon. Similar results are discussed in literature [32,33,34].

The fly ash and quarry dust mix gains strength by virtue of pozzolanic reaction. The efficiency of the binding of the quarry dust and fly ash particles increases with the amount of binding gel created during the pozzolanic reaction, and the MR value improved as a similar results reported in literature [4]. In case of conventional granular subbase material, due to absence of pozzolanic materials, no binding gel is formed. The resilient modulus values for C10QD were found to be

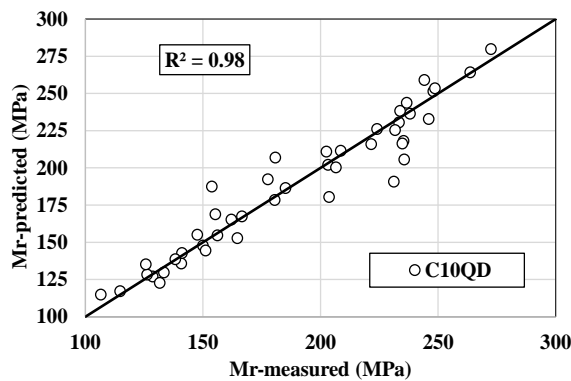


Figure 4. Comparison between measured and predicted resilient modulus values using MR- θ model for C10QD mix

significantly higher than that of conventional GSB material [35].

For prediction of resilient modulus (MR) at different cell pressure, Equation (1) MR- θ model [4] was used as follows:

$$MR = k_1 \cdot \theta^{k_2} \tag{1}$$

where, MR – resilient modulus and θ – bulk stress.

Figure 4 shows the predicted MR vs measured MR plot. The r^2 value of 0.98 shows that the MR- θ model provides good prediction of resilient modulus. The advantage of MR – θ model is that the effect of confining stress and deviator stress is combined for prediction of resilient modulus. The model constants were found to be $k_1 = 1.6387$ and $k_2 = 0.905$.

3. 5. X-Ray Diffraction (XRD) Analysis The X-ray diffraction results for C10QD mix show prominent peaks of $Ca(OH)_2$ (portlandite), ettringite and calcium silicate hydrate (CSH). The results of X-ray diffraction are presented in Table 4. The diffraction angle (2θ) at which compounds are located are in agreement with the literature [4,3,36-39]. It can be seen from the comparison between intensities of peaks of XRD spectra that there is development of $Ca(OH)_2$, CSH and Ettringite in C10QD mix after 7 days of curing.

The quarry dust is cohesion less material having no cementitious and pozzolanic properties. Formation of ettringite causes development of early strength within mix while formation of CSH gels cause development of long-term strength [4]. Hence, it is evident that the strength gaining takes place within the mix due to hydration process due to presence of fly ash and formation of hydration products such as ettringite and CSH.

TABLE 4. X-ray diffraction peak intensities of compounds in fly ash and C10QD mix

Compound	2θ	Fly ash	C10QD (7 days)
$Ca(OH)_2$	24.77°	0	68
$Ca(OH)_2$	33.18°	0	129
$Ca(OH)_2$	40.95°	0	53
CSH	15.81°	0	59
CSH	27.47°	0	87
Ettringite	18.99°	0	47
Ettringite	42.44°	0	81
CaO	54.7°	91	57
SiO ₂	20.7°	470	0
SiO ₂	26.9°	1205	625
Al ₂ O ₃	46.6°	109	73

3. 6. Scanning Electron Microscopy (SEM) The SEM images for C10QD after 7 and 28 days of curing are as shown in Figure 5. The presence of needle shaped ettringite phases and latticelike CSH phases are found in C10QD mix [40,41]. Formation of the CSH which is important cementitious phase causes binding of fly ash and quarry duct particles together causing increment in UCS and resilient modulus [8]. Formation of ettringite causes densification of structure [42]. The presence of ettringite as well as CSH is supported by XRD results.

4. PAVEMENT ANALYSIS

KENLAYER program was used to simulate and analyze conventional pavement with wet mix macadam (WMM) along with granular subbase (GSB) and proposed pavement with C10QD material at subbase provided with crack relief layer (CRL) at top. The pavement sections were assessed for 15 MSA traffic with standard axle single wheel load and 15 years design period. The details of each layer used for analysis are given in Table 5 with reference to IRC 37 [24]. Table 6 represents the details of pavement sections considered for analysis using KENLAYER program.

As per IRC 37 [24], the service life ratio (SLR) of pavement based on fatigue and rutting criteria for both conventional and proposed pavement are calculated using Equations (2) and (3) as follows:

$$\text{SLR (Fatigue)} = (\varepsilon_{t1}/\varepsilon_{t2})^{3.89} \quad (2)$$



Figure 5. SEM image for C10QD mix after 7 days of curing

TABLE 5. Details of pavement sections considered for analysis

Layer	Conventional Section		Proposed Section	
	Material	Thickness	Material	Thickness
Surface	BC+DBM	110 mm	BC+DBM	110 mm
Base	WMM	250 mm	CRL	250 mm
Subbase	GSB	330 mm	C10QD	330 mm

TABLE 6. Details of pavement layers used in KENLAYER for analysis

Layer	Resilient modulus (MPa)	Poisson's ratio
BC+DBM	3000	0.35
Wet mix macadam (WMM)	450	0.35
GSB	110	0.4
C10QD	180	0.3
Subgrade	65	0.4

where ε_{t1} and ε_{t2} = maximum horizontal tensile strains, developed at the bottom of for conventional and proposed pavement, respectively. This service life ratio quantifies the relative remaining fatigue life of pavement section.

$$\text{SLR (Rutting)} = (\varepsilon_{v1}/\varepsilon_{v2})^{4.5337} \quad (3)$$

where ε_{t1} and ε_{t2} = maximum vertical strains, developed at the top of subgrade of conventional and proposed pavement, respectively. This service life ratio quantifies the relative remaining rutting life of pavement section.

The strain values at the top of subgrade and bottom of bituminous layers for conventional and proposed pavement along with SLR values are shown in Table 7.

The strain values at the top of subgrade and bottom of bituminous layers for conventional and proposed pavement along with SLR values are shown in Table 7. The proposed pavement with C10QD mix in subbase layer has 1.20 and 1.26 in fatigue and rutting SLR, respectively. This shows that the performance of proposed pavement with C10QD mix in subbase has 20% and 26% more service life in fatigue and rutting compared to the conventional pavement with GSB, respectively.

TABLE 7. SLR for subbase material GSB and C10QD

Subbase material	Fatigue strain (ε_t) $\times 10^{-4}$	Rutting strain (ε_v) $\times 10^{-4}$	SLR	
			Fatigue	Rutting
GSB	-2.01E-04	3.41E-04	1	1
C10QD	-1.92E-04	3.24E-04	1.20	1.26

5. CONCLUSIONS

Following conclusions can be drawn from the study of fly ash and quarry dust mixes;

The UCS value for C10QD mix was 8.105 MPa after 7 days of curing which fulfils the strength criteria for the mix to be used as subbase material in flexible pavement. C10QD, C20QD and C40QD mixes satisfied durability criteria to be used as subbase material in flexible pavement. C10QD was found to have a resilient modulus

that is five times higher than that of conventional GSB material. This is because of self-cementitious properties of class C fly ash used in the C10QD mix which promotes the strength gaining within the mix. The XRD and SEM analysis for C10QD demonstrated presence of hydration product phases after curing due to which the strength gain takes place within mix. The pavement with C10QD mix in subbase demonstrated 1.20 and 1.26 SLR in fatigue and rutting, respectively compared to conventional pavement. Hence, service life of proposed pavement is more than that of conventional pavement.

The C10QD mix satisfies both strength as well as durability criteria for subbase material in flexible pavement. Class C fly ash is industrial by-product and quarry dust is waste from crushing plants, hence combined use of this material is sustainable and economical. Using such materials in road construction can lead to less consumption of natural aggregates which are depleting. Hence, it is recommended that this mix can be used in subbase layer in flexible pavement along with crack relief layer as per IRC 37 [24].

6. REFERENCES

- Singh, S., and Patel, S. "Potential Use of Fly Ash for Developing Angular-shaped Aggregate." *International Journal of Engineering, Transactions C: Aspects*, Vol. 36, No. 6, (2023), 1114-1120. <https://doi.org/10.5829/ije.2023.36.06c.09>
- Joshi, A. R., Patel, S., and Shahu, J. T. "Utilization of class 'C' Fly ash in flexible pavement system—a review." *Lecture Notes in Civil Engineering*, Vol. 29, (2019), 629-638. https://doi.org/10.1007/978-981-13-6713-7_50
- Nguyen, D. T., and Phan, V. T. A. "Engineering properties of soil stabilized with cement and fly ash for sustainable road construction." *International Journal of Engineering, Transactions B: Applications*, Vol. 34, No. 12, (2021), 2665-2671. <https://doi.org/10.5829/IJE.2021.34.12C.12>
- Patel, S., and Shahu, J. T. "Resilient Response and Permanent Strain of Steel Slag-Fly Ash-Dolime Mix." *Journal of Materials in Civil Engineering*, Vol. 28, No. 10, (2016), 04016106. [https://doi.org/10.1061/\(asce\)mt.1943-5533.0001619](https://doi.org/10.1061/(asce)mt.1943-5533.0001619)
- Shahu, J. T., Patel, S., and Senapati, A. "Engineering Properties of Copper Slag-Fly Ash-Dolime Mix and Its Utilization in the Base Course of Flexible Pavements." *Journal of Materials in Civil Engineering*, Vol. 25, No. 12, (2013), 1871-1879. [https://doi.org/10.1061/\(asce\)mt.1943-5533.0000756](https://doi.org/10.1061/(asce)mt.1943-5533.0000756)
- Yi, Y., Gu, L., and Liu, S. "Microstructural and mechanical properties of marine soft clay stabilized by lime-activated ground granulated blastfurnace slag." *Applied Clay Science*, Vol. 103, (2015), 71-76. <https://doi.org/10.1016/j.clay.2014.11.005>
- Bouaissi, A., Li, L. yuan, Al Bakri Abdullah, M. M., and Bui, Q. B. "Mechanical properties and microstructure analysis of FA-GGBS-HMNS based geopolymer concrete." *Construction and Building Materials*, Vol. 210, (2019), 198-209. <https://doi.org/10.1016/j.conbuildmat.2019.03.202>
- Kanthe, V., Deo, S., and Murmu, M. "Combine use of fly ash and rice husk ash in concrete to improve its properties." *International Journal of Engineering, Transactions A: Basics*, Vol. 31, No. 7, (2018), 1012-1019. <https://doi.org/10.5829/ije.2018.31.07a.02>
- Sankar, B., and Ramadoss, P. "Experimental and Statistical Investigations on Alccofine Based Ternary Blended High-performance Concrete." *International Journal of Engineering, Transactions B: Applications*, Vol. 35, No. 8, (2022), 1629-1640. <https://doi.org/10.5829/IJE.2022.35.08B.19>
- Pachideh, G., Gholhaki, M., Moshatgh, A., and Ash, F. "Performance of Porous Pavement Containing Different Types of Pozzolans." *International Journal of Engineering, Transactions C: Aspects*, Vol. 32, No. 9, (2019), 1277-1283. <https://doi.org/10.5829/ije.2019.32.09c.07>
- Al-Hasan, S. J. A., Balamuralikrishnan, R., and Altarawneh, M. "Eco-Friendly Asphalt Approach for the Development of Sustainable Roads." *Journal of Human, Earth, and Future*, Vol. 1, No. 3, (2020), 97-111. <https://doi.org/10.28991/hef-2020-01-03-01>
- Yooanpot, N., Jamsawang, P., Simarat, P., Jongpradist, P., and Likitlersuang, S. "Sustainable reuse of dredged sediments as pavement materials by cement and fly ash stabilization." *Journal of Soils and Sediments*, Vol. 20, No. 10, (2020), 3807-3823. <https://doi.org/10.1007/s11368-020-02635-x>
- Arif Ali Baig Moghal. "State-of-the-Art Review on the Role of Fly Ashes in Geotechnical and Geoenvironmental Applications." *Journal of Materials in Civil Engineering*, Vol. 29, No. 8, (2017), 1-14. [https://doi.org/10.1061/\(ASCE\)MT.1943-5533.0001897](https://doi.org/10.1061/(ASCE)MT.1943-5533.0001897)
- ASTM C618. "Standard Specification for Coal Fly Ash and Raw or Calcined Natural Pozzolan for Use" (2017). <https://doi.org/10.1520/C0618-17.2>
- Kang, X., Asce, S. M., Kang, G., Chang, K., Ge, L., and Asce, M. "Chemically Stabilized Soft Clays for Road-Base Construction." *Journal of Materials in Civil Engineering*, Vol. 27, No. 7, (2015), 1-9. [https://doi.org/10.1061/\(ASCE\)MT.1943-5533.0001156](https://doi.org/10.1061/(ASCE)MT.1943-5533.0001156)
- Cocka, E. "Class C fly ashes for the stabilization of an expansive soil," *Journal of Geotechnical and Geoenvironmental Engineering*, Vol. 127, No. July, (2001), 568-573.
- Pai, R. R., Bakare, M. D., Patel, S., and Shahu, J. T. "Asserting the Applicability of Copper Slag and Fly Ash as Cemented Base Materials in Flexible Pavement from a Full-Scale Field Study." *Journal of Materials in Civil Engineering*, Vol. 34, No. 4, (2022). [https://doi.org/10.1061/\(asce\)mt.1943-5533.0004123](https://doi.org/10.1061/(asce)mt.1943-5533.0004123)
- Saride, S., and Jallu, M. "Effect of Fly Ash Geopolymer on Layer Coefficients of Reclaimed Asphalt Pavement Bases." *Journal of Transportation Engineering, Part B: Pavements*, Vol. 146, No. 3, (2020), 04020033. <https://doi.org/10.1061/jpeodx.0000169>
- Rosa, M. G., Cetin, B., Asce, A. M., Edil, T. B., Asce, D. M., Benson, C. H., and Asce, F. "Freeze – Thaw Performance of Fly Ash – Stabilized Materials and Recycled Pavement Materials." *Journal of Materials in Civil Engineering*, Vol. 29, No. 2015, (2017), 1-13. [https://doi.org/10.1061/\(ASCE\)MT.1943-5533.0001844](https://doi.org/10.1061/(ASCE)MT.1943-5533.0001844)
- Qamhia, I. I. A., Tutumluer, E., Ozer, H., Boler, H., Shoup, H., and Stolba, A. J. "Durability Aspects of Chemically Stabilized Quarry By-Product Applications in Pavement Base and Subbase." *Transportation Research Record*, Vol. 2674, No. 6, (2020), 339-350. <https://doi.org/10.1177/0361198120919113>
- Ajay, C. H., and Durga Rani, K. "Ferrochrome Slag characterization and its compatibility with Quarry dust in Flexible pavement." *IOP Conference Series: Earth and Environmental Science*, Vol. 982, No. 1, (2022). <https://doi.org/10.1088/1755-1315/982/1/012008>
- U. A. K. "Soft Subgrade Stabilization With Quarry Dust-an Industrial Waste." *International Journal of Research in Engineering and Technology*, Vol. 03, No. 08, (2014), 409-412. <https://doi.org/10.15623/ijret.2014.0308063>

23. Sudhakar, S., Duraisekaran, E., Dilli Vignesh, G., and Kanna, G. D. "Performance Evaluation of Quarry Dust Treated Expansive Clay for Road Foundations." *Iranian Journal of Science and Technology - Transactions of Civil Engineering*, Vol. 45, No. 4, (2021), 2637-2649. <https://doi.org/10.1007/s40996-021-00645-4>
24. IRC 37. "Tentative guidelines for the design of flexible pavements." *Indian Road Congress*, (2012), 108.
25. IS2720 Part 8. "Methods of test for soils, part 8 determination of water content -dry density relation using heavy compaction" (1983).
26. IS: 2720 (Part 10):1991. "Indian Standard: Methods of test for soils, Part 10: Determination of unconfined compressive strength." *Bureau of Indian Standards, New Delhi*, No. Reaffirmed 2006, (1991), 1-6.
27. ASTM D559. "Standard Test Methods for Wetting and Drying Compacted Soil-Cement Mixtures 1" (2018). <https://doi.org/10.1520/D0559>
28. AASHTO T307. "Standard specifications for transportation materials and methods of sampling and testing Part II" (2000).
29. Donato, M., Gouveia, B. G., de Medeiros, A. S., da Silva, M. A. V., and Oda, S. "Mechanical Analysis of Subgrades of Road Pavements in Life Cycle Assessment." *Civil Engineering Journal (Iran)*, Vol. 8, No. 7, (2022), 1492-1506. <https://doi.org/10.28991/CEJ-2022-08-07-012>
30. Turkane, S. D., and Chouksey, S. K. "Partial Replacement of Conventional Material with Stabilized Soil in Flexible Pavement Design." *International Journal of Engineering, Transactions B: Applications*, Vol. 35, No. 5, (2022), 908-916. <https://doi.org/10.5829/ije.2022.35.05b.07>
31. NCHRP. "Harmonized test methods for laboratory determination of resilient modulus for flexible pavement design" (2003).
32. Patel, D., Kumar, R., Chauhan, K. A., and Patel, S. "Experimental and Modeling Studies of Resilient Modulus and Permanent Strain of Stabilized Fly Ash." *Journal of Materials in Civil Engineering*, Vol. 31, No. 8, (2019), 4-9. [https://doi.org/10.1061/\(asce\)mt.1943-5533.0002798](https://doi.org/10.1061/(asce)mt.1943-5533.0002798)
33. Puppala, A. J., Hoyos, L. R., and Potturi, A. K. "Resilient Moduli Response of Moderately Cement-Treated Reclaimed Asphalt Pavement Aggregates." *Journal of Materials in Civil Engineering*, Vol. 23, No. 7, (2011), 990-998. [https://doi.org/10.1061/\(asce\)mt.1943-5533.0000268](https://doi.org/10.1061/(asce)mt.1943-5533.0000268)
34. Zhang, J., Zhang, A., Huang, C., Yu, H., and Zhou, C. "Characterising the resilient behaviour of pavement subgrade with construction and demolition waste under Freeze-Thaw cycles." *Journal of Cleaner Production*, Vol. 300, (2021), 126702. <https://doi.org/10.1016/j.jclepro.2021.126702>
35. Patel, S., and Shahu, J. T. "Comparison of Industrial Waste Mixtures for Use in Subbase Course of Flexible Pavements." *Journal of Materials in Civil Engineering*, Vol. 30, No. 7, (2018), 04018124. [https://doi.org/10.1061/\(asce\)mt.1943-5533.0002320](https://doi.org/10.1061/(asce)mt.1943-5533.0002320)
36. Munasir, N., Triwikantoro, Zainuri, M., Bäßler, R., and Darminto. "Corrosion polarization behavior of Al-SiO₂ composites in 1M and related microstructural analysis." *International Journal of Engineering, Transactions A: Basics*, Vol. 32, No. 7, (2019), 982-990. <https://doi.org/10.5829/ije.2019.32.07a.11>
37. Ramesh, B. A., and Kondraivendhan, B. "Effect of Accelerated Carbonation on the Performance of Concrete Containing Natural Zeolite." *Journal of Materials in Civil Engineering*, Vol. 32, No. 4, (2020), 1-10. [https://doi.org/10.1061/\(asce\)mt.1943-5533.0003050](https://doi.org/10.1061/(asce)mt.1943-5533.0003050)
38. Bura, A. R., and Kondraivendhan, B. "An accelerated carbonation and its effect on concrete containing natural zeolite." *Innovative Infrastructure Solutions*, Vol. 7, No. 3, (2022). <https://doi.org/10.1007/s41062-022-00796-x>
39. Patil, V. G., Somasundaram, B., Kandaiah, S., Ramesh, M. R., and Kumar, S. "High Temperature Corrosion Behavior of High Velocity Oxy Fuel Sprayed NiCrMoFeCoAl-30%SiO₂ and NiCrMoFeCoAl-30%Cr₂O₃ Composite Coatings on ASTM SA213-T22 Steel in a Coal-fired Boiler Environment." *International Journal of Engineering, Transactions A: Basics*, Vol. 35, No. 7, (2022), 1416-1427. <https://doi.org/10.5829/ije.2022.35.07a.19>
40. Kumar, A., and Sivapullaiah, P. V. "Ground granulated blast furnace slag amended fly ash as an expansive soil stabilizer." *Soils and Foundations*, Vol. 56, No. 2, (2016), 205-212. <https://doi.org/10.1016/j.sandf.2016.02.004>
41. Feng, Y., Yang, Q., Chen, Q., Kero, J., Andersson, A., Ahmed, H., Engström, F., and Samuelsson, C. "Characterization and evaluation of the pozzolanic activity of granulated copper slag modified with CaO." *Journal of Cleaner Production*, Vol. 232, (2019), 1112-1120. <https://doi.org/10.1016/j.jclepro.2019.06.062>
42. Zhang, Y., Pan, Y., and Zhang, D. "A literature review on delayed ettringite formation: Mechanism, affect factors and suppressing methods." *Magazine of Concrete Research*, Vol. 73, No. 7, (2021), 325-342. <https://doi.org/10.1680/jmacr.20.00268>

COPYRIGHTS

©2023 The author(s). This is an open access article distributed under the terms of the Creative Commons Attribution (CC BY 4.0), which permits unrestricted use, distribution, and reproduction in any medium, as long as the original authors and source are cited. No permission is required from the authors or the publishers.



Persian Abstract

چکیده

تهی شدن خاکدانه ها و خاک های طبیعی مرغوب، نیاز به استفاده از فرآورده های جانبی صنعتی و مواد زائد در راه سازی را می طلبد. استفاده از ضایعات و فرآورده های جانبی در راه سازی مقادیر زیادی را مصرف می کند و مشکل دفع ایمن آنها را حل می کند. خاکستر بادی کلاس C محصول جانبی نیروگاه های حرارتی است در حالی که گرد و غبار معدن زباله هایی است که در طی فرآیندهای استخراج معدن باقی می ماند. این مطالعه کاربرد خاکستر بادی کلاس C و مخلوط گرد و غبار معدن را برای استفاده در لایه زیرپایه روسازی انعطاف پذیر مورد بررسی قرار داد. خاکستر بادی کلاس C و گرد و غبار معدن با کمک آزمون مقاومت فشاری نامحدود، آزمایش بارگذاری مکرر سه محوری، آزمون دوام و تجزیه و تحلیل ریزساختاری مورد مطالعه قرار گرفت. مخلوط ۹۰ درصد خاکستر بادی به اضافه ۱۰ درصد گرد و غبار معدن با توجه به معیارهای استحکام و دوام برای استفاده به عنوان ماده زیرپایه در روسازی انعطاف پذیر مناسب است. به دلیل تشکیل فازهای سیمانی در طی واکنش پوزولانی، مخلوط پیشنهادی مدول ارتجاعی به طور قابل توجهی نسبت به مواد زیر پایه دانه ای معمولی نشان داد. نسبت عمر مفید روسازی با مخلوط پیشنهادی در مقایسه با روسازی معمولی در خستگی و شیار به ترتیب ۱.۲ و ۱.۲۶ است. استفاده از گرد و غبار معدن و خاکستر بادی در مقادیر زیاد در روسازی انعطاف پذیر یک راه حل اقتصادی و همچنین پایدار برای راه سازی است.



Standards for Selection of Surfactant Compositions used in Completion and Stimulation Fluids

D. G. Petrakov, A. V. Loseva, N. T. Alikhanov, H. Jafarpour*

Saint-Petersburg Mining University, Saint-Petersburg, Russia

PAPER INFO

Paper history:

Received 15 May 2023

Received in revised form 09 June 2023

Accepted 11 June 2023

Keywords:

Critical Concentration of Micelle Formation
Inhibition

Process Fluids

Surfactants

Waterflooding

ABSTRACT

The growing need of the population for energy and hydrocarbon fuel, leads to an accelerated pace of development of the oil industry. In this regard, there is a need to develop new or renew the development of old oil fields. Among a range of existing EOR methods, the use of surfactants is considered as one of the main options aimed for both raising oil production and improving oil recovery. In this work, a study was carried out to define the characteristics and criteria for selection of an effective surfactants which are used in the tertiary scheme of recovery (IOR or EOR) from reservoir formations and especially during Enhanced Oil Recovery (EOR) flooding system. Three cationic surfactants with specific trade names were used in this study. It has been revealed that addition of surfactants positively affects inhibition of clay issues even in a more efficient manner than potassium chloride as one of the most widespread used clay inhibitors. At the end, a comprehensive discussion and suggestions are provided on the importance of temperature, concentration and bottom-hole conditions that affect selection of an optimum surfactant.

doi: 10.5829/ije.2023.36.09c.03

1. INTRODUCTION

Surfactants, well-known substances are used to reduce surface tension on liquid and solid interfaces, are mainly consist of non-polar and polar components. They are widely used in industrial processes, especially, to increase oil recovery factor from depleted reservoir rocks. They own a specific capability to reduce interfacial tension at the "oil-water" interface that is crucial for increasing the efficiency of residual oil displacement [1, 2].

Surfactants have hydrophobic and hydrophilic properties that provide the capability to bind in water and aggregate at the boundary of immiscible phases. The former property belongs to a range of compositional characteristics, such as presence of long-chain hydrocarbon, fluorocarbon, siloxane or short polymer chain [3, 4]. Hydrophilic groups have been classified into anionic (nonpolar lipophilic), cationic (polar hydrophilic), nonionic and zwitterionic (amphoteric) surfactants by Green and Willhite [5].

Polymer flooding by addition of surfactants, as one of the main subgroups of chemical flooding methods, is an effective method of enhanced oil recovery (EOR), which can be applied with a high level of efficiency in both carbonate and terrigenous reservoirs.

Previous review work have identified main criteria according to which a surfactant can be considered effective including capability to:

- dissolve in formation water
- reduce interfacial tension at the oil-water interface
- minimal adsorption
- maintain activity when in contact with fluids
- prevent inhibition of clayey rocks as a part of reservoir
- economically accessible and environmentally safe.

Nonionic surfactants that meet all the above criteria are widely used in the field practice of waterflooding of reservoirs by surface-active substances. Besides using surfactants in waterflooding, they have an impact on rheological and filtration characteristics of process fluids during primary and secondary recovery. Also, the use of surfactants during drilling process is recommended to

*Corresponding Author Email: JafarPour_H@pers.spmi.ru
(H. Jafarpour)

reduce the negative impact of fluid filtrate on permeability of the drilled interval, reduce the hardness of rocks, increase the lubricating properties and prevent clay mud thickening, as well as to emulsify oil and aerate the drilling fluids.

First of all, it is necessary for a surfactant-based mud to have an effect on reservoir rock wetting and to have oil-washing properties. In order to fulfill these conditions the surfactant must take part in dispersion of heterogeneous systems, in the processes of formation or separation of hydrophobic films and have stabilizing properties [6]. To assess these properties it is necessary to take into account the following physico-chemical parameters, such as, change in surface tension, critical concentration of micelle formation and the value of the boundary wetting angle.

Rock wettability controls the movement of fluids in the porous medium during drilling and production stages [6, 7]. For example, hydrophilic rock has low relative permeability to water, and oil cannot be extracted efficiently from hydrophobic skeleton of a porous medium. Thus, a change in the surface wettability of rocks by drilling fluid filtrate during drilling can have a positive or negative effect on reservoir recovery at least in near-wellbore region.

Note that sometimes surfactants become more hydrophobic due to shielding of electrostatic repulsion between the end groups (heads) of surfactants by dissolved electrolytes [8].

Mud invasion can also activate smectite/illite clays and cause further permeability reduction and formation damage. The process of changing wettability is more common at carbonate reservoirs where change of wettability towards more "water-wet" means reduction in the residual oil saturation and increasing water absorption.

It has been suggested that cationic surfactants work efficiently for the case of clay-rich terrigenous reservoirs in which carry negative surface charges [9]. In models of relative permeability and capillary pressure as a result of changes in wettability were proposed and the effects of different mechanisms in oil recovery associated with surfactants are compared as well. In particular, the effect of changes in wettability and reduction of the wetting angle were compared. Numerical simulation results showed that change in wettability plays an important role when the marginal angle is high, and it is effective in early times. The marginal angle plays a very important role with or without the change in wettability and is effective throughout the EOR process.

It is important to have a precise study for optimization of the concentration of surfactant that specially affect the critical concentration in surfactant micelle formation (CCM) in which significantly decreases with the addition of salt [10].

Determination of inhibitory capacity is also important. Clays are negatively charged aluminosilicates, blocks of which are weakly held together by electrostatic forces of attraction due to cations (Na^+ , Ca^{2+} , Mg^{2+} , K^+) [11].

When clays come into contact with water, water molecules are adsorbed on positively charged cations by weak forces (i.e. Van der Waals forces) [12, 13]. The surface of the shale minerals becomes hydrophilic, and the incoming water molecules begin to disturb the internal structure of the shale environment. When the clay particles are finally dispersed in the aqueous phase, electrostatic interaction leads to the formation of a double layer [14, 15].

In addition to the electrostatic forces between water molecules and cations, osmotic swelling promotes the penetration of freely moving water molecules into the clay pores, depending on the concentration gradient [16]. All of these processes lead to the initiation of the swelling process. For this purpose, it is necessary to conduct a test for linear swelling of the clay material.

2. METHODOLOGY AND MATERIALS

To determine surface wettability, edge angle measurements are made using the Kruss droplet shape analyzer shown in Figure 1. The wetting angle is a parameter that determines the wettability of a solid surface with water or another liquid. The wetting angle is influenced by adhesion and cohesion. The ratio of the two determines the shape of the droplet and the extent to which it spreads over the solid. A distinction is made between hydrophilic and hydrophobic surfaces depending on the value of the wetting angle.

If the wetting angle is less than 90° , the surface is called hydrophilic. Liquids will spread widely over such a surface. And angles up to 60° can be called superhydrophilic, where water spreads completely over the surface. The presence of a certain amount of



Figure 1. Device for measuring the edge angle of wetting Easydrop (compiled by the authors)

surfactant in the process liquid can change the value of the wetting angle from a hydrophilic to a hydrophobic.

During this study, according to the experience and knowledge described above, two basic instruments were used to select the optimum surfactant for the process liquids including:

1. EasyDrop DSA 100 tensiometer
2. An instrument for measuring the linear swelling of clays.

In order to investigate the effectiveness of non-inogenic surfactants, five samples of each surfactant were prepared in 0.05, 0.1, 0.25, 0.5 and 1 wt% concentrations. Next, the study was carried out on a tensiometer, the principle of which is schematically shown in Figure 2 [17]. First, the effect of surfactant on wettability was evaluated, the study was conducted as follows:

1. The sample under study was drawn into a syringe.
2. After the syringe is inserted, the needle is dipped into the cuvette, where the medium is isooctane.
3. The scale was set through the software so that the outline of the drop at the bottom of the cuvette was clearly visible.
4. The wetting angle is automatically calculated for the lying droplet.
5. Three measurements are taken in order to get a more accurate value.

After 3 measurements have been made, the cuvette should be washed and dried and degreased with isopropyl alcohol to prevent deliberately false readings. While the wetting-angle cuvette is being prepared, a new isooctane cuvette is placed on the moving stage. The interfacial tension is then measured:

1. The interfacial tension measurement is performed on a hanging drop, so a program change is necessary.
2. The needle is not lowered to the bottom of the cuvette, as space is needed for the hanging drop.
3. Video recording starts automatically when the drops are squeezed out.

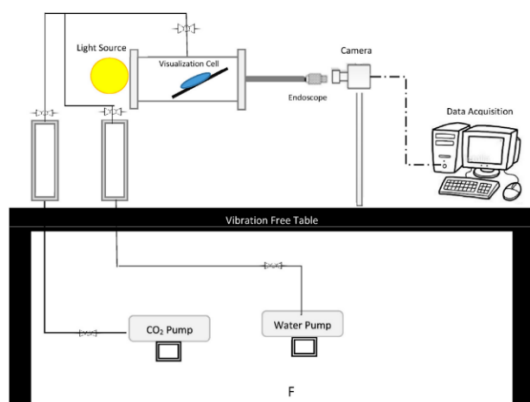


Figure 2. Schematic of the principle of operation of the tensiometer used to measure the wetting angle and surface tension [17]

4. The values calculated directly before the drop is detached from the syringe are recorded.

5. Three measurements are taken in order to get a more accurate value. Average values were reported. In this way a total of at least 6 measurements were performed for each sample. It is possible to take more measurements to reduce the error, but less is not recommended.

After conducting a tensiometer study, there is data on how effectively surfactants reduce interfacial tension and change the wettability of the fluid. Since these reagents will be used in drilling fluids, it is necessary to evaluate their effectiveness in the composition of the process fluid on the rock. For this purpose, an instrument for measuring linear swelling of clays LSM 2100 is used (Figure 3). The study is carried out as follows:

1. On the compactor tablets are made - compressed rock, in the form of a cylinder.
2. This tablet is installed in a container under the measuring device.
3. We carried out calibration, according to instructions LSM 2100.
4. The test liquid is poured into the container.
5. The study was carried out from 6 to 48 hours, depending on the regulations.
6. After a certain time, the program stops the test.
7. The meters are lifted and the tablets are taken out for visual analysis.

Thus, at the end of the test there are the following data: csv file with the measurements of the device, a graph of swelling over time: the change in percentage and absolute value. On the basis of visual inspection it is possible to estimate the depth of penetration of liquid, to see violation of tablet integrity, if the liquid contained colmatant then there is a possibility to see a filtration crust.

According to the methodology described above, samples of an aqueous surfactant solution in 5 concentrations were prepared first. Next, a minimum of 3 measurements of each sample were taken to reduce



Figure 3. Linear clay swelling tester LSM 2100 (compiled by the authors)

measurement error. Figure 4 shows examples of lying droplets, from which the edge wetting angle is calculated, and hanging droplets, from which the interfacial tension forces are determined.

Based on the results of the studies, the data obtained is sufficient to make the primary choice of surfactant for the process fluid.

3. RESULTS

After obtaining all the values, it is necessary to calculate the average value of the indicators for each sample [18]. The calculated values of interfacial tension for each surfactant are summarized in a table, and the results of studies on the tensiometer are presented as graphs, for ease of analysis (Figures 5 and 6).

Based on the data obtained, it is possible to assess the effect of each surfactant on the interfacial tension and wetting properties of the liquid [19]. It is known that there is a critical concentration above which it is not practical to introduce surfactants into the system, as it does not affect the change in the properties of the liquid. This concentration can be determined in the graphs. If after adding 0.05 and 0.1% of surfactant there is a sharp



Figure 4. View of lying and hanging droplets from which the edge wetting angle and interfacial tension forces are determined (compiled by the authors)

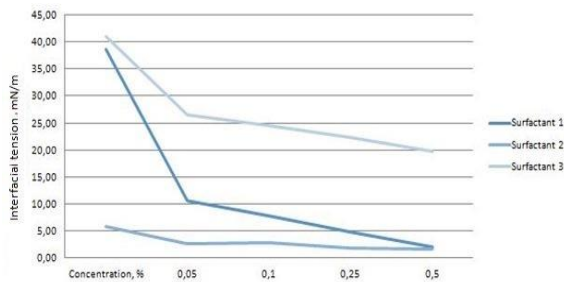


Figure 5. Dependency of interfacial tension on natural logarithm of surfactant concentration (compiled by the authors)

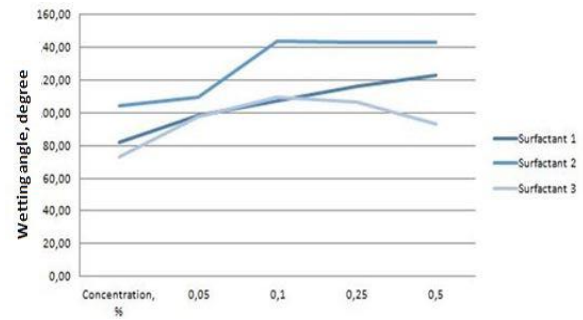


Figure 6. Dependency of boundary wetting angle on natural logarithm of the surfactant (compiled by the authors)

decrease in the force of interfacial tension and the angle becomes more obtuse, then at a concentration above 0.5% the effect decreases and the line becomes more straight. Thus, we can say that the optimal surfactant concentration for solutions is 0.25%. The force of interphase tension of distilled water at the boundary with isooctane is 73 mN/m, so it follows from the obtained data that surfactant 2 is the most effective reagent. This is confirmed by the fact that the interfacial tension force at a concentration of 0.05% was reduced almost by 15-fold. The contact angle has also increased up to 105 degrees, which indicates hydrofibbing of the surface by the liquid treated with this surfactant. The process fluid with these values will prevent the negative effect of the fluid on reservoir properties, and during waterflooding will provide an increase in the oil recovery. These effects are achieved because the surfactants in the solution hydrophobize the rock surface and provide a better yield for hydrocarbons [20, 21].

The use of surfactants in process fluids can also ensure the integrity of the rock skeleton. This is achieved due to the fact that the filtrate will penetrate less into the rock, thereby preventing swelling and cracking of the rock mass. It is possible to check this hypothesis thanks to a device for measuring linear swelling of clays LSM 2100. A comparative study was performed with 4 samples: 2% KCl solution and 3 samples with 0.25% surfactant added. The results are shown in Figure 7.

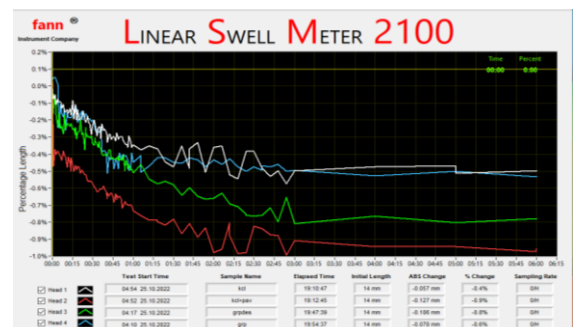


Figure 7. Results obtained from the clay swelling analyzer (compiled by the authors)

4. CONCLUSIONS

It can be concluded that the addition of surfactants has a positive effect on rock inhibition, and that some are better than potassium chloride, which is the most widely used inhibitor of clay. Taken together, these studies allow us to make an initial selection of surfactants for IOR and EOR. The importance of this study is that the LSM2100 test results and the information on the interaction of the system with the surfactant and the rock are sufficient to recommend the use of the surfactant in EOR. It should be noted that the tests carried out are not fundamental to a decision on the choice of surfactant for drilling conditions. For example, when drilling salt formations, it is necessary to evaluate surfactants in a highly mineralized environment, as it is known that mineralization affects surfactant efficiency and may result in the need to increase surfactant concentration to achieve the required performance. Another important factor is temperature, which affects the value of the critical concentration for micellar formation; hence, the need for refinement studies to determine the need to increase or decrease the surfactant concentration in solution. The use of a scanning electron microscope is a promising tool for the study of surfactants, allowing the behaviour of the surfactant in solution to be assessed, as well as its interaction with other chemical reagents present in the dispersion medium. Overall, the results of our study, based on laboratory tests, show that among the three surfactants used in this work, OLBECK (trade name of a cationic surfactant) at a concentration of 0.25 wt% is the most optimal choice.

5. REFERENCES

- Ahmadi, Y., Hasanbaygi, M. and Kharrat, R., "A comparison of natural depletion and different scenarios of injection in the reservoir from the beginning of oil production", *Petroleum Science and Technology*, Vol. 32, No. 21, (2014), 2559-2565. doi: 10.1080/10916466.2013.856445
- Ivanova, A.A., Cheremisin, A.N., Barifcani, A., Iglauer, S. and Phan, C., "Molecular insights in the temperature effect on adsorption of cationic surfactants at liquid/liquid interfaces", *Journal of Molecular Liquids*, Vol. 299, (2020), 112104. doi: 10.1016/j.molliq.2019.112104
- Kamal, M.S., Hussein, I.A. and Sultan, A.S., "Review on surfactant flooding: Phase behavior, retention, ift, and field applications", *Energy & Fuels*, Vol. 31, No. 8, (2017), 7701-7720. doi:10.1021/acs.energyfuels.7b00353
- Kamal, M.S., Sultan, A.S., Al-Mubaiyedh, U.A. and Hussein, I.A., "Review on polymer flooding: Rheology, adsorption, stability, and field applications of various polymer systems", *Polymer Reviews*, Vol. 55, No. 3, (2015), 491-530. doi:10.1080/15583724.2014.982821
- Green, D. and Willhite, G., "Enhanced oil recovery. Richardson, spe textbook series", *Society of Petroleum Engineers*, Texas, USA, (1998).
- Guan, O.S., Gholami, R., Raza, A., Rabiei, M., Fakhari, N., Rasouli, V. and Nabinezhad, O., "A nano-particle based approach to improve filtration control of water-based muds under high pressure high temperature conditions", *Petroleum*, Vol. 6, No. 1, (2020), 43-52. doi:10.1016/j.petlm.2018.10.006
- Grate, J.W., Dehoff, K.J., Warner, M.G., Pittman, J.W., Wietsma, T.W., Zhang, C. and Oostrom, M., "Correlation of oil-water and air-water contact angles of diverse silanized surfaces and relationship to fluid interfacial tensions", *Langmuir*, Vol. 28, No. 18, (2012), 7182-7188. doi:10.1021/la204322k
- Sandyga, M.S., Struchkov, I.A. and Rogachev, M.K., "Research of temperature conditions of organic sediments formation in the productive formation at paraffinic oil well production", *Perm Journal of Petroleum and Mining Engineering*, Vol. 21, No. 2, (2021), 84-93. doi:10.15593/2712-8008/2021.2.6
- Ahmadi, M.A. and Shadzadeh, S.R., "Adsorption of novel nonionic surfactant and particles mixture in carbonates: Enhanced oil recovery implication", *Energy & Fuels*, Vol. 26, No. 8, (2012), 4655-4663. doi:10.1021/ef300154
- Tananykhin, D., Struchkov, I., Khormali, A. and ROSCHIN, P., "Investigation of the influences of asphaltene deposition on oilfield development using reservoir simulation", *Petroleum Exploration and Development*, Vol. 49, No. 5, (2022), 1138-1149. doi:10.1016/S1876-3804(22)60338-0
- Dengaev, A., Shishulin, V., Safiullina, E. and Palyanitsina, A., "Modeling results for the real horizontal heavy-oil-production well of mechanical solids", *Energies*, Vol. 15, No. 14, (2022), 5182. doi:10.3390/en15145182
- Rana, A., Khan, I., Ali, S., Saleh, T.A. and Khan, S.A., "Controlling shale swelling and fluid loss properties of water-based drilling mud via ultrasonic impregnated swcnTs/pvp nanocomposites", *Energy & Fuels*, Vol. 34, No. 8, (2020), 9515-9523. doi:10.1021/acs.energyfuels.0c01718
- Safdel, M., Anbaz, M.A., Daryasafar, A. and Jamialahmadi, M., "Microbial enhanced oil recovery, a critical review on worldwide implemented field trials in different countries", *Renewable and Sustainable Energy Reviews*, Vol. 74, (2017), 159-172. doi:10.1016/j.rser.2017.02.045
- Said, M., Haq, B., Al Shehri, D., Rahman, M.M., Muhammed, N.S. and Mahmoud, M., "Modification of xanthan gum for a high-temperature and high-salinity reservoir", *Polymers*, Vol. 13, No. 23, (2021), 4212. doi:10.3390/polym13234212
- Galkin, V.I., Martyushev, D.A., Ponomareva, I.N. and Chernykh, I.A., "Developing features of the near-bottomhole zones in productive formations at fields with high gas saturation of formation oil", *Journal of Mining Institute*, Vol. 249, (2021), 386-392. doi:10.31897/PMI.2021.3.7
- Gasumov, R.A., Minchenko, Y.S. and Gasumov, E.R., "Development of technological solutions for reliable killing of wells by temporarily blocking a productive formation under alrp conditions (on the example of the cenomanian gas deposits)", *Journal of Mining Institute*, Vol. 258, (2022), 895-905. doi:10.31897/PMI.2022.99
- Guo, Q., Ahmadi, M.H., Lahafdoozian, M., Palyanitsina, A., Kuzichkin, O.R., Alizadeh, S. and Nassabeh, S.M.M., "A laboratory approach on the improvement of oil recovery and carbon dioxide storage capacity improvement by cyclic carbon dioxide injection", *Energy Reports*, Vol. 7, (2021), 1571-1580. doi:10.1016/j.egy.2021.03.012
- Kamal, M.S., Hussein, I.A. and Sultan, A.S., "Review on surfactant flooding: Phase behavior, retention, ift, and field applications", *Energy & Fuels*, Vol. 31, No. 8, (2017), 7701-7720. doi:10.1021/acs.energyfuels.7b00353
- Liu, X., Jiang, R., Li, J. and Huang, W., "Characteristics of shale gas reservoir in jiyang depression and its significance in drilling and exploitation", *International Journal of Engineering, Transactions B: Applications*, Vol. 33, No. 8, (2020), 1677-1686. doi: 10.5829/ije.2020.33.08b.27

20. Nagiredla, S., Joladarashi, S. and Kumar, H., "Rheological properties of the in-house prepared magneto-rheological fluid in the pre-yield region", *International Journal of Engineering, Transactions B: Applications*, Vol. 35, No. 11, (2022), 2238-2246. doi:10.5829/ije.2022.35.11b.19
21. Jalili, B., Mousavi, A., Jalili, P., Shateri, A. and Domiri Ganji, D., "Thermal Analysis of Fluid Flow with Heat Generation for Different Logarithmic Surfaces", *International Journal of Engineering, Transactions C: Aspects*, Vol. 35 No. 12, (2022), 2291-2296. doi:10.5829/ije.2022.35.12c.03

COPYRIGHTS

©2023 The author(s). This is an open access article distributed under the terms of the Creative Commons Attribution (CC BY 4.0), which permits unrestricted use, distribution, and reproduction in any medium, as long as the original authors and source are cited. No permission is required from the authors or the publishers.



Persian Abstract**چکیده**

نیاز روزافزون جمعیت به انرژی و سوخت هیدروکربنی، سرعت توسعه صنعت نفت را تسریع می کند. در این راستا نیاز به توسعه جدید یا تجدید توسعه میدین نفتی قدیمی وجود دارد. در میان طیف وسیعی از روش های EOR موجود، استفاده از سورفکتانت ها به عنوان یکی از گزینه های اصلی برای افزایش تولید نفت و بهبود بازیافت نفت در نظر گرفته می شود. در این کار، مطالعه ای برای تعریف ویژگی ها و معیارهای انتخاب یک سورفکتانت مؤثر که در طرح سوم بازیابی (IOR یا EOR) از سازندهای مخازن و به ویژه در سیستم سیل آبی بهبود یافته بازیابی نفت (EOR) استفاده می شود، انجام گردید. در این مطالعه از سه سورفکتانت کاتیونی با نام تجاری خاص استفاده شد. مشخص شده است که افزودن سورفکتانت ها به طور مثبتی بر مهار مسائل خاک رس حتی به شیوه ای کارآمدتر از کلرید پتاسیم به عنوان یکی از رایج ترین بازدارنده های خاک رس تأثیر می گذارد. در پایان، بحث و پیشنهادات جامعی در مورد اهمیت دما، غلظت و شرایط سوراخ پایین که بر انتخاب یک سورفکتانت بهینه تأثیر می گذارد، ارائه شده است.



Land Covers Classification from LiDAR-DSM Data Based on Local Kernel Matrix Features of Morphological Profiles

B. Asghari Beirami*, M. Mokhtarzade

Department of Photogrammetry and Remote Sensing, Faculty of Geodesy and Geomatics, K. N. Toosi University of Technology, Tehran, Iran

PAPER INFO

Paper history:

Received 07 April 2023
Received in revised form 08 June 2023
Accepted 12 June 2023

Keywords:

LiDAR
Digital Surface Model
Morphological Profiles
Local Kernel Features
Support Vector Machine

ABSTRACT

Accurate land cover classification from the digital surface model (DSM) obtained from LiDAR sensors is a challenging topic that researchers have considered in recent years. In general, the classification accuracy of land covers leads to low accuracy using a single-band DSM image. Hence, it seems necessary to develop efficient methods to extract relevant spatial information, which improves classification accuracy. In this regard, using spatial features based on morphological profiles (MPs) has significantly increased classification accuracy. Despite MPs' efficiency in increasing the DSM's classification accuracy, the classification accuracy results under the situation of limited training samples are not still at satisfactory levels. The main novelty of this paper is to propose a new feature space based on local kernel descriptors obtained from MP for addressing the mentioned challenge of MP-based DSM classification. These innovative feature vectors consider local nonlinear dependencies and higher-order statistics between the morphological features. The experiments of this study are conducted on two well-known DSM datasets of Houston and Trento. Our results show that support vector machine (SVM)-based DSM classification with the new local kernel features achieved an average accuracy of 93.75%, which is much better than conventional SVM classification with single-band DSM and MP features (by about 57% and 11.5% on average, respectively). Additionally, our proposed method outperformed two other DSM classification methods by an average of 4.7%.

doi: 10.5829/ije.2023.36.09c.04

1. INTRODUCTION

Aerial LiDAR is a type of remote sensing sensor that uses laser pulses to measure the distance between the receiver and the earth's surface. Generally speaking, elevation models and 3D point clouds are two important outputs of LiDAR sensors that are used in various fields, including forestry research, geodesy, geology, urban research, and crisis management [1-3]. LiDAR can collect data in all weather and lighting conditions, unlike optical and infrared sensors [4]. LiDAR sensors generate a digital surface model (DSM) as a secondary outcome, which is produced by implementing various techniques like denoising and rasterization on a point cloud. DSM contains elevational data of ground objects, which can be used to distinguish objects of different heights [5].

DSM is typically used as supplemental data to optical or hyperspectral images in order to classify land cover. For instance, Zhang et al. [6] developed a new classification system that categorizes land covers using extinction profiles derived from hyperspectral images and the DSM. The final results of their research show that the integration of spectral features and the DSM increases classification accuracy. Singh et al. [7] introduced a novel deep-learning strategy for classifying land cover using LiDAR and hyperspectral images in their study. The method utilizes sparse stacked autoencoders and morphological profiles, as outlined in literature [7].

Although DSM has been used in several studies as supplementary data, researchers' interest in classifying land covers using a single-band DSM image has recently increased. When few training examples are available,

*Corresponding author Email: b_asghari@email.kntu.ac.ir
(B. Asghari Beirami)

distinguishing between ground cover with only a single-band DSM image results in low accuracy, necessitating the development of more effective techniques. Most alternative approaches hinge on utilizing the spatial and contextual details present in DSM images to enhance classification accuracy, primarily attributable to the superior spatial resolution of LiDAR sensors. One of the primary spatial features used by numerous studies to categorize the DSM image is morphological profiles (MPs). To classify land cover from LiDAR data, Ghamisi and Hoefle [8] proposed a composite kernel SVM classification method based on extinction profiles. Their research culminated in a classification accuracy of roughly 87% for DSM images from the University of Houston dataset. In a separate research project, Wang and colleagues [4] suggested a new approach to DSM image classification utilizing the combination of morphological profiles and deep convolutional networks. He et al. [9] evaluated the performance of spatial transformer networks in integration with morphological features to classify the DSM image after demonstrating the efficiency of deep learning methods in classifying LiDAR data. Transformer networks outperform traditional convolutional neural networks, according to their final findings. A step forward in this direction was taken by Wang and colleagues [10], who developed a superior model for DSM data classification through the integration of dense convolutional neural networks and spatial transformer networks.

According to the literature, deep neural networks underlie the majority of the proposed methods for classifying DSM images, but it should be noted that using deep models comes with its own challenges. For instance, using deep models necessitates tuning thousands or even millions of parameters and involves computational complexity. Some expensive, high-end hardware, such as GPUs, is required to adjust this enormous number of parameters. On the other hand, overfitting, a condition that reduces these networks' effectiveness, is possible when few training samples are available. Therefore, developing accurate, quick, and shallow methods seem necessary.

Recent research in machine vision has shown that using covariance descriptors, which consider linear dependencies, can improve the performance of machine learning techniques on certain tasks, such as face recognition [11]. A more general form of covariance descriptor is the kernel descriptor, which typically performs better than covariance by considering nonlinear dependencies between features and higher-order statistics [12, 13]. In this regard, in remote sensing, Beirami and Mokhtarzade [14] developed local kernel features for classifying hyperspectral images and proving

the efficiency of nonlinear relationships between spectral features in the classification of hyperspectral images. Despite demonstrating the efficiency of local kernel features, their efficiency in increasing the classification accuracy of DSM images is still unknown. In view of the potential of local kernel features to enhance the accuracy of land cover classification, a novel method for extracting features is introduced herein for DSM image classification. The novel feature space put forth in this study takes into account the nonlinear dependences and higher-order statistics between morphological features. For this purpose, in this study, after generating spatial features using MP, local kernel features were generated from them and then fed to machine vector machines (SVM) classifier for classification.

Our motivation for proposing a new DSM classification method based on local kernel matrix features is twofold. First, these features have shown great performance in other fields of image processing, such as hyperspectral image classification [15], particularly in situations with limited training sample sizes. Second, producing these local kernel matrix features is straightforward and does not require advanced hardware, such as GPUs, unlike some other DSM classification methods.

The main novelty of this paper is the introduction of robust and efficient kernel features derived from morphological features for DSM image classification. These new features are expected to significantly improve the classification accuracy of DSM images due to their ability to consider nonlinear dependencies between morphological features.

The present paper is structured as follows: In the second section of this study after introducing the DSM datasets used in this study, we describe the proposed DSM classification approach in detail. In the third section, we report and analyze the classification results. Lastly, we conclude our research in the final section before discussing future study plans.

2. THE PROPOSED APPROACH

In this section, we introduce the dataset used in our study and describe the methodology employed.

2.1. Datasets Researchers in the IEEE competition employed the Houston dataset as a reference collection, which was gathered from the University of Houston campus in 2012. The dataset includes a LiDAR-captured DSM with a density of one point in 2.5 meters and a ground truth map consisting of 15 urban classes such as buildings, water, soil, trees, and roads. Figure 1 depicts the DSM image of the Houston University region.



Figure 1. Houston University LiDAR-DSM

The Trento DSM dataset was acquired by Optech ALTM 3100EA sensor over a rural region located in the southern part of Trento, Italy. The dataset, which comprises 166×600 pixels, has been captured with a spatial resolution of 1m. The Trento dataset has six distinct categories, namely apple trees, buildings, ground, wood, vineyard, and roads. Figure 2 represents the Trento DSM image.

2. 2. Methodology In this subsection, the proposed DSM classification method is introduced after reviewing some related basic concepts.

2. 2. 1. Morphological Profiles Morphological profiles are among the most significant spatial features used to categorize DSM images, as was already mentioned. MPs generally improve classification accuracy because of their high ability to extract geometric properties of objects and classes. MP is built upon two fundamental morphological operators, namely opening (OP) and closing (CL). These operators are established using the essential erosion (\bullet) and dilation (\circ) operators, with the following definitions [16]:

$$OP = (A \bullet B) \circ B \quad (1)$$

$$CL = (A \circ B) \bullet B \quad (2)$$

A DSM image with only one band is denoted as A , while B symbolizes a structuring element (SE) in the equations mentioned earlier. To capture the intricate geometric details of objects, present within the DSM image that come in varying sizes, morphological attributes are generated utilizing SEs of diverse sizes. As a result, if we represent the dimensions of the structural element as L , an MP can be displayed as follows:

$$MP = [OP_L, OP_{L-1}, \dots, A, \dots, CL_{L-1}, CL_L] \quad (3)$$

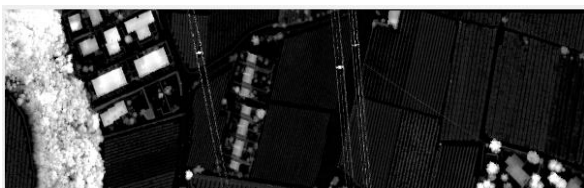


Figure 2. Trento LiDAR-DSM

In the center of an MP lies the primary DSM image, while its sides showcase DSM images that have undergone size-varied structural element operations of opening and closing. The use of disc-shaped SEs is more frequent for creating MPs, according to the research background, because of its isotropic behavior in all directions.

2. 2. 2. Local Kernel Matrix Features By calculating higher-order statistics and nonlinear relationships between features, the local kernel matrix can offer significant improvements in classification accuracy. To illustrate, suppose we have an image with N bands, and we examine a window of size $l \times l$ (containing R pixels) centered around each pixel. We compute every element of the local kernel matrix using the following formula:

$$k(y_i, y_j) = \exp(-\beta \|y_i - y_j\|^2) \quad (4)$$

where y is the vector with size R , which contains the grey-level values of pixels in the local $l \times l$ window, indices i and j represent the i^{th} and j^{th} bands, and β is the scaling parameter of the radial basis function, which is set to 1 in this study by experiment. Since calculating the k in the fixed window size may bias the final results, similar to work conducted by Mirzapour, and Ghassemian [17]. This paper uses a weighted version of Equation (4) for feature generation. To do so, the weight of each pixel in coordinate (r, c) in the local $l \times l$ window is represented by:

$$P = \sqrt{r^2 + c^2} \quad (5)$$

$$weight(r, c) = 1 / (P + 1) \quad (6)$$

To prevent infinity, Equation (6) employs 1 in the denominator. Following the computation of pixel weights within the local $l \times l$ window, the weighted form of Equation (4) can be expressed as follows [14]:

$$k(y_i, y_j) = \exp(-\|W y_i - W y_j\|^2) \quad (7)$$

The vector W consists of weights assigned to every pixel in the $l \times l$ local window. Finally, after calculating k for each pair of features, a weighted local kernel matrix (WLKM) with size $N \times N$ is calculated by Beirami, and Mokhtarzade [15]:

$$K = \begin{bmatrix} k(y_1, y_1) & \dots & k(y_1, y_N) \\ \vdots & \ddots & \vdots \\ k(y_N, y_1) & \dots & k(y_N, y_N) \end{bmatrix} \quad (8)$$

After calculating the WLKMs in the form of equation (8) for each pixel, to further improve the quality of extracted features, the matrix logarithm operator is applied to WLKMs as [16]:

$$\log m(K) = U \log(\Sigma) U^T \quad (9)$$

The eigen-decomposition of Matrix K is used to compute U and Σ . Subsequently, upper or lower triangular elements from $\logm(K)$ serve as the WLKM features. The size of the resulting feature vectors is $N \times (N+1)/2$, with a total of 325 WLKM features generated (which equals $(25 \times 26)/2$, where 25 denotes the number of MP features).

2. 2. 3. Proposed Method This study aims to evaluate the potential improvement in the classification accuracy of DSM images through the integration of WLKM features that have been extracted from MP. A block diagram demonstrating the suggested technique is depicted in Figure 3. Essentially, the methodology put forth in this study consists of three pivotal phases:

- 1) In the first step, morphological profiles are created from a single-band DSM image using equation (3). The use of MP, which contains geometric information, enhances classification accuracy.
- 2) In the second step, the generated features from step 1 are given as input to the WLKM feature generation method. This method can generate features that contain nonlinear dependencies and high-order statistics of MP features.
- 3) In the third stage, the feature vectors generated from the second stage are classified by the SVM classifier using training samples. Finally, the accuracy of classification is evaluated using test samples.

This study's suggested technique is primarily evaluated against two fundamental methodologies. these approaches are based on the SVM classification of single-band DSM and the SVM classification of MP features.

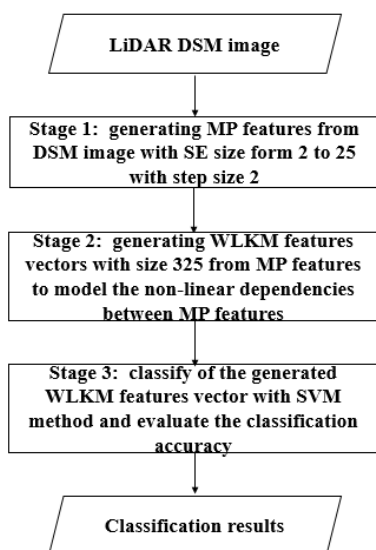


Figure 3. Block diagram of the proposed method

3. EXPERIMENTAL RESULTS

The suggested algorithm was put into practice using the two mentioned DSM datasets. From the ground truth maps of each dataset, training samples are randomly chosen in two sizes: 40 samples per class (case 1) and 80 samples per class (case 2), with the remaining samples serving as test samples to evaluate the classification accuracy. In our study, we utilized the cross-validation technique to adjust the SVM classification parameters. Our assessment of the classification accuracy involved calculating three metrics from the confusion matrix: overall accuracy (OA), average accuracy (AA), and kappa coefficient (k). To ensure statistical significance, we replicated all experiments ten times and calculated the average outcomes. MATLAB 2020b was employed for implementation on a Core i5 4590 3.3GH processor with 8 GIG RAM, with no inclusion of GPU.

3. 1. Experiments on the Houston Dataset

3. 1. 1. Simulation Details To classify DSM, our approach uses three key settings: the MP feature dimension, β in equation 4, and the window size for the WLKM method. We've set the MP dimension to 25 by creating MP with SE sizes ranging from 2 to 25 (in increments of 2). We've also set β to 1. To choose these values, we used trial and error, prioritizing speed and accuracy. To determine the optimum window size of the WLKM method, SVM classification is conducted with Figure 4 presents the classification outcomes for several window sizes (5 to 15) in the initial test of this subsection, which examines the final classification outcomes of the WLKM feature generation method in relation to window size. The results propose window size 13 as the optimal selection for maximum accuracy. Accuracy drops slightly after window size 13, as demonstrated in Figure 4. Although the automatic detection of window size is an interesting topic that will be investigated in future studies, using any window size between 5 and 15 can obtain better results than MP-based classification.

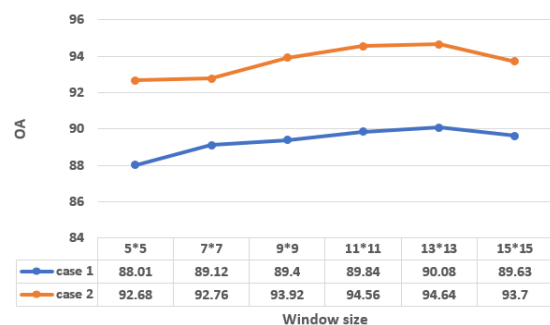


Figure 4. Impact of window size on classification accuracy of WLKM features

3. 1. 2. Analysis of Classification Results

As stated earlier, the proposed WLKM DSM classification method is basically compared with DSM-based and MP-based classification methods. Classification results on each case of training ratio are shown in Table 1. Figure 5 also displays each method's classified images under case 1 of the training sample.

Below are the key results obtained from these experiments:

- It can be understood that local nonlinear dependencies improve the classifier's performance and reduce noise in the classified image. This means that the new WLKM feature vectors of each pixel are similar within the same class and different across different classes.
- Table 1 shows that the classification accuracy of DSM images is very poor (OAs are below 30%), and Figure 5(a) shows that the classified images are very noisy. As a result, the classified maps produced using only the DSM image are not very accurate. Table 1 displays an intriguing finding that increasing

the sample size from 40 to 80 does not lead to a notable improvement in classification accuracy.

- As seen from Table 1, compared to DSM-based classification, using spatial features of MP can hugely increase the classification accuracy by about 50%. Furthermore, classified maps obtained from MP features are smoother than classified images of the previous experiment, as shown in Figure 5(b). Table 1 shows that, similarly to the previous finding, increasing the size of training samples cannot improve classification accuracy.
- According to Table 1, the proposed method based on WLKM features provides the most accurate classified images. Table 1 shows that even with very few training samples, the proposed WLKM-based classification of DSM can still achieve above 90% accuracy (case 1). The image depicted in Figure 5(c) illustrates the smoother and more refined classified image obtained through the utilization of the proposed WLKM approach. Unlike the previous two findings, this method showcased an improvement in classification results by increasing the size of training samples. The effectiveness of WLKM features was demonstrated by their potential to consider nonlinear dependencies and higher-order statistics, which proved highly beneficial in accurately classifying images.

TABLE 1. The Houston dataset's classification outcomes compared across various techniques

Accuracy criteria	Training ratio	Methods		
		DSM	MP	WLKM
OA		22.8	81.64	90.08
AA	Case 1	35.26	83.48	91.43
K×100		23.73	79.92	89.12
OA		28.97	77.25	94.64
AA	Case 2	36.04	78.99	95.46
K×100		24.32	75.1	94.1

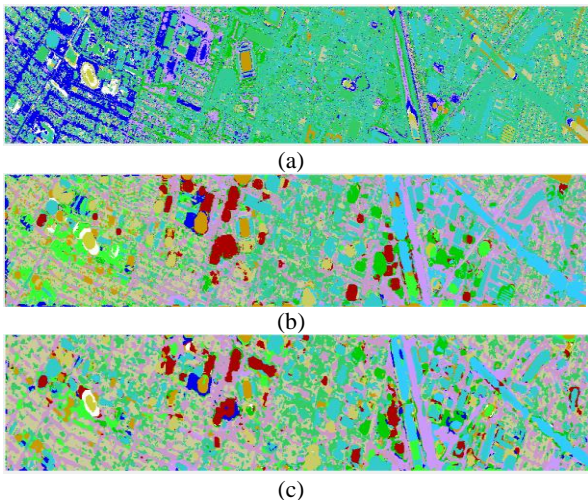


Figure 5. Classified images (a) DSM feature (b) MP features (c) WLKM features

3. 1. 3. Comparison to other DSM Classification Methods

As a result of the limited availability of alternative methodologies and the absence of codes for such approaches, the comparison of the DSM classification method proposed on the basis of WLKM has been restricted to only two state-of-the-art (SOTA) methods. Below are some supplementary descriptions pertaining to these techniques:

- MAP-CNN-SiLU [4]: In this method, morphological and multiattribute profiles are combined with a deep CNN with sigmoid-weighted linear units (SiLU) as activation functions to classify DSM images.
- MP-STN [9]: This method combines MPs with spatial transformation CNN for DSM classification. Using a spatial transformation network (STN), this approach identifies the best CNN inputs.

The classification outcomes of each technique are displayed in Table 2. The results are obtained from the authors' primary literature and compared to those for the WLKM-based method that was suggested.

Table 2 demonstrates that our DSM classification method outperforms the other two methods in competition. One way to express the complexity of the suggested approach is by using the subsequent formula:

$$O(\text{proposed}) = O(\text{MP}) + O(\text{WLKM}) + O(\text{SVM}) \quad (10)$$

TABLE 2. Comparison of suggested methodology and two advanced DSM classification techniques

	MAP-CNN-SiLU		MP-STN		proposed	
	Case1	Case2	Case1	Case2	Case1	Case2
OA	83.22	90.71	86.87	92.87	90.08	94.64
AA	85.94	91.92	89.15	94.18	91.43	95.46
K×100	81.88	89.95	85.80	92.28	89.12	94.10

In which $O(X)$ is the computational complexity of the method X . Computation time of the proposed method on the Houston dataset is about 280 seconds, much faster than some other DSM classification methods such as MAP-CNN-SiLU with 642.09 seconds, as reported in their paper. To sum up, our shallow method for DSM classification, as opposed to the other two deep learning methods, employs a simpler structure that enhances its effectiveness.

3. 2. Experiments on the Trento Dataset

Assessing the WLKM-based classification technique on the Trento DSM dataset is the objective of our second experiment. Due to the unavailability of results of the previously mentioned SOTA for the Trento dataset, we only report the results of two basic approaches. Classification accuracies of DSM-based and MP-based and WLKM-based classification methods are shown in Table 3 for two cases of training ratio.

The efficiency of the proposed method on the second DSM dataset was confirmed by the ultimate findings of Table 1. On average, the WLKM approach outperformed the MP-based method by approximately 9.72%.

TABLE 3. The Trento dataset's classification outcomes compared across various techniques

Accuracy criteria	Training ratio	Methods		
		DSM	MP	WLKM
OA		45.80	82.83	93.42
AA	Case 1	42.47	80.19	93.47
K×100		34.05	77.82	91.25
OA		49.40	87.97	96.83
AA	Case 2	44.32	84.57	96.89
K×100		37.39	84.07	95.75

4. CONCLUSIONS

The classification of DSM images is addressed in this manuscript by means of a new method. The proposed

approach makes use of local kernel matrix features, which are generated from MP features. The proposed method generates MP features containing pixel spatial and geometric characteristics in the first stage. The next step involves generating WLKM features from the MP features. Ultimately, the SVM classifier is applied to categorize the WLKM features that were extracted. By adopting the WLKM-based DSM classification technique, an accuracy rate of more than 90% can be attained, even when working with limited training samples. In subsequent work, we will develop a new WLKM-based method for fusing hyperspectral data with LiDAR data. Future studies will also examine the effectiveness of WLKM features generated from multishape MP features for DSM classification.

5. ACKNOWLEDGMENT

The National Center for Airborne Laser Mapping (NCALM), Xiong Zhou, Minshan Cui, Abhinav Singhania, and Dr. Juan Carlos Fernández Díaz are greatly appreciated by the authors for affording them the Houston data set.

6. REFERENCES

- Sharma, M., Garg, R.D., Badenko, V., Fedotov, A., Min, L. and Yao, A., "Potential of airborne lidar data for terrain parameters extraction", *Quaternary International*, Vol. 575, (2021), 317-327. <https://doi.org/10.1016/j.quaint.2020.07.039>
- Li, X., Chen, W.Y., Sanesi, G. and Laforteza, R., "Remote sensing in urban forestry: Recent applications and future directions", *Remote Sensing*, Vol. 11, No. 10, (2019), 1144. <https://doi.org/10.3390/rs11101144>
- Muhadi, N.A., Abdullah, A.F., Bejo, S.K., Mahadi, M.R. and Mijic, A., "The use of lidar-derived dem in flood applications: A review", *Remote Sensing*, Vol. 12, No. 14, (2020), 2308. <https://doi.org/10.3390/rs12142308>
- Wang, A., He, X., Ghamisi, P. and Chen, Y., "Lidar data classification using morphological profiles and convolutional neural networks", *IEEE Geoscience and Remote Sensing Letters*, Vol. 15, No. 5, (2018), 774-778. <https://doi.org/10.1109/LGRS.2018.2810276>
- Wang, A., Xue, D., Wu, H. and Gu, Y., "Efficient convolutional neural architecture search for lidar dsm classification", *IEEE Transactions on Geoscience and Remote Sensing*, Vol. 60, (2022), 1-17. <https://doi.org/10.1109/TGRS.2022.3171520>
- Zhang, M., Ghamisi, P. and Li, W., "Classification of hyperspectral and lidar data using extinction profiles with feature fusion", *Remote Sensing Letters*, Vol. 8, No. 10, (2017), 957-966. <https://doi.org/10.1080/2150704X.2017.1335902>
- Singh, M.K., Mohan, S. and Kumar, B., "Fusion of hyperspectral and lidar data using sparse stacked autoencoder for land cover classification with 3d-2d convolutional neural network", *Journal of Applied Remote Sensing*, Vol. 16, No. 3, (2022), 034523-034523. <https://doi.org/10.1117/1.JRS.16.034523>

8. Ghamisi, P. and Hoefle, B., "Lidar data classification using extinction profiles and a composite kernel support vector machine", *IEEE Geoscience and Remote Sensing Letters*, Vol. 14, No. 5, (2017), 659-663. <https://doi.org/10.1109/LGRS.2017.2669304>
9. He, X., Wang, A., Ghamisi, P., Li, G. and Chen, Y., "Lidar data classification using spatial transformation and cnn", *IEEE Geoscience and Remote Sensing Letters*, Vol. 16, No. 1, (2018), 125-129. <https://doi.org/10.1109/LGRS.2018.2868378>.
10. Wang, A., Wang, M., Jiang, K., Zhao, L. and Iwahori, Y., "A novel lidar data classification algorithm combined densenet with stn", in IGARSS 2019-2019 IEEE International Geoscience and Remote Sensing Symposium, IEEE. (2019), 2483-2486.
11. Asghari Beirami, B. and Mokhtarzade, M., "Ensemble of log-euclidean kernel svm based on covariance descriptors of multiscale gabor features for face recognition", *International Journal of Engineering, Transactions B: Applications*, Vol. 35, No. 11, (2022), 2065-2071. <https://doi.org/10.5829/IJE.2022.35.11B.01>
12. Wang, L., Zhang, J., Zhou, L., Tang, C. and Li, W., "Beyond covariance: Feature representation with nonlinear kernel matrices", in Proceedings of the IEEE international conference on computer vision. (2015), 4570-4578.
13. Zhang, J., Wang, L., Zhou, L. and Li, W., "Beyond covariance: Sice and kernel based visual feature representation", *International Journal of Computer Vision*, Vol. 129, (2021), 300-320. <https://doi.org/10.1007/s11263-020-01376-1>
14. Beirami, B.A. and Mokhtarzade, M., "Optimized weighted local kernel features for hyperspectral image classification", *Multimedia Tools and Applications*, Vol. 81, No. 15, (2022), 21859-21885. <https://doi.org/10.1007/s11042-022-12452-8>.
15. Asghari Beirami, B. and Mokhtarzade, M., "Spatial-spectral classification of hyperspectral images based on extended morphological profiles and guided filter", *Computer and Knowledge Engineering*, Vol. 2, No. 2, (2020), 2-8. <https://doi.org/10.22067/CKE.V2I2.81519>
16. Fang, L., He, N., Li, S., Plaza, A.J. and Plaza, J., "A new spatial-spectral feature extraction method for hyperspectral images using local covariance matrix representation", *IEEE Transactions on Geoscience and Remote Sensing*, Vol. 56, No. 6, (2018), 3534-3546. <https://doi.org/10.1109/TGRS.2018.2801387>
17. Mirzapour, F. and Ghassemian, H., "Moment-based feature extraction from high spatial resolution hyperspectral images", *International Journal of Remote Sensing*, Vol. 37, No. 6, (2016), 1349-1361. <https://doi.org/10.1080/2150704X.2016.1151568>

COPYRIGHTS

©2023 The author(s). This is an open access article distributed under the terms of the Creative Commons Attribution (CC BY 4.0), which permits unrestricted use, distribution, and reproduction in any medium, as long as the original authors and source are cited. No permission is required from the authors or the publishers.

**Persian Abstract****چکیده**

طبقه بندی دقیق پوشش زمین از مدل سطح دیجیتال (DSM) به دست آمده از سنجنده LiDAR یک موضوع چالش برانگیز است که محققان در سال های اخیر در نظر گرفته اند. به طور کلی، دقت طبقه بندی پوشش های زمین منجر به دقت پایین با استفاده از یک تصویر DSM تک بانده می شود. از این رو، به نظر می رسد توسعه روش های کارآمد برای استخراج اطلاعات مکانی مرتبط، که دقت طبقه بندی را بهبود می بخشد، ضروری به نظر می رسد. در این راستا، استفاده از ویژگی های مکانی مبتنی بر نیمرخ های مورفولوژیکی (MPs) دقت طبقه بندی را به طور چشمگیری افزایش داده است. علیرغم کارایی نیمرخ های مورفولوژیکی در افزایش دقت طبقه بندی تحت شرایط نمونه های آموزشی محدود هنوز در سطح رضایت بخشی نیست. نوآوری اصلی این مقاله، پیشنهاد یک فضای ویژگی جدید بر اساس توصیفگرهای هسته محلی به دست آمده از MP برای حل کردن چالش ذکر شده طبقه بندی DSM مبتنی بر MP است. این بردارهای ویژگی نوآورانه وابستگی های غیرخطی محلی و آمار مرتبه بالاتر بین ویژگی های مورفولوژیکی را در نظر می گیرند. آزمایشات این مطالعه بر روی دو مجموعه داده DSM معروف هیوستون و ترنتو انجام شده است. نتایج نهایی نشان می دهد که طبقه بندی DSM مبتنی بر SVM با ویژگی های هسته محلی جدید به دقت متوسط ۹۳.۷۵ درصد دست یافته است که بسیار بهتر از طبقه بندی SVM معمولی با ویژگی های تک باند DSM و MP است (به طور متوسط حدود ۵۷ درصد و ۱۱.۵ درصد، به ترتیب). علاوه بر این، روش پیشنهادی این پژوهش به طور متوسط ۴.۷٪ از دو روش طبقه بندی DSM دیگر موجود در پیشینه تحقیق بهتر عمل کرده است.



Decimal to Excess-3 and Excess-3 to Decimal Code Converters in QCA Nanotechnology

F. Fouladinia^a, M. Gholami^{*b}

^a Department of Electrical Engineering, Faculty of Energy, Kermanshah University of Technology, Kermanshah, Iran

^b Department of Electrical Engineering, Faculty of Engineering and Technology, University of Mazandaran, Babolsar, Iran

PAPER INFO

Paper history:

Received 16 April 2023

Received in revised form 13 June 2023

Accepted 14 June 2023

Keywords:

Quantum-dot Cellular Automata

Excess-3

Decimal

Energy Dissipation

Nanotechnology

ABSTRACT

Nowadays Quantum-dot Cellular Automata (QCA) is one of the new technologies in nanoscale which can be used in future circuits. Most digital circuits are implemented with CMOS technology, but CMOS has some problems like power consumption and circuit size. So, for solving these problems a new method (QCA) is presented. It is clear that converters play a crucial role in the digital world. So, due to the aforementioned point, in this paper, two digital code converters, containing an excess-3 to decimal, and a decimal to excess-3 code converter are presented. The tile method is used to design proposed circuits in quantum-dot cellular automata (QCA) nanotechnology. The tile method gives a unique block for the majority and NOT gates. This property facilitates integration. Both of the proposed code converters have 1.75 clock cycles delay and have an energy dissipation of about 100meV. In the excess-3 code to decimal converter, 516 cells are used, which occupy an area equal to $0.43\mu\text{m}^2$ also in the decimal to excess-3 code converter. 321 cells are used, which occupy an area equal to $0.28\mu\text{m}^2$.

doi: 10.5829/ije.2023.36.09c.05

1. INTRODUCTION

Nowadays Quantum-dot Cellular Automata (QCA) is one of the new technologies in the nanoscale which can be used in future circuits [1]. Most digital circuits are implemented with CMOS technology, but CMOS has some problems like power consumption and circuit size [2]. So, for solving the aforementioned problems a new method (QCA) is presented. QCA technology can solve scaling issues and presents high frequency up to terahertz [3]. In 1993, this technology was first introduced by Lent et al. [4].

Systems in digital electronic like digital computers are worked in binary form. So, for working and calculating with this type of system, data should be converted to the right codes, here the importance of code converting is felt, and that's why many code converters like decimal to binary, binary to decimal, decimal to excess-3, excess-3 to decimal, etc. were presented by Gholami et al. [5]. Many ICs convert codes. ICs that are based on transistors have some issues like power dissipation and short-channel effects at very low device

sizes [6]. So, utilizing a new method like QCA can be a key step toward solving these problems. Moreover, some methods are presented with the aim of making improvements in the performance of QCA circuits [7]. One of these methods is the tile which is presented by Huang et al. [8]. Tile presents a combined logic function for INV and Majority gates, so the tile method is area efficient because it presents one unique block for INV and Majority gates [9]. Since reducing the occupied area, energy dissipation, and of course, improving the performance is very vital, the technology of integrated circuits was expanded [10-12]. In this paper by using the tile method, two code converters are presented: excess-3 code to decimal (that is the topology of 7443 IC from 74 series IC) and decimal to an excess-3 code. There weren't many papers to present QCA digital code converters, particularly an excess-3 code converter [5], but in the following, some papers about code converters are presented. Raina et al. [9] presented a BCD to seven-segment code. A seven-segment has seven different parts and every part includes a light-emitted diode. This work presents seven circuits for each segment with the gate

*Corresponding Author Email: m.gholami@umz.ac.ir (M. Gholami)

method style. Presenting seven different circuits instead of one circuit is the most important defect of this paper. Kassa et al. [12] presented at first, a full adder (FA); then, with three of that FA, a binary to BCD converter was proposed. This circuit was implemented utilizing the gate method and wasn't optimized as much as possible. Kaity and Singh [13] just like the others, used the gate method and some digital code converters were presented. One of these converters is excess-3 code to the binary that this circuit was implemented with Feynman gate. In this converter, two of the aforementioned gate has been used. Mukherjee et al. [14] proposed a LTeX module with the gate method style in which a two-input LTeX module consisting of 26 cells and 4 clock phases was used to produce outputs. Every LTeX module is a two-input NAND gate with the new structure, then for implementation of 2 to 16 bits binary to gray code converter, this module has been utilized. Karthik [15] presented a simple converter utilizing basic structures of the QCA technology like wire, majority gate, etc. This circuit is converted BCD to excess-3 code and as mentioned before, the gate method is used in this design which has no new idea. You and Jeon [16] designed at first, a majority gate with five inputs is, this majority gate uses 3 clock phases to give an output, then with this majority and the ability to rotate cells in QCA, a BCD to Excess-3 code converter was implemented. As is clear, due to the high number of inputs and outputs in converting decimal to Excess-3 code, this type of converter has not been paid much attention. Therefore, in this paper, the main focus is on designing a decimal to excess-3 and vice versa code converters in QCA nanotechnology. To design the mentioned converters the tile method is utilized with the aim of reducing the size of the circuit and of course, enabling the circuits to be integrated.

inside the cell instead of moving across a conductor like wire, which results in high energy consumption and energy loss. One of the most important gates in this technology is the majority gate, which has the function $Maj(A, B, C) = AB + AC + BC$, and using it, important gates can be implemented. For instance, AND and OR gates (by setting one of the three inputs as binary 0 for AND gate and binary 1 for OR gate), this gate is shown in Figure 2. As can be seen, five cells are used to implement this gate. Another important gate that is very widely used in the implementation of logic circuits is the inverter gate which is shown in Figure 3. Finally, the wire gate in this technology is presented. This gate is responsible for data transmission and has many applications, as it can be shown in Figure 4.

In QCA, clocking is very important because the simultaneous arrival of the inputs of a gate is very necessary to get the correct answer. As can be seen in Figure 5, in this technology clocking has 4 main phases. The first phase is called the switch, which is the increment of the force that prevents the movement of electrons inside each cell, and the movement of electrons gradually becomes difficult. In the next phase, which is called hold, the forces that prevented the movement of electrons inside each cell, reach their maximum amount and, because of that the location of electrons has remained stable or fixed (This way the cell gets new polarization). In the third phase, called release, the amount of the blocking force will be decreased, and electrons are slowly released. Finally, in the fourth phase, known as relax, the cell has no polarity and electrons will move completely free inside the cell. To apply clocking, it is very important to observe the order of the clock phases, at first, the cells should be in the switch phase (with green color for cells), then hold (purple color), then release (light blue color), And finally, relax

2. QCA'S BASIC CONCEPTS

A QCA cell consists of several parts. Two freely moving electrons and four areas are used as wells to trap electrons, known as dots. All of the aforementioned parts are inside a square showing each cell's perimeter. All these cases can be seen in Figure 1. Two valid states can be defined for cells, one is used for logical zero and the other for logical one (known as binary 0 and binary 1 in Figure 1).

One of the advantages of QCA is its very low energy consumption, due to the movement of electrons only

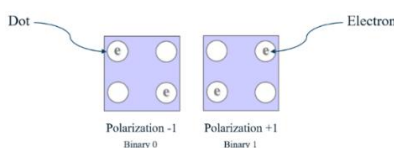


Figure 1. QCA cell and polarization states

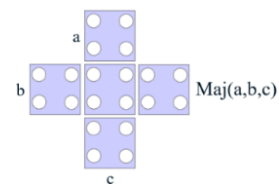


Figure 2. Majority gate in QCA

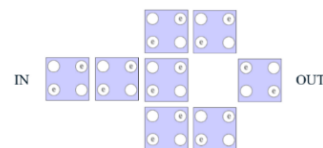


Figure 3. Inverter gate in QCA

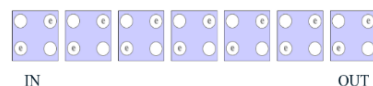


Figure 4. Wire gate in QCA

phase (white color), after a complete clocking cycle, if more phases are needed, second cycle of clocking is started and again clocking is done from the switch phase according to the mentioned method.

Generally, there are several mechanisms for designing and simulating the QCA circuits, the most common method used for design is the gate-based method, and the explanations given are all based on this method. One of the recently used methods to improve circuits is the tile method [8], which is also used in this paper to design and simulate the circuit. As seen earlier, in the gate-based method, there are unique structures for the majority and inverter gates, eliminating the possibility of integrating these circuits, but in the tile-based method, due to the proposed structure, it is possible to integrate the circuit because just one structure is used for both majority and inverter gates. As is shown in Figure 6, a majority gate with three inputs and one output is presented with a tile block. Also in Figure 7, an inverter gate with this method is shown in Figure 8. An example gate is presented that gives $a\bar{b}$ output without any use of an inverter gate.

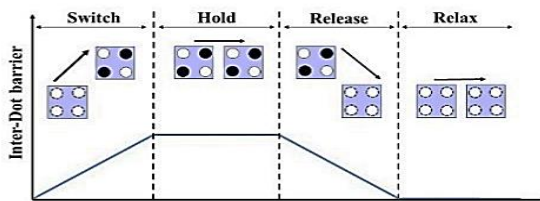


Figure 5. Clocking in QCA

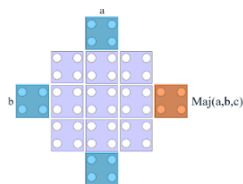


Figure 6. Majority gate in QCA using the Tile method

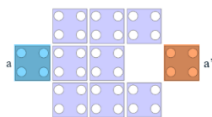


Figure 7. Inverter gate in QCA using the Tile method

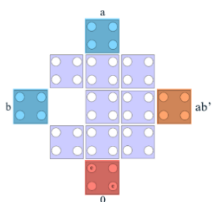


Figure 8. Majority gate in QCA using the Tile method

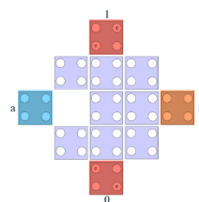


Figure 9. Inverter gate in QCA using the Tile method

Also, as it can be seen the inverter gate can be implemented just like the example that is presented in Figure 8. This type of inverter is shown in Figure 9.

In this inverter, in the first place, the invert of input “a” is calculated, then that value is OR with binary “0” or that value is AND with binary “1”, both of these calculations have the same results, which is the invert of input “a”.

3. PROPOSED DIGITAL CODE CONVERTERS IN QCA CIRCUITS

In this section, two digital converters with tile method are proposed, excess-3 code to decimal and decimal to excess-3 code. At first, a logical circuit for the excess-3 code to decimal converter is presented, then an equivalent circuit for this converter with tile method is given, next step the QCA circuit of the excess-3 code to decimal converter is given, In the following all the mentioned steps for the second converter namely decimal to excess-3 code are presented. To explain about differences between the general and the tile method let’s take the NAND gate as a sample. One of the ways to implement this widely used gate there is a need for a common majority gate plus an inverter gate which means there is a need for 16 cells and 3 phases of the clock for implementing a NAND gate. But if the implementation will be done utilizing the tile method there is a need for 12 cells with just 2 phases of the clock, so it’s clear that utilizing new methods like the tile method can be a key step toward decreasing the size and of course, the latency of the designed circuit.

3.1. Proposed Excess-3 to Decimal Converter 74 series ICs are very popular, widely used, and have many educational, research, and industrial uses. One of these ICs is 7443, which converts excess-3 code to decimal. The internal circuit of this IC can be seen in Figure 10. Also, the truth table of the aforementioned IC is given in Table 1.

As it is seen, this IC includes 4 inputs for the excess-3 numbers and ten outputs for the decimal numbers, ten NAND gates with four inputs and eight NOT gates are used in this circuit. As mentioned, the goal is to implement the circuit in Figure 10. with the tile method in QCA technology. For this purpose, NOT and NAND

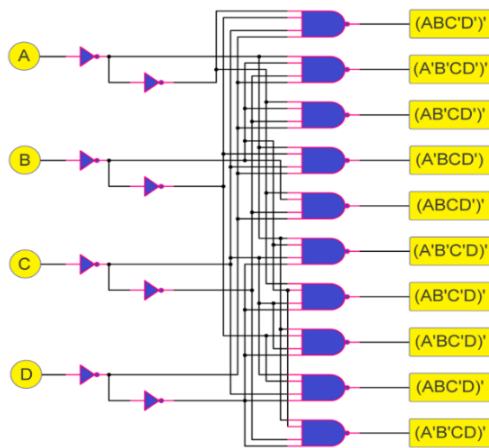


Figure 10. 7443 IC internal circuit

TABLE 1. The truth table of 7443 IC

INPUTS				OUTPUTS									
D	C	B	A	0	1	2	3	4	5	6	7	8	9
0	0	1	1	0	1	1	1	1	1	1	1	1	1
0	1	0	0	1	0	1	1	1	1	1	1	1	1
0	1	0	1	1	1	0	1	1	1	1	1	1	1
0	1	1	0	1	1	1	0	1	1	1	1	1	1
0	1	1	1	1	1	1	1	0	1	1	1	1	1
1	0	0	0	1	1	1	1	1	0	1	1	1	1
1	0	0	1	1	1	1	1	1	1	0	1	1	1
1	0	1	0	1	1	1	1	1	1	1	0	1	1
1	0	1	1	1	1	1	1	1	1	1	1	0	1
1	1	0	0	1	1	1	1	1	1	1	1	1	0

gates are needed. For NOT gate with tile, the gate presented in Figure 9. will be used. For the NAND gate, the gate that can be seen in Figure 11 will be used.

The following QCA circuit of excess-3 to the decimal converter using tile method is shown in Figure 13.

The presented circuit is implemented in three layers, the main layer, the via layer, and the top layer, all of these layers are shown in Figures 14 to 16.

To reduce the occupied area of the circuit as much as possible, its design and implementation have been done in three layers. Also, in this circuit, 516 cells are used, occupying an area equal to $0.43\mu\text{m}^2$. In addition, 6 clock phases have been used in this circuit. The total energy

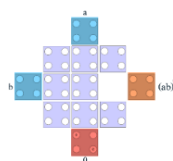


Figure 11. NAND gate in QCA using the Tile method

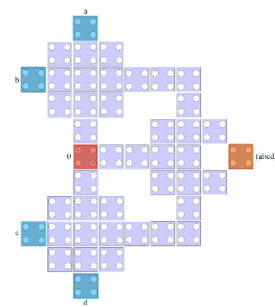


Figure 12. Four inputs NAND gate with tile

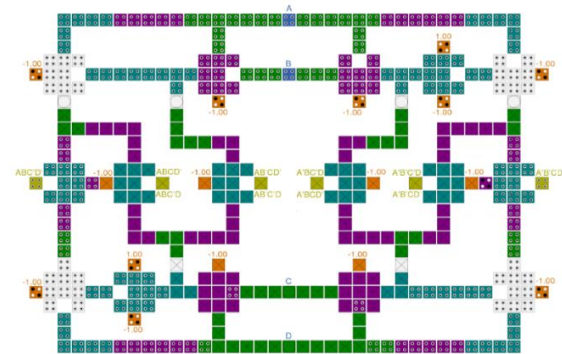


Figure 13. Proposed excess-3 to the decimal converter (7443 IC) QCA circuit

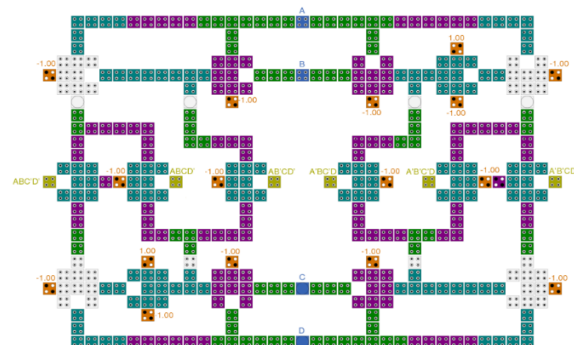


Figure 14. The main layer of the proposed excess-3 to decimal converter (7443 IC) QCA circuit.

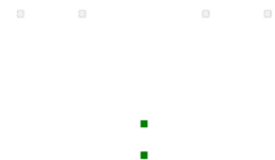


Figure 15. The via layer of proposed excess-3 to decimal converter (7443 IC) QCA circuit.

consumption for this circuit is about $1.14e-001$ eV. As it can be seen from Figure 13. There are not any NOT gates that make the circuit as faster as possible. In this circuit 22 main blocks (which here are tiles and for gate method is majority gate) are used.

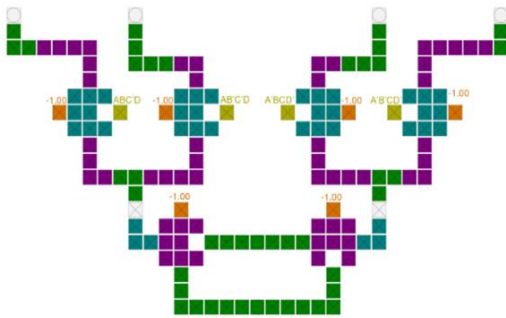


Figure 16. The top layer of proposed excess-3 to decimal converter (7443 IC) QCA circuit

3. 2. Proposed Decimal to Excess-3 Code Converter

In this section, the circuit of a converter is presented which gives an excess-3 code instead of a decimal number. Just like the previously proposed circuit, this circuit is implemented with the tile method. The logical circuit for this converter is given in Figure 17. Also, the truth table for this circuit is presented in Table 2.

TABLE 2. The truth table of decimal to excess-3 code converter

INPUTS										OUTPUTS			
I0	I1	I2	I3	I4	I5	I6	I7	I8	I9	O1	O2	O3	O4
1	0	0	0	0	0	0	0	0	0	0	1	1	
0	1	0	0	0	0	0	0	0	0	0	1	0	0
0	0	1	0	0	0	0	0	0	0	0	1	0	1
0	0	0	1	0	0	0	0	0	0	0	1	1	0
0	0	0	0	1	0	0	0	0	0	0	1	1	1
0	0	0	0	0	1	0	0	0	0	1	0	0	0
0	0	0	0	0	0	1	0	0	0	1	0	0	1
0	0	0	0	0	0	0	1	0	0	1	0	1	0
0	0	0	0	0	0	0	0	1	0	1	0	1	1
0	0	0	0	0	0	0	0	0	1	1	1	0	0

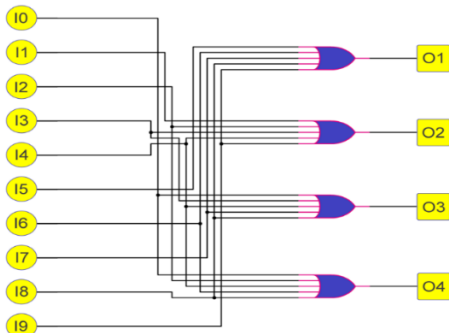


Figure 17. Decimal to excess-3 code converter logical circuit

As it is seen, this converter includes ten inputs for the decimal number (from 0 to 9) and four outputs for the excess-3 number (from 0011 to 1100), and four OR are used in this circuit. In this circuit OR gate which is implemented with the tile method is shown in Figure 18 is used.

In the following, the QCA circuit of decimal to excess-3 converter using the tile method is presented in Figure 19.

Just like the previously proposed circuit, this circuit also is implemented in three layers, the main layer, the via layer, and the top layer, all of these layers are shown in Figures 20 to 22.

Same as the previous circuit, to reduce the occupied area of the circuit as much as possible, its design and implementation have been done in three layers. Also, in this circuit, 321 cells are used occupying an area equal to 0.28 square micrometers. In addition, 7 clock phases

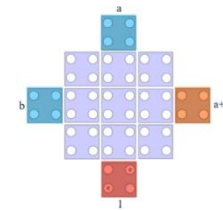


Figure 18. NAND gate in QCA using the Tile method

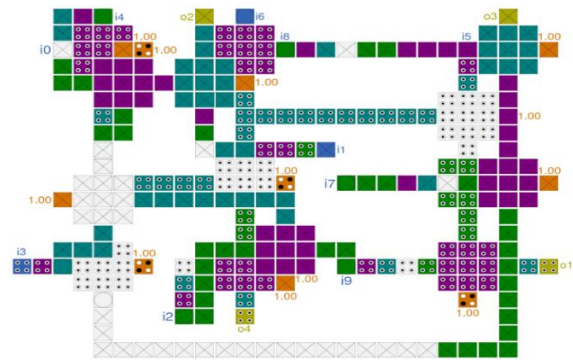


Figure 19. Proposed decimal to excess-3 converter QCA circuit

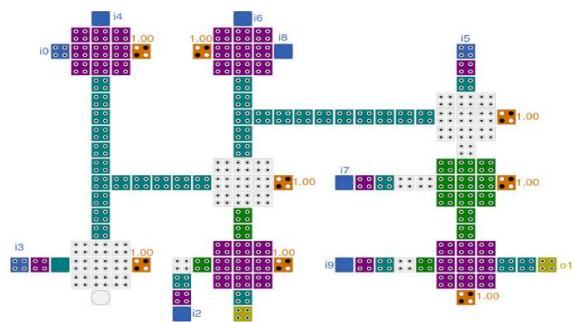


Figure 20. Main layer of proposed decimal to excess-3 converter QCA circuit

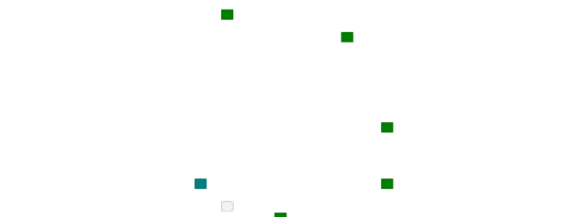


Figure 21. Via layer of proposed decimal to excess-3 converter QCA circuit

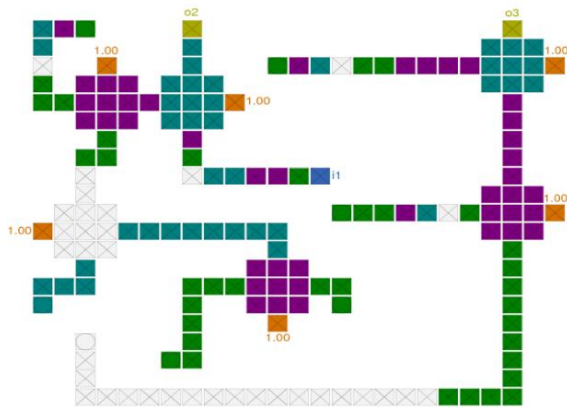


Figure 22. The top layer of the proposed decimal to excess-3 converter QCA circuit

have been used in this circuit. As can be seen from Figure 19. There are zero NOT gates which make the circuit as faster as possible. In this circuit, 14 main blocks (which here are tiles and for gate method is majority gate) are used. The total power consumption for this circuit is about $1.04e-001$ eV.

4. SIMULATIONS AND RESULTS

In this section, the accuracy of the proposed circuits is checked using QCADesigner-E software. QCADesigner-E is one of the most reliable software in the field of QCA, and version 2.2 is used in this paper [17, 18]. This software was developed by the University of Calgary.

Using this software, values such as the number of cells, the number of clock phases, the occupied area, and the power consumption can be extracted. In the following, the simulation results of each of the converters will be given in Figure 23. The inputs of the excess-3 code to decimal converter can be seen. These inputs have produced the outputs in Figure 24. As it is clear from the mentioned figure, the proposed circuit has correctly produced the expected values, for example, for producing (ABC'D') inputs are A=1, B=1, C=0 and D=0 that produce ABC'D' output, with inverting this output the main output is produced (this is shown in Figures 23 and 24). For the next converter, decimal to excess-3 code, in Figure 25. the decimal inputs of this converter can be seen. These inputs have produced the outputs in Figure 26. As it is clear from the outputs, the proposed circuit has correctly produced the expected values, for example, to produce O4 output which one of I0, I2, I4, I6, or I8 is binary "1" the output will be binary "1" (this is shown in Figures 25 and 26). As mentioned before the first proposed circuit had 516 cells and 6 clock phases have been used in it. Also, the total power consumption for this circuit was about $1.14e-001$ eV. The second proposed circuit had 321 cells and 7 clock phases have been used in it. Also, the total power consumption for this circuit was about $1.04e-001$ eV. The most important cell in energy consumption are fixed cells and of course, the central cell which is played as the calculator cell. Because there are no similar works for this type of conversion, we cannot compare the proposed design with other related works. In Table 3. details of the proposed circuits are given.

As it was clear, in the proposed excess-3 to decimal converter, in Figure 23. An excess-3 code equal to 0100 was chosen. After 6 phases of the clocking, the answer was checked in Figure 24. (ABC'D') was supposed to be "0", as it was. To consider another example, 1010 excess-3 code can be chosen. The answer was supposed to be "0" just for the (AB'CD'), it can be seen that the correct answer is obtained. To check the proposed decimal to excess-3 code converter is investigated. In Figure 25, there were 10 different inputs from 0 to 9 of the decimal code. Because $O1 = I8 + I9$ wherever one of these inputs gets the binary "1" O1 output was supposed to be "1", which can be seen in Figure 26.

		Simulation Results									
A	max: 1.00e+000 min: -1.00e+000										
B	max: 1.00e+000 min: -1.00e+000										
C	max: 1.00e+000 min: -1.00e+000										
D	max: 1.00e+000 min: -1.00e+000										

Figure 23. Inputs of proposed excess-3 to decimal converter QCA circuit

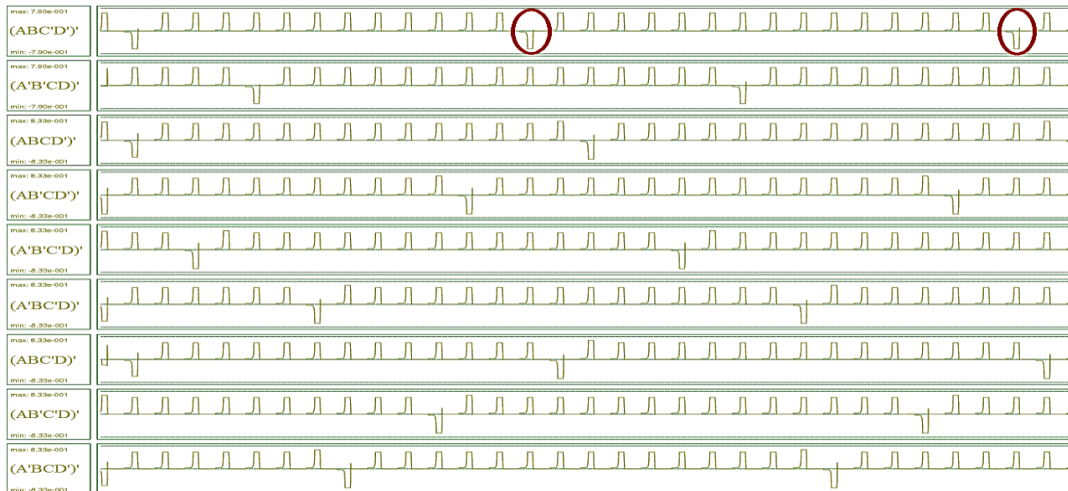


Figure 24. Outputs of proposed excess-3 to decimal converter QCA circuit

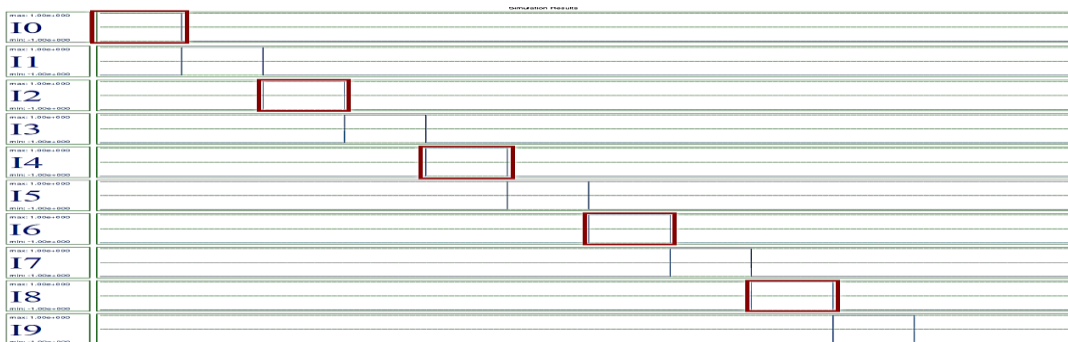


Figure 25. Inputs of proposed decimal to excess-3 converter QCA circuit

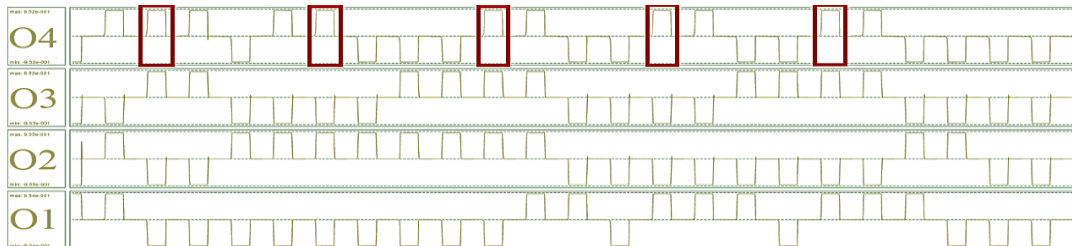


Figure 26. Outputs of proposed decimal to excess-3 converter QCA circuit

TABLE 3. Details of proposed circuits

Items	Excess-3 to Decimal converter	Decimal to Excess-3 converter
Cell count	516	311
Delay (clock phases)	6	7
Main gate count	22	14
Inverter gate count	0	0
Power consumption	1.14e-001 eV	1.04e-001 eV
Designing type	Tile method	Tile method
Ability to integrate	HIGH	HIGH

5. CONCLUSION

In this paper, two digital converters were presented, the first one was for converting excess-3 code to decimal and another one was for converting decimal to excess-3 code. The method that was used in both of them was the tile method. This method has some advantages, with this method circuits can be integrated and get faster because there is no need to use an inverter gate lonely. In the end, both of the proposed circuits were evaluated with QCADesigner-E, and some reports like cell count, delays, power consumption, etc. were presented.

6. REFERENCES

- Alamdar, H., Ardeshir, G. and Gholami, M., "Using universal nand-nor-inverter gate to design d-latch and d flip-flop in quantum-dot cellular automata nanotechnology", *International Journal of Engineering, Transactions A: Basics*, Vol. 34, No. 7, (2021), 1710-1717. doi: 10.5829/ije.2021.34.07a.15.
- Gholami, M., Binaei, R. and Gholamnia Roshan, M., "Novel phase-frequency detector based on quantum-dot cellular automata nanotechnology", *International Journal of Engineering, Transactions B: Applications*, Vol. 33, No. 2, (2020), 269-276. doi: 10.5829/ije.2020.33.02b.11.
- Zoka, S. and Gholami, M., "Two novel d-flip flops with level triggered reset in quantum dot cellular automata technology", *International Journal of Engineering, Transactions C: Aspects*, Vol. 31, No. 3, (2018), 415-421. doi: 10.5829/ije.2018.31.03c.03.
- Lent, C.S., Tougaw, P.D., Porod, W. and Bernstein, G.H., "Quantum cellular automata", *Nanotechnology*, Vol. 4, No. 1, (1993), 49. doi: 10.1088/0957-4484/4/1/004.
- Khakpour, M., Gholami, M. and Naghizadeh, S., "Parity generator and digital code converter in qca nanotechnology", *International Nano Letters*, Vol. 10, No. 1, (2020), 49-59. <https://doi.org/10.1007/s40089-019-00292-8>
- Huang, J., Momenzadeh, M., Schiano, L. and Lombardi, F., "Simulation-based design of modular qca circuits", in 5th IEEE Conference on Nanotechnology, 2005., IEEE. (2005), 533-536.
- Parvane, M., Rahimi, E. and Jafarnejad, F., "Optimization of quantum cellular automata circuits by genetic algorithm", *International Journal of Engineering, Transactions B: Applications*, Vol. 33, No. 2, (2020), 229-236. doi: 10.5829/ije.2020.33.02b.07.
- Huang, J., Momenzadeh, M., Schiano, L., Ottavi, M. and Lombardi, F., "Tile-based qca design using majority-like logic primitives", *ACM Journal on Emerging Technologies in Computing Systems*, Vol. 1, No. 3, (2005), 163-185. <https://doi.org/10.1145/1116696.1116697>
- Raina, B., Verma, C., Gupta, M. and Sharma, V.K., "Binary coded decimal (BCD) seven segment circuit designing using quantum-dot cellular automata (QCA)", in 2021 5th International Conference on Trends in Electronics and Informatics (ICOEI), IEEE. (2021), 126-130.
- Ramesh, B. and Rani, M.A., "Design of binary to bcd code converter using area optimized quantum dot cellular automata full adder", *International Journal of Engineering (IJE)*, Vol. 9, No. 4, (2015), 49-64.
- Chakrabarty, R., Roy, S., Pathak, T. and Kumar Mandal, N., "Design of area efficient single bit comparator circuit using quantum dot cellular automata and its digital logic gates realization", *International Journal of Engineering, Transactions C: Aspects*, Vol. 34, No. 12, (2021), 2672-2678. doi: 10.5829/ije.2021.34.12c.13.
- Kassa, S. and Nema, S., "Energy efficient novel design of static random access memory cell in quantum-dot cellular automata approach", *International Journal of Engineering, Transactions B: Applications*, Vol. 32, No. 5, (2019), 720-725. doi: 10.5829/ije.2019.32.05b.14.
- Kaity, A. and Singh, S., "Optimized area efficient quantum dot cellular automata based reversible code converter circuits: Design and energy performance estimation", *The Journal of Supercomputing*, Vol. 77, No. 10, (2021), 11160-11186. <https://doi.org/10.1007/s11227-021-03693-9>
- Mukherjee, C., Panda, S., Mukhopadhyay, A.K. and Maji, B., "Towards modular binary to gray converter design using ltx module of quantum-dot cellular automata", *Microsystem Technologies*, Vol. 25, (2019), 2011-2018. <https://doi.org/10.1007/s00542-018-4066-0>
- Karthik, K., "An efficient design approach of bcd to excess-3 code converter based on qca", *International Journal of Engineering Research & Technology*, Vol. 6, No. 6, (2017), 310-316.
- You, Y.-w. and Jeon, J.-c., "Design of extendable bcd-excess 3 code convertor using quantum-dot cellular automata", *Journal of Advanced Navigation Technology*, Vol. 20, No. 1, (2016), 65-71.
- Torres, F.S., Wille, R., Niemann, P. and Drechsler, R., "An energy-aware model for the logic synthesis of quantum-dot cellular automata", *IEEE Transactions on Computer-Aided Design of Integrated Circuits and Systems*, Vol. 37, No. 12, (2018), 3031-3041. doi: 10.1109/TCAD.2018.2789782.
- Walus, K., Dysart, T.J., Jullien, G.A. and Budiman, R.A., "Qcadesigner: A rapid design and simulation tool for quantum-dot cellular automata", *IEEE Transactions on Nanotechnology*, Vol. 3, No. 1, (2004), 26-31. doi: 10.1109/TNANO.2003.820815.

COPYRIGHTS

©2023 The author(s). This is an open access article distributed under the terms of the Creative Commons Attribution (CC BY 4.0), which permits unrestricted use, distribution, and reproduction in any medium, as long as the original authors and source are cited. No permission is required from the authors or the publishers.



Persian Abstract

چکیده

امروزه اتوماتای سلولی نقطه کوانتومی (QCA) یکی از فناوری های جدید در مقیاس نانو است که می تواند در مدارهای آینده مورد استفاده قرار گیرد. اکثر مدارهای دیجیتال با فناوری CMOS پیاده سازی می شوند، اما CMOS دارای مشکلاتی مانند مصرف انرژی و اندازه مدار است. بنابراین برای حل این مشکلات روش جدیدی (QCA) ارائه شده است. واضح است که مبدل ها نقش مهمی در دنیای دیجیتال دارند. بنابراین، با توجه به نکته فوق، در این مقاله دو مبدل کد دیجیتال شامل مبدل کد اضافی ۳ به اعشار و یک مبدل اعشاری به بیش از ۳ ارائه شده است. روش کاشی برای طراحی مدارهای پیشنهادی در فناوری نانو اتوماتای سلولی نقطه کوانتومی (QCA) استفاده می شود. روش کاشی یک بلوک منحصر به فرد برای دروازه های اکثریت و NOT می دهد. این ویژگی یکپارچگی را تسهیل می کند. هر دو مبدل کد پیشنهادی دارای ۱.۷۵ تاخیر سیکل ساعت هستند و اتلاف انرژی در حدود ۱۰۰ مگا ولت دارند. در مبدل کد اضافی به اعشار از ۵۱۶ سلول استفاده شده است که مساحتی معادل ۰.۴۳ میکرومتر مربع را نیز در مبدل کد اعشاری به بیش از ۳ اشغال می کند. ۳۲۱ سلول استفاده شده است که مساحتی معادل ۰.۲۸ میکرومتر مربع را اشغال می کند.



Non-destructive Corrosion Monitoring of Reinforced Concrete Steel Rebars in Chloride Media by Smartphone Magnetic and Analog Hall-Effect Sensors

B. Hazrati Dorigh^a, E. Khakzadeh^b, I. Ahadzadeh*^b, R. Salamat-Ahanghari^a

^a Department of Chemistry, Faculty of Basic Sciences, Azarbaijan Shahid Madani University, Tabriz, Iran

^b Department of Physical Chemistry, Faculty of Chemistry, University of Tabriz, Tabriz, Iran

PAPER INFO

Paper history:

Received 24 May 2023

Received in revised form 21 June 2023

Accepted 29 June 2023

Keywords:

Concrete Corrosion

Corrosion Monitoring

Electromagnetic Sensor

Hall-Effect Sensor

Smart Phone

LCR Meter

ABSTRACT

The corrosion of reinforced concrete (RC) is a leading cause of structural failures and engineering problems in current infrastructural aspects; making corrosion monitoring of reinforcements in concrete structures highly important especially from safety point of view. Non-destructive testing (NDT) methods are useful approaches for in-situ detection and evaluation of steel corrosion in RC for monitoring time trend of corrosion of rebars. Recently, some NDT methods such as magnetic and resistive sensors as well as electrochemical monitoring methods such as electrochemical impedance spectroscopy were developed for RC rebar corrosion monitoring. This paper presents a novel approach using modern smartphones equipped with magnetic sensors and commercially available analog Hall-Effect sensors to monitor rebar corrosion within the concrete. Results showed a reasonable sensitivity of the methods to detect and monitor corrosion of rebars with time. In order to check and validate the data obtained in this study, another non-destructive electromagnetic test by a search coil connected to a LCR meter was used to monitor corrosion. The results obtained with this method were consistent with the previous methods. In other words, by using these three methods, it is possible to successfully monitor and determine the severity of corrosion.

doi: 10.5829/ije.2023.36.09c.06

1. INTRODUCTION

To increase the strength of concrete structures, many strategies have been adopted, among these methods is the use of concrete reinforced with rebars, but due to the presence of corrosive species in the environment, the problem of corrosion of rebars has become a global challenge, so these rebars are being continuously inspected and monitored for corrosion [1]. The environment species that cause most of the corrosion of rebars inside structures include chloride, sulfide and carbon dioxide ions, which facilitate the corrosion of the structure with oxygen and some of the negative effects of chloride infiltration into concrete are as follows:

a) It destroys the passive layer of the steel rebar and makes possible the corrosion attack.

b) By reducing the solubility of $\text{Ca}(\text{OH})_2$, it causes the pH of infiltrated water to decrease.

c) Due to the hygroscopic property of salts in concrete (such as NaCl , CaCl_2), it increases the amount of humidity, and d) It increases the electrical conductivity of the concrete [2].

Common methods of reducing corrosion damage of reinforced concrete include correct selection of metal, proper design, cathodic protection, anodic protection, coating and corrosion inhibitors [3].

The whole corrosion process in concrete rebar can be expressed as depicted in Figure 1.

Corrosion of steel in concrete is a result of the dissolution of iron in pore water, which can be indicated as anodic and cathodic reactions mentioned in Equations (1)-(5). At the anodic site, the reaction of Equation (1) occurs:

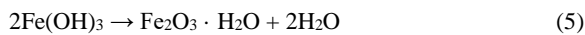
*Corresponding Author Email: ahadzadeh@tabrizu.ac.ir
(I. Ahadzadeh)



In the cathode site, due to the presence of O_2 and H_2O ions, the cathodic reaction is expressed in the form of Equation (2):



If the attacking ions are not present in the pore solution, the reactions of Equations (3)-(5) continue to occur, but in the presence of ions such as chlorine, the reaction of Equation (6) is performed, which prevents the formation of a passive layer on the surface of the rebar [4].



Corrosion of steel bars embedded in reinforced concrete structures reduces the useful life and durability of structures causing premature failure of the structure, which has a significant cost for the inspection and maintenance of the structures that are being destroyed. Therefore, monitoring the corrosion of reinforcements is very important to prevent the premature failure of structures [5-8]. Recently, different methods have been implemented to monitor corrosion in reinforced concrete structures. They are classified into six main categories as follows:

Visual Inspection, Electrochemical Methods, Electromagnetic (EM) Waves, Infrared Thermography (IRT), Optical Sensing Methods, and Elastic Wave Method. Each of these 6 methods is classified into various corrosion monitoring methods. For example, among the various techniques for monitoring corrosion

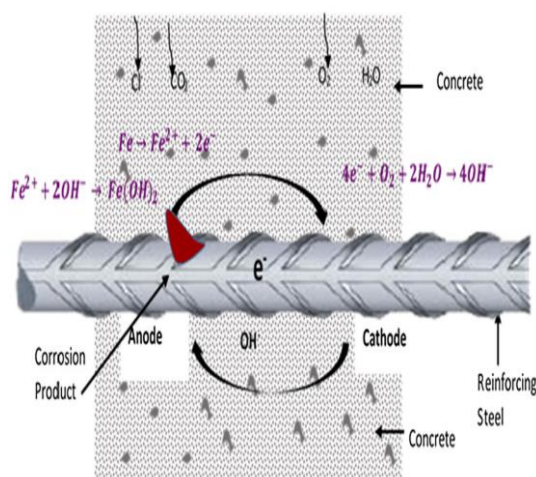


Figure 1. Schematic of corrosion concrete rebar [8]

by electrochemical method, the open circuit potential technique, resistance method, polarization resistance, galvanostatic pulse method (GPM), electrochemical noise (EN), impedance (EIS), and Tafel could be mentioned [9]. Each of these methods has its own disadvantages and advantages. However, it is almost impossible to identify and locate corrosion damage with solely electrochemical devices [10]. Nowadays, monitoring devices such as electromagnetic sensors, acoustic emission analyzers, X-ray machines, industrial CTs, optical fiber sensors, and digital imaging techniques have emerged based on various physical fields. Among these devices, first electromagnetic sensors and then digital image technology are considered as the best methods for monitoring the corrosion of steel buried in reinforced concrete and the deformation of concrete surface [11].

Nowadays, smartphone has become an important tool for corrosion monitoring. The sensors in the smartphone have been used to collect data for processing and evaluation and final explanation [6, 12]. Hall-Effect sensor is one of the types of electromagnetic sensors. The Hall-Effect sensor is a device that is activated by applying a magnetic field. Magnetic flux density intensity and polarity (north and south poles) are two important characteristics of the magnetic field. When the magnetic flux density around the sensor exceeds a certain threshold, the sensor recognizes this issue and produces an output voltage called "Hall voltage". Recently, smartphones have been equipped with a feature in sensors such as magnetic sensors, acceleration sensors, pressure, temperature sensors. Smartphones equipped with a magnetic sensor can be used as a detector to measure the magnetic field [13, 14]. The innovative aspect of this research is the monitoring of steel corrosion in reinforced concrete using the electromagnetic method by the smartphone equipped with the Hall effect sensor.

Zhang et al. [13] have used an innovative magnetic-based corrosion evaluation apparatus to investigate the fundamental relationship between corrosion rate and magnetic induction surrounding steel reinforcement. This apparatus can be embedded directly inside reinforced concrete structures and monitor the rate of corrosion of the reinforcement. The preliminary calibration results show that there is a linear relationship between the weight loss of corrosive reinforcement with the voltage increment detected by the Hall-effect sensor surrounding the corroded reinforcement. This increment in voltage is due to the variation of magnetic field induction [13]. Zhang et al. [15] have presented a non-destructive method for monitoring steel corrosion in reinforced concrete bridges by using a 3D digital micromagnetic sensor. In their research, the setup of the magnetic scanning device and the measurement mode of the micromagnetic sensor have been examined to detect and analyze the leakage of the magnetic field from corroded

reinforced concrete. On the other hand, the numerical analysis model has also been developed and presented based on the linear magnetic charge theory. By comparing magnetic field leakage data and numerical calculations, the authors have concluded that the tangential magnetic field curves cross at different heights near the corrosion zone. As a result, through the intersection of magnetic field curves, it is possible to detect and evaluate the steel corrosion area in reinforced concrete [15]. Li et al. [11] have introduced a novel electro-magnetic monitoring apparatus (EMMA) to monitor the corrosion of reinforced bars in concrete. Novel EMMA has twenty-four Hall-effect sensors embedded and a magnification monitoring probe that can detect variations in the intensity of the magnetic field of reinforced bars in concrete. As their results showed, the magnetic flux varied with the occurrence of corrosion, and this variation increased the Hall-effect voltage at cross-section of the reinforced concrete [11]. Van Steen et al. [16] have used the acoustic emission (AE) technique to monitor corrosion. Results show that AE can detect damage during the corrosion process [16]. Elyasigorji et al. [17] have introduced a DC magnetic field in the vicinity of the reinforcing steel in concrete to detect the corrosion of the prestressing steel of the magnetic flux leakage (MFL) concept in several configurations. The results indicate that the variations in the induced magnetic field are due to the presence of corrosion [17].

The LCR meter method is another modern corrosion monitoring method. The basis of this method is based on the change of parameters L (inductance), C (capacitance), R (resistance) and Q (quality factor) of an electric circuit element applied as sensor. In common researches, the coil is used as a monitoring probe in series with the LCR meter device, and when corrosion occurs, the values of L and Q change according to the amount of corrosion [18].

In this research, a simple and non-destructive method of smartphone and Hall effect sensor methods were used to monitor corrosion. Results were obtained regarding the location of corrosion, intensity and depth of corrosion, and mechanism of corrosion.

2. EXPERIMENTAL

To monitor the corrosion of reinforced concrete, a simulation of industrial structures was used. The smartphone's magnetic sensor and analog Hall-Effect sensor was used to corrosion monitoring and the LCR meter was used to monitor and validate the obtained data.

2.1. Materials A plastic cast with a length of 22.7 cm, a width of 14.9 cm, and a height of 4.9 cm was used to make a reinforced concrete block (Figure 2) [19-22].

The mixing ratio of Portland cement and sand is 1:5. Four rebars were used with a length of 140 mm and a diameter of 8 mm, and the position of the rebars is 40 mm apart and 10 mm deep in the concrete [23-25].

2.2. Methodology In order to monitor the corrosion of reinforced concrete with a smartphone and Hall-Effect sensor, first the rebars in the concrete have been made to undergo intentional accelerated corrosion. Considering that the corrosion of steel is basically a time-consuming process, it is possible to induce the corrosion of the reinforced concrete steel sample by applying direct

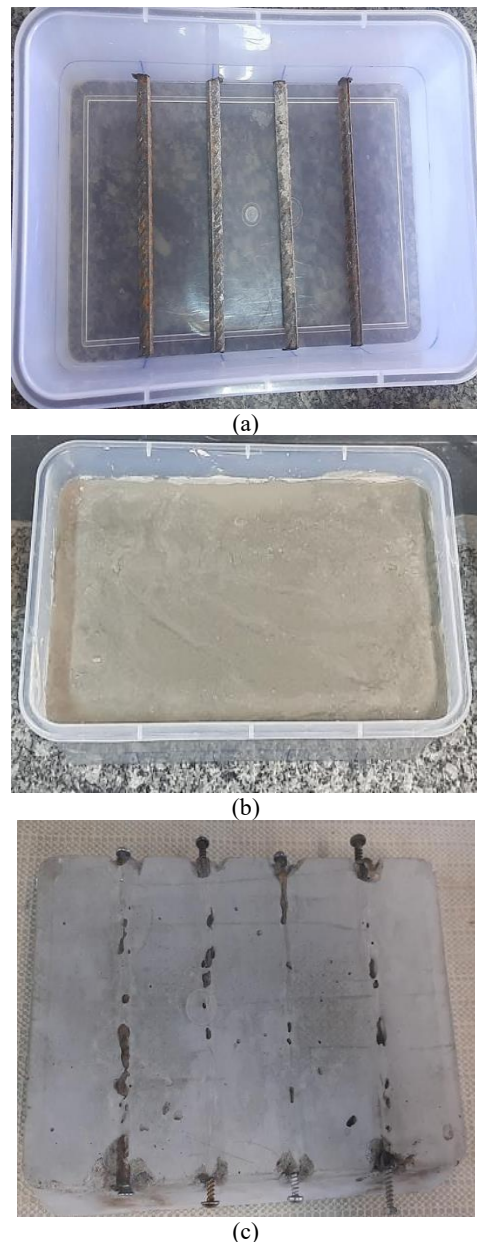


Figure 2. Schematic of steps for preparation of concrete block

current to the steel rebars in contact with a chloride electrolyte. Humidity, temperature, current density, carbon concentration, chlorine concentration, cement content, types of cement, etc. are important factors in the design of an intentional acceleration corrosion test method. The applied current density is known to be an essential parameter for intentionally accelerated corrosion [26]. The schematic of the corrosion process setup is shown in Figure 3. In this research, the applied potential between the cathode and the anode (rebar) is about 30 V by the help of an ADAK PS405 power supply (Iran) to start the corrosion of three rebars, which in the long time causes corrosion of the target rebars and corrosion products cause micro-cracks in the concrete.

According to Figure 4, the areas marked with hatches are the location of the stainless steel cathode on the sponge dipped in salt water, and these points are subject to selective corrosion. Area number 1 (rebar number 2) for 12 hours, area number 2 (rebar number 3) for 14 hours, and area number 3 (rebar number 4) for 10 hours have been subjected to a constant voltage of 30 volts.

After the intentional acceleration of corrosion, at first, a smartphone equipped with a magnetic sensor was employed to monitor the corrosion. The magnetic sensor in Samsung A30s series smartphones is activated by installing the Engineering Toolbox Application. The calibration of magnetic corrosion monitoring devices was necessary before the use of this device to detect corrosion of reinforced concrete structures. The calibration process is performed with the aim of increasing the voltage of the sensor. As shown in Figure 5, a smartphone was used for corrosion monitoring based on a non-destructive (electromagnetic) way.

As shown in Figure 6, a ratiometric linear analog Hall-Effect sensor (OMH3150) was used for corrosion monitoring based on a non-destructive (electromagnetic) method. The output of this sensor is 2.5 volts in the absence of a magnetic field due to the application of 5 volts and when the sensor is placed on the S pole side of the structure, the output voltage value of this sensor increases and when it is placed on the N pole side of the structure, the voltage value. The output of this sensor decreases and finally the voltage changes are proportional to the changes in the intensity of the magnetic field. As the Hall-Effect sensor was moved in different areas of the reinforced concrete surface, the analog output voltage changed.

Finally, according to Figure 7, the LCR meter device (UNI-T(UT,612), China) was used to verify the data obtained. This technique involves the combination of a search coil (about 11 mm in diameter, 25 turns of 0.3 mm copper wire) and a LCR meter device at fixed frequency of 100 kHz. By moving the search coil on the surface of the concrete in regular pattern for corrosion monitoring, the LCR meter device indicates the inductance (L in μH) and quality factor of the inductor (Q , as a dimensionless

number). Finally, it can be concluded that this simple experimental setup employing a search coil can easily be used for monitoring corrosion through recording spatial changes of L and Q parameters by an LCR meter. As the

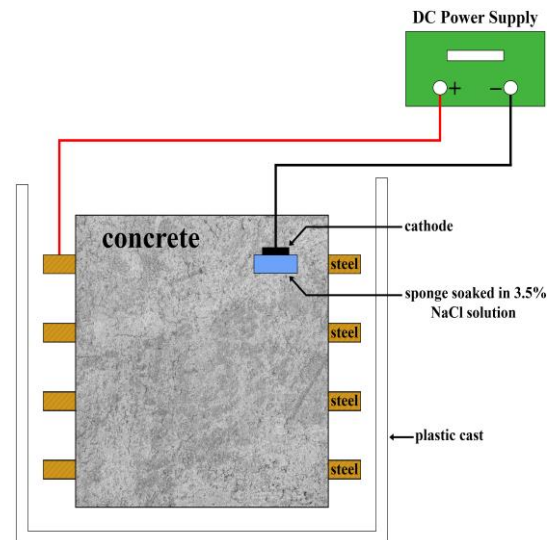


Figure 3. The schematic of the corrosion process setup

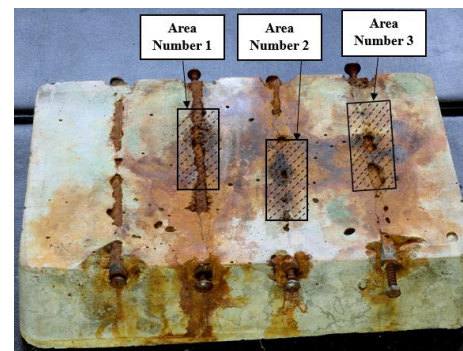


Figure 4. View of the reinforced concrete after intentional corrosion

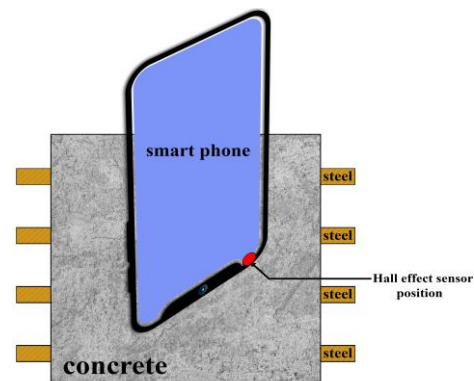


Figure 5. Schematic of corrosion monitoring of rebars in reinforced concrete by a smartphone equipped with a Hall-Effect sensor

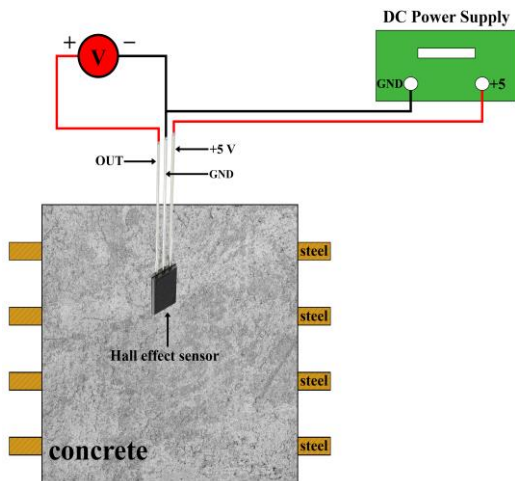


Figure 6. Schematic of corrosion monitoring of rebars in reinforced concrete by an analog Hall-Effect sensor



Figure 7. Schematics of corrosion monitoring of rebars in reinforced concrete by a LCR meter

coil moves on the reinforced concrete surface, the L and Q values change. According to Equation (7), at a frequency of 100 kHz, one can obtain the resistance R (in Ohms) from the relationship between Q (dimensionless number) and L (in μH):

$$R = \frac{(0.628 \times L)}{Q} \tag{7}$$

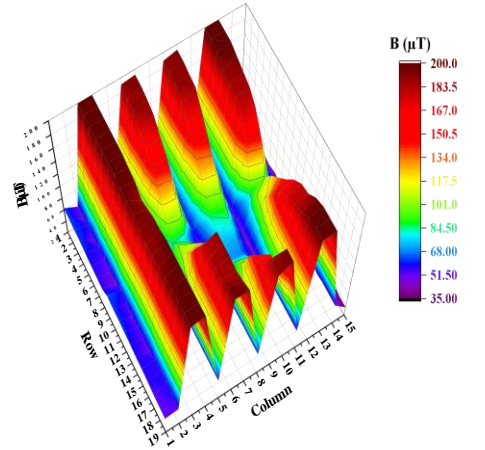
3. RESULTS AND DISCUSSIONS

3. 1. Corrosion Monitoring with a Smartphone Magnetic Sensor

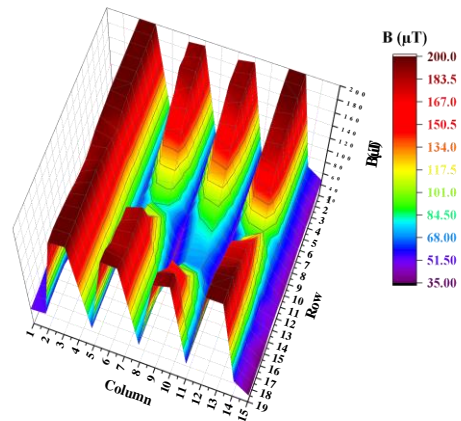
Figure 8 shows the three-dimensional plot of the magnetic field signals measured by the smartphone on concrete and four rebars that had limited corrosion. By analyzing the sensor signals, it is possible to check the corrosion progress of reinforced concrete steel bars.

According to Figure 8, the areas with the highest magnetic field (139.1-200 μT) were not corroded. The

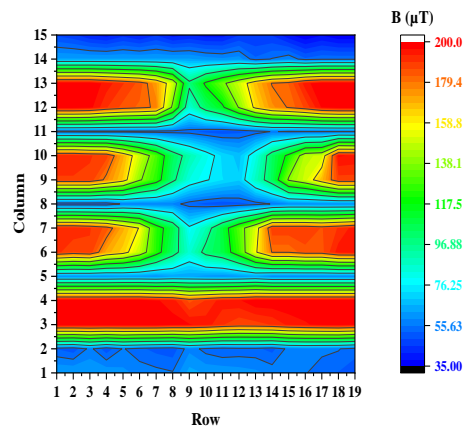
areas with a magnetic field (96.88-139.1 μT) detect rebars that have suffered from partial corrosion. The



(a)



(b)



(c)

Figure 8. (a), (b) The 3D-Colormap and (c) the Contour-Color Fill plots of corrosion monitoring by a smartphone, i.e. magnetic field intensity (μT) at various point of the surfaced concrete block

rebars showing a relatively low magnetic field (55.63-96.88 μT) have suffered from relatively severe corrosion. Concrete itself has a magnetic field of 35-55.63 μT . As a result, rebar 2 is corroded at distances 6 and 7 on the Y-axis (column) and between distances 4 and 14 on the X-axis (row). Rebar 3 is corroded at distances 9 and 10 on the Y-axis (column) and between distances 4 and 14 on the X-axis (row). Rebar 4 is corroded at distances 12 and 13 on the Y-axis, and between distances 6 and 14 on the X-axis. Therefore, the areas drawn in dark blue color represent the intact concrete areas; the areas drawn in light blue color indicate the part where the rebar has been corroded, and the areas drawn in red, orange, and yellow color indicate the areas in which the rebar, in comparison to the areas with light blue, has the greatest magnetic field and is not affected by corrosion.

As shown in Figure 9, the magnetic field of the corroded rebars is between the magnetic field of the non-corroded rebar and concrete. Rebar 1 has the highest magnetic field because it has not been affected by intentional corrosion. Therefore, rebar 2 is more corroded than rebar 4, and rebar 3 is more corroded than rebars 2 and 4. Rebar 3 has the longest length of corrosion. The Hall-Effect sensor is used in corrosion science to detect the metallic properties of metals and the areas of the rebar that have corroded. Therefore, the output signals from the Hall-Effect sensor in the areas with a low magnetic field indicate the area of concrete. By detecting and analyzing the output signals using a smartphone, we find that the magnetic field intensity plots all intersect at the same point and the distance between the intersection points can be used as a measure of the length of the corrosion area.

3. 2. Corrosion Monitoring by a Hall-Effect Sensor

Figure 10 shows the three-dimensional plot of the

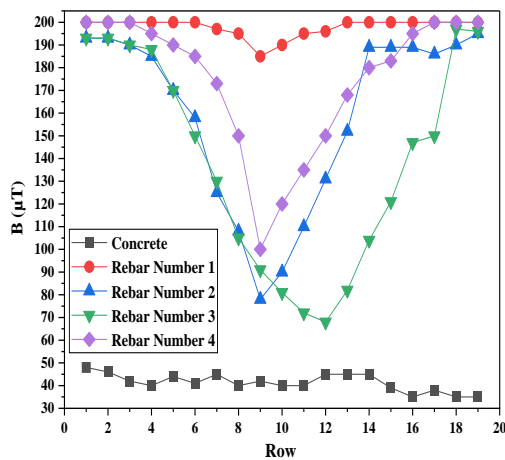


Figure 9. Profile of the concrete block, corroded rebars, and non corroded rebar by a smartphone equipped with a Hall-Effect sensor, i.e. magnetic field intensity (μT)

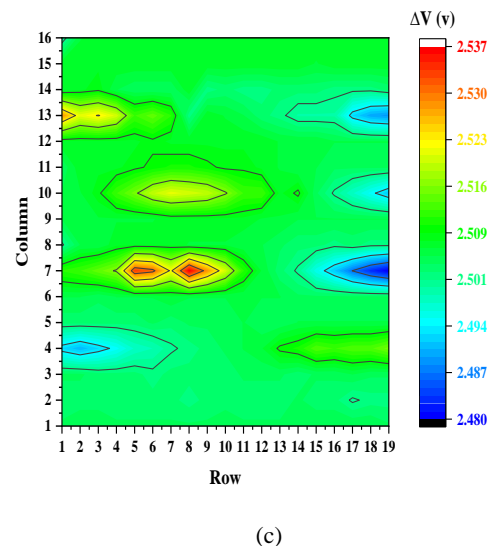
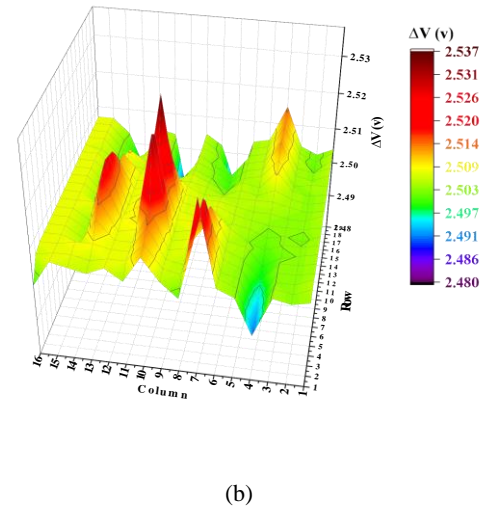
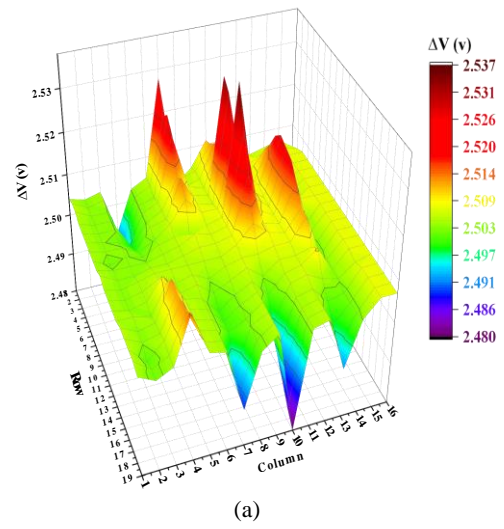


Figure 10. (a), (b) The 3D-Colormap and (c) the Contour-Color Fill plots of corrosion monitoring by a Hall-Effect sensor, potential difference (voltage) at various point of the surfaced concrete block

magnetic field signals as recorded by a Hall-Effect sensor on concrete and four rebars.

According to Figure 10, Rebar 2 has been corroded between distances 6 and 7 on the Y-axis (column) and between distances 1 to 3, 6 to 8 and 16 to 19 on the X-axis (row). Rebar 3 has been corroded between distances 9 and 10 on the Y-axis (column) and between distances 6 to 8, and 8 to 19 on the X-axis. Rebar 4 has been corroded between distances 12 and 13 on the Y-axis (column) and between distances 10 to 13 and 14 to 19 on the X-axis. During smartphone monitoring, the corroded areas in Rebar 2 were detected at distances 7 and 12, in Rebar 3 at distances 6 and 17, and in Rebar 4 between distances 8 to 13 on the X-axis. When the Hall-effect sensor moves from one side of the rebar to the other, the potential difference changes, with the highest and lowest values indicating the peak and valley areas, respectively, as shown in Figure 10 (a and b). The areas shown in green represent the concrete itself and a part of the rebar embedded in the concrete at a lower depth. The areas drawn with red, orange, and yellow colors, respectively indicate the areas with the greatest potential difference. The areas drawn with red, orange, and yellow colors, respectively represent the areas that have the greatest potential difference, and the areas drawn with blue color represent the areas of the rebar that may be corroded. According to these statements, it can be concluded that rebar 1 is not corroded and only in the first rows it may suffer minor corrosion.

Figure 11 shows that by detecting and analyzing the voltage output signals from the Hall-effect sensor, the potential difference of a part of the corroded rebar is between the potential difference of the concrete and that of the non-corroded rebar. Therefore, rebar 3 has the lowest potential difference and has the longest corrosion rate, in agreement with corrosion monitoring results using a smartphone. On the other hand, in rebars 2, 3 and 4, the potential difference is much less in the last rows (16-19) than in the first rows (1-5) due to rebar displacement. Because the rebar 1 may be affected by the corrosion products of other corroded rebars, the potential difference in this rebar is almost small in the first rows compared to the last rows. By comparing Figures 9 and 11, for corrosion monitoring with a smartphone and Hall-Effect sensor, respectively, the magnetic field and potential difference as output signals for corroded rebar are in midway of their corresponding values for concrete and corrosion-free rebar, and rebar number 3 has the lowest magnetic field and potential difference. Because rebar number three has been affected by intentional corrosion for more hours than rebar number two and four, through corrosion monitoring using these two methods, it can be seen that rebar number three has been corroded more and the length of the corrosion zone is long in this rebar.

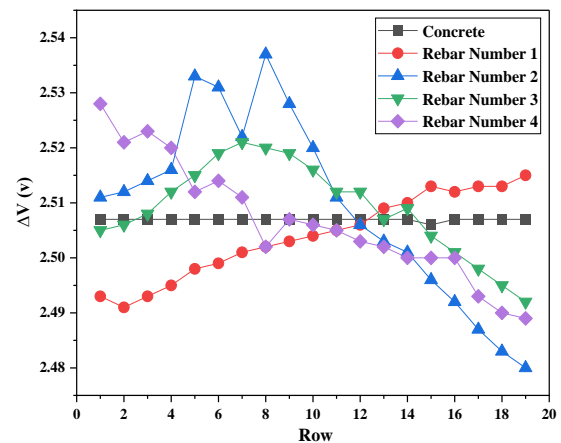


Figure 11. Profile of the concrete block, corroded rebars, and non corroded rebar by a Hall-Effect sensor, potential difference (voltage)

In general, according to the graphs drawn, through corrosion monitoring using these two methods, the corrosion locations can easily be visually identified. The time evolution of corrosion can also be studied. It is possible to select areas with a certain corrosion rate based on the intensity of the field changes and to monitor corrosion without the need to destroy concrete or apply external current to the reinforcement bars, especially in complex structures. Finally, larger diameter rebars can be monitored at greater depth.

3. 3. Corrosion Monitoring by a LCR Meter In order to validate the data obtained from the previous two methods, the LCR meter was used and the results are reported in Figure 1Y. According to Equation (7), the higher the corrosion rate of the rebar, the more the behavior of the coil moves towards being ideal and the Q factor increases and the R-value decreases. Therefore, in areas where the amount of Q increases, it indicates more corrosion of the rebar in that area.

According to the diagrams in Figure 12, the X-axis is row, the Y-axis indicates column and the Z-axis shows R. Rebar 2 is corroded at a distance of 6 in the Y axis (column) and between distances 1.5 to 3 in the X axis (row). Rebar 3 is corroded at distance 9 in the Y axis (column) and between distances 2.5 and 4 in the X axis. Rebar 4 is corroded at a distance of 12 in the Y axis (column) and between 1.5 and 3 in the X axis. The areas drawn with red, orange and yellow colors, respectively represent the areas that have the highest resistance, and the areas drawn with light blue and green colors represent the areas of rebar that are corroded and have the lowest resistance value. In areas where the value of R has decreased, it indicates local corrosion in that area. The results are completely consistent with the two previous methods and confirm the previous results.

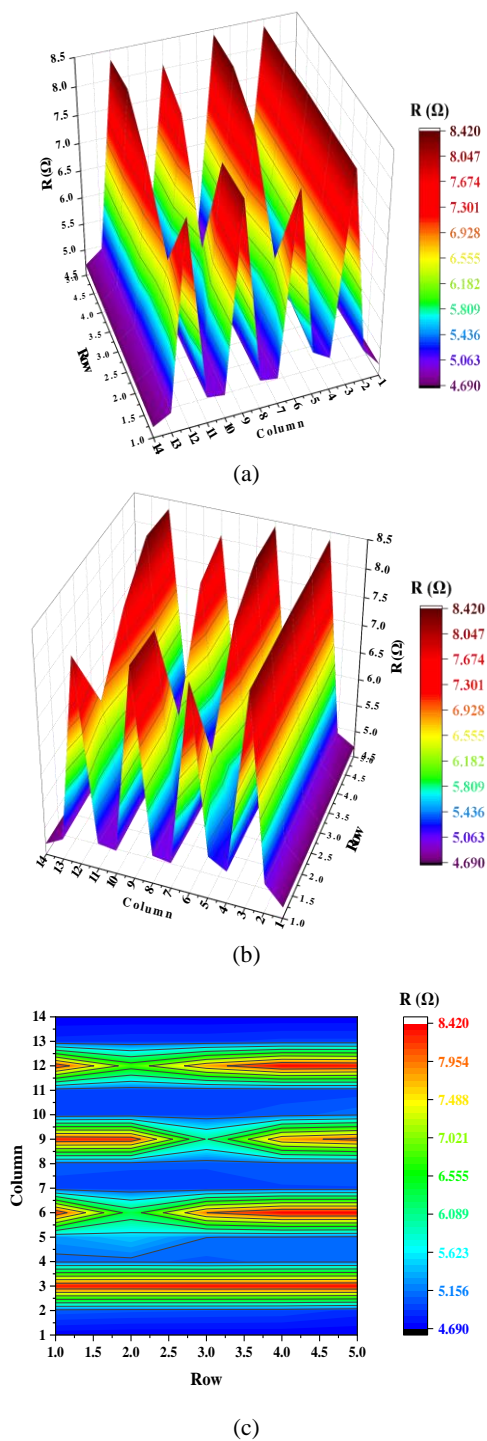


Figure 12. (a), (b) The 3D-Colormap and (c) the Contour-Color Fill plots of corrosion monitoring by a LCR coil sensor

As shown in Figure 13, by detecting and analyzing the output signals from the search coil, the strength value of corroded rebars is between the strength of non-corroded rebar and concrete. Rebar 1 has the highest

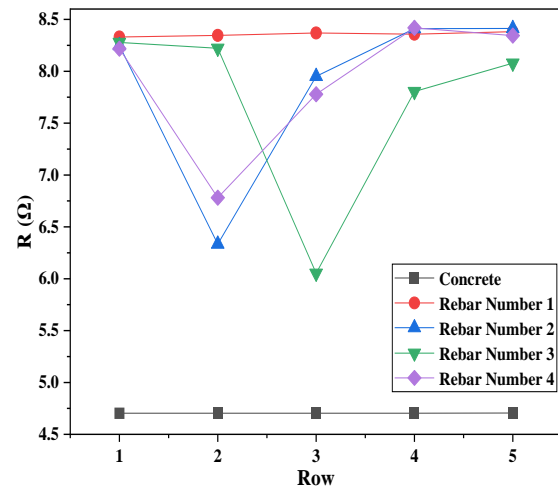


Figure 13. Profile of the concrete block, corroded rebars, and non corroded rebar by a LCR meter, resistance (Ω)

resistance value because it has not been affected by intentional corrosion. Rebar 2 is corroded more than rebar 4, and rebar 3 is corroded more than rebar 2 and 4, which is due to the difference in the duration of selective corrosion.

4. CONCLUSIONS

In this research, two new cost-effective electromagnetic methods were developed to monitor the corrosion of reinforced concrete and the results were compared and verified with the LCR method. The main conclusions are as follows:

1. When the corrosion occurred, the intensity of the induced magnetic field increases of Hall-Effect voltage at the cross-section of reinforced concrete.
2. A smartphone is capable of detecting as well as monitoring corrosion initiation and location of the reinforcement bars inside concrete based on the electromagnetic properties of the corroded reinforced bars.
3. The results of corrosion monitoring by a smartphone and the Hall effect sensor are in agreement with LCR meter and therefore, the smartphone and Hall-effect sensor can be used for monitoring purposes due to ease of operation, small size, and low cost.
4. The advantages of these methods are non-destructiveness, simplicity of use, short test duration, being inexpensive compared to other methods, precise determination of the depth and area of the rebar under corrosion, precise determination of the location of the cut rebar, and to some extent determining the corrosion mechanisms that can be determined by the time evolution of corrosion data.

5. REFERENCES

- Sikarwar, S., Singh, S. and Yadav, B. C., "Review on pressure sensors for structural health monitoring", *Photonic Sensors*, Vol. 7, (2017), 294-304. doi: 10.1007/s13320-017-0419-z.
- Fanijo, E. O. and Brand, A. S., "Anti-corrosion behaviors of corn-based polyols on low carbon steel rebar", *Cleaner Materials*, Vol. 4, (2022), 100066. doi: 10.1016/j.clema.2022.100066.
- Broomfield, J. P., "Corrosion of steel in concrete: understanding, investigation and repair", *CRC Press*, (2023). doi: 10.1201/9781003223016.
- Goyal, A., Pouya, H. S., Ganjian, E. and Claisse, P., "A review of corrosion and protection of steel in concrete", *Arabian Journal for Science and Engineering*, Vol. 43, (2018), 5035-5055. doi: 10.1007/s13369-018-3303-2.
- Daniyal, M. and Akhtar, S., "Corrosion assessment and control techniques for reinforced concrete structures: a review", *Journal of Building Pathology and Rehabilitation*, Vol. 5, (2020), 1-20. doi: 10.1007/s41024-019-0067-3.
- Safaie, N., Hamidi, H. and Vali, M., "A Framework for Analysis of Predictors of Mobile-marketing Use by Expanding Unified Theory of Acceptance and Use of Technology and Artificial Neural Networks", *International Journal of Engineering, Transactions B: Applications*, Vol. 36, No. 05, (2023), 1012-1022. doi: 10.5829/IJE.2023.36.05B.17.
- Shadmand, M., Hedayatnasab, A. and Kohnehpooshi, O., "Strengthening of rc beams using steel plate-fiber concrete composite jackets (finite element simulation and experimental investigation)", *International Journal of Engineering, Transactions A: Basics*, Vol. 35, No. 1, (2022), 73-92. doi: 10.5829/IJE.2022.35.01A.07.
- Quraishi, M., Nayak, D., Kumar, R. and Kumar, V., "Corrosion of reinforced steel in concrete and its control: An overview", *Journal of Steel Structures & Construction*, Vol. 3, No. 1, (2017), 1-6. doi: 10.4172/2472-0437.1000124.
- Azarsa, P. and Gupta, R., "Electrical resistivity of concrete for durability evaluation: a review", *Advances in Materials Science and Engineering*, (2017). doi: 10.1155/2017/8453095.
- Li, Z., Jin, Z., Shao, S. and Xu, X., "Magnetic properties of reinforcement and corrosion products described by an upgraded monitoring apparatus", in Proceedings of the 7th World Conference on Structural Control and Monitoring, Qingdao, China., 1397, (2018).
- Li, Z., Jin, Z., Gao, Y., Zhao, T., Wang, P. and Li, Z., "Coupled application of innovative electromagnetic sensors and digital image correlation technique to monitor corrosion process of reinforced bars in concrete", *Cement and Concrete Composites*, Vol. 113, (2020), 103730. doi: 10.1016/j.cemconcomp.2020.103730.
- Taspika, M., Nuraeni, L., Suhendra, D. and Iskandar, F., "Using a smartphone's magnetic sensor in a low-cost experiment to study the magnetic field due to Helmholtz and anti-Helmholtz coil", *Physics Education*, Vol. 54, No. 1, (2018), 015023. doi: 10.1088/1361-6552/aaefb4.
- Zhang, J., Liu, C., Sun, M. and Li, Z., "An innovative corrosion evaluation technique for reinforced concrete structures using magnetic sensors", *Construction and Building Materials*, Vol. 135, (2017), 68-75. doi: 10.1016/j.conbuildmat.2016.12.157.
- Akimitsu, M., Ono, Y., Cao, Q. and Tanabe, H., "High-Resolution 2D Magnetic Field Measurement of Magnetic Reconnection Using Printed-Circuit Board Coils", *Plasma and Fusion Research*, Vol. 13, (2018), 1202108-1202108. doi: 10.1585/pfr.13.1202108.
- Zhang, H., Liao, L., Zhao, R., Zhou, J., Yang, M. and Xia, R., "The non-destructive test of steel corrosion in reinforced concrete bridges using a micro-magnetic sensor", *Sensors*, Vol. 16, No. 9, (2016), 1439. doi: 10.3390/s16091439.
- Van Steen, C., Verstrynghe, E., Wevers, M. and Vandewalle, L., (2019). "Assessing the bond behaviour of corroded smooth and ribbed rebars with acoustic emission monitoring", *Cement and Concrete Research*, Vol. 120, (2019), 176-186. doi: 10.1016/j.cemconres.2019.03.023.
- Elyasigorji, A., Rezaee, M. and Ghorbanpoor, A., "Magnetic corrosion detection in concrete structures", In International Conference on Sustainable Infrastructure 2019, Leading Resilient Communities through the 21st Century. Reston, VA: American Society of Civil Engineers., (1398), (2019).
- Ha, N., Lee, H. S., and Lee, S., "Development of a Wireless Corrosion Detection System for Steel-Framed Structures Using Pulsed Eddy Currents", *Sensors*, Vol. 21, No. 24, (2021), 8199. doi: 10.3390/s21248199.
- Sivamani, J., Thiyaneswaranb, M. and Navaneethanb, K. S., "Performance Studies on Glass Fiber Reinforced Recycled Aggregate Concrete", *International Journal of Engineering, Transactions B: Applications*, Vol. 36, No. 05, (2023), 904-913. doi: 10.5829/IJE.2023.36.05B.07.
- Mohammadi, Y. and Asilb, M. B., "Utilization of Steel Micro-fiber and Carbon Nanotubes in Self-compacting Lightweight Concrete", *International Journal of Engineering, Transactions B: Applications*, Vol. 36, No. 5, (2023), 955-964. doi: 10.5829/IJE.2023.36.05B.15.
- Pawar, A. J., Patel, M. and Suryawanshi, S. R., "Finite Element Modelling of Laboratory Tests on Reinforced Concrete Beams Containing Recycled Aggregate Concrete", *International Journal of Engineering, Transactions B: Applications*, Vol. 36, No. 5, (2023), 991-999. doi: 10.5829/IJE.2023.36.05B.15.
- Masne, N. and Suryawanshi, S., "Effect of replacement ratio on torsional behaviour of recycled aggregate concrete beams", *International Journal of Engineering, Transactions A: Basics*, Vol. 36, No. 4, (2023), 659-668. doi: 10.5829/IJE.2023.36.04A.06.
- Tumengkol, H., Irmawaty, R., Parung, H. and Amiruddin, A., "Precast Concrete Column Beam Connection Using Dowels Due to Cyclic Load", *International Journal of Engineering, Transactions A: Basics*, Vol. 35, No. 1, (2022), 102-111. doi: 10.5829/IJE.2022.35.01A.09.
- Sijwal, G., Pradhan, P. and Phuvoravan, K., "Lateral Load Carrying Capacity of Concrete-filled Cold-formed Steel Shear Wall", *International Journal of Engineering, Transactions A: Basics*, Vol. 35, No. 1, (2022), 161-171. doi: 10.5829/IJE.2022.35.01A.15.
- Dhundasi, A., Khadirnaikar, R. and Momin, A. I. A., "Stress-strain characteristics of reactive powder concrete under cyclic loading", *International Journal of Engineering, Transactions A: Basics*, Vol. 35, No. 1, (2022), 172-183. doi: 10.5829/IJE.2022.35.01A.16.
- Feng, W., Dong, Z., Liu, W., Cui, H., Tang, W. and Xing, F., "An experimental study on the influence of applied voltage on current efficiency of rebars with a modified accelerated corrosion test", *Cement and Concrete Composites*, Vol. 122, (2021), 104120. doi: 10.1016/j.cemconcomp.2021.104120.

COPYRIGHTS

©2023 The author(s). This is an open access article distributed under the terms of the Creative Commons Attribution (CC BY 4.0), which permits unrestricted use, distribution, and reproduction in any medium, as long as the original authors and source are cited. No permission is required from the authors or the publishers.



Persian Abstract

چکیده

خوردگی بتن مسلح (RC) یکی از دلایل اصلی خرابی سازه و مشکلات مهندسی در جنبه‌های زیر ساختی است که سبب اهمیت پایش خوردگی آرماتورها در سازه‌های بتنی به‌ویژه از نظر ایمنی می‌شود. روش‌های آزمایش غیرمخرب (NDT)، رویکردهای مفیدی جهت تشخیص و ارزیابی لحظه‌ای خوردگی فولاد در RC برای پایش با روند زمانی خوردگی می‌لگردها هستند. اخیراً برخی از روش‌های NDT مانند سنسورهای مغناطیسی و مقاومتی و همچنین روش‌های پایش الکتروشیمیایی مانند طیف‌سنجی امپدانس برای پایش خوردگی می‌لگرد در RC توسعه داده شده‌اند. این مقاله رویکرد جدیدی را با استفاده از تلفن‌های هوشمند مدرن مجهز به حسگرهای مغناطیسی و حسگرهای آنالوگ اثر هال موجود، برای پایش خوردگی می‌لگرد در بتن ارائه می‌کند. نتایج حاکی از حساسیت معقول روش‌های تشخیص و پایش خوردگی می‌لگردها با گذشت زمان برخوردار می‌باشد. در این تحقیق، دو روش توسعه یافته شده، مناسب، امکان‌پذیر و مقرون به صرفه هستند و می‌توانند برای نظارت میدانی قوی می‌لگردها در مهندسی عمران استفاده شوند. به منظور بررسی و اعتبارسنجی داده‌های به‌دست آمده در این پژوهش، از آزمایش غیر مخرب الکترومغناطیسی دیگری توسط یک سیم پیچ جست‌وجوی متصل به یک LCR متر برای نظارت بر خوردگی استفاده شد. نتایج به دست آمده با این روش با روش‌های قبلی مطابقت داشت. به عبارت دیگر، با استفاده از این سه روش می‌توان با موفقیت پایش و شدت خوردگی را تعیین کرد.



Experimental Investigation of Brick-Slabs: Evaluation of the Performance and Ductility of Various Brick Materials

A. Hatif Obaid^a, A. A. Jaafar^a, E. Noroozinejad Farsangi^{*b}

^a Department of Civil Engineering, University of Misan, Amarah, Maysan 62001, Iraq

^b Faculty of Civil and Surveying Engineering, Graduate University of Advanced Technology, Kerman, Iran

PAPER INFO

Paper history:

Received 24 May 2023

Received in revised form 09 July 2023

Accepted 10 July 2023

Keywords:

Brick Slab

Perforated Brick

Gypsum Mortar

ABSTRACT

In this study, five one-way brick slab specimens were manufactured to investigate the behavior of brick slabs composed of various types of bricks (solid bricks, perforated bricks, and cellular concrete blocks (thermostone)). The span ranges from 600 to 800 mm, while the camber ranges from 0 to 30 mm. Previously, cellular concrete blocks, solid and perforated clay bricks were employed as the building materials. These samples were tested by being subjected to flexural three-point loading. The results revealed that increasing camber by 30 mm for solid brick specimens increased ductility, and ultimate strength, by 5.5% and 77.62, respectively. Increasing the span from 600 to 800 mm for solid brick specimens decreased the ultimate strength and ductility by 37.96% and 6.83%, respectively. Cellular concrete blocks can be used in the construction of slabs due to their lightweight and acceptable structural response when compared to solid brick specimens. Due to their good structural performance and lightweight, perforated bricks can be used to build brick slabs. Brittleness and the sudden collapse of the brickwork arch characterized the failure mode in all samples.

doi: 10.5829/ije.2023.36.09c.07

NOMENCLATURE

f_{fb}	Flexural bonding strength in Mpa	W	Weight of brick in Newton
l_b	Length of a brick unit in mm.	w_b	Width of brick unit in mm
l_{mj}	Length of mortar joint in mm	Δu	Ultimate Deflection
P	Failure load in Newton	Δy	Yield Deflection
t_{bar}	Thickness of steel bar in mm		

1. INTRODUCTION

Brick slabs are composed of I-section steel beams that stand on bearing walls with span centers that vary from 70 to 90 cm. Gypsum mortar is utilized to bind together clay brick units and form the spans between steel I-section beams because of the quick setting time of gypsum (See Figure 1). For aesthetic reasons, the brick slab's bottom face may not be plastered with mortar. The brick slab was developed in the late nineteenth century by Victorian architects in Britain. The brick slab eventually reached the majority of nations, including India, Eastern Europe, and North America. It had gained

popularity as a flooring system in various Middle Eastern nations by the mid-20th century, especially in Iran and Iraq. Brick slabs were a well-known technique that was extensively utilized in Iraq. Brick slabs are still utilized in construction in spite of the widespread use of reinforced concrete in the majority of Iraq's regions because of their reasonable cost, speed of construction, lack of need for skilled labor, suitability for narrow areas, and avoidance of forms, casting, reinforcement, and curing. Those from limited-income families commonly use the arch brick slab. It was recently found that ceramic panels and cellular concrete block units are being used in their construction due to the cellular concrete block's

*Corresponding Author Email: noroozinejad@kgut.ac.ir
(E. Noroozinejad Farsangi)



Figure 1. Brick slab after construction

speed of work, thermal insulation, and lightweight (see Figure 2). Brick slabs have significant drawbacks despite their general benefits. In particular, it uses gypsum mortar, which has low moisture resistance and is vulnerable to seismic loadings as a primitive construction technique.

The brick slab system is stable under typical static loading because the arches of the brick slabs predominantly transmit stress loads along the archway to the beams, then transfer stresses to the supporting beams or walls. Due to its geometric shape, the brick slab structure is often described as a one-way slab [1]. As suggested a revolutionary two-way method in 2003, the vulnerabilities of conventional one-way brick slabs are Investigated. A steel grid was created by the suggested technique, in which a series of steel transversal beams that crossed through the main I-beams were used. The disjointed steel transversal beams will subsequently be an element of a steel grid that enables the distribution of applied loads in two-way directions. The brick slab system, which was developed and constructed, was found to improve the diaphragm's action and resistance to gravity and seismic stresses [2]. A research investigation was conducted on how the existing structures performed during the 2003 Bam earthquake. The result demonstrates that brick slabs with the supporting two X bracings that are welded at the end of the slab corner as indicated in Figure 3 performed well when subjected to lateral loads [3]. Pourfalah et al. [4] conducted research on the experimental study of placing a layer of concrete on the top of brick slab in 2009. The result demonstrated that strength, ductility, and seismic performance had all



Figure 3. Sample with two X-bracings on the floor slab during construction [4]

increased. Experimental research has been done on the in-plane seismic response of traditional and strengthened brick slab diaphragms. The findings indicate that the seismic response, integrity, and ductility of end arch spans were improved by using simultaneous diagonal bracing and steel tension ties [5]. The ferrocement layer and the brick slab's corresponding effects increased stiffness, ductility and flexural strength, without considerably adding to the weight of the slabs [6]. According to finite element analysis, a brick slab in southern Iraq's seismic performance was examined, and the results demonstrated that flexural forces rather than membrane stresses dominate behavior of the brick slab. The tensile stresses were high, but the slab's compressive stresses were smaller than the allowable stress. In steel support beams, displacement, stress, and strain were generally within acceptable limits [7]. An historic American boarding school for girls in Merzifon, Turkey, with a one-way masonry brick slab, has been evaluated for its seismic sensitivity and structural behavior. The top of the structure and the connection areas between steel beams and brick arches exhibited the highest compression and tension loads, based on the results of the static tests [8]. Slant-jack arch masonry slabs are considered semi-rigid roofs, and improving them can make them more rigid. A layer of reinforced concrete can be poured on masonry buildings to increase their seismic performance after being retrofitted with slant-brick slabs. The results demonstrate that the most economical method for jack arch retrofitting is to add a concrete layer [9]. According to the result of an experimental investigation of standard and retrofitted brick slabs in a single-story 3D steel building, the double X strapping approach can greatly improve the other two techniques in regards to stiffness in plane, capacity, and even energy dissipation [10]. Flexural failure was the main mode of failure for the cellular concrete block (thermostone) roof structure. There was no evidence of cellular concrete block crushing through the test at the point where the unit of cellular concrete block split almost entirely in the center [11]. The proposed ferrocement sandwich slab is a possible replacement for the conventional brickwork slab [12]. The suggested approach and its use are validated by achieving a good correlation between the analytical



(a) cellular concrete blocks



(b) ceramic panels

Figure 2. Construction of a brick slab

findings and the observed fragility features in field testing [13]. It is noted that a significant factor in the structural damage anticipated for the Fertek building is slab discontinuities on the gallery floor [14]. The severe damage that out-of-plane accelerations cause to masonry infill walls makes load-bearing masonry structures extremely vulnerable to seismic damage and potential collapse. Largely enhanced accelerations occur on the face of the laden infill wall as a result of the dynamic interaction between the vibrating structure, slab diaphragms, and the infill wall loaded out-of-plane, leading to significantly increased inertia forces [13]. The use of new lightweight materials in building applications is encouraged by their increased thermal and mechanical properties [15]. In all combinations, the early age strength is reached, but the dosage of 10% alcoline results in a stronger effect [16]. With 10% waste glass and 20% waste clay brick, the flexural strength at 400°C increased by 56% and 69%, respectively. All combination mixes also demonstrated greater strength than the control [17]. According to the feedback earlier in this section, no in-depth research has been done on the behavior of brick slabs constructed from various types of bricks (solid, and perforated bricks), cellular concrete block units (thermostone), and mortar made with gypsum, which are the majority of regularly used materials in their construction, particularly in Iraq. As a result, the purpose of this study is to gather information and provide statistics about how the brick slabs made of solid bricks, perforated bricks, and cellular concrete blocks behave. Five one-way brick slab specimens were manufactured in order to demonstrate the effects of span length, camber, and brick types utilized on the structural behavior of brick slabs and were experimentally tested.

2. EXPERIMENTAL PROGRAM

2. 1. Materials Properties

2. 1. 1. Clay Bricks The most common type of brick used in brick slab construction is clay brick. According to IQS 24-1989 the bricks were subjected to testing, and the findings are summarized in Table 1.

2. 1. 2. Gypsum Mortar Gypsum and water are mixed to form the gypsum mortar. Gypsum mortar testing is done in accordance with the Iraqi Reference Guide (1042-2011). Table 2 illustrates the test results.

2. 1. 3. Cellular Concrete Blocks Thermostone, an instance of a precast lightweight cellular concrete block, is made of cellular concrete. As stated in Figure 4, its mechanical and physical characteristics have been evaluated in accordance with the Iraqi Reference Guide (810-2009). The results satisfy Iraqi standards (IQS 1441-2013). Table 3 demonstrates the test results.

TABLE 1. Test results for clay brick properties

Type of brick	Solid clay Bricks	Perforated clay Bricks	Limit of IQS No.25 /1988
Per. of Perforated [%]	0	24.44	25% Max
Density [kg/m ³]	1500	1207	-
Dimension [mm]	233.0×113.0×72.0	235.20×114.63×73.46	L*, W* =± 3%
Rupture Modulus [MPa]	2.0	1.2	-
Efflorescence	Light	Light	-
Water Absorption [%]	10 units: 25 1 unit: 25	22 23	26 28
Average Compressive Strength [MPa]	10 units: 9 1 unit: 8	7 6	9 7

TABLE 2. Properties of gypsum mortar

Property	Test Result	Limit of IQS No.28/2010 [20]
Fineness [%]	5	8 % Maximum
Time Setting [Minute]	13	(for brick slab using 15 max) [8-25]
Compressive Strength [MPa]	3	3 [MPa] Minimum
Rupture Modulus [MPa]	0.7	-
Gypsum / Water	0.39	-



(a) Dimensions test



(f) Density test



(d) Compressive strength test



(e) Modulus of rupture test

Figure 4. Cellular concrete block tests

2. 1. 4. Cement, Aggregate, and Water The bottom faces of the specimens used in this study are plastered with cement mortar. This mortar was produced using sand (S) and ordinary Portland cement (C). The C:S ratio for this mix was 1:2 with a W/C of 0.5. Ordinary Portland cement mechanical and physical characteristics have been tested in accordance with the Iraqi Reference Guide (No. 198-1990). The test findings are given in Table 4, while chemical properties are tested according to the Iraqi Reference Guide (472-1993). The results of

TABLE 3. Test results of cellular concrete blocks

Dimension Test	Standard Dimension [mm]	Test Result [mm]	Limit of IQS 1441/2013
Length	600	+2	
Height	200	-0.5	± 3 mm for any dimension
Thickness	100	+1	
Specimen [mm]	Average weight for 2 cubes [kg]	Average volume for 2 cubes [m ³]	Density [kg/m ³]
	0.51	0.00095	536.80
(100×100×100)	Compressive strength [MPa]		Class according to Limit of IQS 1441/2013
	One unit	2.16	1.60
	Average for two cubes	2.20	2
600×200×100	Modulus of rupture [MPa] average for two unit		-
	600×200×100		

the tests are shown in Table 5. Sand is available as natural silica sand. Its grading is tested according to Iraqi standards (IRQ No. 30/1984). Test results are satisfactory by Iraqi standards (IQS No. 45/1984) as shown in Table 6. Drinking water is used for mixing all the cement and gypsum mortar, as well as curing specimens and other testing of the materials. Drinking water satisfied the Iraqi standard (IQS 1703/2018).

TABLE 4. Properties for cement and plastering mix

Physical and Mechanical Properties	Test Result	Limit of IQS No.5/2019
Fineness [m ² /kg]	254.30	≥ 250
Time Setting Initial [Hour: Minute]	0: 59	≥ 45 Minutes
Final [Hour: Minute]	8: 2	≤ 10 Hours
Compressive Strength [MPa]		
2- Days	19.0	≥ 10
28- Days	34.2	≥ 32.5

TABLE 5. Chemical properties of cement

Chemical Property	Content [%]	Limit of IQS No.5/2019
MgO	2.65	≤ 5 %
SO ₃	2.20	≤ 2.8 %
Loss of Ignition	3.11	≤ 4 %
Insoluble Materials	1.15	≤ 1.5 %
Lime Saturation Factor	0.86	0.66 – 1.02

TABLE 6. Sand test result

Sieve Size [mm]	Cumulative Retained [%]	Cumulative Passing [%]	Limit of IQS No.45/1984-Zone No.2
10 [mm]	0	100	100
4.75 [mm]	0	100	90-100
2.36 [mm]	10	90	75-100
1.18 [mm]	16	84	55-90
600 [Micron]	45	55	35-59
300 [Micron]	72	28	8-30
150 [Micron]	94.5	5.5	0-10
Material Finer Than 75 Micron		1.1	5 % Max
Fineness Modulus		2.375	[2.3-3.1] ASTM C33M/13 [18]

2. 1. 5. Flexural Bonding Strength

According to Khalaf, tests and calculations were done to determine the flexural bond strength between solid, perforated clay brick, cellular concrete block units, and gypsum mortar. A new test procedure was proposed by Khalaf. According to this approach, three-point loading caused a flexural bond failure parallel to the bed joint when bricks were manufactured using two brick units arranged in a Z-shape. Two assumptions are made for calculating the values of the flexural bond strength (f_{fb}). The first is a linear stress distribution, and the second type of stress distribution is a parabolic distribution. In this study, flexural bond strength values based on two assumptions were determined by using Equation 1 for linear stress distribution and, Equation (2) for parabolic stress distribution. The results of the tests are summarized in Table 7.

$$f_{fb} = \frac{(0.5l_b^2 - l_b t_{bar} + 0.5t_{bar}^2)P + (0.75l_b^2 - 1.25l_b t_{bar} + 0.5t_{bar}^2)W}{(0.333l_m^2 w_b)(1.5l_b - t_{bar})} \quad (1)$$

$$f_{fb} = \frac{(0.5l_b^2 - l_b t_{bar} + 0.5t_{bar}^2)P + (0.75l_b^2 - 1.25l_b t_{bar} + 0.5t_{bar}^2)W}{(0.42l_m^2 w_b)(1.5l_b - t_{bar})} \quad (2)$$

2. 2. Specimen Manufacturing

The experimental program emphasizes one-way testing of brick slab specimens. Five samples are fabricated using perforated, solid clay bricks, and cellular concrete blocks with a workable gypsum mixture to bind units together and fill gaps between them. Cement mortar as plastering of 10 mm in thickness is applied on the bottom face of the specimens. The compressive strength of cement paste used for plastering is (50×50×50) mm cubes and (160×40×40) mm prisms, whereas the flexural strength is 35.7 MPa and 7 MPa, respectively. After 28 days of

TABLE 7. Test Results of flexural bonding strength according to Khalaf [22]

Specimen Type	Test Result	
	Average (Two Samples) by Linear Stress Distribution [MPa]	Average (Two Samples) by Parabolic Stress Distribution [MPa]
Solid Clay Bricks	0.321	0.253
Perforated Clay Bricks	0.410	0.324
Cellular Concrete Blocks	0.254	0.200

plastering five samples with cement mortar, to prepare the samples for testing and to have a good overview of the cracks during the test, a white coating layer is put over the plastering coating. The main variables that are considered for these samples are span length (600-800) mm, camber height (30) mm, and brick types (solid bricks, perforated bricks, cellular concrete blocks (thermostone)) are used in construction of specimens to show their effects on the behavior of the brick slab. Table 8 summarized the specimens' details and Figure 5 shows the construction process of brick slab specimens.

2. 3. Procedure Testing All five specimens are subjected to a line load with three-point bending. Brick slabs are tested using a hydraulic piston with a 10-ton capability. At each load step, the load is progressively increased and applied monotonically in equal increments. Two steel rods support the slab specimen on either side. A dial gauge with a 50-mm capacity is used to measure the displacement at the midpoint of the span. A crack microscope is used to view the cracks. The applied load at a slab's midspan is measured using a calibrated load cell. Figure 6 depicts an image of the test setup, and Figure 7 shows a plan of the test setup.

3. RESULTS AND DISCUSSIONS

The main objectives of this study are to investigate behavior of brick slabs made of various bricks (solid clay

TABLE 8. Specimens' details

No.	Specimens Symbol	Span Length [mm]	Width [mm]	Camber Height [mm]	Type of Bricks Used
1	Js-60-0	600	320	0	Solid brick
2	Js-80-0	800	320	0	Solid brick
3	Js-80-3	800	320	30	Solid brick
4	Jv-60-0	600	320	0	Perforated brick
5	Jc-60-0	600	320	0	Cellular concrete block

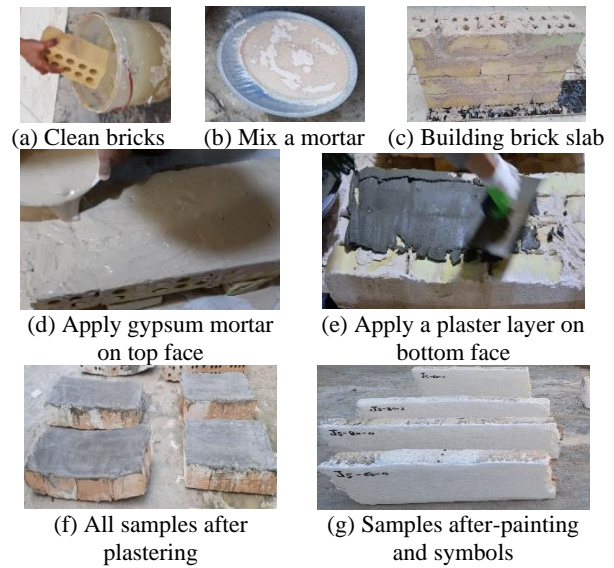


Figure 5. Steps for preparing brick slab specimens



Figure 6. Test setup image

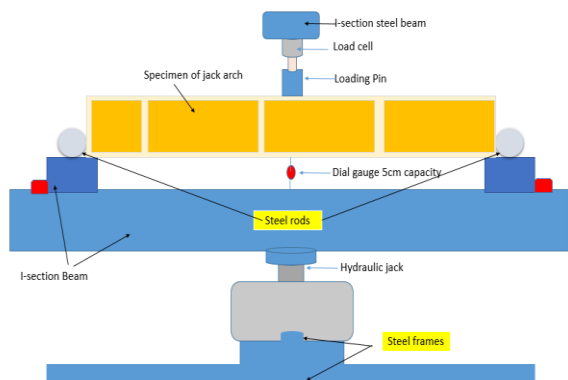


Figure 7. Test setup strategy

bricks, perforated clay bricks and, cellular concrete blocks (thermostone)) subjected to flexural three-point loading (line load). The results of the tests are presented regarding the ultimate load, load-deflection at the slab's mid-span, ductility index, and failure mode.

3. 1. Ultimate Strength The results of ultimate load for brick are shown in Table 9 and Figure 8. The effects of the type of bricks used in the construction of the brick slab on ultimate loads are studied by using three brick types. These are solid, perforated clay bricks, and cellular concrete blocks with a span length of 600 mm. The results indicate that the specimen with perforation bricks Jv-60-0 has a greater ultimate load than the specimens with solid clay bricks Js-60-0 and cellular concrete blocks Jc-60-0 by 37.4 and 41.07%, respectively. These results are due to the fact that the flexural bonding strengths between brick units and gypsum mortar are higher than those between cellular concrete block units as mentioned in the flexural bonding tests in the previous section. Also, the poor mechanical properties of cellular concrete blocks compared to clay bricks are expected. To study the effect of span length on the ultimate loads of brick slabs are considered for samples made with solid bricks. The selected span is between 600 and 800 mm. The results show a clear decrease in the ultimate loads when increasing the span length for solid clay brick samples. The findings indicate that when the span was increased from 600 to 800 mm for Js-80-0 the ultimate loads decreased by 37.96%. Increasing camber has an impact on the brick slab's ultimate loads, which are tested on specimens. For this purpose, a camber of 30 mm is used for specimens made of solid clay bricks. The results show an increase in the ultimate loads for specimens when the camber is increased. Increasing camber from 0 to 30 mm for Js-80-3 improves ultimate loads by 77.62%.

TABLE 9. Test results

No.	Specimens Symbol	Ultimate Load [kN]	Weight [kg]
1	Js-60-0	3.53	40
2	Js-80-0	2.19	51
3	Js-80-3	3.89	52
4	Jv-60-0	4.85	33
5	Jc-60-0	3.44	14

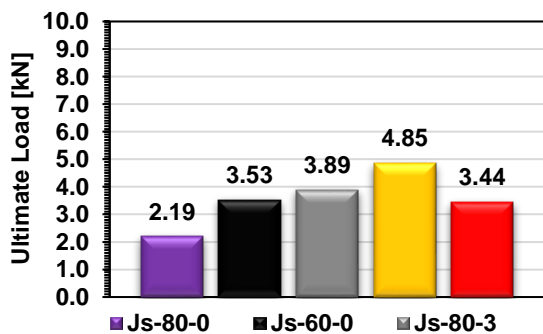


Figure 1. Ultimate loads for brick specimens

3. 2. Load-Deflection Curves and Ductility Index

The ability of a material to resist plastic deformation under load is called ductility. The ductility index ($\mu\Delta$) is defined as the proportion of total displacement (Δu) to elastic limit displacement (Δy) [19, 20]. The point at which strength behavior is believed to switch from elastic to plastic is the elastic limit deflection. The approach for calculating the ductility indices for each tested specimen in the current experimental study is based on Figure 9. The load-deflection curves for brick slab specimens are shown in Figure 10. This figure depicts the load-deflection curves of all five brick slab specimens, Js-60-0, Js-80-0, and Js-80-3, Jv-60-0, and Jc-60-0. It is seen clearly show that the specimens made from perforated and solid clay brick behave approximately linearly until they reach their ultimate load. A sudden failure occurs after reaching ultimate loads. The loading-deflection curve for specimen Jc-60-0, depicts a sample made with a cellular concrete block (thermostone block) and gypsum mortar that has been widely used in recent years in the construction of brick slabs. It is obvious from this figure that the samples behave similarly to the behavior of brick specimens made with solid and perforated clay

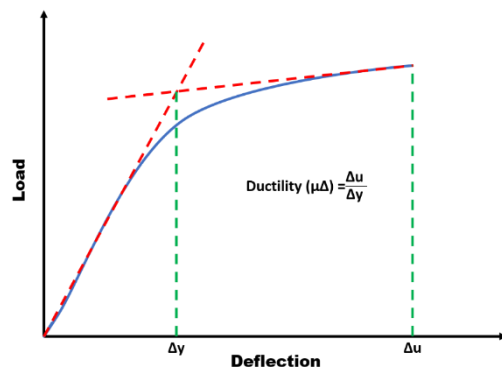


Figure 9. The ductility index calculation approach [23, 24]

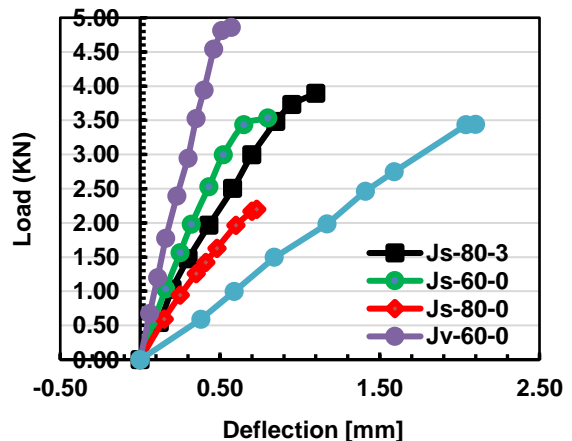


Figure 10. Load-deflection curves for specimens

bricks, where the behavior is linear until reaching their ultimate strength. As soon as the maximum load is reached, an abrupt failure occurs. This linear behavior of jack-arch slab specimens made with solid, and perforated bricks, and cellular concrete blocks bonded together using gypsum mortar is due to the fact that they are brittle materials and do not exhibit the ductility of ductile materials. From previous load-deflection curves, the specimen Jv-60-0 has a higher stiffness than the specimens Js-60-0, and Jc-60-0. The specimen Js-80-3 has a higher stiffness than Js-80-0.

Ductility index results for brick slab specimens are shown in Figure 11 and Table 10. The effects of the type of bricks used in the construction of the brick slab on the ductility index are studied by using three brick types, solid, and perforated bricks, and cellular concrete blocks (thermostone) for a span length of 600 mm. The results show that the specimen with solid bricks, Js-60-0 has a greater ductility index than the specimens with perforated clay bricks Jv-60-0 and cellular concrete blocks Jc-60-0 by 4.46 and 13.59%, respectively. To investigate how span length affects the ductility index of brick slab is also considered for samples made with solid bricks. The selected span is between 600 and 800 mm. The findings indicate that by increasing the span from 600 to 800 mm for Js-80-0 the ductility index decreased by 6.83%. Also, the effect of increasing camber height on the ductility index of the brick slab is investigated. For this purpose, one camber of 30 mm is used for specimens made of solid clay bricks. The results show an increase in the ductility index for the specimens when the camber is increased. The results showed an increase in camber of 30 mm for the specimen Js-80-3 which improve the ductility index by 5.50%. From the above results of ductility index, all-control brick slab specimens have a very low ductility index as a result of consistent materials, clay bricks, gypsum mortar, and cement (plastering), which are not ductile and brittle. Also, cellular concrete blocks do not have ductile properties.

4. FAILURE MODES

Failure modes for all brick slab specimens are shown in Figure 12 (a-e). For those specimens, failure is

characterized in all brick slabs made from solid, and perforated brick specimens by the sudden collapse of brickwork slabs due to initiate cracks at the joining brick units together. Due to the fact that the bond joints between brick units are the weakest part of the element, this characterized failure in the control of conventional brick slab samples. The failure mode is characterized by a brittle failure, this is due to the brick slab constituent materials that are brittle and have low tensile strength. The observation made during the test show that the specimens' compression faces are not crushed, and the clay bricks do not break or break, see Figure 12 (a-d). For brick slab specimens made with cellular concrete blocks, the failure mode is similar to that of brick slabs made with perforated and solid clay brick specimens. The failure is characterized by brittleness and the sudden collapse of cellular concrete block. The fracture occurs in the cellular concrete block unit at mid-span instead of in the bond joint between units. This failure mechanism occurs because cellular concrete blocks have brittle and low tensile strength. During the test of this specimen, no crushing in the compression face occurred, see Figure 12 (e). From the above explanation, the flexural failure mode is dominates the brick slab specimens at mid-span for brick slab specimens made with cellular concrete block and nearer the bond joint at mid-span for brick slab specimens made with perforated and solid clay brick.

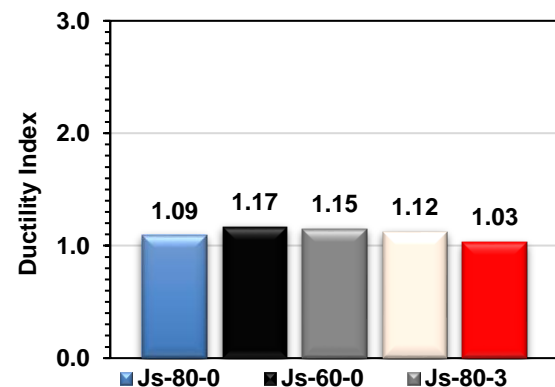


Figure 11. Ductility index results for specimens

TABLE 10. Sample test results

Specimens Symbol	Ultimate Load [kN]	Ultimate Deflection [mm]	Yield Load [kN]	Yield Deflection [mm]	Ductility [$\Delta u/\Delta y$]	Weight [kg]
Js-60-0	3.53	0.80	3.50	0.68	1.17	40
Js-80-0	2.19	0.73	2.16	0.67	1.09	51
Js-80-3	3.89	1.10	3.73	0.95	1.15	52
Jv-60-0	4.85	0.57	4.80	0.50	1.12	33
Jc-60-0	3.44	2.10	3.43	2.03	1.03	14

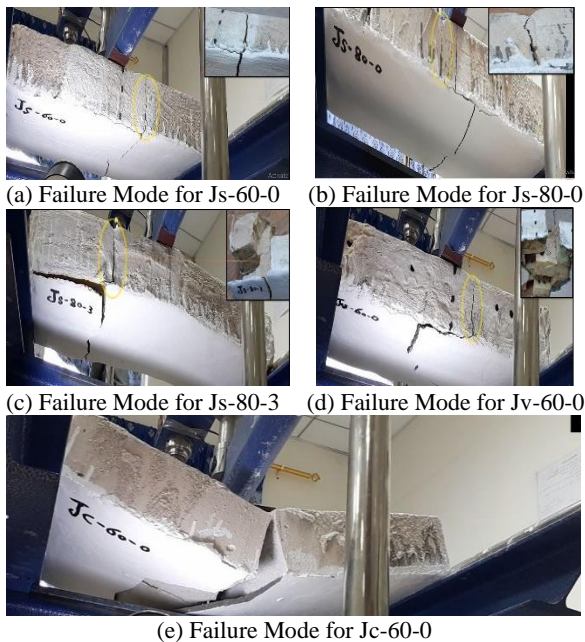


Figure 12. Mode of failure for specimen

5. CONCLUSIONS

Steel I-section beams that are supported by bearing walls with span centers ranging from 70 to 90 cm make up brick slabs. The behavior of brick slabs made of different types of bricks solid bricks, perforated bricks, and cellular concrete blocks (thermostone) was examined in this study using five one-way brick slab specimens. While the camber varies from 0 to 30 mm, the span is between 600 and 800 mm. Previously, the buildings were constructed of cellular concrete blocks and solid and perforated clay bricks. Flexural three-point loading is used to test these samples. The results revealed that increasing camber by 30 mm for solid brick specimens increased ductility, and ultimate strength, by 5.5%, and 77.62, respectively. Increasing span from 600 to 800 mm for solid brick specimens decreased the ultimate strength and ductility by 37.96% and 6.83%, respectively. Conclusion based on the study's findings showed that cellular concrete blocks can be used in the construction of slabs due to their lightweight and acceptable structural response when compared to solid brick specimens. Due to their good structural performance and light weight, perforated bricks can be used to build brick slabs. Brick slab specimens generally exhibit flexural failures. Brittleness and the sudden collapse of the brickwork arch characterized the failure mode in all samples. The authors suggest adopting this kind of slab when constructing residential buildings because it is quick to construct, inexpensive, and suitable for narrow spaces when applying the required engineering techniques.

6. RECOMMENDATIONS FOR FUTURE RESEARCH

1. To increase strength, we should increase the bond strength between brick units, and mortar used.
2. Our main emphasis in this study was on experimental work. We are currently creating the empirical equations and finite element models for the methodology covered in this paper. This, in our opinion, should be covered in a different study.

7. REFERENCES

1. Maheri, M.R., Pourfallah, S. and Azarm, R., "Seismic retrofitting methods for the jack arch masonry slabs", *Engineering Structures*, Vol. 36, (2012), 49-60. doi: 10.1016/j.engstruct.2011.11.018.
2. Maheri, M.R. and Rahmani, H., "Static and seismic design of one-way and two-way jack arch masonry slabs", *Engineering Structures*, Vol. 25, No. 13, (2003), 1639-1654. doi: 10.1016/S0141-0296(03)00143-3.
3. Zahraei, S.M. and Heidarzadeh, M., "Destructive effects of the 2003 bam earthquake on structures", (2007).
4. Pourfallah, S., Maheri, M. and Najafgholipour, M., "Experimental investigation of the jack arch slab retrofitted by concrete layer", in ICCD03: 3rd International Conference on Concrete & Development. (2009), 523-533.
5. Shakib, H., Mirjalili, A., Dardaei, S. and Mazroei, A., "Experimental investigation of the seismic performance of retrofitted masonry flat arch diaphragms", *Journal of Performance of Constructed Facilities*, Vol. 29, No. 4, (2015), 04014115. doi: 10.1061/(asce)cf.1943-5509.0000611.
6. Resan, S. and Dawood, A., "Behavior of customary jack-arch slabs in south of iraq", *Journal of University of Babylon*, Vol. 23, No. 2, (2015), 441-452.
7. Dawood, A.O., "Seismic analysis of traditional jack-arch slab in south of iraq", *Al-Qadisiyah Journal for Engineering Sciences*, Vol. 8, No. 3, (2015).
8. Ozdemir, M.A., Kaya, E.S., Aksar, B., Seker, B., Cakir, F., Uckan, E. and Akbas, B., "Seismic vulnerability of masonry jack arch slabs", *Engineering Failure Analysis*, Vol. 77, (2017), 146-159. doi: 10.1016/j.engfailanal.2017.02.008.
9. Raeisi, D.M., Veysmoradi, S., Yousefi, S. And Eghbali, M., "Application of reinforcement concrete layer method for retrofit of slant jack arch roofs in masonry buildings", (2017).
10. Zahrai, S., "Structure-earthquake", doi: 10.22068/IJCE.13.3.278.
11. Alfeehan, A.A. and Alkerwei, R.H., "Structural behavior for low cost roof system of steel frame and thermo-stone blocks", *Engineering and Technology Journal*, Vol. 32, No. 12 part A, (2014), 433-444. doi.
12. Obaid, A.H. and Jaafer, A.A., "Experimental investigation of ferrocement sandwich composite jack arch slab", *Asian Journal of Civil Engineering*, Vol. 23, No. 7, (2022), 1155-1168. doi: 10.1007/s42107-022-00467-3.
13. Güney, D., Aydin, E. and Öztürk, B., "The evaluation of damage mechanism of unreinforced masonry buildings after van (2011) and elazig (2010) earthquakes", in Journal of Physics: Conference Series, IOP Publishing. Vol. 628, (2015), 012066.
14. Ozturk, B., "Seismic behavior of two monumental buildings in historical cappadocia region of turkey", *Bulletin of Earthquake*

- Engineering*, Vol. 15, (2017), 3103-3123. doi: 10.1007/s10518-016-0082-6.
15. El Wardi, F.Z., Ladouy, S., Khabbazi, A., Ibaaz, K. and Khaldoun, A., "Unfired clay-cork granules bricks reinforced with natural stabilizers: Thermomechanical characteristics assessment", *Civil Engineering Journal*, Vol. 7, No. 12, (2021), 2068-2082. doi: 10.28991/cej-2021-03091778.
 16. Balamuralikrishnan, R. and Saravanan, J., "Effect of addition of alccofine on the compressive strength of cement mortar cubes", *Emerging Science Journal*, Vol. 5, No. 2, (2021), 155-170. doi: 10.28991/esj-2021-01265.
 17. Hasan, Z.A., Abdulridha, S.Q. and Abeer, S., "Sustainable mortar made with local clay bricks and glass waste exposed to elevated temperatures", *Civil Engineering Journal*, Vol. 7, No. 8, (2021), 1341-1354. doi: 10.28991/cej-2021-03091729.
 18. ASTM, C., "Standard specification for concrete aggregates", *Philadelphia, PA: American Society for Testing and Materials*, (2003).
 19. Pujol, S. and Ramirez, J., "Proposed modifications to aci 318-95 tension development and lap splice for high-strength concrete. Discussion and closure", *ACI Structural Journal*, Vol. 97, No. 5, (2000).
 20. Abdulraheem, M.S., "Experimental investigation of fire effects on ductility and stiffness of reinforced reactive powder concrete columns under axial compression", *Journal of Building Engineering*, Vol. 20, (2018), 750-761. doi: 10.1016/J.JOBE.2018.07.028.

COPYRIGHTS

©2023 The author(s). This is an open access article distributed under the terms of the Creative Commons Attribution (CC BY 4.0), which permits unrestricted use, distribution, and reproduction in any medium, as long as the original authors and source are cited. No permission is required from the authors or the publishers.



Persian Abstract

چکیده

این مطالعه، پنج نمونه دال آجری یک طرفه برای بررسی رفتار دال‌های آجری متشکل از انواع آجر (آجرهای توپر، آجرهای سوراخ‌دار و بلوک‌های بتنی سلولی (ترموستون)) ساخته شد. دامنه دهانه بین ۶۰۰ تا ۸۰۰ میلی متر است، در حالی که دامنه از ۰ تا ۳۰ میلی متر است. قبلاً از بلوک‌های بتنی سلولی و آجرهای سفالی جامد و سوراخ‌دار به عنوان مصالح ساختمانی استفاده می‌شد. این نمونه‌ها با بارگذاری سه نقطه‌ای خمشی آزمایش می‌شوند. نتایج نشان داد که افزایش کمر به میزان ۳۰ میلی‌متر برای نمونه‌های آجر جامد، شکل‌پذیری و استحکام نهایی را به ترتیب ۵.۵ درصد و ۷۷.۶۲٪ افزایش داد. افزایش دهانه از ۶۰۰ به ۸۰۰ میلی‌متر برای نمونه‌های آجر جامد، مقاومت نهایی و شکل‌پذیری را به ترتیب ۳۷.۹۶٪ و ۶.۸۳٪ کاهش داد. بلوک‌های بتنی سلولی به دلیل سبک بودن و واکنش سازه‌ای قابل قبولی که در مقایسه با نمونه‌های آجری جامد دارند، می‌توانند در ساخت دال‌ها استفاده شوند. آجرهای سوراخ‌دار به دلیل عملکرد سازه‌ای خوب و وزن سبکی که دارند می‌توانند برای ساخت اسلب آجری استفاده شوند. شکندگی و فروریختن ناگهانی طاق آجرکاری، حالت شکست را در همه نمونه‌ها مشخص می‌کند.



Experimental Work on the Effect of Under-reamed Pile Geometry on the Pullout Capacity of Sand

A. W. Al-Bayati, M. A. AL-Neami*, F. H. Rahil

Civil Engineering Department, University of Technology, Baghdad, Iraq

PAPER INFO

Paper history:

Received 18 April 2023

Received in revised form 09 July 2023

Accepted 14 July 2023

Keywords:

Under-reamed Piles

Enlarge Pile

Bulb Spacing

Pullout Load

ABSTRACT

This work presents an experimental study that investigates the behavior of both conventional and under-reamed piles embedded in a single layer of sand with varying relative densities and examines piles in different soil layers, subjected to pullout static monotonic loading. The study focuses on the influence of the spacing ratio between under-reams and the number of bulbs on the pile's ultimate pullout load. A uniform pile stem, a pile with a single bulb, and a pile with twin bulbs were the three varieties of small-scale models of aluminum piles that were utilized. The pile's measurements were 25 mm in shaft diameter by 550 mm in height, with a 62.5 mm bulb diameter. To establish their impact on the uplift capability of an under-reamed pile in sand, the current work examines the location, spacing between bulbs, and the number of bulbs. At 35% relative density, the influence of various bulb spacing ratios S/D_u is investigated ($S/D_u = 1.0$, $S/D_u = 1.25$, $S/D_u = 1.5$, $S/D_u = 1.75$, and $S/D_u = 2$). The test results revealed that the maximum ultimate pullout capacity is achieved when the bulb spacing ratio is $S/D_u = 1.5$. The pullout capacity increases 3.5 times for a single bulb and 7 times for a double bulb compared with a straight pile under the same condition, as well as an under-reamed pile in a dense or medium sand layer overlain by loose sand rises to a peak before capacity declines. Load-displacement curves and initial stiffness improve compared to homogeneous, loose, sandy soil.

doi: 10.5829/ije.2023.36.09c.08

1. INTRODUCTION

The under-reamed piles are enlarged piles constructed insitu with single or more bulbs around a pile shaft to resist compressive loading, uplift loading, and ground movement. They are a type of deep foundation for different structures, such as offshore platforms, multi-story buildings, and transmission towers. Das and Shin [1], Khatri et al. [2] explained that belled pile are very promising in terms of tensile load resistance and suited for soil that experiences ground movements as a result of seasonal moisture variation. These piles had been introduced first in India for use in expansive soil, which is classified as problematic soil. Soil layers and pile dimensions greatly affect the load capacity of an under-reamed pile. Hassan [3] reported that under-reamed piles are considered a good foundation technique due to being the safest and most economical foundation. Patra et al.

[4] evaluated experimentally and discovered that the maximum uplift load capacity for medium-dense ($DR = 52\%$) over dense conditions ($DR = 80\%$) was greater than for dense conditions overlaid on medium-dense conditions. Liu et al. [5] concluded that the uplifted movement of the belled pile decreases when the uplift loading is increased to its maximum. Bose and Krishnan [6] demonstrated that for a given displacement, the pile resistance to pullout load increases with surface finishes ranging from smooth to rough. In addition, when the slenderness ratio increases, the pile resistance at any axial displacement increases exponentially. Nazir et al. [7] demonstrated that the embedment ratio (L/D) has a main consequence on the support of any increasing pullout load, and increases in the angle of the base and stem diameter result in a slightly reduced failure displacement and net uplift capacity. Harris et al. [8] studied experimentally the effects of varying the under-reamed

*Corresponding Author Institutional E-mail:
40008@uotechnology.edu.iq (M. A. Al-Neami)

angle, θ (20° , 30° , 40° , 60° , and 75°), on uplift capacity and load-deformation curves. The results showed that the capacity drops off when the bulb angle of the under-ream pile is increased, which is especially apparent at an angle of 75° . Christopher and Gopinath [9] showed that when the space between two bulbs was increased up to 150 mm, an increase in pile capacity occurred. The improvement in load-carrying capacity becomes smaller as the spacing increases. Moayedi and Mosallanezhad [10] indicated that the pullout resistance increases by more than 60% when the under-reams is positioned at the base of the pile and reduces by around 4% when it is installed at a depth corresponding to 33% of the pile's length. Schafer and Madabhushi [11] made a study to clarify the impact of different layers of soil, and they concluded that the uplift capacity gradually rises, and the installation of a lower layer of dense sand under a higher layer of loose sand improves an under-reamed pile foundation's peak uplift capability but has no influence on the displacement necessary to achieve this peak. Substituting clay for the overlying loose sand layer can raise the uplift even more. Nasr et al. [12] showed that the uplift capability of a belled base piles installed in sandy soil with various unit weights increases when the ratio of embedment length to base diameter (L/D_b) rises. Sakr et al. [13] and Sakr et al. [14] performed an experimental study to clarify the influence of under-reamed pile factors such as position, spacing between bulbs, and bulb numbers on the pullout loading. They noticed that the pile pullout load increased with increasing under-ream diameter, number of bulbs, and relative density. Alhassani [15] conducted numerical research using the ABAQUS program to explore the behaviour of the under-reamed pile under the pullout, lateral, and compression loads. The results of the testing models revealed that the uplift pile capacity of SURP and DURP is much greater than that of a straight pile for all L/D pile ratios. Al-Tememy et al. [16] used PLAXIS-3D software to examine a model of the steel pipe pile installed in dry sand. Based on the outcomes, the relative density of the sand has an influence on the peak resistance pullout load of vertical piles. When the relative density of sand improves from 40% to 60%, the ultimate pullout load of a vertical pile increases by around 35%–56%. Goudar and Kamatagi [17] tested the influence of two distinct geometries of aluminum model pile groups, L/D ratios, and S/D spacing ratios. The investigation employed uniform pile section and enlarged base (Belled) piles embedded in locally accessible sandy soil. It was discovered that the load-carrying capability of a belled model pile increases at a greater L/D ratio. However, the extension angle enhanced the load-carrying capacity by 40% over straight piles. Furthermore, (S/D) exhibits large variability in bearing capability.

Under-reamed piles are used to enhance the performance and stability of foundations in weak soil

conditions, control settlement, improve lateral, uplift stability, and provide a cost-effective solution for constructing buildings and structures on challenging soil types. Experimental findings can contribute to the development of improved construction techniques for under-reamed piles. By understanding the behavior of these piles under uplift loads, researchers can suggest optimized installation procedures, reducing construction costs and potential issues during installation. Finally, the conventional pile used to estimate the improvement of adding one or double bulbs to the uniform pile shaft.

There are a lack of comprehensive experimental studies specifically focused on the behavior of under-reamed piles subjected to pullout loads. This could result in a scarcity of data regarding factors such as load-displacement behavior, failure mechanisms, and load transfer characteristics and The interaction between the under-reamed pile and different types of soil, including cohesionless and different soil strata, may not be fully understood. The influence of various soil properties, such as shear strength, soil density on the pullout behavior of under-reamed piles may require further investigation

So, this research shed light on the behavior of load-displacement curve of under-reamed piles, both single and double bulb configurations, improves compared to straight piles when embedded in loose, medium, and dense sandy soil. On other hand, the investigation studies the performance of piles in different soil layers and its effect on the load- displacement curves when subjected to pullout load. Furthermore, an experimental work was conducted in the current study to evaluate the effect of under-reamed pile's geometry (the distance between bulbs and the number of bulbs) on the uplift resistance load with varying relative densities of dry sand.

2. METHODOLOGY

2. 1. Soil Properties Sand soil used is classified as (SP) poorly graded according to the USCS. Various tests are made on this sand per ASTM specifications to obtain its properties (physical and mechanical), as shown in Table 1. Three states of relative density were used to achieve the goal of the study (the loose, medium, and dense states).

2. 2. Pile Model Three small-scale models of aluminum piles used of length 550 mm in length were used, with a bulb diameter of 62.5 mm for a 25 mm pile diameter. Three pile shapes were adopted in this study: the straight pile and multi under-reamed piles (single bulb and two bulbs) with different vertical spacings between bulbs. The design of the under-reamed pile and under-reams was carefully chosen per the Indian Code (IS 2911) specification [18]. Table 2 depicts the pile model properties used in the study, and Figure 1 depicts its shape.

TABLE 1. Soil used properties

Property	Value	Specification
Maximum unit weight kN/m^3	17.1	ASTM D 4253
Minimum unit weight kN/m^3	14.88	ASTM D 4254
Effective Size,		
D_{30}	0.12	ASTM D 422 and ASTM D 2487
D_{10}	0.195	
D_{60}	0.28	
Friction angle at 35% R_D ($\gamma_{\text{used}}=15.6$) kN/m^3	30°	
Friction angle at 55% R_D ($\gamma_{\text{used}}=16.0$) kN/m^3	35°	ASTM D 3080
Friction angle at 75% R_D ($\gamma_{\text{used}}=16.5$) kN/m^3	39°	

TABLE 2. Model piles used

Description	Notation	Dimension
Pile length, mm	L	550
Pile diameter, mm	D	25
Under-reams diameter, mm	$D_u/D_p=2.5$	62.5
	$1D_u$	62.5
	$1.25D_u$	78
Bulb spacing ratio	$1.5D_u$	93
C-C (S/D_u)	$1.75D_u$	109
	$2D_u$	125
Upper angle of under-reams pile, degree	$\emptyset 1$	45
Lower angle of under-reams pile, degree	$\emptyset 2$	45

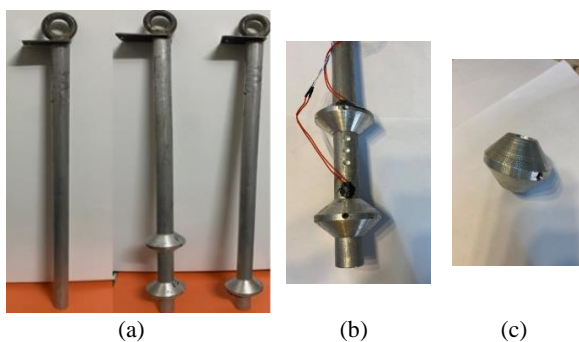


Figure 1. Pile geometries considered, a. conventional pile, single and double under-reamed piles, b. bulb spacing c-c, c. under-reamed geometries

2. 3. Pile Model Preparation and Testing

To prepare the soil bed, a steel container measuring (650 mm × 650 mm × 750 mm) was used, and to avoid the effect of lateral friction, a rubber layer was applied to the

inner faces of the container. The soil was poured into the container and tamped to the desired density; after that, the pile model was put precisely in its location during the soil preparation (see Figure 2).

A strain-controlled pullout system was used with a 0.25 mm/min sustained rate until the displacement reached 30 mm. In addition, all the pile model tests were carried out at a static monotonic load; as it has been reported by Qian et al. [19].

3. RESULTS AND DISCUSSION

Outcomes of effectiveness of relative density, number of bulbs, and bulb spacing ratio on the ultimate pullout capacities and their discussions are described below. Schafer and Madabhushi [11], the ultimate capacity was determined according to the clear breakpoint (maximum uplift load before failure). Vali et al. [20] and Kumar et al. [21] used the double tangent technique to evaluate the ultimate pullout carrying capacity. It was discovered that the outcomes were 99 percent similar between the two methods.

3. 1. Influence of Relative Density Figures 3, 4, and 5 depict the pullout load-displacement relation for the conventional pile, and the one and two under-reamed piles, respectively. All figures show that the pull-out load increases as the relative density increases to some limiting values, after which the value becomes nearly constant and insensitive to the change in displacement that continues to increase. This behavior is attributed to the roughness between the soil and the pile skin. The ultimate pullout carrying capacity of the different types of model piles is shown in Table 3.

Table 4 shows the improvement in the pullout load of one and two under-reamed piles in three relative densities compared to a conventional pile. A good enhancement is observed compared to the straight pile was detected.

By evaluating the results for a single pile (P) and after adding one bulb PSUR and two bulbs PDUR, it was



Figure 2. Under-reamed pile test

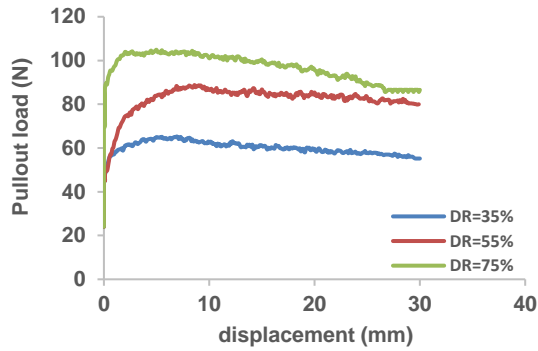


Figure 3. The load-displacement curves for the conventional pile

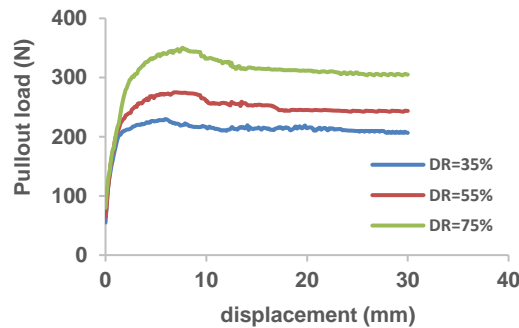


Figure 4. The load-displacement curves for single under-reamed pile

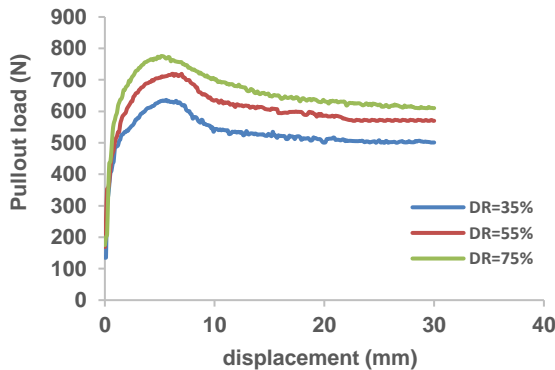


Figure 5. The load-displacement curve for double under-reamed pile

TABLE 3. Pullout load value of the different types of model pile

Relative density (DR%)	Pullout carrying capacity (N)		
	Conventional pile	One under-reamed pile	two under-reamed pile
35%	65	229.7	637
55%	90	275	719
75%	107	350	775

TABLE 4. Uplift loading improvements of one and two under-reamed piles

Soil types	% Degree of Improvement	
	One under-reamed pile	two under-reamed pile
Loose	250 %	800%
Medium	205 %	700%
Dense	227 %	600%

obvious that raising the relative density increased the pullout load and caused a corresponding decrease in the displacement for all types of piles. In all cases, a double under-reamed pile had the higher pullout force than a single under-reamed pile. It indicates that increasing the number of under-reams will improve its pullout capacity. However, this comes at the expense of more concrete being used to make bulbs. Therefore, under-reamed piles perform better when buried in loose, medium-density sand.

3. 2. Influence The Bulb Spacing

In order, to study the under-reams spacing ratio S/D_u effect, the relative density was kept constant throughout this set of tests. The bulbs were spaced at $S/D_u = 1.0$, $S/D_u = 1.25$, $S/D_u = 1.5$, $S/D_u = 1.75$, and $S/D_u = 2$, where D_u is the bulb diameter. Figure 6 shows the load-deformation curves for various spacings between bulbs. The results of the pullout load indicate that the best value was obtained when $S/D_U = 1.5$; below and above this ratio, the pullout load decreases. This behavior is mainly attributed to the load gated from the above bulb and between the two bulbs and its effect on the failure zone. Figure 7 shows the highest value of the ultimate uplift capacity for each experiment conducted by changing the distance between the two bulbs.

3. 3. Influence of the Number of Bulbs

Figure 8 shows the results of increasing the number of under-reams to $D_u/D_p = 2.5$ with various relative densities. It

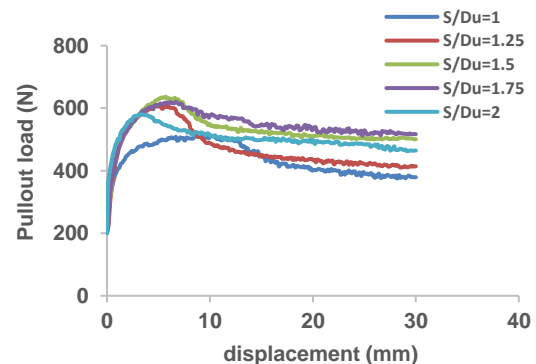


Figure 6. The load-displacement curve of different vertical spacing between the bulbs

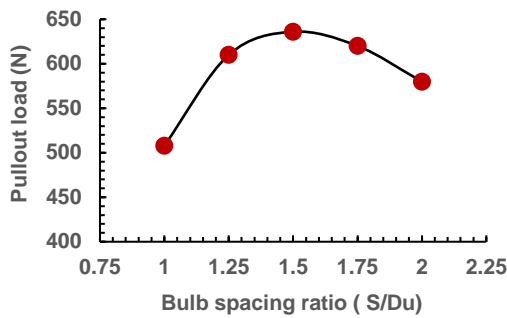


Figure 7. The ultimate pullout capacity with different vertical spacing between the bulbs

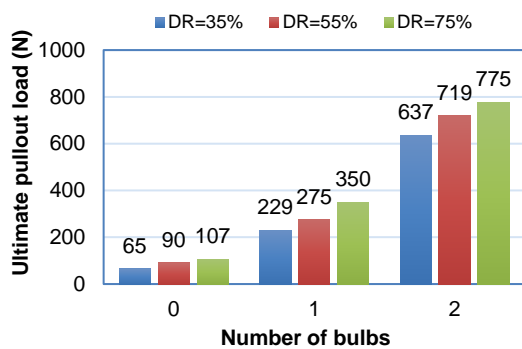


Figure 8. Variation of ultimate pullout load with bulb number

can be noted that the ultimate pullout capacity increases as the number of bulbs increases, which means that increasing the number of bulbs has an important effect on the ultimate pullout load. Also, it can be observed that the increasing number of bulbs is greater when the sand is in a loose state. This behavior is caused by the surrounding soil adhering to the under-ream, which has the advantages of increasing soil strength and reducing deformation.

3. 4. The Behavior of Under-Reamed Piles Under Pullout Loads in Layered Stratum

As a result, this study tries to provide a clear image of the under-reamed pile anchored to a two-layers system. Figure 9 shows the problem statement model of (single and double bulbs) in the soil's layers.

Hence, the study could shed light on the load-displacement response of a single and double under-reamed pile embedded in a dense and medium sand layer overlain by loose sand is shown in Figures 10 and 11.

The load-displacement response of an under-reamed pile placed in a dense or medium sand layer overlain by loose sand shows a rise to a peak before a decline in capacity caused by soil arching at large displacements. The overall form of the curve is quite similar to that observed in a homogenous loose sand bed, but the

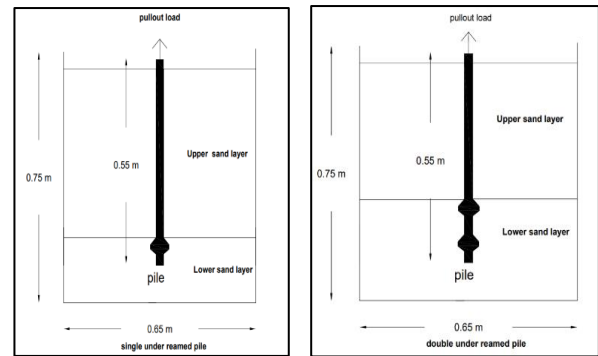


Figure 9. embedded test model

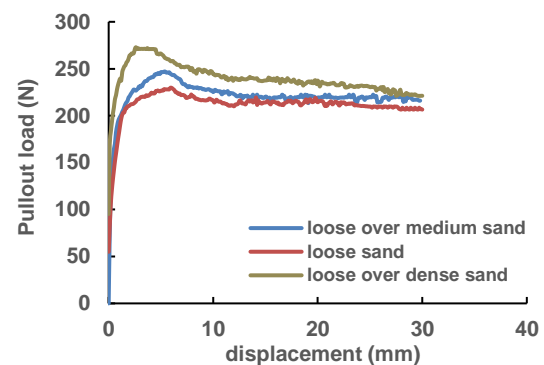


Figure 10. Load -displacement curve of single under-reamed pile

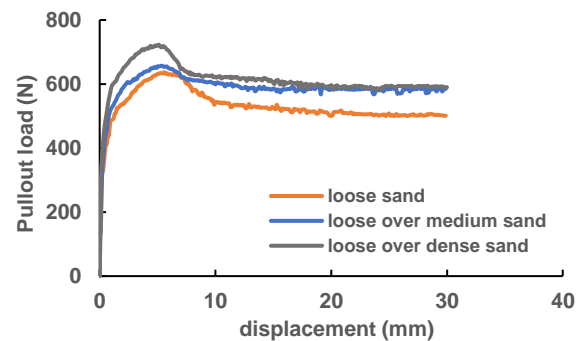


Figure 11. Load -displacement curve of double under-reamed pile

ultimate capacity is substantially higher. This indicates that the bottom dense layer of sand has a significant influence on the peak capacity of the under-reamed pile. The initial stiffness measured at a small strain is slightly higher than that measured in homogenous loose sand. Table 5 illustrated the ultimate pullout loading for the belled pile in layered soil.

A double under-reamed pile will initially show more powerful resistance to pullout load than a single under-reamed pile due to the extra bearing surface and load

TABLE 5. ultimate pullout load for under-reamed pile embedded in soil layered system

Type of soil	Ultimate pullout load (N)	
	Single under-reamed pile	Double under-reamed pile
Medium sand overlined by loose sand	247	657
Dense sand overlined by loose sand	271	720

distribution given by the two under-reams, the load-displacement curve for a double under-reamed pile may demonstrate higher initial stiffness and load-carrying capability. The inclusion of two under-reams can improve load distribution and contribute to a more progressive displacement progression before the peak or ultimate load.

4. CONCLUSIONS

The influence of the number of bulbs and spacing between under-reams in the under-reamed pile was investigated with various relative densities to examine the pullout load of an under-reamed pile subjected to the axial pullout force. Following conclusions result from the study's outcomes:

1. In terms of increasing pullout capacity, under-reamed pile is more advantageous in different relative densities composed of loose and dense.
2. Spacing between bulbs affected on pullout capacity. When spacing is less than 1.25 Du, the pile doesn't work effectively. When spacing between bulbs is 1.25–1.5 Du, the pile and soil work together as one block, which enhances the maximum uplift load. After this value, decrease in the maximum load is very clear.
3. Rate of pullout load for a single under-reamed pile rises from no bulb to one bulb by up to 200%. For double under-reamed piles, where it surpasses 700%, the influence of an increase in the number of bulbs on pullout loads is particularly significant.
4. For a two-under reamed pile, the influence of increasing the number of bulbs on a pullout capacity is more advantageous, but this necessitates using more concrete for bulb formation.
5. In the term of layered soil, load-displacement response of an under-reamed pile placed in a dense or medium sand layer overlain by loose sand shows a rise to a peak before a decline in capacity. In general, there is an improvement in the load-displacement curves and show higher initial stiffness compared with homogeneous loose sandy soil.

5. REFERENCES

1. Das, B.M. and Shin, E.C., "Ultimate uplift capacity of metal piles in sand", *International Journal of Offshore and Polar Engineering*, Vol. 2, No. 03, (1992). <https://onepetro.org/ijope>
2. Khatri, V.N., Kumar, A., Gupta, S., Dutta, R.K. and Gnananandarao, T., "Numerical study on the uplift capacity of under-reamed piles in clay with linearly increasing cohesion", *International Journal of Geotechnical Engineering*, Vol. 16, No. 4, (2022), 438-449. <http://dx.doi.org/10.1080/19386362.2019.1660527>
3. Abbas, H.O., "Laboratory evaluation of effective parameters on uplift force under reamed pile in expansive soil", *Geotechnical and Geological Engineering*, Vol. 38, (2020), 4243-4252. <https://link.springer.com/article/10.1007/s10706-020-01292-8>
4. Patra, N.R., Deograthias, M. and James, M., "Pullout capacity of anchor piles", *Electronic Journal of Geotechnical Engineering (EJGE)*, Vol. 340, (2004), 2004. <https://www.researchgate.net/>
5. Wenbai, L., Jian, Z. and Tei-Mohr, M., "Uplift bearing tests and calculations of belled piles in loess of arid regions", (2004). https://scholarsmine.mst.edu/icchge/5icchge/session01/15?utm_source=scholarsmine.mst.edu%2Ficchge%2F5icchge%2Fsession01%2F15&utm_medium=PDF&utm_campaign=PDFCoverPages
6. Bose, K.K. and Krishnan, A., "Pullout capacity of model piles in sand", *Indian Geotechnical Society Chennai Chapter, Student Competition Paper*, (2009), 49-54. <https://www.semanticscholar.org>
7. Nazir, R., Moayedi, H., Pratikso, A. and Mosallanezhad, M., "The uplift load capacity of an enlarged base pier embedded in dry sand", *Arabian Journal of Geosciences*, Vol. 8, (2015), 7285-7296. <http://dx.doi.org/10.1007/s12517-014-1721-3>
8. Harris, D.E. and Madabhushi, G.S.P., "Uplift capacity of an under-reamed pile foundation", *Proceedings of the Institution of Civil Engineers-Geotechnical Engineering*, Vol. 168, No. 6, (2015), 526-538. <https://doi.org/10.1680/jgeen.14.00154>
9. Christopher, T. and Gopinath, M.B., "Parametric study of under-reamed piles in sand", *International Journal of Engineering Research & Technology (IJERT)*, Vol. 5, No. 7, (2016), 577-581. <https://doi.org/10.17577/IJERTV5IS070450>
10. Moayedi, H. and Mosallanezhad, M., "Uplift resistance of belled and multi-belled piles in loose sand", *Measurement*, Vol. 109, (2017), 346-353. <https://doi.org/10.1016/j.measurement.2017.06.001>
11. Schafer, M. and Madabhushi, S.P.G., "Uplift resistance of enlarged base pile foundations", *Indian Geotechnical Journal*, Vol. 50, (2020), 426-441. <https://doi.org/10.1007/s40098-019-00369-3>
12. Nasr, A., Azzam, W. and Abd Elgwad, A., "Experimental study of enlarged base pile under tension load in sand", *Journal of Engineering Research*, Vol. 6, No. 2, (2022), 40-44. <https://doi.org/10.21608/erjeng.2022.143680.1072>
13. Sakr, M., Nasr, A., Basha, A. and Khaffaf, M., "Comparative study on the behavior of under-reamed piles under vertical uplift loads in sand", *International Journal of Innovative Science Engineering and Technology*, Vol. 9, No. 01, (2022), 28-44. https://ijiset.com/vol9/v9s1/IJISSET_V9_I01_03.pdf
14. Sakr, M., Nasr, A., Basha, A. and Khaffaf, M., "Experimental and analytical assessment of the pullout capacity of axially loaded under-reamed pile in cohesionless soil", *Innovative Infrastructure Solutions*, Vol. 8, No. 1, (2023), 73. <http://dx.doi.org/10.1007/s41062-023-01046-4>
15. Alhassani, A., "Analysis of under-reamed piles subjected to different types of load in clayey soil", *International Journal of*

- Engineering, Transactions B: Applications*, Vol. 34, No. 8, (2021), 1940-1948. <https://doi.org/10.5829/ije.2021.34.08b.15>
16. Al-Tememy, M., Al-Neami, M. and Asswad, M., "Finite element analysis on behavior of single battered pile in sandy soil under pullout loading", *International Journal of Engineering, Transactions C: Aspects*, Vol. 35, No. 6, (2022), 1127-1134. <https://doi.org/10.5829/ije.2022.35.06c.04>
 17. Goudar, S. and Kamatagi, A., "An experimental evaluation of axial load bearing capacity of belled and straight piles embedded in sand", *International Journal of Engineering, Transactions B: Applications*, Vol. 35, No. 8, (2022), 1599-1607. <https://doi.org/10.5829/ije.2022.35.08b.16>
 18. Dxl, R., "Is: 2911 (part iii). Indian standard code of practice for design and construction of pile foundations. Underreamed piles ", (1980). <https://law.resource.org/pub/in/bis/S03/is.2911.3.1980.pdf>
 19. Qian, Z.-z., Lu, X.-l., Han, X. and Tong, R.-m., "Interpretation of uplift load tests on belled piers in gobi gravel", *Canadian Geotechnical Journal*, Vol. 52, No. 7, (2015), 992-998. <https://doi.org/10.1139/cgj-2014-0075>
 20. Vali, R., Mehrenejad Khotbehsara, E., Saberian, M., Li, J., Mehrenejad, M. and Jahandari, S., "A three-dimensional numerical comparison of bearing capacity and settlement of tapered and under-reamed piles", *International Journal of Geotechnical Engineering*, Vol. 13, No. 3, (2019), 236-248. <https://doi.org/10.1080/19386362.2017.1336586>
 21. Kumar, A., Khatri, V.N. and Gupta, S.K., "Effect of linearly increasing cohesion on the compression and uplift capacity of the under-reamed pile in clay", *SN Applied Sciences*, Vol. 2, (2020), 1-17. <https://doi.org/10.1007/s42452-020-2111-y>

COPYRIGHTS

©2023 The author(s). This is an open access article distributed under the terms of the Creative Commons Attribution (CC BY 4.0), which permits unrestricted use, distribution, and reproduction in any medium, as long as the original authors and source are cited. No permission is required from the authors or the publishers.

**Persian Abstract****چکیده**

این کار یک مطالعه تجربی را ارائه می‌کند که به بررسی رفتار شمع‌های معمولی و کم‌پرده‌شده در یک لایه ماسه با تراکم‌های نسبی متفاوت می‌پردازد و شمع‌ها را در لایه‌های مختلف خاک بررسی می‌کند. در معرض بارگذاری یکنواخت ایستا خروجی. این مطالعه بر روی تأثیر نسبت فاصله بین زیرپوش‌ها و تعداد لامپ‌ها بر بار خروجی نهایی شمع متمرکز است. یک ساقه شمعی یکنواخت، یک شمع با یک حباب تکی و یک شمع با حباب‌های دوقلو سه نوع از مدل‌های کوچک مقیاس شمع‌های آلومینیومی بودند که مورد استفاده قرار گرفتند. اندازه‌های شمع ۲۵ میلی‌متر در قطر شفت در ۵۵۰ میلی‌متر در ارتفاع، با قطر لامپ ۶۲.۵ میلی‌متر است. برای تعیین تأثیر آنها بر روی قابلیت بالا بردن یک شمع زیردریایی شده در ماسه، کار فعلی مکان، فاصله بین لامپ‌ها و تعداد لامپ‌ها را بررسی می‌کند. در تراکم نسبی ۳۵ درصد، تأثیر نسبت‌های مختلف فاصله لامپ S/D_u بررسی می‌شود ($S/D_u = 1.0$, $S/D_u = 1.25$, $S/D_u = 1.5$, $S/D_u = 1.75$ و $S/D_u = 2$). نتایج آزمایش نشان داد که حداکثر ظرفیت خروجی نهایی زمانی حاصل می‌شود که نسبت فاصله لامپ $S/D_u = 1.5$ باشد. ظرفیت خروجی ۳.۵ برابر برای یک لامپ تک لامپ و ۷ برابر برای یک لامپ دوپل در مقایسه با یک شمع مستقیم در شرایط مشابه افزایش می‌یابد. و همچنین یک شمع کم‌آرام‌شده در یک لایه ماسه متراکم یا متوسط که با ماسه شل پوشیده شده است، قبل از کاهش ظرفیت به اوج می‌رسد. منحنی‌های بار-جابجایی و سفتی اولیه در مقایسه با خاک همگن، سست و شنی بهبود می‌یابند



Performance Analysis of High-K Dielectric Heterojunction High Electron Mobility Transistor for RF Applications

E. Radhamma^a, D. Vemana Chary^a, A. Krishnamurthy^b, D. Venkatarami Reddy^c, D. Sreenivasa Rao^d, Y. Gowthami^d, B. Balaji^{*d}

^a Department of Electronics and Communication Engineering, Teegala Krishna Reddy Engineering College, Meerpet, Hyderabad, TS, India

^b Department of Electronics and Communication Engineering, Princeton Institution of Engineering and Technology for Women, Hyderabad, India

^c Department of Electronics and Communication Engineering, Kodada Institute of Technology and Science for Women, Kodad, TS, India

^d Department of Electronics and Communication Engineering, Koneru Lakshmaiah Education Foundation, Green Fields, Vaddeswaram, Andhra Pradesh-522502, India

PAPER INFO

Paper history:

Received 12 June 2023

Received in revised form 24 June 2023

Accepted 05 July 2023

Keywords:

Silicon Dioxide

Radio Frequency

Transconductance

High Conductivity

High Electron Mobility Transistor

ABSTRACT

We have designed and simulated a 10-nanometer regime gate High Electron Mobility Transistor (HEMT) with an undoped region (UR) under the gate with high k dielectric as hafnium oxide (HfO₂). The thickness of metal gate(G) and undoped regions are equal but length of channel(C) is not equivalent. The proposed Undoped under the gate dielectric High Electron Mobility Transistor reduces the maximum electric field(V) in the channel region and increases the drain current significantly. The High-K dielectric High Electron Mobility Transistor structure obtained a saturated Ion current of 60% higher than the conventional structure. For High critical Power and High-frequency Power transmission Amplifiers utilizes the AlGaIn/GaN/SiC-based High Electron Mobility Transistor with an undoped region under the gate with High-K Hafnium oxide. The Proposed advanced High Electron Mobility Transistor Produces a higher Drain current (Id), 54% high transconductance (Gm) with Low On-Resistance (Ron), and High conductivity in comparison to typical High Electron Mobility Transistor. In Addition to these improved characteristics, the Electric field along the Y direction is also observed. The proposed structure formed by Low-k Dielectric materials in the process of Silicon Dioxide(SiO₂) and High-k dielectric being Titanium Dioxide (TiO₂) and Hafnium Oxide (HfO₂) created more opportunities in Power electronics and radio frequency operations.

doi: 10.5829/ije.2023.36.09c.09

1. INTRODUCTION

The technology develops year to year, there is drastic demand for VLSI devices as its device dimensions are scaled down to nanometer technology and more evident of short channel effects. In submicron technology, the channel length is very less i.e. less than 5 nanometer innovation and able to control the nanodevices due to decreases in gate length and subsequent undesirable conditions of Drain Induced Barrier Lowering (DIBL). To suppress the short channel effects, Double Gate (DG) structure, Triple Gate (TG) structure, and Nanowire (GAA) structures are excellent scalability over the conventional devices in nanometer technology [1].

The traditional Metal Oxide Semiconductor Field Effect Transistors (MOSFETs) are considered moderate and slower devices compared to Nanomaterial Oxide Nanowire High Electron Mobility Transistors (NWHEMTs). Therefore, Gallium Nitride (GaN) HEMT devices have a large bandgap, larger critical electric field, higher electron drift velocity, and attained good thermal conductivity and good thermal stability [2]. The optoelectronic devices such as high-power devices utilize the III-V bandgap semiconductors being Aluminum nitride, Gallium nitride, and Low-k dielectric material such as Silicon dioxide being SiO₂ and High-K dielectric material being hafnium oxide represented as HfO₂ and Titanium Dioxide (TiO₂) [3]. Due to its heterostructure undoped channel is possible in Nanowire HEMT and

*Corresponding Author Email: yahividi@gmail.com (B. Balaji)

attained higher breakdown voltages due to its higher band gap semiconductors being Gallium nitride (GaN) and Silicon dioxide as SiO₂ and high -k dielectric material (HfO₂) [4].

The Nanowire High Electron Mobility Transistor (HEMT) is a specific Heterostructure field effect transistor (H-FET) and it gives very high realization at RF and microwave frequencies as well as exhibits lower noise [5]. The working principle of HEMT is based on two-dimensional electron gas due to its heterostructure and less electron collision. The HEMT gives high current (Ion) at lower gate voltages (V_{GS}). Due to its high current and various heterostructures, Nanowire HEMT is suitable for finds applications in Radio Frequency design including cellular mobile telecommunications, broadcast radio receivers, and radar communications [6].

Nanowire High Electron Mobility Transistor (GaN-HEMT) are extensively used for a wide variety of material properties high electron saturation velocity, high breakdown electric field, and minimizing the Gate Induced Drain Lowering (GIDL) [7] by the implementation of underlap. Therefore, the effective length of the gate decreases, obviously decreasing the on current (Ion) and degrading the gate controllability of silicon (Si) and Silicon dioxide (SiO₂) as low-k dielectric Nanomaterial and high-k dielectric Nanomaterial in the process of Hafnium oxide (HfO₂) based Nanowire HEMT devices [8, 9].

Nanowire HEMT was invented based on Nanomaterial oxide being Low-k Dielectric Nano and Titanium Dioxide (TiO₂) will work without doping due to its high carrier concentration, resulting in the distribution of non-uniform dopants and reducing the dopant scattering. The self-heating effect is the major concern in GaN-based HEMT due to increases in channel temperature [10, 11]. To reduce the self-heating effect and thermal resistance in the device, continuous efforts are made. But few efforts have been taken to reduce both in the nanodevices. To reduce the self-heating effect and thermal resistance in the device, the GaN-based HEMT is passivated. The Silicon carbide (6H-SiC) establishes a good quality interface with GaN-HEMT to reduce the leakage current in the device [12].

The Organization of the paper is as follows: Design of Undoped 5 nm regime gate Nanowire HEMT, mesh view, Electric field, and potential distribution are discussed in the second section. In the third section, the results of various materials and their performance comparison are discussed. The final section is discussed with conclusion

2. STRUCTURE OF PROPOSED DEVICE

The proposed 5 nm regime gate with an undoped region Nanowire High Electron Mobility Transistor is shown in Figure 1. The U-HEMT is made of high-k hafnium oxide

(HfO₂) material and device dimensions are measured in nanometers using the Silvaco TCAD ATLAS simulator [13]. The new device has an undoped region with HfO₂ compared with the conventional device. The length of metal gate is L_g=0.005 μm and metal gate with a work function of 4.87eV. The length of the device, spacing between gate-source and gate-drain, and length of the undoped high-k dielectric material (HfO₂) region are L_d=0.032μm, L_{gs}=0.015μm, L_{ds}=0.015μm, and L_u=0.08μm, respectively. The undoped region under the gate reduces the electric field in the channel region and increases the drain current significantly [14, 15]. The undoped Nanowire HEMT mesh view is shown in Figure 2, where the grid spacing on both axes is not equal [16]. Electric field distribution and potential distribution of the new structure are shown in Figures 3 and 4. The speed and performance parameters of the device is depending on the gate length [17, 18]. Channel doping increases will increase the drain current. Silvaco ATLAS Simulator is used to simulate the Undoped HEMT under a 5 nanometer gate regime with high-k dielectric material being hafnium oxide (HfO₂) and extracted all electrical parameters [11]. In this proposed structure, Silicon Carbide (6H-SiC) is used as a substrate instead of Silicon (Si) [19].

DC characteristics and RF characteristics of Undoped Nanomaterial oxide HEMT with HfO₂ are analyzed for different material combinations that have been obtained by using the ATLAS simulator, where the length of the gate is 0.005μm [20, 21]. The undoped HEMT device dimensions are shown in Table 1 and Gate length (5nm) is a very important parameter. The High-k dielectric, 5 nm regime gate HEMT used various materials and methods for simulation of the device as shown in Tables 2 and 3.

HfO₂ has a high dielectric constant (typically around 20-25), than traditional gate dielectrics like silicon dioxide (SiO₂). This property enables the formation of a thicker dielectric layer, facilitating better gate control over the channel and reducing gate leakage current. The high-k dielectric nature of HfO₂ allows for a higher gate capacitance per unit area compared to low-k dielectrics. This increased gate capacitance enhances the control of charges in the channel region, resulting in enhanced device performance, reduced threshold voltage variation, and lower leakage current. Mitigation of Short-Channel Effects: Incorporating HfO₂ as a high-k dielectric beneath the gate helps alleviate short-channel effects in HEMTs. These effects, such as threshold voltage roll-off and drain-induced barrier lowering (DIBL), can detrimentally impact device performance. The high-k dielectric layer helps mitigate these effects and improves the scalability of HEMT devices.

The high-k dielectric Hafnium Dioxide (HfO₂) material insertion in the HEMT model presents several advantages over previous works, making it highly

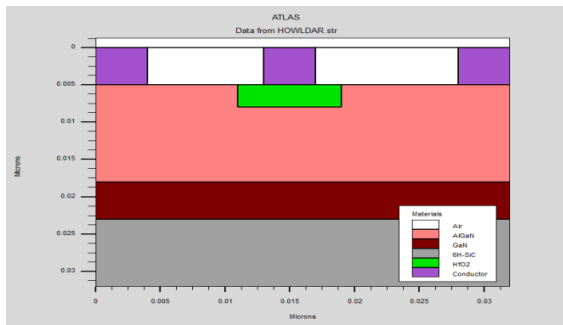


Figure 1. Cross-sectional View of High-k Dielectric AlGaIn/GaN HEMT

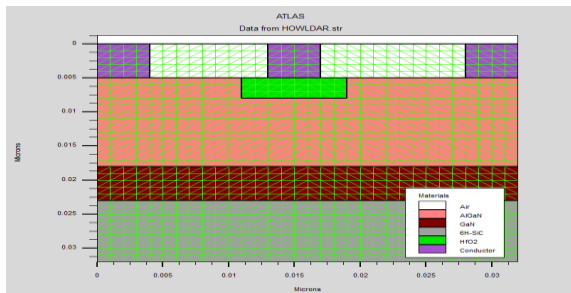


Figure 2. Mesh View of High-k Dielectric AlGaIn/GaN HEMT Structure

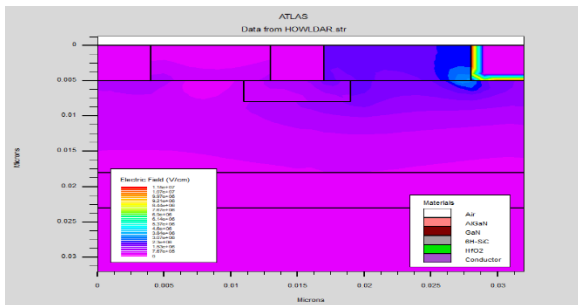


Figure 3. Electric Field Distribution of High-k Dielectric AlGaIn/GaN Device

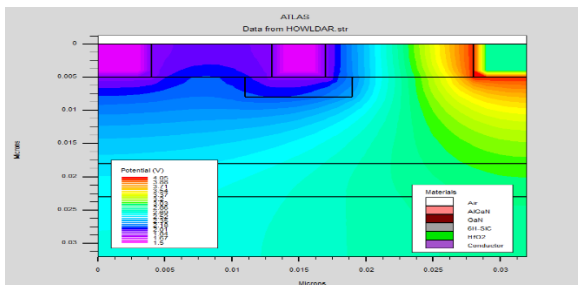


Figure 4. Potential Distribution of high-k dielectric AlGaIn/GaN Device

suitable for real-time applications. HfO₂ material insertion in the proposed HEMT model delivers

improved device performance across key metrics such as higher transconductance, lower gate leakage current, and enhanced linearity. These enhancements translate into superior signal amplification, increased operational efficiency, and overall improved device functionality. Mitigation of Short-channel effects, including threshold voltage roll-off and drain-induced barrier lowering, present challenges in HEMTs. HfO₂ material insertion effectively addresses these issues by reducing channel length dependence and improving device behavior at smaller dimensions. HfO₂ material offers improved gate control and reduced gate leakage current, resulting in lower power consumption compared to previous works.

By integrating Hafnium Dioxide (HfO₂) into the gate structure of AlGaIn HEMTs, a notable improvement in breakdown voltage can be achieved compared to previous dielectric materials. HfO₂ exhibits exceptional thermal stability, making it a highly reliable choice for the gate structure of AlGaIn HEMTs with reduced gate length. The compatibility of HfO₂ with standard semiconductor fabrication processes allows for seamless integration into existing manufacturing techniques. This compatibility greatly simplifies the production and scalability of AlGaIn/GaN HEMTs with HfO₂ gate structures, making it more practical for large-scale

TABLE 1. Utilized Device performance Parameters

Parameter used for device	Value
Device Length	0.032μm
Length of the Gate	0.005μm
Source to Gate space	0.015μm
Gate to drain Space	0.015μm
Length of undoped region	0.008μm
Length of Source	0.004μm
Length of Drain	0.004μm
Doping of Channel(D _c)	1x10 ²⁰ cm ⁻³
Work function =	4.87eV

TABLE 2. Utilized Methods for simulation of Proposed structure

Method Model	Description
Gummel	Used as solution method in subsequent solve statement.
Newton trap	Newton solver for SHJ models and SIS models
maxtrap	Specified by the parameter of the method statement and trap is enabled.
Gummel	Specifies the name of the output file where the structure information will be stored after every iteration

deployment. It brings enhancements in breakdown voltage, improved thermal stability for high-temperature applications, and compatibility with existing fabrication processes.

The proposed model introduces a novel approach to transistor design by combining several unique features, High Electron Mobility Transistors (HEMTs) with a reduced gate length, a Silicon Carbide (SiC) substrate, and Hafnium Oxide (HfO₂) materials beneath the gate. HEMT model incorporates a shorter gate length compared to conventional designs. This reduction enhances device performance by improving current flow control, enabling faster switching speeds, and minimizing signal distortions. In contrast to traditional HEMTs that use standard semiconductor substrates, our model utilizes a Silicon Carbide (SiC) substrate. SiC includes high thermal conductivity, excellent mechanical strength, and a wide bandgap. These properties enable higher breakdown voltage and lower on-state resistance. An essential aspect of our model is the integration of Hafnium Oxide (HfO₂) as a material beneath the gate. HfO₂ is a high-k dielectric material that improves gate control, reduces leakage current, and enhances electrostatics. By incorporating HfO₂ beneath the gate, our model achieves superior device performance, increased reliability, and reduced power consumption

3. RESULTS AND DISCUSSIONS

If the gate voltage (V_G) is less than the V_t i.e threshold voltage, then the device is OFF state, then minority charge carriers are flows from the source [22], obviously subthreshold current. The Gate voltage (V_g) more than the threshold voltage (V_t) is known as ON Current. The drain current (I_d) Vs Drain voltage (V_d) for different material combinations used as shown in Figure 5 [23].

The undoped region with 5nm regime gate high-k dielectric material being hafnium oxide (HfO₂) Nanowire HEMT drains current as shown in Figure 6, where gate length is kept 5 nm and observed that leakage current (I_{off}) is the same [24]. The higher ON current resulted for AlGa_{0.3}N/GaN/SiC than other material combinations [25].

The drain conductance(*g_d*) Vs various drain voltages is shown in Figure 7. The AlGa_{0.3}N/GaN/SiC drain

conductance is improved compared to other material combinations [26, 27].

$$Drain\ Conductance(G_d) = \frac{\delta I_{ds}}{\delta V_{ds}} \tag{1}$$

The high Transconductance is required for the proper gain of the amplifier, and it is set with different gate [28] voltages (V_{gs}) as shown in Figure 8.

$$Transconductance(G_m) = \frac{\delta I_{ds}}{\delta V_{gs}} \tag{2}$$

The simulated on-resistance (Ron) Vs drain voltage (V_d) as shown in Figure 9. As drain conductance

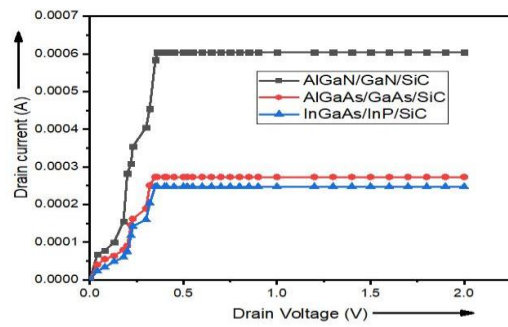


Figure 5. Variation of Drain current Vs Drain voltage for different hetero combination material

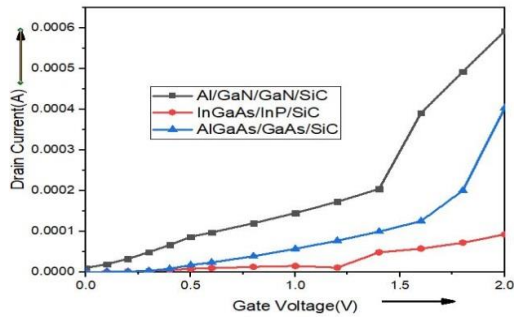


Figure 6. Variation of I_d Vs V_{gs} for different hetero combination materials

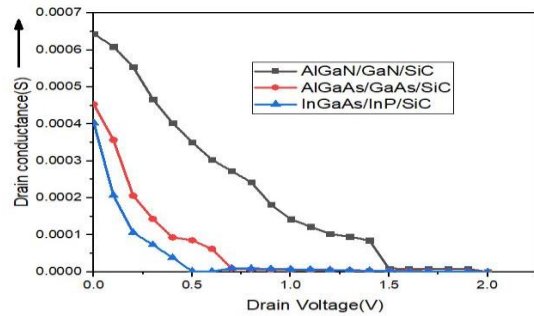


Figure 7. Variation of G_d Vs V_{ds} for different hetero combination materials

TABLE 3. Utilized Models for simulation of Proposed structure

Material Model	Description
conmob	Concentration Dependent
srh	Uses fixed minority carrier lifetimes
Auger	Used as high current densities
fldmob	Parallel Electric Field Dependence

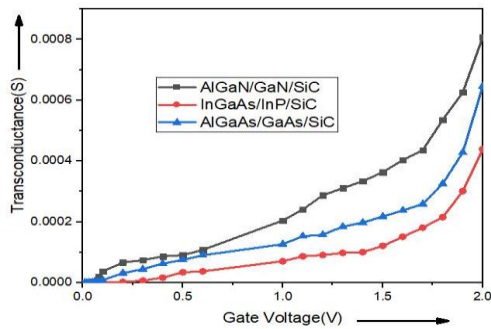


Figure 8. Variation of G_m Vs V_{gs} for different hetro combination materials

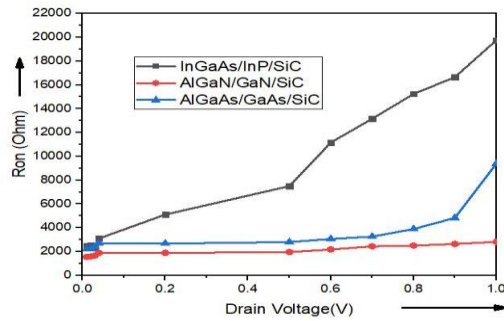


Figure 9. Variation of R_{on} Vs V_{ds} for different hetro combination materials

increases the corresponding on-resistance decreases for various materials [29]. The electric field distribution of the proposed undoped HEMT structure under the 5 nm regime gate with HfO_2 is shown in Figure 10. The undoped HEMT electric field concentration improved compared to conventional devices [30].

The performance parameters of the proposed HEMT as shown in Table 4. From the obtained results it is observed that AlGaIn/GaN/SiC Nanowire HEMT possesses good performance compared with two material HEMT structures.

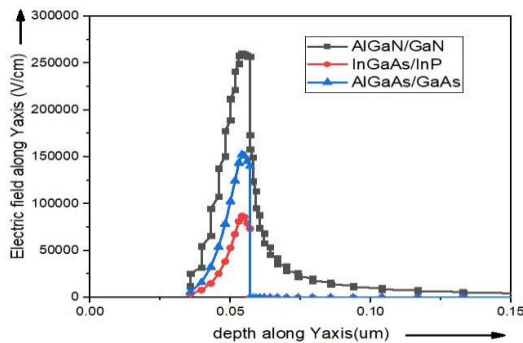


Figure 10. Electric Field Along Y-axis for different hetro combination materials

TABLE 4. Performance metrics for proposed structure

Parameter	AlGaIn/GaN/SiC	AlGaAs/GaAs/SiC	InGaAs/InP/SiC
Ion(A)	5.92E-04	1.70E-04	2.21E-05
Ioff(A)	1.39E-13	2.90E-17	9.27E-12
Ion/Ioff	4.20E+09	5.80E+12	2.30E+06
Gd(S)	6.43E-04	4.53E-04	4.03E-04
Ron(ohms)	1.56E+02	2.20E+02	2.48E+02
Vth(V)	0.2	0.35	0.5
Gm(S)	8.07E-04	6.46E-04	4.38E-04

SiC is a wide-bandgap semiconductor known for its excellent thermal conductivity, high breakdown electric field strength, and ability to operate at high temperatures.

The state of the art in SiC-based HEMTs with AlGaIn/GaN as the channel material showcases several notable features. Firstly, these devices offer impressive power density, enabling them to handle high voltages and currents with minimal power losses. Secondly, their high-frequency operation is excellent, making them suitable for microwave and millimeter-wave frequencies.

SiC substrates provide exceptional thermal conductivity and material properties, allowing HEMTs to operate reliably at high temperatures. Additionally, GaN-on-SiC technology has surpassed GaN-on-silicon (GaN-on-Si) due to SiC's superior thermal management, reduced parasitic effects, and higher breakdown voltage capabilities.

AlGaIn/GaN HEMTs can accommodate higher voltages and currents, enabling greater power density. GaN possesses a broader bandgap than InGaAs and AlGaAs, leading to improved operation at high temperatures and enhanced breakdown voltage characteristics. AlGaIn/GaN HEMTs exhibit remarkable high-frequency characteristics due to the superior electron mobility of the 2D electron gas (2DEG) formed at the AlGaIn/GaN interface. GaN demonstrates superior thermal conductivity in comparison to InGaAs and AlGaAs, facilitating efficient dissipation of heat. This attribute is particularly valuable in high-power applications. AlGaIn/GaN HEMTs exhibit lower parasitic effects, such as reduced gate leakage and drain-source capacitance.

Recent advancements in GaN technology have contributed to a reduction in manufacturing costs associated with AlGaIn/GaN HEMTs.

4. CONCLUSION

The paper presents a design and simulation-based 10nm gate regime advanced High Electron Mobility Transistor (HEMT) with an undoped region under the gate using the

Silvaco TCAD simulator. The undoped region of the new HEMT structure made of high k material as hafnium oxide (HfO₂) material with AlGaN as channel, and silicon carbide (SiC) as the substrate. The GaN material-based advanced HEMT with high k material being hafnium oxide (HfO₂) under the metal gate obtained High Current (Ion), increased Ion/Ioff ratio, high trans conductance, high drain conductance, and low ON resistance, respectively. Therefore, the proposed HEMT device with a high-k dielectric material, Hafnium oxide (HfO₂) under the gate has preferred as the best material for high power and high-frequency applications.

5. REFERENCES

- Liao, B., Zhou, Q., Qin, J. and Wang, H., "Simulation of algan/gan hemts' breakdown voltage enhancement using gate field-plate, source field-plate and drain field plate", *Electronics*, Vol. 8, No. 4, (2019), 406. <https://doi.org/10.3390/electronics8040406>
- Gowthami, Y., Balaji, B. and Srinivasa Rao, K., "Performance analysis and optimization of asymmetric front and back pi gates with dual material in gallium nitride high electron mobility transistor for nano electronics application", *International Journal of Engineering, Transactions A: Basics* Vol. 36, No. 7, (2023), 1269-1277. doi: 10.5829/ije.2023.36.07a.08.
- Wu, Y., Jacob-Mitos, M., Moore, M.L. and Heikman, S., "A 97.8% efficient gan hemt boost converter with 300-w output power at 1 mhz.", *IEEE Electron Device Letters*, Vol. 29, No. 8, (2008), 824-826. <https://doi.org/10.1109/LED.2008.200092>
- Kwak, H.-T., Chang, S.-B., Kim, H.-J., Jang, K.-W., Yoon, H.S., Lee, S.-H., Lim, J.-W. and Kim, H.-S., "Operational improvement of algan/gan high electron mobility transistor by an inner field-plate structure", *Applied Sciences*, Vol. 8, No. 6, (2018), 974. <https://doi.org/10.3390/app8060974>
- Gowthami, Y., Balaji, B. and Rao, K.S., "Design and performance evaluation of 6nm hemt with silicon sapphire substrate", *Silicon*, Vol. 14, No. 17, (2022), 11797-11804. <https://doi.org/10.1007/s12633-022-01900-7>
- Kumar, P.K., Balaji, B. and Rao, K.S., "Performance analysis of sub 10 nm regime source halo symmetric and asymmetric nanowire mosfet with underlap engineering", *Silicon*, Vol. 14, No. 16, (2022), 10423-10436. <https://doi.org/10.1007/s12633-022-01747-y>
- Howldar, S., Balaji, B. and Srinivasa Rao, K., "Design and qualitative analysis of hetero dielectric tunnel field effect transistor device", *International Journal of Engineering, Transactions C: Aspects*, Vol. 36, No. 6, (2023), 1129-1135. doi: 10.5829/ije.2023.36.06c.11.
- Karimi, G. and Shirazi, S., "Ballistic (n, 0) carbon nanotube field effect transistors\iv characteristics: A comparison of n= 3a+ 1 and n= 3a+ 2", *International Journal of Engineering, Transactions A: Basics*, Vol. 30, No. 4, (2017), 516-522. doi: 10.5829/idosi.ije.2017.30.04a.09.
- Dixit, A. and Gupta, N., "A compact model of gate capacitance in ballistic gate-all-around carbon nanotube field effect transistors", *International Journal of Engineering, Transactions A: Basics*, Vol. 34, No. 7, (2021), 1718-1724. doi: 10.5829/IJE.2021.34.07A.16.
- Chakrabarty, R., Roy, S., Pathak, T. and Kumar Mandal, N., "Design of area efficient single bit comparator circuit using quantum dot cellular automata and its digital logic gates realization", *International Journal of Engineering, Transactions C: Aspects*, Vol. 34, No. 12, (2021), 2672-2678. doi: 10.5829/ije.2021.34.12c.13.
- Kobayashi, K., Hatakeyama, S., Yoshida, T., Piedra, D., Palacios, T., Otsuji, T. and Suemitsu, T., "Current collapse suppression in algan/gan hemts by means of slant field plates fabricated by multi-layer sicc", *Solid-state Electronics*, Vol. 101, (2014), 63-69. <https://doi.org/10.1016/j.sse.2014.06.022>
- Roy, A., Mitra, R. and Kundu, A., "Influence of channel thickness on analog and rf performance enhancement of an underlap dg algan/gan based mos-hemt device", in 2019 Devices for Integrated Circuit (DevIC), IEEE. (2019), 186-190.
- Nishitani, T., Yamaguchi, R., Asubar, J., Tokuda, H. and Kuzuhara, M., "Improved on-state breakdown characteristics in algan/gan mos-hemts with a gate field plate", in 2019 Compound Semiconductor Week (CSW), IEEE. (2019), 1-2.
- Mehrabani, A.H., Fattah, A. and Rahimi, E., "Design and simulation of a novel hetero-junction bipolar transistor with gate-controlled current gain", *International Journal of Engineering, Transactions C: Aspects*, Vol. 36, No. 03, (2023), 433. doi: 10.5829/ije.2023.36.03c.01.
- Herrera, F.A., Hirano, Y., Iizuka, T., Miura-Mattausch, M., Kikuchi, H., Navarro, D., Mattausch, H.J. and Ito, A., "Compact modeling for leading-edge thin-layer mosfets with additional applicability in device optimization toward suppressed short-channel effects", in 2019 Electron Devices Technology and Manufacturing Conference (EDTM), IEEE. (2019), 29-31.
- Smith, J.A., Takeuchi, H., Stephenson, R., Chen, Y., Hytha, M., Mears, R.J. and Datta, S., "Experimental investigation of n-channel oxygen-inserted (oi) silicon channel mosfets with high-k/metal gate stack", in 2018 76th Device Research Conference (DRC), IEEE. (2018), 1-2.
- Kumar, S. and Sahoo, G., "A random forest classifier based on genetic algorithm for cardiovascular diseases diagnosis (research note)", *International Journal of Engineering, Transactions B: Applications*, Vol. 30, No. 11, (2017), 1723-1729. doi: 10.5829/ije.2017.30.11b.13.
- Canali, C., Majni, G., Minder, R. and Ottaviani, G., "Electron and hole drift velocity measurements in silicon and their empirical relation to electric field and temperature", *IEEE Transactions on Electron Devices*, Vol. 22, No. 11, (1975), 1045-1047. <https://doi.org/10.1109/T-ED.1975.18267>
- Emami, N. and Kuchaki Rafsanjani, M., "Extreme learning machine based pattern classifiers for symbolic interval data", *International Journal of Engineering, Transactions B: Applications*, Vol. 34, No. 11, (2021), 2545-2556. doi: 10.5829/IJE.2021.34.11B.17
- Huang, H., Liang, Y.C., Samudra, G.S., Chang, T.-F. and Huang, C.-F., "Effects of gate field plates on the surface state related current collapse in algan/gan hemts", *IEEE Transactions on Power Electronics*, Vol. 29, No. 5, (2013), 2164-2173. <https://doi.org/10.1109/TPEL.2013.2288644>
- Mizutani, T., Ohno, Y., Akita, M., Kishimoto, S. and Maezawa, K., "A study on current collapse in algan/gan hemts induced by bias stress", *IEEE Transactions on Electron Devices*, Vol. 50, No. 10, (2003), 2015-2020. <https://doi.org/10.1109/TED.2003.816549>
- Meng, Q., Lin, Q., Jing, W., Han, F., Zhao, M. and Jiang, Z., "Tcad simulation for nonresonant terahertz detector based on double-channel gan/algan high-electron-mobility transistor", *IEEE Transactions on Electron Devices*, Vol. 65, No. 11, (2018), 4807-4813. <https://doi.org/10.1109/TED.2018.2869291>
- Ping, A., Chen, Q., Yang, J., Khan, M.A. and Adesida, I., "Dc and microwave performance of high-current algan/gan heterostructure field effect transistors grown on p-type sic substrates", *IEEE Electron Device Letters*, Vol. 19, No. 2, (1998), 54-56. <https://doi.org/10.1109/55.658603>

24. Kamath, A., Patil, T., Adari, R., Bhattacharya, I., Ganguly, S., Aldhaferi, R.W., Hussain, M.A. and Saha, D., "Double-channel algan/gan high electron mobility transistor with back barriers", *IEEE Electron Device Letters*, Vol. 33, No. 12, (2012), 1690-1692. <https://doi.org/10.1109/LED.2012.2218272>
25. Palacios, T., Chakraborty, A., Heikman, S., Keller, S., DenBaars, S. and Mishra, U., "Algan/gan high electron mobility transistors with ingan back-barriers", *IEEE Electron Device Letters*, Vol. 27, No. 1, (2005), 13-15. <https://doi.org/10.1109/LED.2005.860882>
26. Lee, D.S., Gao, X., Guo, S., Kopp, D., Fay, P. and Palacios, T., "300-ghz inaln/gan hemts with ingan back barrier", *IEEE Electron Device Letters*, Vol. 32, No. 11, (2011), 1525-1527. <https://doi.org/10.1109/LED.2011.2164613>
27. Shinohara, K., Regan, D., Corrión, A., Brown, D., Burnham, S., Willadsen, P., Alvarado-Rodriguez, I., Cunningham, M., Butler, C. and Schmitz, A., "Deeply-scaled self-aligned-gate gan dh-hemts with ultrahigh cutoff frequency", in 2011 International Electron Devices Meeting, IEEE. (2011), 19.11. 11-19.11. 14.
28. Kumar, V., Lu, W., Schwindt, R., Kuliev, A., Simin, G., Yang, J., Khan, M.A. and Adesida, I., "Algan/gan hemts on sic with f t of over 120 ghz", *IEEE Electron Device Letters*, Vol. 23, No. 8, (2002), 455-457. <https://doi.org/10.1109/LED.2002.801303>
29. Shinohara, K., Yamashita, Y., Endoh, A., Hikosaka, K., Matsui, T., Mimura, T. and Hiyamizu, S., "Ultrahigh-speed pseudomorphic ingaas/inalas hemts with 400-ghz cutoff frequency", *IEEE Electron Device Letters*, Vol. 22, No. 11, (2001), 507-509. <https://doi.org/10.1109/55.962645>
30. Fouladinia, F. and Gholami, M., "Decimal to excess-3 and excess-3 to decimal code converters in qca nanotechnology", (2022). <https://doi.org/10.21203/rs.3.rs-2218039/v1>

COPYRIGHTS

©2023 The author(s). This is an open access article distributed under the terms of the Creative Commons Attribution (CC BY 4.0), which permits unrestricted use, distribution, and reproduction in any medium, as long as the original authors and source are cited. No permission is required from the authors or the publishers.

**Persian Abstract**

چکیده

ما یک گیت رژیم 10 نانومتري ترانزیستور تحرک الکترونی بالا (HEMT) را با یک منطقه خنثی (UR) در زیر دروازه با مواد دی الکتريک با k بالا که اکسید هافنیوم (HfO₂) است، طراحی و شبیه سازی کرده ایم. ضخامت دروازه و مناطق undoped برابر است اما طول کانال برابر نیست. ترانزیستور تحرک الکترونی بالا در زیر دی الکتريک گیت، حداکثر میدان الکتريکی (V) را در منطقه کانال کاهش می دهد و جریان تخلیه را به طور قابل توجهی افزایش می دهد. ساختار ترانزیستور تحرک الکترونی بالا دی الکتريک High-K جریان یون اشباع شده 60٪ بالاتر از ساختار معمولی را به دست آورد. برای قدرت بحرانی بالا و فرکانس بالا تقویت کننده های انتقال قدرت با استفاده از AlGaN / GaN / SiC مبتنی بر ترانزیستور تحرک الکترون بالا با یک منطقه undoped زیر دروازه با مواد دی الکتريک بالا K به عنوان اکسید هافنیوم. ترانزیستور پیشرفته تحرک الکترون بالا پیشنهادی جریان تخلیه بالاتر (Id)، ترانسرسانانس بالا 54٪ (Gm) با مقاومت کم (Ron) و هدایت بالا در مقایسه با ترانزیستور تحرک الکترون بالا معمولی تولید می کند. علاوه بر این ویژگی های بهبود یافته، میدان الکتريکی در امتداد جهت Y نیز مشاهده می شود. ساختار پیشنهادی تشکیل شده توسط مواد دی الکتريک کم k در فرایند سیلیکون دی اکسید (SiO₂) و مواد دی الکتريک با کیفیت بالا مانند دی اکسید تیتانیوم (TiO₂) و اکسید هافنیوم (HfO₂) فرصت های بیشتری را در زمینه های الکترونیک قدرت و فرکانس رادیویی VLSI ایجاد کرده است.



Mode Shape Change Based System Identification: An Improvement using Distributed Computing and Roving Technique

B. Patel*, U. K. Dewangan

Department of Civil Engineering, National Institute of Technology, Raipur, India

PAPER INFO

Paper history:

Received 05 June 2023

Received in revised form 04 July 2023

Accepted 09 July 2023

Keywords:

Machine Learning

Automation

Structural Health Monitoring

Distributed Computing Technique

Dynamic Response

Inverse System Identification

ABSTRACT

Structure health monitoring is still a challenging issue despite continuous research efforts since a long time. Modeshape changes are a remarkable symptom of the damaged element location in structural system identification. In this paper, various mode shape based prediction techniques are applied to a common structural model. A cantilever beam model is formulated using the distributed mass and stiffness matrix based finite element modelling. Multiple damages are introduced in the above cantilever beam even with two, three and four member damage combinations. The results does not provide a concrete solution on the damage element location prediction. Further, in the computational part, the distributed computing technique using element-to-element matrix multiplications is applied. The Roving technique is also applied, which acts as a counter for self-automation. The proposed approach provides a better damage element location prediction even for the multiple damaged member combinations. The roving technique means an element scanning technique, which works with a computer clock speed. The novelty of the approach is that the method is simple and it could be applied to other structures. While scanning as automation no element is left out. Another beauty of the method is that no prior damage elements are assumed as many statistical based approaches assumed in prior. This approach could be a better way to the automation process, for the system identification and machine learning tools.

doi: 10.5829/ije.2023.36.09c.10

NOMENCLATURE

m	Number of modes considered
h	Length of the element (mm)
M	Distributed mass matrix (N)
C	Damping coefficient matrix
K	Stiffness matrix (N/mm)
t	Time period (s)
$u(t)$	Structural response matrix in terms of displacement (mm)
$\dot{u}(t)$	Structural response matrix in terms of velocity (mm/s)
$\ddot{u}(t)$	Structural response matrix in terms of acceleration (mm/s ²)

Greek Symbols

ϕ	Modal amplitude of the structural system
$\bar{\phi}$	Modified normalized modal amplitude of the structural system
λ	Square of the frequency (Hz)
$ud_{\bar{\phi}}$	Modal amplitude of the undamage structural system
$dam_{\bar{\phi}}$	Modified normalized modal amplitude of the damage structural system

Subscripts

d	Damage case
i	Natural number to denote mode number
j	Natural number to denote node number
u	Undamage case

1. INTRODUCTION

Mode shapes data are the significant field response data for any vibration based structural system identification [1]. These data are widely used for damage identification, damage location prediction, assessment of its severity, and the estimation of the future life of the structure [2].

Various methods have been proposed based on the mode shape response and its derivatives, such as the modal assurance criterion (MAC), cumulative damage factor method (CDF), mode shape based damage index method (MSDI), coordinate modal assurance criterion (COMAC), mode shape difference method (MSD), machine learning-based approaches, mode shape

*Corresponding Author Institutional Email:

bpatel.phd2018.ce@nitrr.ac.in (B. Patel)

curvature method (MSC), and many more [3-15]. In addition, various other techniques are employed which are not modal parameter based, such as the wave propagation based approach, neural networking, machine learning and frequency response function (FRF) method [16-18]. The aforementioned techniques are limited to predicting and locating the damage. The mode shape based prediction techniques; MAC method and COMAC method are useful for finding the presence of damage [19-21]. The MSD method predicts the damage location and was noticed that, for the higher modes, the difference in modal curvature exhibits several peaks, which could result in a false indication of damage [22]. The mode shape curvature demonstrated that a useful indication of the location of the damage is the variation in the curvature mode between an undamaged and damaged structure [22]. Studies based on bridge assessment have been performed by Jayasundara et al. [23]. The CDF method [9, 24] and the MSDI [25] could identify 2, 3, and 4 number of damaged member combinations, the possibility of a false signal exists in cases of extremely small damage. Additionally, if the damage number is larger, there is a risk of a false alert. The reason behind the multiple member damage element location false output is that most of the algorithm has taken normal/regular matrix multiplications that lead the elements of the matrices to mix when computing the eigenvalue and eigenvector. For small damage, the element could be in order to catch the fine damage. The structural member is discretised to the different number of small finite elements. With an increase in the number of elements, during the formulation, the number of equations also increases hence its prediction will be more complex. For such a case, more research is necessary and it is covered in section 3.3. Machine learning-based approaches, such as neural networks and support vector machines, can also be used for mode shape extraction [26].

Currently, there is no reported literature on mode shape based system identification for multiple damage combinations using Distribute Computation Technique (DCT) and Roving Technique (RT). Hence, the primary goal of this research is to propose a new algorithm DCT and RT, and use it for an improvement in the current algorithm. In this paper, the damage caused by both changes in mass and stiffness as well as only the stiffness change, are considered. Another goal is to provide a common approach to improve the computational part of the existing techniques for mode shape based system identifications. Further, for the single damage case, many research works have been published. In order to identify the structural system with multiple damages, the RT means a scanning location technique which will work with a computer clock speed. The novelty of this paper is that the method is simple and automated and it provides a common algorithm for any mode shape based structural system identification. The method leads to a better way

on automation process for system identification and for future machine learning techniques.

2. THEORETICAL DEVELOPMENT

2. 1. Damage Assessment Methods The damage assessment methods based on the modal amplitude response, are mentioned in this section. Although there are many other methods by various researchers, in this paper the authors have compared the developed method on these indexes hence only the following methods are discussed.

2. 1. 1. Modal Assurance Criterion (MAC) This technique makes use of the baseline data, i.e., the mode shape response of the structure in the initial stage and of the damage condition. This method provides a single response for the whole system. The MAC is given by Equation (1) [19-21].

$$MAC = \frac{\sum_{i=1}^m |\phi_i^T \phi_i^d|^2}{\sum_{i=1}^n |\phi_i \phi_i^T| \sum_{i=1}^m |\phi_i^d \phi_i^{dT}|} \quad (1)$$

2. 1. 2. Coordinate MAC (COMAC) Method This method also makes use of the baseline data, i.e., the mode shape response of the structure in the initial stage and of the damage condition. This method provides response at the individual nodes. The COMAC is given by Equation (2) [21].

$$COMAC = \frac{|\sum_{i=1}^m \phi_{i,j} \phi_{i,j}^d|^2}{\sum_{i=1}^m (\phi_{i,j})^2 \sum_{i=1}^m (\phi_{i,j}^d)^2} \quad (2)$$

2. 1. 3. Mode Shape Difference (MSD) Method This method also makes use of the baseline data, i.e., the mode shape response of the structure in the initial stage and of the damage condition. The absolute modal value of intact and damaged cases for the particular element will be used to determine the MSD value. The MSD is given by Equation (3) [22].

$$MSD = \sum_{i=1}^m |\phi_{i,j}^d - \phi_{i,j}| \quad (3)$$

2. 1. 4. Mode Shape Curvature (MSC) Method This method also makes use of the baseline data, i.e., the curvature of the mode shape of the structure in the initial stage and of the damage condition. The curvature of the mode shape is determined, by taking the second derivative of the mode shape. The damage could be located more precisely by this method. MSC for the structural system is given by Equation (4) [22, 23].

$$MSC = \left| \left(\frac{\phi_{j+1}^d - 2\phi_j^d + \phi_{j-1}^d}{h^2} \right) - \left(\frac{\phi_{j+1} - 2\phi_j + \phi_{j-1}}{h^2} \right) \right| \quad (4)$$

2. 1. 5. Cumulative Damage Factor (CDF) Method

This method also makes use of the baseline data, i.e., the curvature of the mode shape response of the structure in the initial stage and of the damage condition. CDF is the damage indicator whose value depends on the MSC. For any particular node of the structure, say the j^{th} node, this damage indicator value is given by Equation (5) [24, 25].

$$CDF_j = \frac{1}{m} \sum_{i=1}^m (MSC_j^d - MSC_j) \tag{5}$$

2. 1. 6. Mode Shape Damage Index Method (MSDI)

This method also makes use of the baseline data, i.e., the the derivative from the mode shape response of the structure in the initial stage and of the damage condition. This method is based on the comparison of the normalized modal amplitude of damage and the undamaged state of the structural system. The MSDI for a particular node is given by Equation (6) [26].

$$MSDI = \frac{\overline{\phi_i} - \overline{\phi_i^d}}{\overline{\phi_i}} \tag{6}$$

The above indices based methods are applied on a common cantilever beam model for the damage element location detection which is explained in section 3.2.

2. 2. Distributed Computing Technique (DCT)

A DCT is a method to perform computations over numerous matrices for superior results and fault tolerance. This method is based on the application of the vectorize operation for matrix multiplication [27] to modify the computational part, of the system represented by the matrix form. While performing the regular/common matrix multiplication of any two matrices, let's say K and Q , as demonstrated below:

$$K = \begin{bmatrix} a_{11} & a_{12} \\ a_{21} & a_{22} \end{bmatrix}_{2 \times 2} \tag{7}$$

$$Q = \begin{bmatrix} b_{11} & b_{12} \\ b_{21} & b_{22} \end{bmatrix}_{2 \times 2} \tag{8}$$

On regular/common matrix multiplication, the product will come out as:

$$R = K \times Q \tag{9}$$

$$R = \begin{bmatrix} (a_{11} \cdot b_{11}) + (a_{12} \cdot b_{21}) & (a_{11} \cdot b_{12}) + (a_{12} \cdot b_{22}) \\ (a_{21} \cdot b_{11}) + (a_{22} \cdot b_{21}) & (a_{21} \cdot b_{12}) + (a_{22} \cdot b_{22}) \end{bmatrix} \tag{10}$$

Equation (10) illustrates that the matrix output at $R(1,1)$ location represents the mix behaviour $K(1,1).Q(1,1) + K(1,2).Q(2,1)$. Hence, element property is mixed completely in regular/common multiplication. On the

other hand, when doing vectorize operation for matrix multiplication, the product will come out as:

$$S = K * Q = \begin{bmatrix} a_{11} * b_{11} & a_{12} * b_{12} \\ a_{21} * b_{21} & a_{22} * b_{22} \end{bmatrix}_{2 \times 2} \tag{11}$$

Here, $*$ represents the term-by-term matrix multiplication.

By observing the S matrix properties from Equation (11), it can be easily observed that the element property doesn't get mixed, hence the individual element property is not lost. Say, for example if K is a stiffness and Q is the response and if they are connected by a relationship like $K.Q = F$ and if F is a unit matrix. It will not mix the other locations elements property, rather it will be one to one means for the same element location. The benefit is that damage could be located, as the position of the individual element is not lost. For the division of matrix again the same element to element operation are considered in the computation process.

2. 3. Roving Technique (RT)

The RT is, scanning each element one by one for the computation process. This technique is using an automatic counter which is starting from one to the number of elements (e) just like a for-end loop. For example for element_number $i=1$ to e for $i = 1:e$
The algorithm
end

3. METHODOLOGY

3. 1. Finite Element Modelling

A cantilever beam was employed as the beam specimen for the study. The beam considered is 200 mm long, its width is 9 mm and its depth is 50 mm. The Young's modulus (E) for the specimen material is 69.1 N/mm², Poisson's ratio is 0.334 and the density of the specimen material is 2668.32 x 10⁻¹⁰ N/mm³.

The finite element method is used for further analysis. The beam is discretized to 10 elements and the finite element model is shown in Figure 1(a). The two noded beam elements are used for discretization as shown in Figure 1(b). The nodal unknown will be vertical deflection (u_1 at node 1 and u_3 at node 2) and rotation about the z -axis (u_2 at node 1 and u_4 at node 2) at each node. The degree of freedom then is 2 at each node.

For the study, a total of 20 damage cases are taken into account. For this, four locations were selected at random at a distance of 40 mm, 100 mm, 120 mm, and 160 mm. Figure 1(a) illustrates the specifics. These damage positions are represented by D1, D2, D3, and D4, respectively. The width of damage is considered insignificant, and its depth was measured in terms of percentage reductions in depth as 20

%, 30 %, 40 %, and 60 % reductions. The reduction in mass to 40 % and 60 % has also been considered. Figure 1(c) represents the damage considered. Three different damage combination has been presented. Cases 1 to 12 represent the 2 members' damage at a time. Cases 13 to 17 represents the damage scenario for 3 member damages at a time, and Cases 19 and 20 represents for 4 member damage at a time. All these cases are taken as any random combination for the demonstration purpose. Also, the damage in terms of depth reduction only and combined mass and depth reduction is considered. All of these cases are mentioned in Table 1.

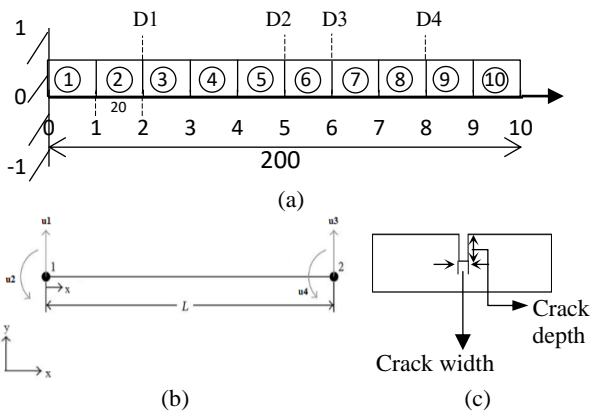


Figure 1. (a) Beam element (b) Vertical section of the crack damage region (c) Finite element model of a cantilever beam with damage positions

TABLE 1. The various damage cases for the cantilever beam

Damage case	Location of damage	Imposed damages	
		Depth reduction (%)	Mass reduction (%)
Case 1	D1, D2	0.2	-
Case 2	D1, D3	0.2	-
Case 3	D1, D4	0.2	-
Case 4	D2, D3	0.2	-
Case 5	D2, D4	0.2	-
Case 6	D3, D4	0.2	-
Case 7	D1, D2	0.4	0.4
Case 8	D1, D3	0.4	0.4
Case 9	D1, D4	0.4	0.4
Case 10	D2, D3	0.4	0.4
Case 11	D2, D4	0.4	0.4
Case 12	D3, D4	0.4	0.4
Case 13	D1, D2, D3	0.3	-
Case 14	D1, D2, D4	0.3	-
Case 15	D1, D3, D4	0.3	-

Case 16	D1, D2, D3	0.4	0.4
Case 17	D1, D2, D4	0.4	0.4
Case 18	D1, D3, D4	0.4	0.4
Case 19	D1, D2, D3, D4	0.2	-
Case 20	D1, D2, D3, D4	0.6	0.6

3. 2. Mode Shape based Prediction Techniques

Since the mode shape based methods taken into consideration for the study are baseline based methods, it is necessary to estimate the modal response for both the initial condition and after damage. These responses are determined using MATLAB programming. Additionally, the damage detection and localization indicators for the various methods has been determined using these responses, for the damage case 20 i.e. four members damages at a time considering damages in terms of both the depth and mass reduction.

Initially, various mode shape based prediction techniques mentioned in section 2.1, are applied to a common structural model a cantilever beam, for the different multiple damage combinations. It has been observed from Table 2 that the results do not provide a concrete solution for the identified damage element location prediction. The MAC method and COMAC method are useful for finding the presence of damage only. The methods such as MSD, MSC, CDF and MSDI could identify 2, 3, and 4 damages simultaneously. The possibility of a false signal exists in cases of extremely small damage. Additionally, if the damage number is larger, there is a risk of a false alert. Table 2 makes it clear that the identified damage location and the actual damage location are not precisely the same. The reason behind this is as follows:

- a) In the above the normal/regular matrix multiplication rules are followed which leads the elements of the matrices in which the element properties of different elements get mixed while computing the eigenvalue and eigenvector. As a result, it gives the mixing of different properties of elements at the damage position as per Equation (10).

TABLE 2. Mode shape based prediction techniques

S. No.	Methods	Actual damage location (mm)	Identified damage location (mm)
1.	MAC	40, 100, 120, 160	-
2.	COMAC	40, 100, 120, 160	-
3.	MSD	40, 100, 120, 160	32, 105, 129, 152
4.	MSC	40, 100, 120, 160	39, 101, 122, 161
5.	CDF	40, 100, 120, 160	38, 103, 121, 162
6.	MSDI	40, 100, 120, 160	39, 101, 122, 161

b) For the very small damage prediction, the number of elements could be increased theoretically for computation.

Therefore, more research is necessary, which has been covered in Section 3.3.

3. 3. An Improvement using the Distribute Computing and Roving Technique In the following section, all the matrix operation follows the distributed computing as per Equation (12). In structural dynamics, for the linear structural system, the general form of the equation of motion is given by Equation (12):

$$M\ddot{u}(t) + C\dot{u}(t) + Ku(t) = 0 \tag{12}$$

Equations (13) represents the stiffness matrix for damage localization as the difference between the stiffness matrix of the undamaged structure and the damaged structure, and Equation (14) represents the mass matrix for damage localization as the difference between the mass matrix of the undamaged structure and the damaged structure.

$$\bar{K} = K_u - K_d \tag{13}$$

$$\bar{M} = M_u - M_d \tag{14}$$

The global matrix of the system is used to determine the element location for inverse problems. In a way similar to the method by which the global stiffness matrix is created, the global mass matrix is also created, using a distributed type of mass matrix rather than a lumped method. Further, the solution to the problem for Equation (12) is reduced to the solution to Equation (15) for the multiple degrees of freedom system.

$$(\bar{K} - \lambda_{(i,i)} \bar{M}) \bar{\phi} = 0 \tag{15}$$

For the cantilever beam, the lumped mass matrix is used for global matrix formulation. The stiffness matrix for damaged and undamaged elements is given below:

$$k_{ui} = \begin{bmatrix} 987000 & 9870000 & -987000 & 9870000 \\ 9870000 & 131600000 & -9870000 & 65800000 \\ -987000 & -9870000 & 987000 & -9870000 \\ 9870000 & 65800000 & -9870000 & 131600000 \end{bmatrix}$$

where, i= element numbers 1, 2, 4, 5, 8 and 10 are for undamaged elements

$$k_{dj} = \begin{bmatrix} 123375 & 1233750 & -123375 & 1233750 \\ 1233750 & 16450000 & -1233750 & 8225000 \\ -123375 & -1233750 & 123375 & -1233750 \\ 1233750 & 8225000 & -1233750 & 16450000 \end{bmatrix}$$

where, j=element numbers 3, 6, 7 and 9 are for the damaged elements.

From the above element matrices, it has been observed that, when a structure is damaged, the stiffness value of the damaged element changes. Hence, after assembling the stiffness matrix, the value of the

particular element in the global stiffness matrices changes; all other values remain unchanged. The regular matrix multiplication leads the elements of the matrices to mix when computing the eigenvalue and eigenvector. As a result, the damaged element's position is lost. The DCT mentioned in subsection 2.2 is applied for calculating $\lambda_{(i,i)}$ and $\bar{\phi}$ to ensure that the position of the specific element is not lost and the damage could be located. The modal amplitude value $\bar{\phi}_i$ is used for each of the mode shape based prediction techniques addressed in subsection 2.1.

The RT is done by scanning each element one by one. Basically, the technique is using an automatic counter which is starting from one to the number of elements (e) just like a for-end loop. The RT for the MAC method is given below:

```
for i = 1: m
    y1 = square(mode(ud_φ'(i) * (dam_φ(i)))
    y3 = mode(dam_φ(i) * (dam_φ'(i)))
end
```

```
for i = 1: n
    y2 = mode(ud_φ(i) * (dam_φ'(i)))
end
```

$$MAC = y1/(y2 * y3)$$

The MATLAB code for the RT of MAC method is given above. The Similar procedure has been followed for all the mode shape based prediction techniques addressed in subsection 2.1.

4. RESULTS

The system identification predictions based on mode shape changes have been improved for better damage location prediction. The algorithm applies DCT and RT. It has been observed that the damage existence and location predicted for the particular element could be visualized in Figures 2 to 7. A total of 20 damage cases are considered in this paper; the authors have shown the developed method for Case 20 in the following section.

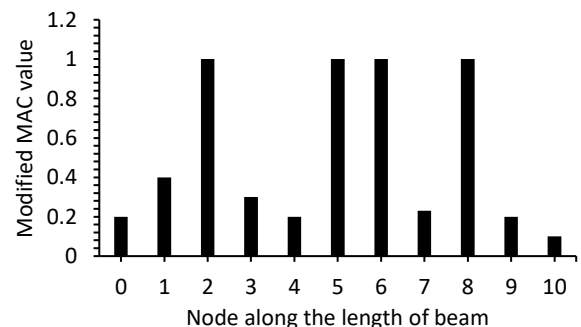


Figure 2. Plot for modified MAC value, for 4 elements damage

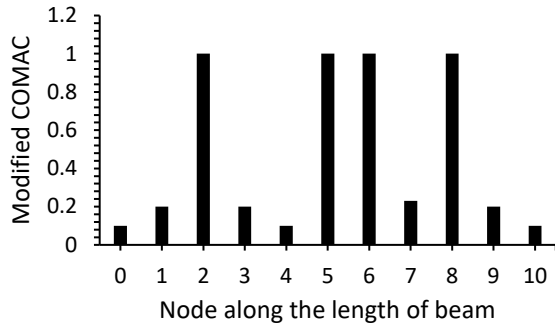


Figure 3. Plot for modified COMAC value, for 4 elements damage

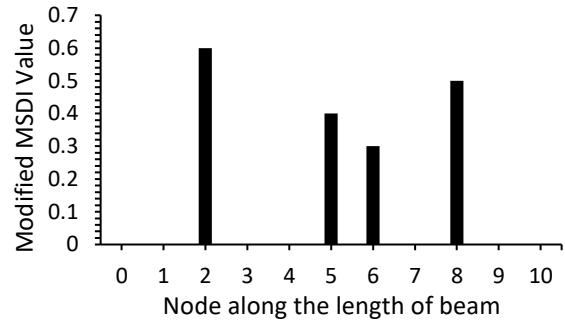


Figure 7. Plot for modified MSDI value, for 4 elements damage

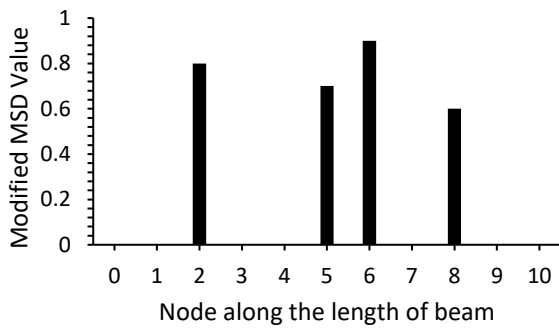


Figure 4. Plot for modified MSD value, for 4 elements damage

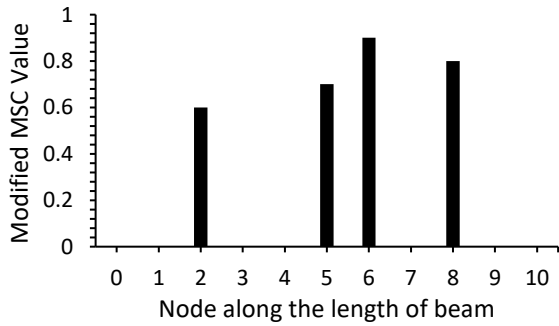


Figure 5. Plot for modified MSC value, for 4 elements damage

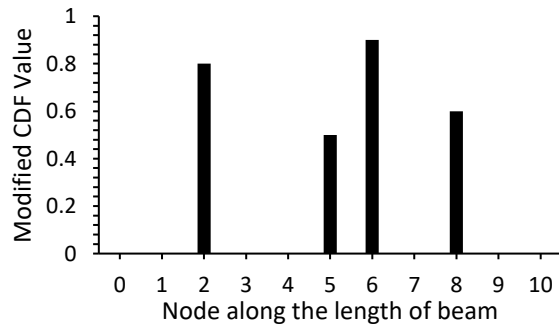


Figure 6. Plot for modified CDF value, for 4 elements damage

With a significant change in the numerical value, the approach identifies a system with multiple damages, as well as it is very clear from Table 3 also. The results conclude that the modified method practice predicts better damage element locations even for the multiple damaged member combinations.

TABLE 3. Multiple damage location identification by modified algorithms, for Damage Case 20

S. No.	Method	Multiple Damage location (For damage case 20)	
		Actual damage location (mm)	Identified damage location (mm)
1.	Modified MAC method	40	40
		100	100
		120	120
2.	Modified COMAC method	160	160
		40	40
		100	100
3.	Modified MSD method	120	120
		160	160
		40	40
4.	Modified MSC method	100	100
		120	120
		160	160
5.	Modified CDF method	40	40
		100	100
		120	120
6.	Modified MSDI	160	160
		100	100
		120	120

5. CONCLUSION

In this study, the mode shape change based system identification predictions improvement is performed for the better prediction of damage location using the mode shape data. The improvement has been done, using the DCT and the RT.

1. When a structure is damaged, the value of the mass and stiffness matrices of that particular element in the global matrix changes at that location while all the other elements' parameter remains unchanged. In the case of normal/regular matrix multiplication, the matrix properties at the element location damaged/non-damaged elements get mixed during the eigenvalue and eigenvector computation, as a result, the damaged element's position is lost.
2. Hence, the DCT is performed while computing the eigenvalue and eigenvector which is incorporated to the existing algorithms. The benefit of doing so is that damage could be located, as the position of the individual element is not lost.
3. The implementation of DTC and RT is capable of small damages cases also.
4. An improvement using the DCT and RT shows the better for finding locations even for the multiple members' damage combinations which are taken as the random combination.

In the age of the forthcoming computer era, the RT means a scanning location technique which will work with a computer clock speed. Hence it will be a better solution for the automation process, of the machine learning technique. This paper will provide a landmark submission for an unknown element

6. REFERENCES

1. Patel, B. and Dewangan, U., "A baseline free method for multiple damage identification and localization using the roving mode shape response", *International Journal of Engineering, Transactions B: Applications*, Vol. 36, No. 5, (2023), 946-954. doi: 10.5829/IJE.2023.36.05B.11.
2. Fan, W. and Qiao, P., "Vibration-based damage identification methods: A review and comparative study", *Structural Health Monitoring*, Vol. 10, No. 1, (2011), 83-111. doi: 10.1177/1475921710365419.
3. Beskhyroun, S., Wegner, L.D. and Sparling, B.F., "New methodology for the application of vibration-based damage detection techniques", *Structural Control and Health Monitoring*, Vol. 19, No. 8, (2012), 632-649. doi: 10.1002/stc.456.
4. Xu, Y. and Zhu, W., "Non-model-based damage identification of plates using measured mode shapes", *Structural Health Monitoring*, Vol. 16, No. 1, (2017), 3-23. doi: 10.1177/1475921716655974.
5. Pandey, A. and Biswas, M., "Experimental verification of flexibility difference method for locating damage in structures", *Journal of Sound and Vibration*, Vol. 184, No. 2, (1995), 311-328. doi: 10.1006/jsvi.1995.0319.
6. Shi, Z., Law, S. and Zhang, L.M., "Structural damage detection from modal strain energy change", *Journal of Engineering Mechanics*, Vol. 126, No. 12, (2000), 1216-1223. doi: 10.1006/jsvi.1998.1878.
7. Pandey, A., Biswas, M. and Samman, M., "Damage detection from changes in curvature mode shapes", *Journal of Sound and Vibration*, Vol. 145, No. 2, (1991), 321-332. doi: 10.1016/0022-460X(91)90595-B.
8. Huang, T., Chaves-Vargas, M., Yang, J. and Schröder, K.-U., "A baseline-free structural damage indicator based on node displacement of structural mode shapes", *Journal of Sound and Vibration*, Vol. 433, (2018), 366-384. doi: 10.1016/j.jsv.2018.07.001.
9. Yazdanpanah1a, O. and Seyedpoor, S., "A new damage detection indicator for beams based on mode shape data", *Structural Engineering and Mechanics*, Vol. 53, No. 4, (2015), 725-744. doi: 10.12989/sem.2015.53.4.725.
10. Ratcliffe, C.P., "Damage detection using a modified laplacian operator on mode shape data", *Journal of Sound and Vibration*, Vol. 204, No. 3, (1997), 505-517. doi: 10.1006/jsvi.1997.0961
11. Shi, Z., Law, S. and Zhang, L., "Damage localization by directly using incomplete mode shapes", *Journal of Engineering Mechanics*, Vol. 126, No. 6, (2000), 656-660. doi: 10.1061/(ASCE)0733-9399(2000)126:6(656).
12. Nahvi, H. and Jabbari, M., "Crack detection in beams using experimental modal data and finite element model", *International Journal of Mechanical Sciences*, Vol. 47, No. 10, (2005), 1477-1497. doi: 10.1016/j.ijmecsci.2005.06.008.
13. Prashant, S.W., Chougule, V. and Mitra, A.C., "Investigation on modal parameters of rectangular cantilever beam using experimental modal analysis", *Materials Today: Proceedings*, Vol. 2, No. 4-5, (2015), 2121-2130. doi: 10.1016/j.matpr.2015.07.214.
14. The-Hung Duong, "On the use of mode shape curvature for multi-crack detection in beam like structures", *International Journal of Civil Engineering and Technology*, Vol. 10, No. 6, (2019), 54-65. doi: 10.34218/IJCET.10.6.2019.006.
15. Roy, K., "Structural damage identification using mode shape slope and curvature", *Journal of Engineering Mechanics*, Vol. 143, No. 9, (2017), 04017110. doi: 10.1061/(ASCE)EM.1943-7889.0001305.
16. Patel, B. and Dewangan, U., "The behaviour of wave propagation for structural system identification: A comparative study", *International Journal of Engineering, Transactions C: Aspects*, Vol. 35, No. 12, (2022), 2305-2312. doi: 10.5829/ije.2022.35.12c.05.
17. Patel, B. and Dewangan, U., "Damage detection techniques to identify the unknown damage parameters from the structural response data in beam: A review", *Recent Trends in Civil Engineering: Select Proceedings of ICRTICE 2019*, (2021), 175-183. doi: 10.1007/978-981-15-5195-6_13.
18. Siow, P.Y., Ong, Z.C., Khoo, S.Y. and Lim, K.-S., "Damage sensitive pca-frf feature in unsupervised machine learning for damage detection of plate-like structures", *International Journal of Structural Stability and Dynamics*, Vol. 21, No. 02, (2021), 2150028. doi: 10.1142/S0219455421500280.
19. West, W.M., "Illustration of the use of modal assurance criterion to detect structural changes in an orbiter test specimen", (1986).
20. Allemang, R.J., "The modal assurance criterion—twenty years of use and abuse", *Sound and Vibration*, Vol. 37, No. 8, (2003), 14-23. doi.
21. Pastor, M., Binda, M. and Harčarik, T., "Modal assurance criterion", *Procedia Engineering*, Vol. 48, (2012), 543-548. doi: 10.1016/j.proeng.2012.09.551.

22. Wahab, M.A. and De Roeck, G., "Damage detection in bridges using modal curvatures: Application to a real damage scenario", *Journal of Sound and Vibration*, Vol. 226, No. 2, (1999), 217-235. doi: 10.1006/jsvi.1999.2295.
23. Jayasundara, N., Thambiratnam, D., Chan, T. and Nguyen, A., "Vibration-based dual-criteria approach for damage detection in arch bridges", *Structural Health Monitoring*, Vol. 18, No. 5-6, (2019), 2004-2019. doi: 10.1177/1475921718810011
24. Shah, A., Jayprakash, V. and Vesmawala, G., "A comparative study on vibration-based damage identification and localization methods", in IOP Conference Series: Materials Science and Engineering, IOP Publishing. Vol. 1004, (2020), 012005.
25. Duvnjak, I., Damjanović, D., Bartolac, M. and Skender, A., "Mode shape-based damage detection method (msdi): Experimental validation", *Applied Sciences*, Vol. 11, No. 10, (2021), 4589. doi: 10.3390/app11104589.
26. Hsieh, Y.-A. and Tsai, Y.J., "Machine learning for crack detection: Review and model performance comparison", *Journal of Computing in Civil Engineering*, Vol. 34, No. 5, (2020), 04020038. doi: 10.1061/(ASCE)CP.1943-5487.0000918
27. Maxfield, B., *Essential mathcad for engineering, science and math*. 2009, Elsevier, London, UK. Reproduced with permission of the copyright owner.

COPYRIGHTS

©2023 The author(s). This is an open access article distributed under the terms of the Creative Commons Attribution (CC BY 4.0), which permits unrestricted use, distribution, and reproduction in any medium, as long as the original authors and source are cited. No permission is required from the authors or the publishers.

**Persian Abstract****چکیده**

نظارت بر سلامت ساختار هنوز یک موضوع چالش برانگیز است، علیرغم تلاش‌های تحقیقاتی مستمر از زمان طولانی. تغییرات حالت یک علامت قابل توجه از محل عنصر آسیب دیده در شناسایی سیستم ساختاری است. در این مقاله، تکنیک‌های مختلف پیش‌بینی شکل مبتنی بر حالت برای یک مدل ساختاری رایج اعمال می‌شود. یک مدل تیر کنسول با استفاده از مدل‌سازی المان محدود مبتنی بر ماتریس جرم و سختی توزیع شده فرموله می‌شود. صدمات متعدد در تیرهای کنسول فوق حتی با ترکیبات آسیب دو، سه و چهار عضو وارد می‌شود. نتایج یک راه حل مشخص در مورد پیش‌بینی مکان عنصر آسیب‌دیده ارائه نمی‌دهد. علاوه بر این، در بخش محاسباتی، تکنیک محاسبات توزیع شده با استفاده از ضرب ماتریس عنصر به عنصر اعمال می‌شود. تکنیک **Roving** نیز به کار می‌رود که به عنوان یک شمارنده برای خودکارسازی خود عمل می‌کند. رویکرد پیشنهادی پیش‌بینی مکان عنصر آسیب‌بتری را حتی برای ترکیب‌های چند عضو آسیب‌دیده فراهم می‌کند. تکنیک رووینگ به معنای تکنیک اسکن المان است که با سرعت ساعت کامپیوتری کار می‌کند. نکته جدید این روش این است که روش ساده است و می‌توان آن را برای ساختارهای دیگر اعمال کرد. در حین اسکن به عنوان اتوماسیون هیچ عنصری از قلم نیفتاده است. یکی دیگر از زیبایی‌های روش این است که هیچ عنصر آسیب‌دیده قبلی در نظر گرفته نمی‌شود، همانطور که بسیاری از رویکردهای مبتنی بر آمار در گذشته فرض شده بودند. این رویکرد می‌تواند راه بهتری برای فرآیند اتوماسیون، برای شناسایی سیستم و ابزارهای یادگیری ماشین باشد.



Design of a Printed Circuit Board for Real-time Monitoring and Control of Pipeline's Cathodic Protection System via IoT and a Cloud Platform

I. E. K. Mekki^{*a,b}, A. Kessar^a, R. Mouaz^a

^a Institute of maintenance and Industrial Safety, University of Oran 2 Mohamed Ben Ahmed, B.P 170, El M'Naouer, Oran, Algeria

^b Laboratoire d'Ingénierie en Sécurité Industrielle et Développement Durable (LISIDD), University of Oran 2 Mohamed Ben Ahmed, Algeria

PAPER INFO

Paper history:

Received 04 May 2023

Received in revised form 29 June 2023

Accepted 30 June 2023

Keywords:

Remote Monitoring

Pipeline Corrosion

Maintenance

Internet of Things

Printed Circuit Board

ABSTRACT

The integration of Internet of Things (IoT) and cloud-based cathodic protection (CP) systems is an innovative approach that can lead to improve pipeline protection from corrosion. Using a printed circuit board (PCB) to measure and control current and voltage makes it possible to monitor PC systems in real time. The web interface that is connected to the PCB circuit through IoT technology provides a platform for instant evaluation of the data obtained, thereby enabling early detection of potential problems. One of the key benefits of real-time monitoring is improved data management and security. The data obtained can be stored on a cloud server, making it easier to access and analyze. This eliminates the need for manual inspections, which can be time-consuming and error-prone. Additionally, real-time monitoring can reduce downtime, as problems can be detected and resolved quickly, preventing the need for lengthy manual inspections and maintenance. This innovative approach has tremendous potential for the future of pipeline protection and corrosion control. The developed PCB circuit features a mobile UART that provides program protection, and the interface can control multiple PCB cards and relays independently. The monitoring system can be updated without interrupting data acquisition. The use of open-source software, database hosting, and low-cost PCB development facilitates commercialization. This study could inspire new applications in asset management and monitoring.

doi: 10.5829/ije.2023.36.09c.11

1. INTRODUCTION

Pipelines are critical infrastructure that plays a vital role in the movement of energy and other essential products. They are durable and can withstand a variety of environmental conditions, but require regular maintenance and inspections to ensure their reliability and safety [1]. Corrosion is a natural process that occurs when metals react with the harsh environment, causing material loss and structural changes in the metal [2].

Corrosion is one of the biggest challenges facing pipelines because it weakens the pipeline material over time. To prevent corrosion, pipeline operators use coatings and protective materials, as well as CP systems that use electrical currents to prevent corrosion [3].

Another challenge is the potential for property damage to pipelines by external factors such as construction, natural disasters and human activities. To mitigate this risk, pipeline operators use a variety of measures, including the use of aerial and ground surveys, regular monitoring of construction activities in the vicinity of pipelines. In the oil industry, pipelines are often subjected to harsh conditions, including exposure to corrosive liquids and gases, high temperatures, and pressures. These conditions can increase the risk of corrosion and make it more challenging to protect the pipeline from corrosion. CP is often regarded as the most effective way of avoiding pipeline corrosion [1].

Corrosion properties of materials can significantly affect the durability and reliability of oil and gas systems,

*Corresponding Author Email: ibrahim_kmekki@yahoo.fr
(I. E. K. Mekki)

which can result in additional costs for companies to control corrosion [4].

Cloud computing and IoT are often combined to enhance modern technological applications. Cloud computing offers internet-based access to computer resources that are flexible, reliable, and decentralized, while IoT is a system of internet-connected devices that gather and send data. When these two technologies are utilized together, it is known as Cloud-IoT [5]. In this integration, the Cloud supplies the essential framework for storing, handling, and organizing IoT data, whereas IoT provides the devices and data.

Advanced communication and internet technologies, such as IoT [6], Cloud [7], Artificial Intelligence (AI) [8], and high-speed internet, are being utilized in various fields such as the development of autonomous trains [9], rail transportation [10], in construction [11], smart energy [12] and smart grid [13], healthcare [14], smart water [15], surveillance [16] and smart cities [17]. In these applications, smart sensors are used to monitor, identify possible problems, anticipate incidents, and improve safety while using less energy.

This collection [18-23] includes articles on gas detection, management of air or water quality using sensors, and machine learning. These articles cover equipment configuration, sensor use, decision support systems, intelligent management of air/water quality and a dashboard for the water distribution network and provide real-time data.

The following papers, discussed in the literature, explore various emerging techniques and technologies for monitoring and control of CP systems in underground pipelines. These include the implementation of wireless sensors networks (WSN) [24], Cloud-based systems and real-time data analysis. These approaches involve the utilization of different processing units, PCBs, communication networks, and protocols. The integration of these solutions into databases and platforms.

Kodali and Soratkal [25] utilized message queuing telemetry transport (MQTT) in a prototype designed for remote monitoring and control using Wi-Fi. They established connections between sensors and actuators with ESP8266, leveraging a Cloud platform for data analysis and visualization. The system also integrated a customized graphical interface to improve user interaction. Mononen and Mattila [26] have proposed an affordable open-source supervisory control and data acquisition (SCADA) system that utilizes a microprocessor to process data and transmit it to the Cloud through the user datagram protocol (UDP) and an ethernet frame. Medrano et al. [27] developed an affordable SCADA system using IoT technology. The system connects field devices to remote terminal units using the transmission control protocol (TCP), internet protocol (IP) and is based on a NoSQL database. Kara et al. [28] propose the design and construction of linear wireless sensor networks (LWSN) for use in monitoring

CP in exceedingly difficult areas. Li and Wang [29] developed a terminal device with an S3C2440A microprocessor and various sensors for parameter monitoring. It ensures secure remote data transmission and storage in the Cloud using a 4G DTU communication module and the TCP protocol.

A hybrid architecture was proposed by Singh et al. [30] to monitor oil pipelines by combining 2.4 GHz-based ZigBee, LoRa and Wi-Fi communications to overcome the problems of using one of these two architectures alone. Aba et al. [31] combined an Arduino and a Wi-Fi module, programmed and used them to produce a wireless communication device that communicates with the ThingSpeak IoT analytics platform. As mentioned by Puviarasi et al. [32], it is possible to ensure appropriate pressure in the pipelines through continuous monitoring via the ThingSpeak Cloud network. In the event of abnormal sensor readings, a GSM900A module connected to the Raspberry Pi sends an alert SMS to the workers. According to Priyanka et al. [33], the utilization of Wi-Fi IoT modules enables wireless interaction with Cloud servers through MQTT protocol and hypertext transfer protocol (HTTP). Additionally, the web Monitor platform facilitates real-time data analysis and control, enhancing the optimization of oil pipeline transportation management. Chavala et al. [34] proposed an architecture to monitor the management metrics of oil pipelines through the utilization of IoT and LoRa WAN network. They performed simulations using the OPNET simulator to assess the effectiveness of the suggested technology. Yas and Al Qassab [35] developed a monitoring system using an Arduino Mega microcontroller and the ESP-01 module, with real-time monitoring on the Blynk IoT platform.

Li et al. [36] have created a distributed mixed reality and IoT system for operating and maintaining an underground pipeline network. Overall, these papers highlight the potential of IoT technology in improving the efficiency and reliability of CP systems for underground pipelines, along with the requirement to persist in exploring and advancing in this field. The authors have proposed different frameworks and systems for monitor and control CP in a diverse manner.

The use 4G DTU communication, Wi-Fi, ZigBee and LoRa modules to communicate between devices. They integrate TCP/IP, MQTT, HTTP, UDP, and Ethernet frame to handle data processing and transmission to the Cloud platform. Additionally, they investigate various platforms such as the BLYNK IoT platform, the ThingSpeak IoT analytics platform, and connectivity options through the ThingSpeak Cloud network and LoRa WAN network, among others to communicate between devices and the Cloud networks. Furthermore, the research explores the choice of database, considering both MySQL, a relational database management system, and NoSQL options.

Our research introduces a cost-effective solution that effectively addresses the limitations encountered in commercial systems through the utilization of open-source hardware and software technologies.

Several references have explored the use of PCB in previous works [28-31, 33]. It is important to mention that our contribution is unique in the following aspects, which sets it apart from other works:

-In the design of our PCB, we have chosen a different hardware configuration than what is commonly used. Instead of combining an Arduino Nano V3 microcontroller and the Wi-Fi module (BOLT IoT) [33], we have opted to use a single component, the Wi-Fi ESP_12E module, which offers integrated Wi-Fi capabilities better suited for IoT applications.

-To enhance the hardware security of program access, we did not use the ESP8266-based NodeMCU development board as stated by Kodali and Soratkal [25], but rather an ESP_12E.

However, it should be noted that the ESP_12E does not have a direct method for power supply and program transfer. Additional circuits are required to provide a voltage of 3.3 V to power our microcontroller. The program transfer is done using a USB to UART TTL serial adapter. Once the transfer is complete, the adapter is disconnected and removed, ensuring a secure connection.

-The processing power of the Arduino Nano (ATmega328) is set at 16 MHz, which is suitable for general tasks, whereas the ESP-12E (ESP8266) operates at a higher frequency range of 80-160 MHz, thus providing enhanced processing capacity.

-To ensure connectivity, we established a wireless connection to the Cloud server using Wi-Fi.

-Furthermore, data is efficiently transmitted through the utilization of the HTTP protocol. We opted to store the database using MySQL. It is worth mentioning that we did not utilize any IoT platforms such as BLYNK IoT [35] platform or ThingSpeak IoT [31] in our work.

The goal of the proposed PCB is to provide a more affordable and reliable solution for monitoring and managing pipelines using open source based IoT technology. Additionally, there were no costs incurred in implementing the IoT technology and maintaining the Cloud server. We have implemented the hardware and software sections ourselves, from scratch; we made it without using any prepared tools or software. There are challenges related to security and connectivity due to the limitations in coverage, the requirement to operate with both 12V/5V DC voltages. To address the limitation of having only one analog input on the ESP_12, there is a need to develop multiple analog inputs capable of acquiring both voltage and current analog values.

Several sections make up the paper's structure. Section 2 discusses the strategies for protecting pipes against corrosion. The limitations of traditional pipeline monitoring methods are examined in section 3. hardware

and software solutions to monitoring and control are detailed in section 4 along with a novel real-time monitoring system that makes use of Cloud networks. Section 5 presents the results of tests conducted to evaluate the effectiveness of the monitoring and control systems, as well as their respective methodologies. Finally, section 6 provides a conclusion based on the findings presented in the previous sections.

2. CATHODIC PROTECTION (CP)

CP is a technique that prevents metal corrosion by making the metal surface the cathode in an electrochemical cell. To do this, direct current is applied to the metal and connected to a more easily corroded metal (anode) that provides electrons. The flow of electrons from the anode to the cathode neutralizes the corrosion process and protects the metal. This method is often used to protect metal structures in contact with water, such as ships, pipelines, and offshore oil platforms. The two CP methods that can be used are: Sacrificial anode: involves using a metal with higher susceptibility to corrosion as the anode, physically connected to the metal to be protected.

Impressed current: involves an electrical current impressed onto the metal and a separate anode supplying electrons. and that's what we are going to use in our system.

3. THE LIMITS OF TRADITIONAL CP MONITORING

Traditional CP involves the need to regularly move technicians to take potential readings along pipelines using a multimeter. The measurements are recorded on checklists and sent to an engineer for analysis, processing and interpretation. However, this method can no longer be considered effective as the actions and information returned are not performed in real time, which does not allow for constant and effective monitoring. Consequently, it is necessary to upgrade this method of monitoring CP. Figure 1 shows the classic supervision.

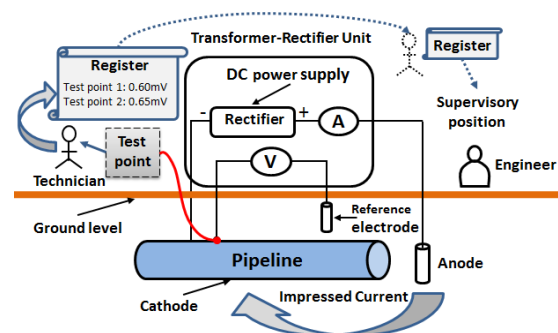


Figure 1. Classic supervision

4. A PROPOSED REAL-TIME MONITORING SOLUTION FOR CP

As a solution, an automatic monitoring system was proposed that eliminates the technician actor and the register as shown in Figure 2.

The system is made up of two major components:

The transmitter is installed at each measuring point and functions as a voltmeter, sending the measured values to the supervisory station in real time.

The receiver, which is installed at the supervisory station, and can be software or a web application, receives the data and performs a variety of operations such as displaying potential values, plotting curves against time, storing all values in a database [37], and automatically notifying in the event of a danger. It will be able to control the biocide injection pump remotely.

4. 1. The CP System With Cloud Networks Topology

We have proposed the Cloud networks as topology on this system according to the importance of the factors and priority in realization (minimum cost, reliability, short and easy to install, and accessible for remote control).

Each model will be connected to an internet modem through this topology, allowing each one to send its own data to the Cloud and display it in an interface.

Securing Cloud data by controlling user access and eligibility to restrict usage to authorized users only [38]. Figure 3 shows Topology through the Cloud.

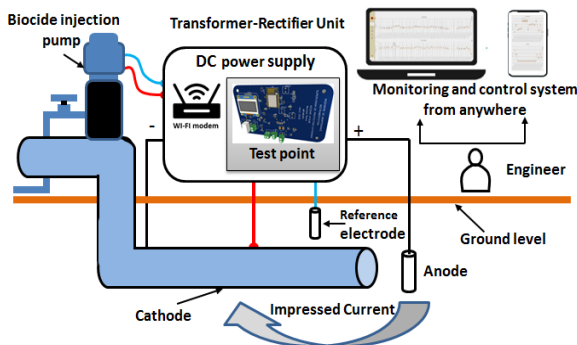


Figure 2. Proposed solution for real-time supervision and control of the CP

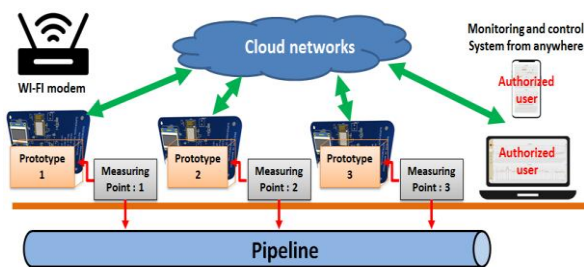


Figure 3. Topology through the Cloud

4. 2. Materials and Methods for Supervision This section discusses a remote CP system that is capable of measuring current and voltage potential. To improve CP monitoring, we are developing a web page that displays sensor readings in a graphical format that can be accessed from anywhere in the world. The task is divided into two sections: hardware and software. Figure 4 shows the supervision process.

4. 2. 1. Hardware section In this part, we need the different circuits and electronic components to realize our PCB. The use of printed circuit boards in expensive switchboards can significantly reduce the cost of CP installations. Inexpensive and readily available sensors can provide reliable monitoring data at low cost.

The six most important blocks that make up our PCB are:

1. Wi-Fi module (ESP_12E) for make the connection between the web interface that transfers the measured data.
2. The voltage regulation: Pre-regulation circuit DC/DC 12/5V, the circuit (EUP3458VIR1) regulates the output voltage to 5V, voltage regulator 3.3 V (AMS1117-3.3).
3. Relay circuit (G6S-2-12V) to control the biocide injection pump, requiring a 12V power supply.
4. UART / USB (FT232) to transfer data and programs from the PC to the circuit.
5. Voltage divider with two resistors in series (the voltage module was used with a range of 16.5 V, $R1=30k\ \Omega$, $R2=750\Omega$).
6. OLED Display 0.96 (SSD1306) to display the voltage and current values.

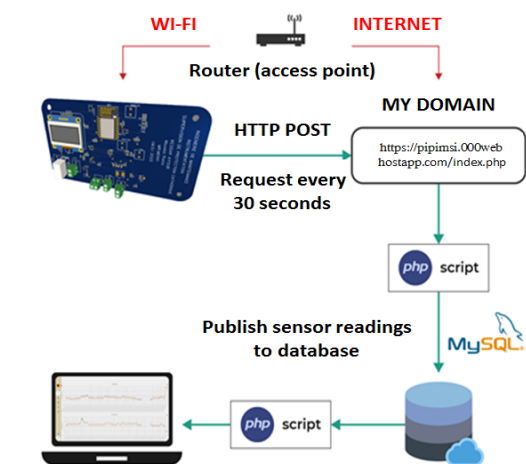


Figure 4. The supervision process

On the online, open-source Easy EDA platform, the PCB layout and design are completed, with proper component placement and high-quality wiring ensuring a 0% short-circuit rate. The result as PCB design is shown in Figure 5.

We worked with JLCPCB to create five printed circuit boards (PCBs), two of which were assembled with modules and components. The total cost for manufacturing and assembly was €116.99.

In practice, miniature PCBs with a Wi-Fi modem are used to integrate them into a Transformer-Rectifier Unit (TRU) to connect multiple remote measurement points. The TRU ensures a continuous supply of 24V DC between the anode and the pipeline weld for enhanced cathodic protection.

The power supply of our PCB is provided by a pre-regulator that delivers a voltage of 3.3V. Voltage and current sensors are connected to the PCBs using voltage dividers. The system is scalable, allowing for the connection of unlimited measurement points. Voltage data is securely transmitted via Wi-Fi to an IoT platform and the Cloud, enabling real-time analysis and adjustments to the rectifier as needed.

The IoT technology enables communication between the PCB and the web interface.

4. 2. 2. Software Section After finishing the design of our PCB, we began writing scripts in a variety of programming languages in order to get our system running in real time. Among these scripts we find:

- C++ script

We utilized the C++ programming language to develop a measuring device that enables the measurement of potential and transmission to the Cloud IoT through the HTTP POST communication protocol.

The analog-to-digital converter is used to convert the input value analog to voltage value. We used two resistors R1 and R2 are connected in series like a divider tension.

V_{in} applied as input to the two resistors and the output voltage V_{out} is measured across R2.

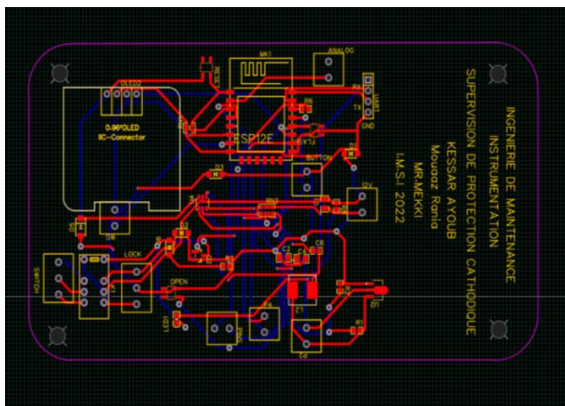


Figure 5. PCB design

$$V_{out} = \frac{R2}{R1 + R2} \cdot V_{in} \quad (1)$$

After numerical computation, we find:

$$\frac{R2}{R1 + R2} = 0.2 \quad (2)$$

Means that :

$$V_{in} = 5 \cdot V_{out} \quad (3)$$

V_{out} : is the potential measured by ESP_12E in pin A0, then we can say that : $V_{out} = A0$

$V_{in} = 3.3V$: is the potential can be provided to power the ESP_12E board.

$$V_{in} = 5 \cdot A0 \quad (4)$$

In this case V_{in} will be in bits but we need the equivalent in volts, the ESP 8266 receives potential values in bits from 0 to 1024 bits, therefore:

$$Adc_volt = \frac{(A0 \cdot 5)}{1024} \quad (5)$$

- Server

To ensure accessibility of the web interface from anywhere with an internet connection, we have created an account on a free server, "000webhost.com" which allows us to load our scripts (MySQL, PHP, HTML, and CSS support), as well as having the possibility of providing us with a local database.

- Database Creation

We have set up a MySQL database on our server, with a storage capacity of 1 GB, meeting our specific needs. To ensure the system's accuracy and reliability, the measurement potential data (input) must be suitably stored in a dedicated table called TBO within the Cloud IoT environment.

- Creating an SQL table (TBO)

We can create a table in the database using this SQL code.

- Communication

We needed to establish a link between the PHP script and the database. A connexion script is shown in Figure 6.

- Display on the database

/public_html/conexion.php

```

1 <?php
2
3 $user = "our user id ";
4 $pass = "our password ";
5 $server = "localhost";
6 $db = "our id db ";
7 $con = mysqli_connect($server, $user, $pass, $db);
8
9 ?>
```

Figure 6. A connexion script

We have created a PHP script to receive the data from the PCB and send it to the TBO table.

- Web Interface

After acquiring the data, we needed a script to convert the data into graphs and tables.

For this, we used HTML, CSS, and a free API called "Highchart" written in JavaScript. The cloud server's data is shown on the web interface in JSON format for organized transmission. The communication between the cloud and the web interface is facilitated by employing the respective API key, which plays a vital role in enabling seamless communication between the IoT device and the cloud, utilizing the HTTP protocol.

4. 3. Materials and Methods Control Part After measuring the current and voltage potentials, we need to control the impressed current biocides injection pump remotely in case of problems.

For this purpose, we have created another web interface to control the measuring points. The control process is shown in Figure 7.

- Database preparation

In the same server we have created our database, username, password and SQL tables.

After the preparation of the database, we will create files responsible for the creation of the control interface. The following files:

- Entering and accessing the database.
- Managing HTTP requests.
- Displaying the control buttons.
- A CSS file to customize the appearance of the web page.

- Database insertion

PHP scripts are used for storing and retrieving output states that are stored within a MySQL database. The store and retrieve output states are shown in Figure 8.

- Handling HTTP requests

We will create a PHP script to receive incoming requests and interact with the MySQL database. PHP script to receive the requests is shown in Figure 9.

```

$sql = "INSERT INTO Outputs (name, board, gpio, state)
VALUES ('" . $name . "', '" . $board . "', '" . $gpio . "', '" . $state . "')";

if ($conn->query($sql) === TRUE) {
    return "New output created successfully";
}
else {
    return "Error: " . $sql . "<br>" . $conn->error;
}
$conn->close();
}

function deleteOutput($id) {
    global $servername, $username, $password, $dbname;

    // Create connection
    $conn = new mysqli($servername, $username, $password, $dbname);
    // Check connection
    if ($conn->connect_error) {
        die("Connection failed: " . $conn->connect_error);
    }

    $sql = "DELETE FROM Outputs WHERE id='" . $id . "'";

    if ($conn->query($sql) === TRUE) {

```

Figure 8. Store and retrieve output states

```

1 <?php
2 include_once('esp-database.php');
3
4 $action = $id = $name = $gpio = $state = "";
5
6 if ($_SERVER["REQUEST_METHOD"] == "POST") {
7     $action = test_input($_POST["action"]);
8     if ($action == "output_create") {
9         $name = test_input($_POST["name"]);
10        $board = test_input($_POST["board"]);
11        $gpio = test_input($_POST["gpio"]);
12        $state = test_input($_POST["state"]);
13        $result = createOutput($name, $board, $gpio, $state);
14
15        $result2 = getBoard($board);
16        if (!$result2->fetch_assoc()) {
17            createBoard($board);
18        }
19        echo $result;
20    }
21    else {
22        echo "No data posted with HTTP POST.";
23    }
24 }
25

```

Figure 9. PHP script to receive the requests

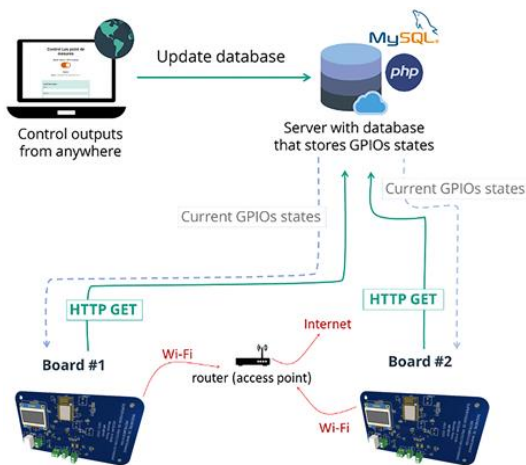


Figure 7. The control process

- Creation of control buttons

This is the page that gives access to the control of the measurement points. The control buttons are shown in Figure 10. In the beginning, we will generate the output's name, its board ID, and the corresponding connection number.

5. TESTS AND RESULTS

To test the operation of our electronic board, we used the humidity and temperature sensor DHT11.

5. 1. Supervision Part We have connected the DHT11 to measure the temperature and humidity of the environment. Our graph in Figure 11 is available in the web site: <https://pipimsi.000webhostapp.com/chart.php>.

Control of Measurement points

You should first put your board settings

Boards

Create New Output

Name

Board ID

GPIO Number

Initial GPIO State

Create Output

Note: refresh the page to see your newly created buttons or to remove deleted buttons.

Figure 10. Control buttons

Control of Measurement points

You should first put your board settings

The pump relay - Board 1 - GPIO 14 ([Delete](#))



Boards

Board 1 - Last Request Time: 2023-04-26 00:57:43

Create New Output

Name

Board ID

GPIO Number

Initial GPIO State

Create Output

Note: refresh the page to see your newly created buttons or to remove deleted buttons.

Figure 12. Relay control

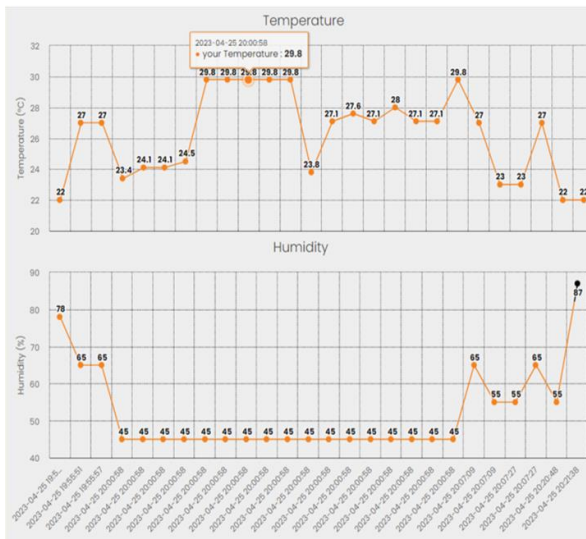


Figure 11. DHT11 monitoring

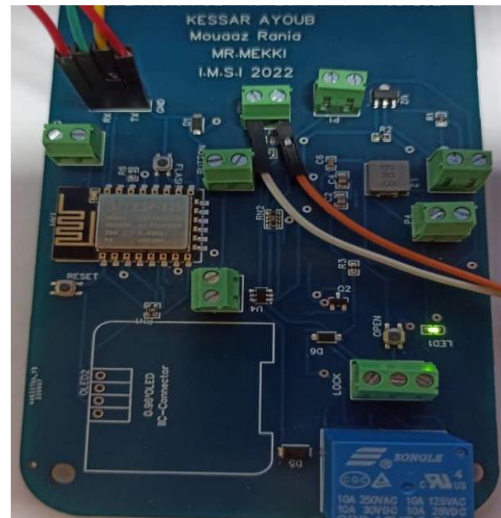


Figure 13. The relay works correctly by lighting the Led

5. 2. Control Part A button has been created to control the relay which is a switch for controlling the injection pump. The relay control is shown in Figure 12.

The led on the relay lights up, which means that the relay is working and that the temperature has dropped. Figure 13 shows the relay correctly works by lighting the Led.

The proposed electronic board is ready to be installed in a classic cathodic protection station for corrosion protection. To be able to perform all measurements and control relays in real-time via IoT, the new system had to be connected to the pipeline and have access to WiFi. All this work allows us to design and evaluate our PCB. Depending on the number of sensors and actuators required, multiple cards can be connected.

Further research in this field could consider the integration of advanced optimization algorithms into the proposed system to improve pipeline surveillance and decision-making. For instance, potential algorithms include machine learning [40], deep learning [41], Bayesian network (BN) [42, 43], BN combined with genetic algorithm (GA) [44], GA, Particle Swarm Optimization (PSO) and Firefly Algorithm (FFA) meta-heuristic optimization algorithms [45], multi-objective optimisation techniques [46], and adaptive intelligent systems [47].

Advanced optimization algorithms, including hybrid and metaheuristic heuristics, adaptive and self-adaptive algorithms, as well as island algorithms, have been widely employed to address complex decision-making issues. These algorithms have demonstrated their effectiveness in various domains such as online learning [48], planning [49], multi-objective optimization [50], transportation [51, 52], medicine [53], data classification [54], and other relevant fields.

6. CONCLUSION

This paper has demonstrated the design and implementation of a stand-alone CP system for pipeline monitoring. The proposed system allows the acquisition of real-time data on voltage potential and current, which is crucial to protect pipelines from corrosion. The web interface provides real-time visualization of the measured data in the form of graphs, tables and also allows remote control of the relays for managing the biocide injection pump. However, there are improvements that can be made to this system such as using more reliable communication protocols and adding a memory card for data storage. Overall, this system has great potential for CP of pipelines and can be adapted for other similar applications.

7. REFERENCES

- Ma, Q., Tian, G., Zeng, Y., Li, R., Song, H., Wang, Z., Gao, B. and Zeng, K., "Pipeline in-line inspection method, instrumentation and data management", *Sensors*, Vol. 21, No. 11, (2021), 3862. doi: <https://doi.org/10.3390/s21113862>.
- Mattsson, E., "Basic corrosion technology for scientists and engineers, CRC Press, (2023).
- Bai, X., Zhao, Y. and Xu, L., "Study on corrosion prevention and treatment in long-distance oil and gas pipeline", in IOP Conference Series: Earth and Environmental Science, IOP Publishing. Vol. 384, No. 1, (2019), 012178. doi: 10.1088/1755-1315/384/1/012178.
- Fayomi, O., Akande, I. and Odigie, S., "Economic impact of corrosion in oil sectors and prevention: An overview", *Journal of Physics: Conference Series*, Vol. 1378, No. 2, (2019), 022037. doi: 10.1088/1742-6596/1378/2/022037.
- Ahmad, F. and Faisal, M., Challenges generated by the integration of cloud and iot, in Cloud iot. 2022, Chapman and Hall/CRC: New York.3-23.
- Ali, Z.H., Ali, H.A. and Badawy, M.M., "Internet of things (iot): Definitions, challenges and recent research directions", *International Journal of Computer Applications*, Vol. 128, No. 1, (2015), 37-47. doi: 10.5120/ijca2015906430.
- Ramchand, K., Chhetri, M.B. and Kowalczyk, R., "Enterprise adoption of cloud computing with application portfolio profiling and application portfolio assessment", *Journal of Cloud Computing*, Vol. 10, (2021), 1-18. doi: <https://doi.org/10.1186/s13677-020-00210-w>.
- Singh, P., Elmi, Z., Lau, Y.-y., Borowska-Stefańska, M., Wiśniewski, S. and Dulebenets, M.A., "Blockchain and ai technology convergence: Applications in transportation systems", *Vehicular Communications*, (2022), 100521. doi: <https://doi.org/10.1016/j.vehcom.2022.100521>.
- Singh, P., Dulebenets, M.A., Pasha, J., Gonzalez, E.D.S., Lau, Y.-Y. and Kampmann, R., "Deployment of autonomous trains in rail transportation: Current trends and existing challenges", *IEEE Access*, Vol. 9, (2021), 91427-91461. doi: <https://doi.org/10.1109/ACCESS.2021.3091550>.
- Singh, P., Elmi, Z., Meriga, V.K., Pasha, J. and Dulebenets, M.A., "Internet of things for sustainable railway transportation: Past, present, and future", *Cleaner Logistics and Supply Chain*, Vol. 4, (2022), 100065. doi: <https://doi.org/10.1016/j.clscn.2022.100065>.
- Dave, B., Kubler, S., Främling, K. and Koskela, L., "Opportunities for enhanced lean construction management using internet of things standards", *Automation in Construction*, Vol. 61, (2016), 86-97. doi: <https://doi.org/10.1016/j.autcon.2015.10.009>.
- Orumwense, E.F. and Abo-Al-Ez, K., "Internet of things for smart energy systems: A review on its applications, challenges and future trends", *AIMS Electronics and Electrical Engineering*, Vol. 7, No. 1, (2023), 50-74. doi: <https://doi.org/10.3934/electreng.2023004>.
- Mazhar, T., Irfan, H.M., Haq, I., Ullah, I., Ashraf, M., Shloul, T.A., Ghadi, Y.Y. and Elkamchouchi, D.H., "Analysis of challenges and solutions of iot in smart grids using ai and machine learning techniques: A review", *Electronics*, Vol. 12, No. 1, (2023), 242. doi: <https://doi.org/10.3390/electronics12010242>.
- Rayan, R.A., Zafar, I. and Tsagkaris, C., "Iot technologies for smart healthcare", *Advances in Data Science and Analytics: Concepts and Paradigms*, (2023), 181-202. doi: <https://doi.org/10.1002/9781119792826.ch8>.
- Hemdan, E.E.-D., Essa, Y.M., Shouman, M., El-Sayed, A. and Moustafa, A.N., "An efficient iot based smart water quality monitoring system", *Multimedia Tools and Applications*, (2023), 1-25. doi: <https://doi.org/10.1007/s11042-023-14504-z>.
- Mahor, V., Bijrothiya, S., Rawat, R., Kumar, A., Garg, B. and Pachlasiya, K., Iot and artificial intelligence techniques for public safety and security, in Smart urban computing applications. 2023, River Publishers: New York.111.
- Bhosale, S.A., *Artificial intelligence and iot for smart cities*, in Smart Urban Computing Applications. 2023, River Publishers: New York.207.
- Khaleghi Abbasabadi, M., Esmaili Zand, H.R., Khodabakhshi, S., Gholami, P. and Rashidi, A., "Synthesis of new functionalized reduced graphene oxide quantum dot composite for high-performance NO₂ gas sensor", *Research on Chemical Intermediates*, Vol. 47, (2021), 2279-2296. doi: <https://doi.org/10.1007/s11164-020-04393-4>.
- Gheibi, M., Taghavian, H., Moezzi, R., Waclawek, S., Cyrus, J., Dawiec-Lisniewska, A., Koci, J. and Khaleghiabbasabadi, M., "Design of a decision support system to operate a NO₂ gas sensor using machine learning, sensitive analysis and conceptual control process modelling", *Chemosensors*, Vol. 11, No. 2, (2023), 126. doi: <https://doi.org/10.3390/chemosensors11020126>.
- Kiyan, A., Gheibi, M., Akrami, M., Moezzi, R. and Behzadian, K., "A comprehensive platform for air pollution control system operation in smart cities of developing countries: A case study of tehran", *Environmental Industry Letters*, Vol. 1, No. 1, (2023), 10-27. doi: <https://doi.org/10.15157/EIL.2023.1.1.10-27>.
- Gholami, P., Rashidi, A., Khaleghi Abbasabadi, M., Pourkhalil, M., Jahangiri, M. and Izadi, N., "Synthesis and characterization of zno-functionalized multiwall carbon nanotubes nanocomposite as NO_x gas sensor", *Research on Chemical Intermediates*, Vol. 46, (2020), 3911-3927. doi: <https://doi.org/10.1007/s11164-020-04181-0>.

22. Kiyani, A., Gheibi, M., Akrami, M., Moezzi, R., Behzadian, K. and Taghavian, H., "The operation of urban water treatment plants: A review of smart dashboard frameworks", *Environmental Industry Letters*, Vol. 1, No. 1, (2023), 28-45. doi: <https://doi.org/10.15157/EIL.2023.1.1.28-45>.
23. Kiyani, A., Gheibi, M., Moezzi, R. and Behzadian, K., "Smart dashboard of water distribution network operation: A case study of tehran", *Environmental Industry Letters*, Vol. 1, No. 1, (2023), 46-63. doi: <http://dx.doi.org/10.15157/EIL.2023.1.1.46-63>.
24. Kia, G. and Hassanzadeh, A., "Hyrep: A hybrid low-power protocol for wireless sensor networks", *International Journal of Engineering, Transactions A: Basics*, Vol. 32, No. 4, (2019), 519-527. doi: <https://doi.org/10.5829/ije.2019.32.04a.09>.
25. Kodali, R.K. and Soratkal, S., "Mqtt based home automation system using esp8266", in 2016 IEEE Region 10 Humanitarian Technology Conference (R10-HTC), IEEE. (2016), 1-5. doi: [10.1109/R10-HTC.2016.7906845](https://doi.org/10.1109/R10-HTC.2016.7906845).
26. Mononen, T. and Mattila, J., "A low-cost cloud-extended sensor network for supervisory control", in 2017 IEEE International Conference on Cybernetics and Intelligent Systems (CIS) and IEEE Conference on Robotics, Automation and Mechatronics (RAM), IEEE. (2017), 502-507. doi: [10.1109/ICCIS.2017.8274827](https://doi.org/10.1109/ICCIS.2017.8274827).
27. Medrano, K., Altuve, D., Belloso, K. and Bran, C., "Development of scada using a rtu based on iot controller", in 2018 IEEE International Conference on Automation/XXIII Congress of the Chilean Association of Automatic Control (ICA-ACCA), IEEE. (2018), 1-6. doi: [10.1109/ICA-ACCA.2018.8609700](https://doi.org/10.1109/ICA-ACCA.2018.8609700).
28. Kara, A., Al Imran, M.A. and Karadag, K., "Linear wireless sensor networks for cathodic protection monitoring of pipelines", in 2019 International Conference on Mechatronics, Robotics and Systems Engineering (MoRSE), Bali, Indonesia, IEEE. (2019 of Conference), 233-236. doi: <https://doi.org/10.1109/MoRSE48060.2019.8998664>.
29. Li, L. and Wang, Y., "Sensing terminal for big data oil and gas pipeline corrosion monitoring", in 2020 International Conference on Computer Network, Electronic and Automation (ICCNEA), IEEE. (2020), 279-283. doi: [10.1109/ICCNEA50255.2020.00064](https://doi.org/10.1109/ICCNEA50255.2020.00064).
30. Singh, R., Baz, M., Narayana, C.L., Rashid, M., Gehlot, A., Akram, S.V., Alshamrani, S.S., Prashar, D. and AlGhamdi, A.S., "Zigbee and long-range architecture based monitoring system for oil pipeline monitoring with the internet of things", *Sustainability*, Vol. 13, No. 18, (2021), 10226. doi: <https://doi.org/10.3390/su131810226>.
31. Aba, E.N., Olugboji, O.A., Nasir, A., Olutoye, M. and Adedipe, O., "Petroleum pipeline monitoring using an internet of things (iot) platform", *SN Applied Sciences*, Vol. 3, (2021), 1-12. doi: <https://doi.org/10.1007/s42452-021-04225-z>.
32. Puviarasi, R., Dineshkumar, T., Babu, V.S. and Partheeban, P., "Design and development of smart portable system for underground pipeline leakage monitoring based on iot", in Journal of Physics: Conference Series, IOP Publishing, Vol. 1964, No. 6, (2021), 062065. doi: [10.1088/1742-6596/1964/6/062065](https://doi.org/10.1088/1742-6596/1964/6/062065).
33. Priyanka, E.B., Maheswari, C. and Thangavel, S., "A smart-integrated iot module for intelligent transportation in oil industry", *International Journal of Numerical Modelling: Electronic Networks, Devices and Fields*, Vol. 34, No. 3, (2021), e2731. doi: [10.1002/jnm.2731](https://doi.org/10.1002/jnm.2731).
34. Chavala, L.N., Singh, R. and Gehlot, A., "Performance evaluation of lora based sensor node and gateway architecture for oil pipeline management", *International Journal of Electrical and Computer Engineering*, Vol. 12, No. 1, (2022), 974. doi: [10.11591/ijece.v12i1.pp974-982](https://doi.org/10.11591/ijece.v12i1.pp974-982).
35. Yas, A.K. and Al Qassab, A., "Oil and gas pipelines monitoring using iot platform", *Iraqi Journal of Information and Communication Technology*, Vol. 6, No. 1, (2023), 9-27. doi: <https://doi.org/10.31987/ijict.6.1.209>.
36. Li, W., Ye, Z., Wang, Y., Yang, H., Yang, S., Gong, Z. and Wang, L., "Development of a distributed mr-iot method for operations and maintenance of underground pipeline network", *Tunnelling and Underground Space Technology*, Vol. 133, (2023), 104935. doi: <https://doi.org/10.1016/j.tust.2022.104935>.
37. Wu, Q., Chen, X., Yu, H., Liu, Q. and Yang, Y., "Real-time data visualization method for oil pipeline monitoring based on internet of things", IOP Conference Series: Materials Science and Engineering, Vol. 768, No. 5, (2020), 052124. doi: [10.1088/1757-899X/768/5/052124](https://doi.org/10.1088/1757-899X/768/5/052124).
38. Mansouri, N., "An efficient task scheduling based on seagull optimization algorithm for heterogeneous cloud computing platforms", *International Journal of Engineering, Transactions B: Applications*, Vol. 35, No. 2, (2022), 433-450. doi: <https://doi.org/10.5829/ije.2022.35.02b.20>.
39. Datasheet. *Electronic components datasheet search*. 2023; Available from: <https://www.alldatasheet.com/>.
40. Ismail, M.F.H., May, Z., Asirvadam, V.S. and Nayan, N.A., "Machine-learning-based classification for pipeline corrosion with monte carlo probabilistic analysis", *Energies*, Vol. 16, No. 8, (2023), 3589. doi: <https://doi.org/10.3390/en16083589>.
41. Ferreira, A.D.M., Afonso, S.M., Willmersdorf, R.B. and Lyra, P.R., "Multiresolution analysis and deep learning for corroded pipeline failure assessment", *Advances in Engineering Software*, Vol. 162, (2021), 103066. doi: <https://doi.org/10.1016/j.advengsoft.2021.103066>.
42. Li, Y.-T., He, X.-N. and Shuai, J., "Risk analysis and maintenance decision making of natural gas pipelines with external corrosion based on bayesian network", *Petroleum Science*, Vol. 19, No. 3, (2022), 1250-1261. doi: <https://doi.org/10.1016/j.petsci.2021.09.016>.
43. Zhang, J., Ai, Z., Guo, L. and Cui, X., "Reliability evaluation of a disaster airflow emergency control system based on bayesian networks", *International Journal of Engineering, Transactions B: Applications*, Vol. 33, No. 11, (2020), 2416-2424. doi: <https://doi.org/10.5829/ije.2020.33.11b.32>.
44. Liu, X., Zheng, J., Fu, J., Nie, Z. and Chen, G., "Optimal inspection planning of corroded pipelines using bn and ga", *Journal of Petroleum Science and Engineering*, Vol. 163, (2018), 546-555. doi: <https://doi.org/10.1016/j.petrol.2018.01.030>.
45. Seghier, M.E.A.B., Keshtegar, B., Tee, K.F., Zayed, T., Abbassi, R. and Trung, N.T., "Prediction of maximum pitting corrosion depth in oil and gas pipelines", *Engineering Failure Analysis*, Vol. 112, (2020), 104505. doi: <https://doi.org/10.1016/j.engfailanal.2020.104505>.
46. Gong, C. and Zhou, W., "Multi-objective maintenance strategy for in-service corroding pipelines using genetic algorithms", *Structure and Infrastructure Engineering*, Vol. 14, No. 11, (2018), 1561-1571. doi: <https://doi.org/10.1080/15732479.2018.1459744>.
47. Khussanov, Z., Prokhorov, O., Prokhorov, V., Tevyashev, A., Turdybekova, D. and Shatalov, O., "Adaptive intelligent system for monitoring and controlling the parameters of pipelines electrochemical corrosion protection", in 2022 International Conference on Smart Information Systems and Technologies (SIST), IEEE. (2022), 1-7. doi: <https://doi.org/10.1109/SIST54437.2022.9945734>.
48. Zhao, H. and Zhang, C., "An online-learning-based evolutionary many-objective algorithm", *Information Sciences*, Vol. 509, (2020), 1-21. doi: <https://doi.org/10.1016/j.ins.2019.08.069>.
49. Kavooosi, M., Dulebenets, M.A., Abioye, O., Pasha, J., Theophilus, O., Wang, H., Kampmann, R. and Mikijeljević, M., "Berth scheduling at marine container terminals: A universal

- island-based metaheuristic approach", *Maritime Business Review*, Vol. 5, No. 1, (2019), 30-66. doi: <https://doi.org/10.1108/MABR-08-2019-0032>.
50. Pasha, J., Nwodu, A.L., Fathollahi-Fard, A.M., Tian, G., Li, Z., Wang, H. and Dulebenets, M.A., "Exact and metaheuristic algorithms for the vehicle routing problem with a factory-in-a-box in multi-objective settings", *Advanced Engineering Informatics*, Vol. 52, (2022), 101623. doi: <https://doi.org/10.1016/j.aei.2022.101623>.
51. Dulebenets, M.A., "An adaptive polyloid memetic algorithm for scheduling trucks at a cross-docking terminal", *Information Sciences*, Vol. 565, (2021), 390-421. doi: <https://doi.org/10.1016/j.ins.2021.02.039>.
52. Sumi, L. and Ranga, V., "Intelligent traffic management system for prioritizing emergency vehicles in a smart city", *International Journal of Engineering, Transactions B: Applications*, Vol. 31, No. 2, (2018), 278-283. doi: 10.5829/ije.2018.31.02b.11.
53. Rabbani, M., Oladzaad-Abbasabady, N. and Akbarian-Saravi, N., "Ambulance routing in disaster response considering variable patient condition: Nsga-ii and mopso algorithms", *Journal of Industrial and Management Optimization*, Vol. 18, No. 2, (2022), 1035-1062. doi: 10.3934/JIMO.2021007.
54. Gholizadeh, H., Fazlollahtabar, H., Fathollahi-Fard, A.M. and Dulebenets, M.A., "Preventive maintenance for the flexible flowshop scheduling under uncertainty: A waste-to-energy system", *Environmental Science and Pollution Research*, (2021), 1-20. doi: <https://doi.org/10.1007/s11356-021-16234-x>.

COPYRIGHTS

©2023 The author(s). This is an open access article distributed under the terms of the Creative Commons Attribution (CC BY 4.0), which permits unrestricted use, distribution, and reproduction in any medium, as long as the original authors and source are cited. No permission is required from the authors or the publishers.



Persian Abstract

چکیده

ادغام اینترنت اشیا (IoT) و سیستم‌های حفاظت کاتدی مبتنی بر ابر (CP) یک رویکرد نوآورانه است که می‌تواند منجر به بهبود حفاظت خط لوله در برابر خوردگی شود. استفاده از برد مدار چاپی (PCB) برای اندازه‌گیری و کنترل جریان و ولتاژ، نظارت بر سیستم‌های رایانه شخصی را در زمان واقعی ممکن می‌سازد. رابط وب که از طریق فناوری IoT به مدار PCB متصل می‌شود، بستری را برای ارزیابی فوری داده‌های به دست آمده فراهم می‌کند و در نتیجه امکان تشخیص زودهنگام مشکلات احتمالی را فراهم می‌کند. یکی از مزایای کلیدی نظارت در زمان واقعی، بهبود مدیریت داده‌ها و امنیت است. داده‌های به دست آمده را می‌توان در یک سرور ابری ذخیره کرد و دسترسی و تجزیه و تحلیل آن را آسان تر می‌کند. این امر نیاز به بازرسی‌های دستی را که می‌تواند زمان بر و مستعد خطا باشد را از بین می‌برد. علاوه بر این، نظارت بلادرنگ می‌تواند زمان خرابی را کاهش دهد، زیرا مشکلات را می‌توان به سرعت شناسایی و حل کرد و از نیاز به بازرسی‌های دستی طولانی و نگهداری جلوگیری کرد. این رویکرد نوآورانه پتانسیل فوق‌العاده‌ای برای آینده حفاظت از خط لوله و کنترل خوردگی دارد. مدار PCB توسعه‌یافته دارای یک UART متحرک است که حفاظت از برنامه را فراهم می‌کند و رابط می‌تواند چندین کارت PCB و رله را به‌طور مستقل کنترل کند. سیستم مانیتورینگ را می‌توان بدون وقفه در جمع‌آوری داده‌ها به روز کرد. استفاده از نرم‌افزار منبع باز، میزبانی پایگاه داده و توسعه PCB کم‌هزینه، تجاری‌سازی را تسهیل می‌کند. این مطالعه می‌تواند الهام بخش برنامه‌های کاربردی جدید در مدیریت و نظارت دارایی باشد.



Catalytic Upgrading of Bio-oil from *Ulva lactuca* using Amberlyst-15 Catalyst: Experimental and Kinetic Model

A. Amrullah^a, O. Farobie^b, W. Fatriasari^c

^a Department of Mechanical Engineering, Lambung Mangkurat University, Banjarmasin, South Kalimantan, Indonesia

^b Department of Mechanical and Biosystem Engineering, Faculty of Agricultural Engineering and Technology, IPB University (Bogor Agricultural University), IPB Darmaga Campus, Bogor, Indonesia

^c Research Center for Biomass and Bioproducts, National Research and Innovation Agency (BRIN), Jl. Raya Bogor KM. 46 Cibinong, Indonesia

PAPER INFO

Paper history:

Received 22 May 2023

Received in revised form 08 June 2023

Accepted 12 June 2023

Keywords:

Amberlyst-15 Catalyst

Bio-oil

Ulva Lactuca

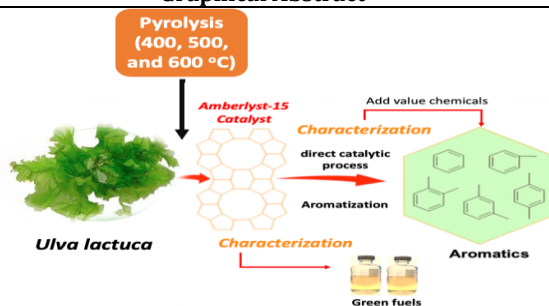
Kinetic Model

ABSTRACT

Catalytic pyrolysis of *Ulva lactuca* macroalgae was studied over Amberlyst-15 catalyst at temperature 400, 500, and 600 °C. The comparison between catalytic and non-catalytic pyrolysis in the conversion of *Ulva lactuca* was determined. Intriguingly, it was found that Amberlyst-15 catalyst improved bio-oil production efficiency. The highest bio-oil yield of 29.54 wt% was achieved at 600 °C with the presence of an Amberlyst-15 catalyst. Furthermore, Amberlyst-15 catalyst could enhance gas production by over 73.88%. It could be attributed due to the catalytic pyrolysis could promote more small molecules that are more volatile through a cracking process. Elemental and functional groups in pyrolytic bio-oils were identified via GC-MS analysis. The acidity and structure of Amberlyst-15 catalyst significantly affected the distribution of product components, especially the formation of aromatic hydrocarbons, with a 27.78% relative yield. The first-order kinetic model showed that the production of aromatic hydrocarbons follows Arrhenius law.

doi: 10.5829/ije.2023.36.09c.12

Graphical Abstract



1. INTRODUCTION

Due to its widespread availability and capacity to be farmed on a massive scale, biomass has become an attractive option for renewable energy use in recent years [1, 2]. Rising oil prices and concerns about the impact of human activity on the environment drive these trends.

Biomass is a readily available and cost-effective energy source that may be used for various purposes, including generating heat and electricity, manufacturing chemicals, and providing fuel for transportation [3]. Therefore, researchers are looking for different energy sources, such as substituting biomass with lignocellulosic materials, agricultural wastes, and aquatic environment waste. In

*Corresponding Author Institutional Email: apip.amrullah@ulm.ac.id
(A. Amrullah)

recent years, macroalgae and aquatic macrophytes have received a lot of attention since their production rate is more significant than that of agricultural and forest biomass [1, 4]. In addition, the limited data on the pyrolysis of aquatic biomass [5, 6] demonstrated that algal bio-oil is greater than lignocellulosic bio-oil in several aspects.

The thermochemical and biochemical/biological processing technologies are the two basic techniques by which biomass obtained from various resources can be converted into a form of energy that can be utilized. The thermochemical process can undergo several stages, including pyrolysis/gasification, liquefaction, and combustion [7-9]. However, digestion and fermentation are both viable options for biochemical conversion [10]. Thermochemical conversion of biomass via pyrolysis provides an alternative route to fuel production [3, 11]. Pyrolysis is the thermally decomposition of organic compounds into several phases of an energy-rich product in an atmosphere free of oxygen. The pyrolysis process generates several different final products, including liquids (bio-oil) and solids (bio-char), and gases (syngas) [12]. In this context, the term "bio-oil" refers to the liquid byproduct of pyrolysis. It is a complex mixture of hydrocarbons and water. There is potential for this oil to be used as a chemical feedstock and an alternative to transportation fuel [13, 14]. However, from several pyrolysis studies for bio-oil production, such as purun tikus [15], empty fruit bunch (EFB) [16], and Crofton weed [17], the characteristics of bio-oils obtained contain high acetic acids, which directly cannot be used. Therefore, there is an urgent need to improve the quality of bio-oil obtained from pyrolysis.

To address this issue and improve the quality of bio-oil, in-situ catalytic pyrolysis is the term employed to describe improving the quality of the bio-oil product directly within the reactor. This process involves the use of catalysts and a biomass mixer. Several researchers investigated catalytic pyrolysis using zeolite, and they noticed that the bio-oil produced undergoes deoxygenation and produces aromatic hydrocarbons and nitrogen-containing molecules [18, 19]. Thangalazhy-Gopakumar et al. [20] examined the catalytic pyrolysis of *Chlorella vulgaris* biomass with HZSM-5 and found that the aromatic hydrocarbon increased from 0.9% to 25.8%. Hematkah et al. [21] investigated the direct pyrolysis of the microalgae *Spirulina* sp. with the zeolite-based catalysts at 425-625 °C. The introduction of the catalyst increased both the high heat value and the bio-oil energy yield. Thus, the use of zeolite-based catalysts during co-pyrolysis may be a new route for high-value-added compound production. It also increases the aromatic oil by causing deoxygenation, decarboxylation, and dehydration [22].

Anand et al., [23] used several catalysts (ZYH, ZYNa, MgO, ZrO₂, and TiO₂) to catalytically pyrolyze

Shizochytrium limacinum biomass at 350–800 °C. At 400 °C, ZYH60, TiO₂, and ZYH30 catalysts enhanced nitrogen-containing compounds by 12.22, 12.75, and 19.32 area%. They saw that the catalyst enhanced the amide dehydration process, producing nitriles. Wang et al. [24] observed similar results while studying *Enteromorpha* growth. Bio-oil had 13.77–36.2% nitrogen compounds. Mg-Ce/ZSM-5 catalysts produced the most nitrogen-containing compounds, while ZSM-5 catalysts produced less. Catalytic pyrolysis of *Chlorella vulgaris* was studied by Zainan et al. [25] using a range of Ni-supported zeolites catalyst concentrations. More hydrocarbons and fewer oxygenated and acidic compounds were generated during catalytic pyrolysis than non-catalytic pyrolysis. Catalyst processing did not alter bio-oil yield. However, it had an impact on the composition. According to Uslamin et al. [26], loading Ga onto ZSM-5 changes the acidic characteristics by adding Lewis acid sites and replacing Bronsted acid sites, enhancing aromatic compound selectivity. Therefore, proper acid sites are crucial in developing catalysts since they affect the system's selectivity and coke generation [27].

Previous studies give insights that acid catalyst could enhance the hydrocarbon and suppress the oxygenated compounds. However, bio-oil production from *U. lactuca* with the presence of Amberlyst-15 has not been studied well. Therefore, this study aims to investigate the effect of temperature and catalyst on product distribution and kinetic model in detail. The novelty of this finding highlights the use of Amberlyst-15 catalyst to enhance the high aromatic yields that can improve bio-oil quality. A systematic analysis of bio-oil and bio-char products was also evaluated to determine their physicochemical properties.

2. MATERIALS AND METHODS

2. 1. Preparation of Raw Materials *Ulva lactuca* feedstock was collected from Ekas Beach (Lombok Island, West of Nusa Tenggara, Indonesia). Deionized water and ordinary tap water were used to remove sand and other contaminants from the sample. After washing, samples were dried overnight at 105 °C in an oven. The macroalgae were dried, then pulverized into a powder, and sieved at 0.25 mm. Amberlyst-15 catalysts were purchased from Merck KGaA (Darmstadt, Germany) with a particle size of 0.355-1.18 mm, a concentration of H₂ ion concentration of 4.7 meq./g dry, surface area 50 m²/g, porosity 0.36 ml pore/mL bead, pore diameter 240 Å.

2. 2. Reaction procedure A 20 g of feedstock was fed into the reactor (350 mm height, 38 mm inner diameter). The experimental set up is shown in Figure 1.

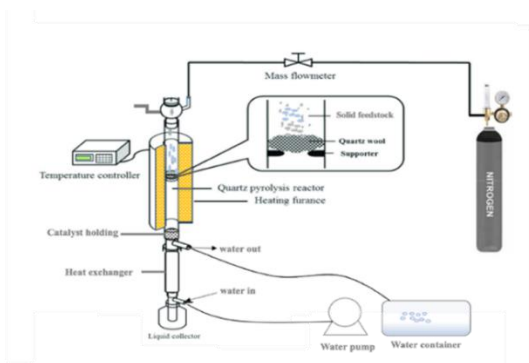


Figure 1. Experimental apparatus

Before each experiment, 2 wt% of the catalyst was suspended from the reactor's top in a quartz hopper. After evaluating the device for gas tightness, 30 mL/min of continuous N_2 was utilized to remove excess air. Subsequently, the reactor's temperature was increased from its initial setting of 25°C to the desired temperatures of 400, 500, and 600°C. Prior studies support this condition. After heating to appropriate temperatures, the reactor was maintained for 1 h. A thermocouple measured the reactor's temperature. The measuring cylinder contained condensable volatiles. The atmosphere was purged of non-condensable gas. By using ether solvent, the organic and aqueous fractions were separated. The reactor was cooled after each analysis. Every preliminary step had to be repeated to determine the quantity of bio-oil produced and get the correct data. The amount of biochar produced was determined by comparing the initial and final masses of the quartz reactor. The percentage of gas produced (in terms of weight) was calculated as the mass difference between the bio-oil and bio-char yields. The following formulas are used to determine product yield [8].

$$\text{Bio-oil yield (wt\%)} = \frac{(W_2) - (W_1)}{\text{Weight of feedstock}} \times 100 \quad (1)$$

$$\text{Bio-char yield (wt\%)} = \frac{(W_4) - (W_3)}{\text{Initial mass of feedstock (g)}} \times 100 \quad (2)$$

$$\text{Gas yield (wt\%)} = 100\% - (\text{bio-oil yield (wt\%)} + \text{bio-char yield (wt\%)}) \quad (3)$$

where w_1 is empty measuring cylinder weight, w_2 is measuring cylinder weight with bio-oil, w_3 is empty reactor weight, and w_4 is reactor weight after reaction.

2. 3. Feedstock and Products Analysis for the study on thermal degradation, a Shimadzu DTG-60 was used for thermogravimetric analysis (TGA). For this study, 5-7 mg of biomass was heated from 25 - 900 °C at a rate of 10 °C per minute in an N_2 atmosphere. FT-IR was performed using a NEXUS670, and the sample

powder was immersed in KBr before analysis. The spectral band that was utilized was 4000 to 400 cm^{-1} . Scans have been captured at a resolution of 4 cm^{-1} . A new baseline was established for the original data, and the adjusted data was then normalized. Bio-oil was investigated using gas chromatography and mass spectrometry (GC/MS-QP2010 SE-Shimadzu, Japan) with an Rtx®-5MS capillary column. Before introducing the bio-oil to the GC/MS, it was diluted with dichloromethane in a 1:4 volume ratio (v/v). The oven was heated to 40 °C for one minute. After that, the temperature was raised to 10°C per minute for several minutes until it reached to 150 °C. The temperature rose at a rate of 10 °C per minute until it reached 300°C, where it remained stable for 30 minutes. Lastly, the device was kept at a temperature of 250 °C. The GC/MS was filled with up to 1 L of the bio-oil that had been dissolved. The compounds that comprise bio-oil have been identified using the mass spectra in the NIST2008 c2.0/Xcalibur data set. The ultimate analysis was performed with the assistance of a CHNS/O analyzer, and the findings were previously reported [8].

3. RESULTS AND DISCUSSION

3. 1. TGA Analysis of the Feedstock and Catalyst

Initially, the thermal degradation properties of the original feedstock and Amberlyst-15 were investigated to identify the structural stability and produced types, which is essential for a reasonable elucidation of Amberlyst-15's practical function during the pyrolysis process. The TG and DTG curves of the raw material are displayed in Figure 2(a).

There are three primary steps in the pyrolysis of raw materials. Internal moisture was driven out in the first phase (between 100 and 260 °C), and low molecular weight components were volatilized as indicated by Chen et al. [28] and Dewangan et al. [29]. It was formerly argued that temperatures from 268 to 498 °C were essential for the decarboxylation, depolymerization, and cleavage of carbohydrates, lipids, and proteins during stage 2 of the reaction [30]. This trend was also in line with previous research reported by White et al. [31 and D'Almeida et al. [32], who mentioned that the temperature range of 300–500 °C was responsible for the decomposition process of lipids and proteins. The third stage of biochar pyrolysis occurred at temperatures between 415 and 657 °C, and it was characterized by a steady, soft weight loss [33]. The TG and DTG curves of the Amberlyst-15 catalyst are illustrated in Figure 2(b).

The temperature profile at which catalyst degradation began could potentially be calculated with the use of this interpretation. The heating process typically consists of three distinct phases of degradation. The process started at room temperature and increased to 110 °C when water

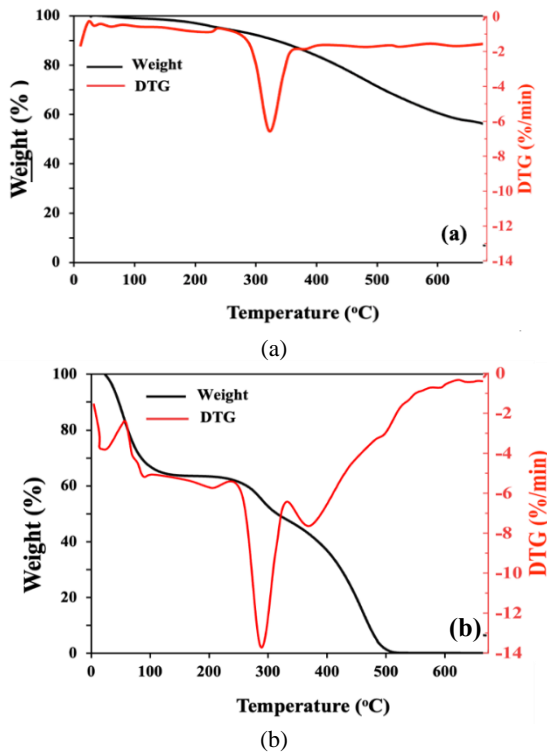


Figure 2. (a) The TG and DTG curves of raw material, (b) The TG and DTG curves of the catalyst

was evaporated. The subsequent stage, between 280 and 480 °C, had the most significant weight loss, and the third stage, between 500 and 700 °C, showed the least weight loss.

3. 2. Product Yield Distribution

3. 2. 1. Effect of Temperature The effects of temperature (400, 500, and 600 °C) on the pyrolysis of macroalgae (*Ulva lactuca*) were investigated in the presence of nitrogen for 60 min. Figure 3 illustrates the observed percentage of product yield that was achieved.

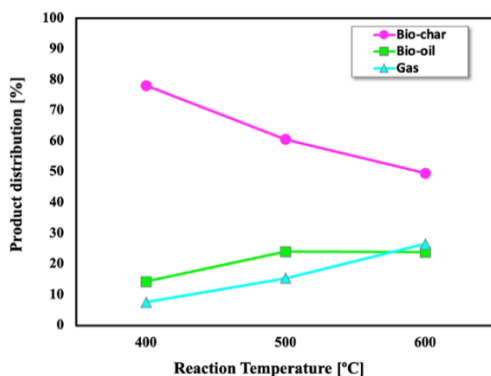


Figure 3. Effect of pyrolysis temperature on products yield distribution

At a pyrolysis temperature of 400 °C, the bio-oil produced was 14.32 wt%. Increasing the reaction temperature from 400 to 500 °C increased bio-oil production. However, it dropped during the reaction from 500 °C to 600 °C. The highest bio-oil production (24.05 wt%) was achieved at 500 °C. However, as the temperature was increased to 600 °C, the bio-oil production dropped to 23.87 %. Therefore, 500 °C was optimal for the pyrolysis of *Ulva lactuca* algae, resulting in the complete breakdown of all algae links and a high liquid yield. Several research teams noticed an increase in char production after observing a rise in the re-polymerization of the decomposition intermediates [3, 34, 35]. At temperatures above 400 °C, some short-chain liquid products are converted into non-condensable gases, increasing the yield of gases. These results follow the former research of Yorgun et al. [36], who reported that higher temperatures, longer reaction times, and lower heating rates lead to greater yields of gaseous products. Furthermore, biochar yield decreased with increasing temperature, possibly due to a secondary reaction occurring at elevated temperatures [37].

3. 2. 2. Effect of Catalyst Addition Catalysts (Amberlyts-15) can be used to significantly modify the product yield from the pyrolysis of algal biomass. The yield production comparison of catalytic and non-catalytic pyrolysis yields is shown in Figure 4.

It was found that employing the Amberlyst-15 catalyst throughout the pyrolysis increased the amount of bio-oil produced, which reached 24.9 wt% to 29.54 wt%. In terms of gaseous production, Amberlyst-15 produced 21.57 wt% of gas. This percentage continued to increase as the reaction temperature increased to 600 °C, because greater temperatures caused algae to break down quickly [38]. In contrast, the biochar yield was decreased by employing the Amberlyst-15 catalyst. A similar situation was found in the experimental results of catalytic pyrolysis by Tan et al. [39]. So, the acidity-basicity, pore size, and surface area of catalysts make it possible to turn

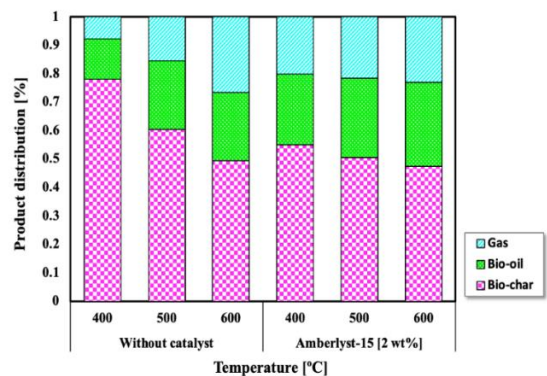


Figure 4. Effect of catalyst addition on products yield distribution

most biomass into products [40]. Mo et al. [37] applied catalytic pyrolysis of macroalgae and obtained 43.6 % bio-oil at 400 °C, which was higher than this study. This may be due to adjustments in the reactor types that were employed.

3.3. Characterization of bio-oil

3.3.1. FT-IR of Bio-oils Bio-oil has been analyzed using FT-IR to determine the presence of the various functional groups, as indicated by its different fundamental vibrational bands (Figure 5).

The presence of a -OH functional group was determined by observing a band at 3039 – 3158 cm^{-1} . These results, along with the previous result by Pato et al. [41] and Asadpour et al. [42], found that the dominant peak was at 3419.03 cm^{-1} , referring to the stretching vibrations of the -OH group. The asymmetric and symmetric -CH vibrations corresponded to two different vibrational bands at 2916 and 2850 cm^{-1} , respectively. The high hydrocarbon concentration in the bio-oil obtained at 600 °C allowed for observing the band with a high intensity of -CH. In the meantime, the basic vibration of ketone was detected in all of the bio-oils between 1698 and 1700 cm^{-1} . This bright band was detected in non-catalytic bio-oil containing more acid and ester molecules. A lower band at 1698 cm^{-1} was identified, which was attributed to the amide's conjugated carbonyl group, as reported by Biswas et al. [43]. Furthermore, the C = C vibration of alkenes, generated during the pyrolysis of macroalgae, was shown as the fundamental vibration at 1399–1408 cm^{-1} . At 1164–1214 cm^{-1} , the primary groups of aromatic compounds were found to be stretching; this showed that bio-oil was composed of aromatic compounds. Several groups associated with out-of-plane C-H bending have been found in the band region from 700 to 800 cm^{-1} . All bio-oils had similar peak patterns in their spectra; only the strength of the functional bands varied. The fundamental vibration of ketones and acids showed the lipid content

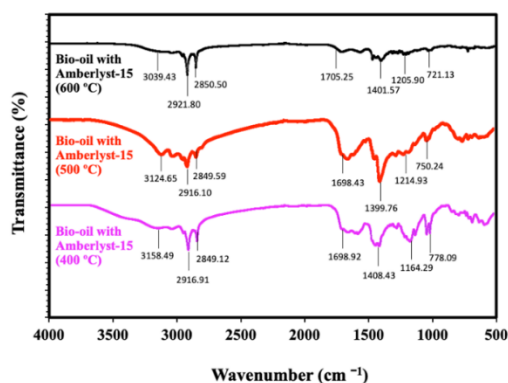
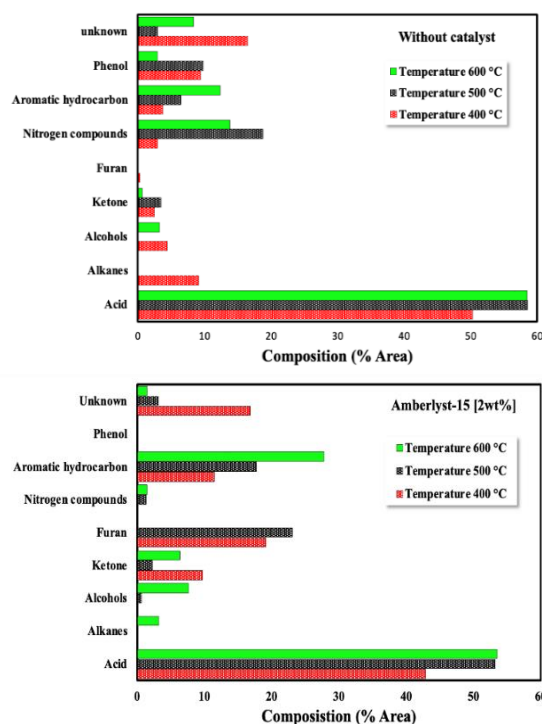


Figure 5. Fourier transform-infra red spectroscopy (FT-IR) of bio-oils

of macroalgae that changed into ester or amide compounds.

3.3.2. GC/MS Analysis of Bio-oil To identify the components found in bio-oils, a GC-MS analysis was carried out. It was shown that bio-oils used in catalytic reactions had a different chemical composition than those used in non-catalytic reactions. The percentages of peak areas for each type of chemical are shown in Figure 6(a). Based on their functional groups, the compositions of pyrolysis volatiles, such as phenols, furans, alkanes, and ketones, as well as acids, alcohols, aromatic hydrocarbons, and N-containing mixtures, were determined.

It can be observed that most of the *Ulva lactuca* pyrolysis bio-oil contains acids (50.3–58.5%), ketones (0.65– 3.5%), N-containing mixtures (3.1–18.8%), aromatic hydrocarbons (3.7–12.4%), phenol (2.9–9.7%) followed by a temperature of 400–600 °C respectively, as well as several other chemical compositions which are only found at a temperature of 400 °C such as alcohol (4.5%), alkanes (9.2%) and small amounts of furan. Introducing a catalyst to the pyrolysis reaction resulted in a significant change in the bio-oil's chemical composition. Catalytic pyrolysis (*Ulva lactuca*-Amberlyst-15 at 400–600 °C) bio-oil majorly contains acid (42.8–53.5%), ketones (2.3–9.7%), N-containing mixtures (1.3–1.5%), aromatic hydrocarbons (11.5–



(a)

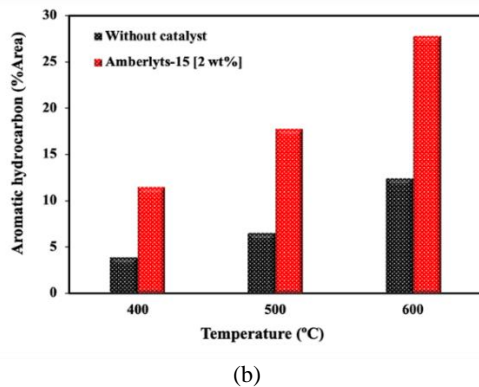


Figure 6. (a) GC/MS analysis of bio-oil (non-catalytic and catalytic pyrolysis), (b) The aromatics hydrocarbon produced from *Ulva lactuca* with and without catalyst

27.8%), at temperature 400–600 °C, respectively. This finding was also in line with a previous study by Xia et al. [44], who observed that at high temperatures, the polymerization and dehydrogenation of oxygen-containing organics probably led to aromatics formation. On the other hand, several chemical compositions were not detected at all reaction temperatures, including furan (19.1–23.1%), which was only detected at 400 and 500 °C, alcohol (0.6–7.6%) at 500 and 600 °C, and approximately 1.5–16% chemical composition that was not detected in pyrolysis integrated with the catalyst. Figure 6(a) shows that phenols, nitrogen-containing chemicals, furans, aromatic compounds, and acids dominate the pyrolysis bio-oil derived from the original macroalgae sample. However, due to the high oxygen concentration and corrosive, the acids can quickly degrade bio-oil, decreasing its quality. In addition, bio-oil can be challenging to utilize due to its high nitrogen concentration and complicated chemical composition. Therefore, it is essential to transform the bio-oils composition towards aromatic hydrocarbons and lower the concentration of acids and nitrogen-containing compounds. Amberlyst-15 and other catalysts substantially promoted the number of aromatic compounds while substantially reducing the formation of acids, phenols, and furans.

Figure 6(b) shows the aromatics hydrocarbon produced from *Ulva lactuca* without and with the Amberlyst-15 catalyst.

It can be pointed out that the aromatic hydrocarbon content in the bio-oil produced by catalytic pyrolysis of macroalgae increased as temperature, reaching a higher level than the original feedstock at temperatures ranging from 400 to 600 °C (11.5–27.8% area). Decarboxylation reactions contributed to hydrocarbon formation during catalytic pyrolysis [45].

3. 4. Rate of Aromatic Hydrocarbon Production

The kinetics of aromatic hydrocarbon production during

pyrolysis were examined to quantify the aforementioned temperature impacts. Assuming that the conversion process follows the first-order Arrhenius rate law in terms of the amount of aromatic hydrocarbons, the following equation can be obtained:

$$\frac{dah_x}{dt} = k_0 \left\{ \exp\left(\frac{-E_a}{RT}\right) \right\} (ah_0 - ah_x) \quad (4)$$

which leads to

$$ah_0 - ah_x = ah_0 \exp\left[-k_0 \left\{ \exp\left(\frac{-E_a}{RT}\right) \right\} t\right] \quad (5)$$

$$ah_{production} = \frac{ah_x}{ah_0} = 1 - \exp\left[-k_0 \left\{ \exp\left(\frac{-E_a}{RT}\right) \right\} t\right] \quad (6)$$

where ah_0 is the initial amount of aromatic hydrocarbon [%], ah_x is the amount of aromatic hydrocarbon of pyrolyzed bio-oil [%], k_0 is a pre-exponential factor [s^{-1}], E_a is activation energy [J/mol], R is the gas constant [$J \text{ mol}^{-1} \text{ K}^{-1}$], t is time [min], T is temperature [K].

The parameters in Equation (3) have been determined by fitting the experimental data of aromatic hydrocarbon production shown in Figure 7.

The production rates of aromatic hydrocarbons could be well explained by using an Arrhenius equation of the first order. By addressing kinetic parameters, activation energy (E_a) refers to the energy needed to break a bond for a reaction to occur. In contrast, the pre-exponential factor (A) denotes the rate at which the reaction takes place [46]. Catalytic pyrolysis (*Ulva lactuca*-Amberlyst-15) had an activation energy (E_a) of 15.3 kJmol^{-1} and pre-exponential factor (A) of 35.1 min^{-1} which was lower than that for the original pyrolysis feedstock (43.31 kJmol^{-1} , 47.5 min^{-1}) respectively. It shows that using Amberlyst-15 lowers the energy barrier of the pyrolysis process. This means that even though Amberlyst-15 may lower the energy barrier, pyrolysis steam in the pores of the catalyst goes more slowly. This is another reason solid material gets lower slowly when Amberlyst-15 is used because the reaction rate is slow; a second reaction occurred on the catalyst's surface, which led to coking [47].

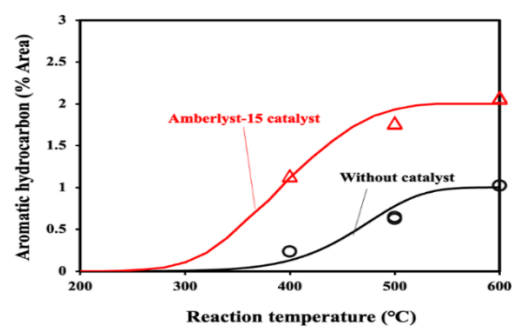


Figure 7. The aromatic hydrocarbon production from the experiment (symbol) and kinetic model (line) for both catalytic and non-catalytic pyrolysis

4. CONCLUSION

One possible thermochemical strategy for improving bio-oil yields and quality is the catalytic pyrolysis of *Ulva lactuca* aquatic biomass. At a maximum temperature of 600 °C, the Amberlyst-15 catalyst produced the greatest amount of bio-oil (29.54 wt%), in contrast to the non-catalytic pyrolysis yield (23.87 wt%). The composition of the pyrolysis liquid yield is improved by exchanging radicals, cracking, or compound ordering during catalytic pyrolysis. The acidity and framework of Amberlyst-15 significantly affected the distribution of product components, particularly aromatic hydrocarbon yield. In generating aromatic hydrocarbons in the upgraded bio-oils, the Amberlyst-15 catalyst was the most active, resulting in the greatest relative percentage of 27.78%. Finally, the production of aromatic hydrocarbons was modeled with first-order kinetics and an Arrhenius equation rate constant, and the reaction parameters were determined for both catalytic and non-catalytic pyrolysis.

5. ACKNOWLEDGEMENT

The present study was supported by the Indonesian Ministry of Research, Technology and Higher Education Grant Number 113/E5/PG.02.00.PT/2022. Amrullah is also grateful to the Department of Mechanical Engineering, Lambung Mangkurat University, South Kalimantan, Indonesia.

6. REFERENCES

- Lu, Q., Zhou, M. xing, Li, W. tao, Wang, X., Cui, M. shu, and Yang, Y. ping. "Catalytic fast pyrolysis of biomass with noble metal-like catalysts to produce high-grade bio-oil: Analytical Py-GC/MS study." *Catalysis Today*, Vol. 302, (2018), 169-179. <https://doi.org/10.1016/j.cattod.2017.08.029>
- Leong, W. H., Lim, J. W., Lam, M. K., Uemura, Y., and Ho, Y. C. "Third generation biofuels: A nutritional perspective in enhancing microbial lipid production." *Renewable and Sustainable Energy Reviews*, Vol. 91, (2018), 950-961. <https://doi.org/10.1016/j.rser.2018.04.066>
- Biswas, B., Singh, R., Krishna, B. B., Kumar, J., and Bhaskar, T. "Pyrolysis of azolla, sargassum tenerrimum and water hyacinth for production of bio-oil." *Bioresource Technology*, Vol. 242, (2017), 139-145. <https://doi.org/10.1016/j.biortech.2017.03.044>
- Mironova, N., Mateyuk, O., Biletska, H., Shevchenko, S., Kazimirova, L., Artamonov, B., Kravchuk, V., and Bloschynskyi, I. "Parametric Assessment of Macrophytes Ecological Niches in Solving Problems of Sand Quarry Lakes Phytomelioration," *Journal of Human, Earth, and Future*, Vol. 3, No. 4, (2022), 423-429.
- Amrullah, A., Farobie, O., Septarini, S., and Satrio, J. A. "Synergetic biofuel production from co-pyrolysis of food and plastic waste: reaction kinetics and product behavior." *Heliyon*, Vol. 8, No. 8, (2022), e10278. <https://doi.org/10.1016/j.heliyon.2022.e10278>
- Farobie, O., Syaftika, N., Masfuri, I., Rini, T. P., Lanank Es, D. P. A., Bayu, A., Amrullah, A., Hartulistiyoso, E., Moheimani, N. R., Karnjanakom, S., and Matsumura, Y. "Green algae to green fuels: Syngas and hydrochar production from *Ulva lactuca* via sub-critical water gasification." *Algal Research*, Vol. 67, No. 1, (2022), 102834. <https://doi.org/10.1016/j.algal.2022.102834>
- Yi, B., Chen, M., Gao, Y., Cao, C., Wei, Q., Zhang, Z., and Li, L. "Investigation on the co-combustion characteristics of multiple biomass and coal under O₂/CO₂ condition and the interaction between different biomass." *Journal of Environmental Management*, Vol. 325, (2023), 116498. <https://doi.org/10.1016/j.jenvman.2022.116498>
- Amrullah, A., Farobie, O., Bayu, A., Syaftika, N., Hartulistiyoso, E., Moheimani, N. R., Karnjanakom, S., and Matsumura, Y. "Slow Pyrolysis of *Ulva lactuca* (Chlorophyta) for Sustainable Production of Bio-oil and Biochar." *Sustainability (Switzerland)*, Vol. 14, No. 6, (2022), 1-14. <https://doi.org/10.3390/su14063233>
- Yang, G., Hu, Q., Hu, J., Yang, H., Yan, S., Chen, Y., Wang, X., and Chen, H. "Hydrogen-rich syngas production from biomass gasification using biochar-based nanocatalysts." *Bioresource Technology*, Vol. 379, (2023), 129005. <https://doi.org/10.1016/j.biortech.2023.129005>
- Batubara, F., Turmuzi, M., Irvan, I., and Yanqoritha, N. "Variations of Organic Loading Rate on Tofu Wastewater Degradation using Upflow Anaerobic Sludge Blanket Reactor by Modified Stover-Kincannon Model." *International Journal of Engineering Transactions C: Aspects*, Vol. 36, No. 3, (2023), 490-496. <https://doi.org/10.5829/ije.2023.36.03c.08>
- Chen, X., Chen, Y., Yang, H., Wang, X., Che, Q., Chen, W., and Chen, H. "Catalytic fast pyrolysis of biomass: Selective deoxygenation to balance the quality and yield of bio-oil." *Bioresource Technology*, Vol. 273, (2019), 153-158. <https://doi.org/10.1016/j.biortech.2018.11.008>
- Chow, M. C., Jackson, W. R., Chaffee, A. L., and Marshall, M. "Thermal treatment of algae for production of biofuel." *Energy and Fuels*, Vol. 27, No. 4, (2013), 1926-1950. <https://doi.org/10.1021/ef3020298>
- French, R., and Czernik, S. "Catalytic pyrolysis of biomass for biofuels production." *Fuel Processing Technology*, Vol. 91, No. 1, (2010), 25-32. <https://doi.org/10.1016/j.fuproc.2009.08.011>
- Biswas, B., Pandey, N., Bisht, Y., Singh, R., Kumar, J., and Bhaskar, T. "Pyrolysis of agricultural biomass residues: Comparative study of corn cob, wheat straw, rice straw and rice husk." *Bioresource Technology*, Vol. 237, (2017), 57-63. <https://doi.org/10.1016/j.biortech.2017.02.046>
- Amrullah, A., Farobie, O., and Widyanto, R. "Pyrolysis of purun tikus (*Eleocharis dulcis*): Product distributions and reaction kinetics." *Bioresource Technology Reports*, Vol. 13, (2021), 100642. <https://doi.org/10.1016/j.biteb.2021.100642>
- Idris, R., Chong, W. W. F., Ali, A., Idris, S., Hasan, M. F., Ani, F. N., and Chong, C. T. "Phenol-rich bio-oil derivation via microwave-induced fast pyrolysis of oil palm empty fruit bunch with activated carbon." *Environmental Technology and Innovation*, Vol. 21, (2021), 101291. <https://doi.org/10.1016/j.eti.2020.101291>
- Cheng, S., Shu, J., Xia, H., Wang, S., Zhang, L., Peng, J., Li, C., Jiang, X., and Zhang, Q. "Pyrolysis of Crofton weed for the production of aldehyde rich bio-oil and combustible matter rich bio-gas." *Applied Thermal Engineering*, Vol. 148, (2019), 1164-1170. <https://doi.org/10.1016/j.applthermaleng.2018.12.009>
- Xie, Q., Addy, M., Liu, S., Zhang, B., Cheng, Y., Wan, Y., Li, Y., Liu, Y., Lin, X., Chen, P., and Ruan, R. "Fast microwave-assisted catalytic co-pyrolysis of microalgae and scum for bio-oil production." *Fuel*, Vol. 160, (2015), 577-582. <https://doi.org/10.1016/j.fuel.2015.08.020>
- Yu, J., Maliutina, K., and Tahmasebi, A. "A review on the production of nitrogen-containing compounds from microalgal

- biomass via pyrolysis." *Bioresource Technology*, Vol. 270, (2018), 689-701. <https://doi.org/10.1016/j.biortech.2018.08.127>
20. Thangalazhy-Gopakumar, S., Adhikari, S., Chattanathan, S. A., and Gupta, R. B. "Catalytic pyrolysis of green algae for hydrocarbon production using H+ZSM-5 catalyst." *Bioresource Technology*, Vol. 118, (2012), 150-157. <https://doi.org/10.1016/j.biortech.2012.05.080>
 21. Hematkah, R., Majidian, N., Hallajisani, A., and Samipoorgiri, M. "Investigation of catalytic pyrolysis of spirulina for bio-oil production." *Arabian Journal of Chemistry*, Vol. 16, No. 5, (2023), 104691. <https://doi.org/10.1016/j.arabjc.2023.104691>
 22. Hita, I., Cordero-Lanzac, T., Bonura, G., Cannilla, C., Arandes, J. M., Frusteri, F., and Bilbao, J. "Hydrodeoxygenation of raw bio-oil towards platform chemicals over FeMoP/zeolite catalysts." *Journal of Industrial and Engineering Chemistry*, Vol. 80, (2019), 392-400. <https://doi.org/10.1016/j.jiec.2019.08.019>
 23. Anand, V., Gautam, R., and Vinu, R. "Non-catalytic and catalytic fast pyrolysis of Schizochytrium limacinum microalga." *Fuel*, Vol. 205, (2017), 1-10. <https://doi.org/10.1016/j.fuel.2017.05.04>
 24. Wang, S., Cao, B., Liu, X., Xu, L., Hu, Y., Afonaa-Mensah, S., Abomohra, A. E. F., He, Z., Wang, Q., and Xu, S. "A comparative study on the quality of bio-oil derived from green macroalga *Enteromorpha clathrata* over metal modified ZSM-5 catalysts." *Bioresource Technology*, Vol. 256, (2018), 446-455. <https://doi.org/10.1016/j.biortech.2018.01.134>
 25. Zainan, N. H., Srivatsa, S. C., Li, F., and Bhattacharya, S. "Quality of bio-oil from catalytic pyrolysis of microalgae *Chlorella vulgaris*." *Fuel*, Vol. 223, (2018), 12-19. <https://doi.org/10.1016/j.fuel.2018.02.166>
 26. Uslamin, E. A., Luna-Murillo, B., Kosinov, N., Brujninex, P. C. A., Pidko, E. A., Weckhuysen, B. M., and Hensen, E. J. M. "Gallium-promoted HZSM-5 zeolites as efficient catalysts for the aromatization of biomass-derived furans." *Chemical Engineering Science*, Vol. 198, (2019), 305-316. <https://doi.org/10.1016/j.ces.2018.09.023>
 27. Limlamthong, M., and Yip, A. C. K. "Recent advances in zeolite-encapsulated metal catalysts: A suitable catalyst design for catalytic biomass conversion." *Bioresource Technology*, Vol. 297, (2020), 122488. <https://doi.org/10.1016/j.biortech.2019.122488>
 28. Chen, L., Yu, Z., Fang, S., Dai, M., and Ma, X. "Co-pyrolysis kinetics and behaviors of kitchen waste and *Chlorella vulgaris* using thermogravimetric analyzer and fixed bed reactor." *Energy Conversion and Management*, Vol. 165, (2018), 45-52. <https://doi.org/10.1016/j.enconman.2018.03.042>
 29. Dewangan, A., Pradhan, D., and Singh, R. K. "Co-pyrolysis of sugarcane bagasse and low-density polyethylene: Influence of plastic on pyrolysis product yield." *Fuel*, Vol. 185, (2016), 508-516. <https://doi.org/10.1016/j.fuel.2016.08.011>
 30. Chen, C., Fan, D., Zhao, J., Qi, Q., Huang, X., Zeng, T., and Bi, Y. "Study on microwave-assisted co-pyrolysis and bio-oil of *Chlorella vulgaris* with high-density polyethylene under activated carbon." *Energy*, Vol. 247, (2022), 123508. <https://doi.org/10.1016/j.energy.2022.123508>
 31. White, J. E., Catallo, W. J., and Legendre, B. L. "Biomass pyrolysis kinetics: A comparative critical review with relevant agricultural residue case studies." *Journal of Analytical and Applied Pyrolysis*, Vol. 91, No. 1, (2011), 1-33. <https://doi.org/10.1016/j.jaap.2011.01.004>
 32. D'Almeida, A. L. F. S., Barreto, D. W., Calado, V., and D'Almeida, J. R. M. "Thermal analysis of less common lignocellulose fibers." *Journal of Thermal Analysis and Calorimetry*, Vol. 91, No. 2, (2008), 405-408. <https://doi.org/10.1007/s10973-007-8606-6>
 33. Chen, C., Zeng, T., Qi, Q., Qiu, H., Zhao, J., and Fan, D. "Microwave catalytic pyrolysis production and characterization of *Chlorella vulgaris* under different compound additives." *Journal of the Energy Institute*, Vol. 100, (2022), 160-169. <https://doi.org/10.1016/j.joei.2021.11.008>
 34. Kumar, A., Biswas, B., and Bhaskar, T. "Effect of cobalt on titania, ceria and zirconia oxide supported catalysts on the oxidative depolymerization of prot and alkali lignin." *Bioresource Technology*, Vol. 299, (2020), 122589. <https://doi.org/10.1016/j.biortech.2019.122589>
 35. Ye, Y., Zhang, Y., Fan, J., and Chang, J. "Novel method for production of phenolics by combining lignin extraction with lignin depolymerization in aqueous ethanol." *Industrial and Engineering Chemistry Research*, Vol. 51, No. 1, (2012), 103-110. <https://doi.org/10.1021/ie202118d>
 36. Yorgun, S., and Yildiz, D. "Slow pyrolysis of paulownia wood: Effects of pyrolysis parameters on product yields and bio-oil characterization." *Journal of Analytical and Applied Pyrolysis*, Vol. 114, (2015), 68-78. <https://doi.org/10.1016/j.jaap.2015.05.003>
 37. Mo, L., Dai, H., Feng, L., Liu, B., Li, X., Chen, Y., and Khan, S. "In-situ catalytic pyrolysis upgradation of microalgae into hydrocarbon rich bio-oil: Effects of nitrogen and carbon dioxide environment." *Bioresource Technology*, Vol. 314, (2020), 123758. <https://doi.org/10.1016/j.biortech.2020.123758>
 38. Yaman, E., Yargic, A. S., Ozbay, N., Uzun, B. B., Kalogiannis, K. G., Stefanidis, S. D., Pachatouridou, E. P., Iliopoulou, E. F., and Lappas, A. A. "Catalytic upgrading of pyrolysis vapours: Effect of catalyst support and metal type on phenolic content of bio-oil." *Journal of Cleaner Production*, Vol. 185, (2018), 52-61. <https://doi.org/10.1016/j.jclepro.2018.03.033>
 39. Tan, H., Yang, M., Chen, Y., Chen, X., Fantozzi, F., Bartocci, P., Tschentscher, R., Barontini, F., Yang, H., and Chen, H. "Preparation of aromatic hydrocarbons from catalytic pyrolysis of digestate." *Chinese Journal of Chemical Engineering*, Vol. 57, (2022), 1-9. <https://doi.org/10.1016/j.cjche.2022.09.002>
 40. Pütün, E. "Catalytic pyrolysis of biomass: Effects of pyrolysis temperature, sweeping gas flow rate and MgO catalyst." *Energy*, Vol. 35, No. 7, (2010), 2761-2766. <https://doi.org/10.1016/j.energy.2010.02.024>
 41. Pato, U., Ayu, D. F., Riftyan, E., Restuhadi, F., Pawenang, W. T., Firdaus, R., Rahma, A., and Jaswir, I. "Cellulose Microfiber Encapsulated Probiotic: Viability, Acid and Bile Tolerance during Storage at Different Temperature." *Emerging Science Journal*, Vol. 6, No. 1, (2022), 106-117. <https://doi.org/10.28991/ESJ-2022-06-01-08>
 42. Asadpour, R., Sapari, N. B., Hasnain Isa, M., and Kakooei, S. "Further study of adsorption of crude oils onto acetylated corn silk and its kinetics and equilibrium isotherm." *International Journal of Engineering, Transactions B: Applications*, Vol. 32, No. 2, (2019), 284-291. <https://doi.org/10.5829/ije.2019.32.02b.07>
 43. Biswas, B., Fernandes, A. C., Kumar, J., Muraleedharan, U. D., and Bhaskar, T. "Valorization of *Sargassum tenerrimum*: Value addition using hydrothermal liquefaction." *Fuel*, Vol. 222, (2018), 394-401. <https://doi.org/10.1016/j.fuel.2018.02.153>
 44. Xia, S., Yang, H., Lei, Shuaishuai, Lu, W., Cai, N., Xiao, H., Chen, Y., and Chen, H. "Iron salt catalytic pyrolysis of biomass: Influence of iron salt type." *Energy*, Vol. 262, (2023), 125415. <https://doi.org/10.1016/j.energy.2022.125415>
 45. LI, B., FENG, B., WU, K., and YANG, T. "Hydrodeoxygenation of lignin derived bio-oil into aromatic hydrocarbons over Ni-Cu-Ru/HZSM-5 catalyst." *Journal of Fuel Chemistry and Technology*, Vol. 51, No. 3, (2023), 358-365. [https://doi.org/10.1016/s1872-5813\(22\)60016-6](https://doi.org/10.1016/s1872-5813(22)60016-6)
 46. Zhang, S., Liang, Y., Qian, X., Hui, D., and Sheng, K. "Pyrolysis kinetics and mechanical properties of poly(lactic acid)/bamboo particle biocomposites: Effect of particle size distribution."

Nanotechnology Reviews, Vol. 9, No. 1, (2020), 524-533.
<https://doi.org/10.1515/ntrev-2020-0037>

47. Shahdan, N. A., Balasundram, V., Ibrahim, N., Isha, R., and Manan, Z. A. "Catalytic Co-pyrolysis of empty fruit bunch and

high-density polyethylene mixtures over rice husk ash: Thermogravimetric, kinetic and thermodynamic analyses." *Cleaner Engineering and Technology*, Vol. 9, (2022), 100538.
<https://doi.org/10.1016/j.clet.2022.100538>

COPYRIGHTS

©2023 The author(s). This is an open access article distributed under the terms of the Creative Commons Attribution (CC BY 4.0), which permits unrestricted use, distribution, and reproduction in any medium, as long as the original authors and source are cited. No permission is required from the authors or the publishers.



Persian Abstract

چکیده

تجزیه در اثر حرارت کاتالیزوری ماکروجلبک *Ulva lactuca* بر روی کاتالیزور Amberlyst-15 در دمای ۴۰۰، ۵۰۰ و ۶۰۰ درجه سانتیگراد مورد مطالعه قرار گرفت. مقایسه بین تجزیه در اثر حرارت کاتالیزوری و غیر کاتالیستی در تبدیل *Ulva lactuca* تعیین شد. به طرز جالبی مشخص شد که کاتالیزور Amberlyst-15 راندمان تولید روغن زیستی را بهبود می بخشد. بالاترین بازده روغن زیستی با ۲۹.۵۴ درصد وزنی در دمای ۶۰۰ درجه سانتی گراد با حضور کاتالیزور Amberlyst-15 بدست آمد. علاوه بر این، کاتالیزور Amberlyst-15 می تواند تولید گاز را تا بیش از ۷۳.۸۸ درصد افزایش دهد. این را می توان به این دلیل نسبت داد که تجزیه در اثر حرارت کاتالیزوری می تواند مولکول های کوچک بیشتری را که از طریق فرآیند ترک خوردگی فرار هستند، ترویج کند. گروه های عنصری و عاملی در روغن های زیستی پیرولیتیک از طریق آنالیز GC-MS شناسایی شدند. اسیدیته و ساختار کاتالیزور Amberlyst-15 به طور قابل توجهی بر توزیع اجزای محصول، به ویژه تشکیل هیدروکربن های آروماتیک، با بازده نسبی ۲۷.۷۸٪ تأثیر گذاشت. مدل سینتیکی مرتبه اول نشان داد که تولید هیدروکربن های آروماتیک از قانون آرنیوس پیروی می کند.



Design of a Circular Patch Antenna with Parasitic Elements for 5G Applications

S. Lamultree^{*a}, M. Phalla^a, P. Kunkritthanachai^a, C. Phongcharoenpanich^b

^a Faculty of Engineering, Rajamangala University of Technology Isan Khonkaen Campus, Khonkaen, Thailand

^b School of Engineering, King Mongkut's Institute of Technology Ladkrabang, Bangkok, Thailand

PAPER INFO

Paper history:

Received 20 May 2023

Received in revised form 26 June 2023

Accepted 09 July 2023

Keywords:

Circular Patch Antenna

Wideband Antenna

Parasitic Elements

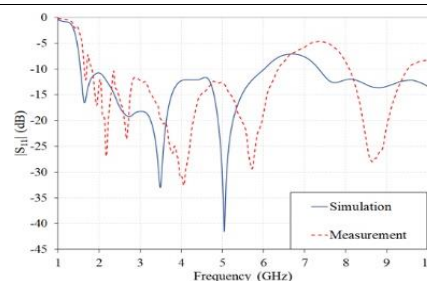
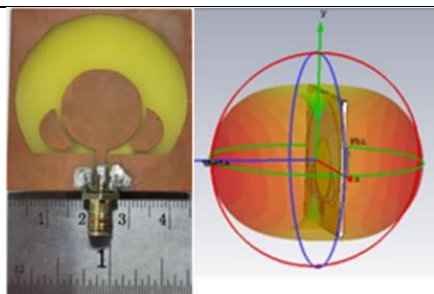
5G Applications

ABSTRACT

A design of a wideband bidirectional pattern antenna, accomplished by the integration of a circular patch, crescents as parasitic elements, encompassed by a circular ring adjoining the ground plane, to operate over the mid-band 5G sub-6 GHz applications is reported. It is come up with a copper grazed on FR4 substrate with relative permittivity of 4.3 and height of 1.6 mm. The proposed antenna is fed by a 50-ohm coplanar waveguide, which is printed on the same side of the radiating circular patch. A concise antenna model with dimensions of $45 \times 45 \times 0.6 \text{ mm}^3$ was made up and investigated to affirm the simulation outcomes. Good consistency was confirmed between experimental and simulation results. The proposed antenna has the benefit of bidirectional pattern with a good gain of 5.24 dBi and wide bandwidth covering of 111.4% (1.81-6.36 GHz) — it is one of good postulants for 5G new radiation application especially for indoor environment, narrow, and long path services area like corridor, tunnel, and train station, etc.

doi: 10.5829/ije.2023.36.09c.13

Graphical Abstract



NOMENCLATURE

w	width of the substrate	h	thickness of the substrate
l	length of the substrate	CR	circular ring
r_1	radius of the circular patch	CPW	coplanar waveguide
r_2	radius of the enforced-radiation circular ring	CWBPA	compact wideband bidirectional pattern antenna
r_m	radius of the crescent	DGS	defected ground structure
g_2	gap between the radiating circular patch and crescent	FBW	fractional bandwidth
s	space between the crescent and ground plane	GND	ground plane
t	thickness of copper layer	IBW	impedance bandwidth
l_f	length of feeding strip	RCP	radiating circular patch
w_f	width of feeding strip	RLBW	return loss bandwidth
l_g	length of ground plane	NR	new radio
g	gap between feed line and ground plane	UWB	ultra-wideband

*Corresponding Author Email: suthasinee.la@rmuti.ac.th (S. Lamultree)

Please cite this article as: S. Lamultree, M. Phalla, P. Kunkritthanachai, C. Phongcharoenpanich, Design of a Circular Patch Antenna with Parasitic Elements for 5G Applications, *International Journal of Engineering, Transactions C: Aspects*, Vol. 36, No. 09, (2023), 1686-1694

1. INTRODUCTION

With the swift enlargement of fifth generation (5G) and beyond wireless networks and exploitation of higher data transmission rates, increasing provocations have been resulted in advocate a large scale of ultramodern utility frameworks and utilizations with high reliability, low latency, lately [1, 2]. One of the 5G plans is to employ the sub-6 GHz band — n34(2010–2025 MHz), n38 (2570–2620 MHz), n40 (2300–2400 MHz), n41 (2496–2690 MHz), n46 (5150–5925 MHz), n77 (3300–4200 MHz), n79 (4400–5000 MHz), etc. — which, also covered mid-band of 5G (2 to 6 GHz), leading high data rates, huge capacity as well as good coverage from the essential number of available spectrums [3, 4]. Modern wireless communications stretch out to new standard applications, algorithms, propagation techniques [5, 6], vigorous hardware defiance as well as the relevant antenna design [7-10] fulfilling human needs. As the performance of the antenna results considerable influence on the accomplishment of the plenary communication systems. Lately, research on 5G antenna is very attractive and has been a continuing process [11-13]. For literal applications, the extensively utilized compact size and broadband antennas are more delightful [14-20]. Since, wideband antennas are a good advancement in the 5G new radiation (NR) applications and upcoming generations of wireless communication systems, as it would handle at widen frequency extend accordingly receding the use of miscellaneous antennas in a single device shrinking the mutual coupling and intervention in the system as well as economizing financial plan.

Massive wideband antennas were conducted and developed continuously over the past decade with multitudinous techniques [21-25]. To improve the impedance bandwidth (IBW), different shapes of main radiator had been modified as well as the ground plane (GND) structures [14, 18, 25]. Ghobadi, and Majidzadeh [14] presented the ultra-wideband (UWB) antenna that printed on FR4 substrate and operated over 2.9-16 GHz by applying a semi-circle-shaped-slot cutting from the GND to improve IBW. A microstrip-fed printed monopole antenna for super wide band antenna was introduced by Balani et al. [18] to obtain wide bandwidth, the main radiating patch had been modified by adjoining a pair of ears at the upper part of the radiator as well as modifying its partial GND, making its geometry complexity. With super wide IBW, the stabilized radiation properties with less distortion mainly at higher frequency could not avoid. Koma'rudin et al. [25] presented the staircase-shaped steps adding to the bottom section of the main radiator patch to ameliorate the IBW; however, the antenna geometry was more complicated gathering with the multi-layers structure. Varamini et al. [16] and Wang et al. [22] presented metasurface

techniques to make the widen bandwidth and antenna gain. Even though the planar scales of metasurface antennas are normally bulky, stint its utilization. Asmeida et al. [23] introduced the combination of adding different shapes of slot on the radiator and defected ground structure (DGS) to improve the IBW of 74.6% as well as preserve the polarity bandwidth. In addition, others possible techniques for refining the bandwidth of the antenna were implemented — the complexity of fractal structure [16, 21, 24], adding slots [17, 19], the stubs and addition elements of modified radiators [18, 20, 23], and parasitic loading [4, 15, 24], so on. Others in demand method to grant an expedient matching tuning mechanism by using balun and coupled feed was realized by Ta et al. [7] and Asmeida et al. [23]. Notwithstanding, the compactness and wideband coverage antenna for the 5G NR and upcoming generation wireless terminal stands still demand in taking steps forward the proportions and radiation properties to be stable.

This article, a study and design of a compact wideband bidirectional pattern antenna (CWBPA) for mid-band of 5G applications operated frequency ranging from 2 to 6 GHz which included the sub-6 GHz is proffered. The profit of this presented antenna is that the concise size, facile fabric, and bidirectional pattern operating over wide bandwidth. With these advantages, thereby, the proposed antenna is one of good selectness for 5G application—installing as the antenna at the base station especially along the narrow and long path service propagation areas like corridor, tunnel, train station and so on. The resultant of the supplemented elements of antenna fabrication will be analyzed and evaluated. In the study, the pivotal preliminary parameters are reckoned by using the formulas in section 2. From those parameters, simulation was kept on operated by CST microwave studio [26] to numerically discover the final set of parameters. Numerical and substantiation results are revealed thoroughly.

2. THE RATIONALE OF ANTENNA DESIGN

This section narrates the construction of the evolved antenna and the reasoning to the rear of using a pair of crescents in the design. In the design process, the coplanar waveguide (CPW) fed circular patch (Ant #1) was considered in the beginning. It comprised of a radiating circular patch (RCP) of radius r_1 printed on top of an FR4 substrate of the width w (a value 45 mm), the substrate length l (a value 45 mm) and fed by a 50- Ω CPW of GND length l_g , fed line width w_f , fed line length l_f and gap between feed line and GND g as shown in Figure 1(a). The Ant #1 provided an omnidirectional pattern with wide IBW (3.08-10 GHz) as depicted in Figures 2 (a) and 3. Subsequently, Ant #2 was formed by adding a circular ring (CR) of radius r_2 extending the

GND, as shown in Figure 1(b), to impose the radiation pattern propagating in forward and backward directions as plotted in Figure 2(b). An unintentional sake of this CR was that it also leashed the 10 dB return loss bandwidth (RLBW) to be widened (covered 1.8 to 9 GHz) and tended to be dual band since the $|S_{11}|$ around 4.8 GHz was worsened as shown in Figure 3. At this stage, a 10 dB RLBW covering the interested frequency band ranging from 2 to 6 GHz was uncompleted. The final stage of completing the CWBPA, a pair of crescents of radius r_m was gathered in the structure as parasitic elements beside the RCP with the gap g_2 of 1 mm as shown in Figure 1(c). Consequently, the 10 dB RLBW over the interested frequency band as well as the bidirectional pattern was achieved as shown in Figures 2(c) and 3.

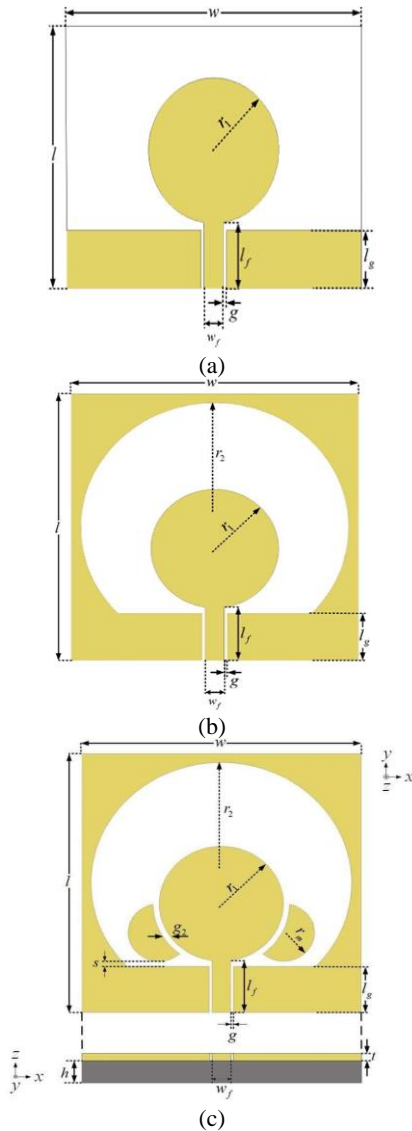


Figure 1. The structure of the developed antenna: (a) Ant #1 (b) Ant #2 and (c) proposed antenna

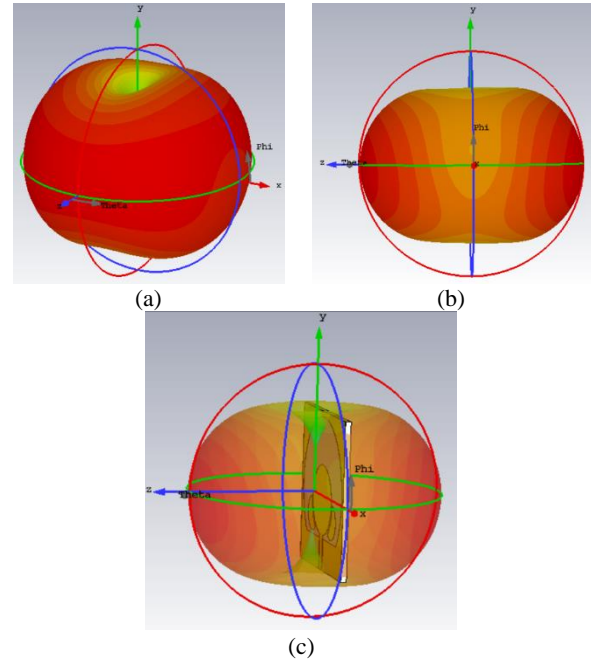


Figure 2. 3D radiation pattern of: (a) Ant #1 (b) Ant #2 and (c) proposed antenna

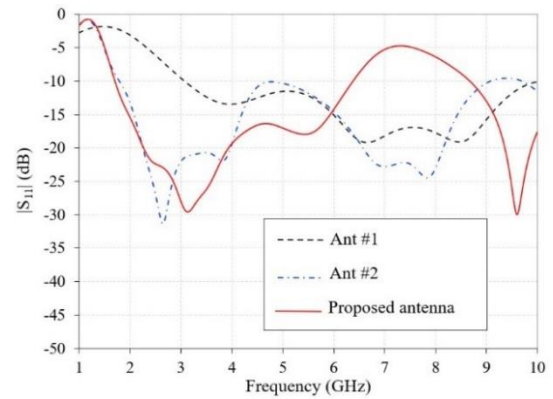


Figure 3. Comparing $|S_{11}|$ among three antennas

Based on the ensuing formulas, the initial parameters of the presented antenna are calculated and assigned [27].

$$r = \frac{F}{\left\{ 1 + \frac{2h}{\pi \epsilon_r F} \left[\ln \left(\frac{\pi F}{2h} \right) + 1.7726 \right] \right\}^{1/2}} \quad (1)$$

where, F is a function of resonant frequency for the dominant mode of TE_{11} as shown in Equation (2)

$$F = \frac{8.791 \times 10^9}{f_r \sqrt{\epsilon_r}} \quad (2)$$

r is referred to the design radius of the RCP of r_1 and an CR of radius r_2 ; ϵ_r is the relative permittivity of the FR4 substrate of 4.3; h is the thickness of the substrate of 0.16

cm. Note that the unit of h in Equation (1) is in cm. f_r is a resonant frequency—the radius of RCP of r_1 is designed to resonate 4 GHz while the radius of CR of r_2 is designed for f_r of 2 GHz. Considering the fringing effect in the above formulas, the initial r_1 of 10 mm and r_2 of 21 mm are come by, respectively. For the strip line of 50- Ω impedance matching, the width w_f and length l_f of feed line are computed by Equations (3)-(5) [27]:

$$\frac{w_f}{h} = \frac{2}{\pi} \left[\frac{B-1-\ln(2B-1)}{+\frac{\epsilon_r-1}{2\epsilon_r} \left\{ \ln(B-1) + 0.39 - \frac{0.61}{\epsilon_r} \right\}} \right] \quad (3)$$

where $B = 60\pi^2(Z_0\sqrt{\epsilon_r})^{-1}$ and Z_0 is the characteristic impedance of 50 Ω .

$$l_f = \lambda/4\sqrt{\epsilon_{\text{eff}}} \quad (4)$$

where ϵ_{reff} is the effective dielectric constant of the substrate.

$$\epsilon_{\text{reff}} = \frac{\epsilon_r+1}{2} + \frac{\epsilon_r-1}{2} \sqrt{1 + \frac{12h}{w_f}} \quad (5)$$

For the gap g between feed line and GND of CPW, it is related the 50-ohm impedance Z_0 in Equation (6) [28]:

$$Z_0 = 30\pi K'(k) / \sqrt{\epsilon_{\text{eff}}} K(k) \quad (6)$$

where $K(k)$ and $K'(k)$ are the complete elliptic integral of the first kind

$$K(k) = \int_0^{\phi} \frac{d\theta}{\sqrt{1-k^2\sin^2\theta}}, \quad \begin{cases} 0 \leq k^2 < 1 \\ 0 \leq \phi < \frac{\pi}{2} \end{cases} \quad (7)$$

$$K'(k) = K(k') = \sqrt{1-k^2} \quad (8)$$

where the ratio of $K(k)/K'(k)$ and k is defined as follows:

$$\frac{K(k)}{K'(k)} = \begin{cases} \frac{\pi}{\ln[2(1+\sqrt{k'})/(1-\sqrt{k'})]} & 0 \leq k \leq 0.707 \\ \frac{1}{\pi} \ln[2(1+\sqrt{k})/(1-\sqrt{k})] & 0.707 \leq k \leq 1 \end{cases} \quad (9)$$

and

$$k = w_f / (2g + w_f) \quad (10)$$

As the results, the w_f of 3 mm, l_f of 10 mm and g of 0.45 mm are assigned throughout the report. Note that the length of GND below the RCP of l_g is 9 mm.

Moreover, the radius r_m of the crescent beside the RCP is as initially calculated by Equation (11) [29]:

$$r_m = \frac{72 - sf_m}{2.25f_m} \quad (11)$$

where f_m is the design frequency (the unit of f_m in Equation (11) is in GHz), and s is the spacing between the crescent and GND (the value of 1 mm) and the unit of r_m is in mm.—this work the radius r_m is designed at the frequency of 4.8 GHz, therefore, the initial r_m is 6 mm.

All satisfactory parameters are acquired using the CST simulation and sorted in Table 1. To confirm the simulation outcome, a prototype of CWBPA is made up following the designed dimensions in Table 1 as shown in Figure 4. The CWBPA prototype is soldered to a 50-ohm SMA connector for extending to a coaxial feed line. The $|S_{11}|$, 2D radiation patterns and antenna gain of the presented CWBPA are evaluated and demonstrated by using E5063A network analyzer.

3. RESULTS AND DISCUSSION

The simulation and measured results of the proposed CWBPA are exposed in this section. In the simulation process, the SMA connector excludes the antenna model to focus on only antenna properties. However, the antenna model with SMA is considered in the final stage. From the developed CWBPA by adding a pair of crescents in the previous section, the radius r_m , gap between patch g_2 and the spacing s are demonstrated.

TABLE 1. Selected best values for parameters of the CWBPA

Parameter	Value (mm)	Parameter	Value (mm)
w	45	t	0.035
l	45	l_f	10
r_1	10	w_f	3
r_2	21	l_g	9
r_m	5	g	0.45
g_2	1	h	1.6
s	1		

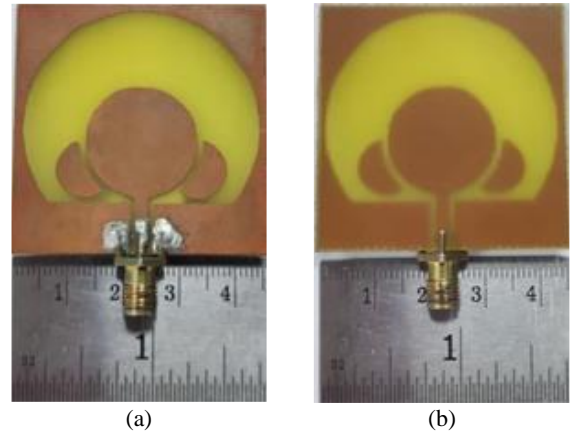


Figure 4. CWBPA prototype: (a) front view, (b) rear view

The effect of r_m on $|S_{11}|$ is considered by varying r_m 3 to 7 mm as plotted in Figure 5. Noticeably, the larger radius, as the narrower 10 dB RLBW is attained. For the compelling frequency band ranging from 2 to 6 GHz for mid-band 5G, the smaller r_m offers the $|S_{11}|$ worsened around 4.8 GHz, while the r_m of 6 and 7 mm cannot offer the 10 dB return loss over the considering band. This work, the radius r_m of 5 mm is selected because it proffers a good $|S_{11}|$ over the considering frequency band.

Moreover, the varying gab g_2 between the crescent and the RCP of values 0, 1 and 2 mm is also studied on its effect to the $|S_{11}|$ as shown in Figure 6. Obviously, the $|S_{11}|$ is worsened when the crescent adjoins the RCP ($g_2=0$) — it provides the narrow RLBW covering 1.7 to 2.54 GHz and 4.43 to 5.05 GHz. The larger gab g_2 yields the wider 10 dB RLBW — for the g_2 of 1, and 2 mm, it covers the frequency ranging from 1.71 to 6.38 GHz, and 1.72 to 6.43 GHz, respectively. Nonetheless, focusing on the interesting frequency band (2 to 6 GHz), g_2 of 1 mm furnishes the overall trend of $|S_{11}|$ better than the value 2 mm since g_2 of 2 mm offers the $|S_{11}|$ near the value -10 dB at 4.5 GHz. For that reason, the g_2 of 1 mm is selected. Additionally, the influence of the space between the crescent and GND, s , is also considered by varying the spacing s of 1, 3 and 6 mm as depicted in Figure 7. The further the spacing s as the wider 10 dB RLBW is achieved, contrast to the worsen $|S_{11}|$ occurrence around 4.5 GHz. Among these three different values, the spacing s of 1 mm impacts on the excellent $|S_{11}|$ over the interesting frequency band. Accordingly, the spacing s of 1 mm is chosen. Therefore, the CWBPA is achieved with the 10 dB RLBW of 1.71–6.38 GHz. At the final stage of the design, for the interested band (2 to 6 GHz), the proposed CWBPA comes up with the total efficiency of more than 81.7%, the minimum and maximum simulated gains of 2.63 dBi and 5.55 dBi and minimum and maximum measured gains of 2.33 dBi and 5.24 dBi, respectively as shown in Figure 8.

To affirm the simulation, the experimental process of testing $|S_{11}|$ and radiation pattern of the developed

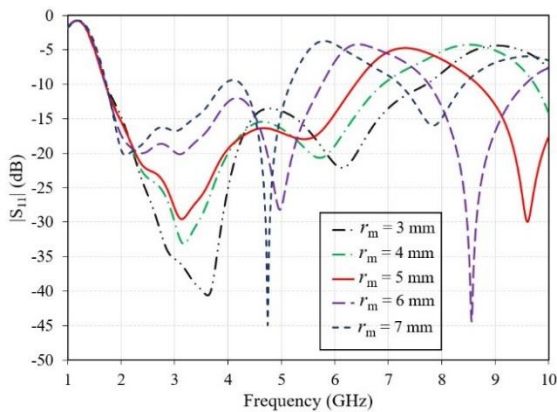


Figure 5. $|S_{11}|$ for various r_m

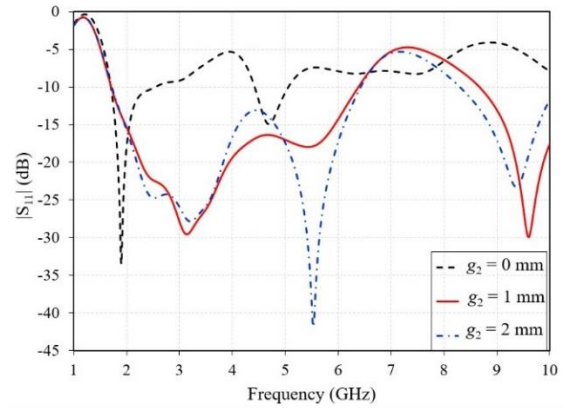


Figure 6. $|S_{11}|$ for various g_2

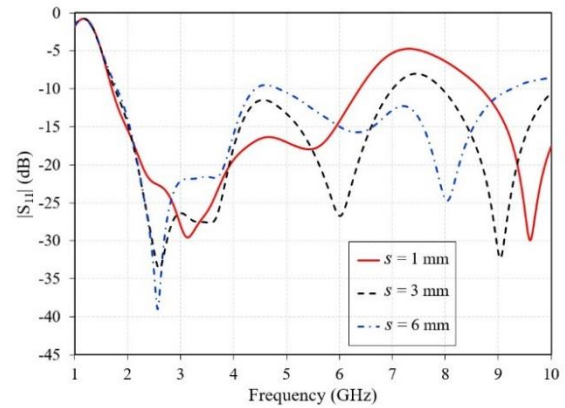


Figure 7. $|S_{11}|$ for various s

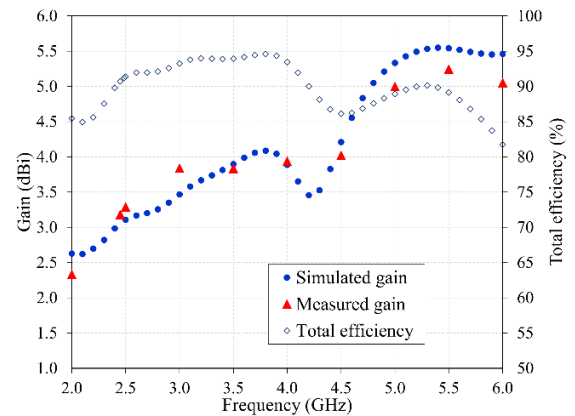


Figure 8. Gain and efficiency of the developed CWBPA

CWBPA is set up. Figure 9 exhibits the numerical and experimental $|S_{11}|$ for various frequency ranging from 1 GHz to 10 GHz. Visibly, the measured $|S_{11}|$ are reasonably in nice agreement the simulation results covering the 10 dB RLBW over the mid-band of 5G applications — the measured $|S_{11}|$ is 1.81–6.36 GHz covered the fractional bandwidth (FBW) of 111.4% and

the simulation is 1.55–6.01 GHz covered the FBW of 118%. Note that the simulation in Figure 9 includes the SMA connector where with it is like the actual ambient that the antenna is connected to the cable via SMA connector.

Besides the impedance characteristics, the 2D radiation pattern in xz - and yz -planes at the frequencies of 2, 4 and 6 GHz is also examined as demonstrated in Figures 10-12. Evidently, the tested radiation patterns follow the common trend and acceptable agreement with the simulated results and the values do not deviate much from each other. The deviation is likely to be from a minor difference in the numerical and experimental setup. This proposed CWBPA yields a bidirectional pattern, linear polarization, peak simulated gains of 2.63/3.89/5.46 dBi and tested gains of 2.33/3.94/5.05 dBi at the operating frequencies of 2/4/6 GHz, respectively. In addition, the simulated and measured HPBWs in xz -plane are 162.6/104.3/65.2 degree and 157/88/48 degree, respectively. For yz -plane, the simulated and measured results are 84.4/73.3/53.4 degree and 86/62/56 degree, respectively. Note that the level of cross-polarization in xz -plane is less than -20 dB for all intended frequency ranges, while the high level of cross-polarization in yz -plane is achieved at a frequency higher than 4 GHz.

Over and above, the performance of the proposed CWBPA was bearded comparison with current compact,

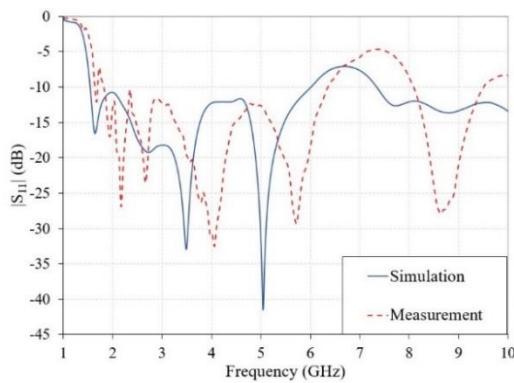


Figure 9. Simulated and measured $|S_{11}|$

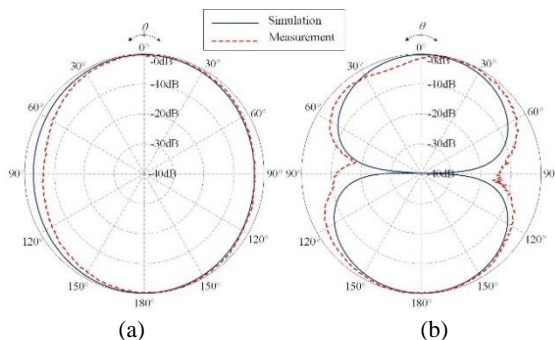


Figure 10. Radiation pattern at 2 GHz: (a) xz -plane and (b) yz -plane

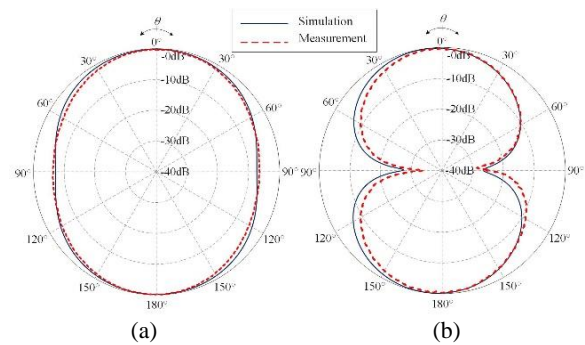


Figure 11. Radiation pattern at 4 GHz: (a) xz -plane and (b) yz -plane

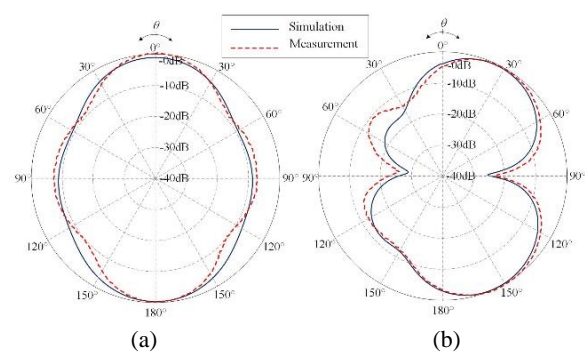


Figure 12. Radiation pattern at 6 GHz: (a) xz -plane and (b) yz -plane

wideband and 5G antennas published between 2017 to 2023 as tabulated in Table 2. The antenna implemented by Paul et al. [4] using RT5880, larger dimension offering an omnidirectional pattern with lower gain covering the narrower bandwidth was proposed. The geometry of the antenna was uncomplicated. The antenna dimensions reported in literature [7, 12-13, 25] had a larger size, more complexity, provided unidirectional pattern covering narrower bandwidth. Ta et al. [7] and Saleh et al. [13] offered a higher gain, while Cai et al. [12] offered a lower gain compared to this work. The antenna offered by Koma'rudin et al. [25] faintly higher gain. The antenna implemented by Samsuzzaman and Tariqul Islam [17] using FR4 substrate, approximately the same electric proportions offering a bidirectional pattern with faintly lower gain, but it operated covering wider bandwidth. Additionally, Yazdani et al. [10] proposed the array arrangement antenna implemented by different material, larger size, provided the stable bidirectional pattern covering three different bands, narrower bandwidth, and higher gains in the second and the third bands. Another work, the smaller proportions antenna, implemented by the same material, more complicated structure, provided a bidirectional pattern with lower gain covering a narrower bandwidth was presented by Sonu et al. [20]. Asmeida et al. [23] implemented an omnidirectional pattern using different

TABLE 2. Comparison between previous studies and this current research

Ref.	Size (λ)	Sub.	Patt.	FBW (%)	Gain (dBi)	Com.
[4]	0.36×0.36×0.01	RT 5880	Omni	44.5	3.51	L
[7]	n/a×0.87×0.02	RT 5880	Uni	36.2	5.8	M
[10]	0.31×0.28×0.002	RO 4003	Bi	9.5/21.9/12.2	1/6/10	L
[12]	1.65×0.83×0.08	FR4	Uni	35.3	3.5	H
[13]	1.07×1.07×0.61	RT 5880	Uni	21.4	12.7	H
[17]	0.29×0.29×0.01	FR4	Bi	126.85	4.85	L
[20]	0.20×0.22×0.01	FR4	Bi	61.1	3.5	M
[23]	0.28×0.35×0.08	RT 5880	Omni	74.6	3.6	L
[25]	0.66×0.76×0.01	Felt	Uni	79.8	5.51	M
This work	0.27×0.27×0.01	FR4	Bi	111.4	5.24	L

material with a slightly larger dimension, proffered a narrower bandwidth and lower gain than this proposed CWBPA. With a simple fabric, concise proportions, bidirectional pattern covered wideband transition sub-6 GHz 5G NR; thereby, this proposed CWBPA is one of the good candidates for 5G NR applications.

λ means a free-space wavelength at the lowest operated frequency; abbreviations: n/a (not applicable), Sub. (substrate of material), Patt. (pattern), Uni (unidirectional), Omni (omnidirectional), Bi (bidirectional), Com. (complexity), L (low), M (medium), H (high).

In this work, a single antenna has been studied, designed, analyzed, and illustrated its effecting in the basic antenna theory and tested in the laboratory. The 10 dB return loss, radiation pattern and gain of the single antenna have been evaluated. Nevertheless, it conveys some significant concepts for the antenna design and application.

4. CONCLUSION

A design of a CWBPA, contrived by the circular patch, circumscribed in the circular ring, incorporated with the parasitic elements beside the radiating patch, covering the sub-6 GHz 5G NR frequency band has been reported. It is printed on the top side of FR4 substrate, fed by 50-ohm CPW, and adjoined to the coaxial line via SMA connector. The key role of ameliorating the 10 dB return loss bandwidth of the presented antenna is that the pair of parasitic crescents as disclosed. This CWBPA yields the corresponding FBW of 111.4% (1.81–6.36 GHz) covering the mid-band 5G application, linearly polarized, peak gain of 5.24 dBi and the total efficiency of more than 81.7%. The experimental $|S_{11}|$, 2D radiation pattern and gain insist nifty the simulation results. With the

compactness proportions, an effortless structure, bidirectional pattern accompanied by wideband operation frequency and high gain, this proposed antenna is one of good potential candidates for subbase station antenna to service at indoor environment, the long and narrow path areas like troll, train station, tunnel, sky train stations, etc.

5. ACKNOWLEDGMENTS

This research project is supported by Rajamangala University of Technology Isan. Contract No. ENG3/66.

6. REFERENCES

1. Sonkki, M., Antonino-Daviu, E., He, D. and Myllymäki, S., "Advanced simulation methods of antennas and radio propagation for 5g and beyond communications systems", *International Journal of Antennas and Propagation*, Vol. 2020, (2020), 1-3. <https://doi.org/10.1155/2020/4387494>
2. Dicandia, F.A., Fonseca, N.J., Bacco, M., Mugnaini, S. and Genovesi, S., "Space-air-ground integrated 6g wireless communication networks: A review of antenna technologies and application scenarios", *Sensors*, Vol. 22, No. 9, (2022), 3136. <https://doi.org/10.3390/s22093136>
3. Hussain, S., Qu, S.-W., Sharif, A.B., Abubakar, H.S., Wang, X.-H., Imran, M.A. and Abbasi, Q.H., "Current sheet antenna array and 5g: Challenges, recent trends, developments, and future directions", *Sensors*, Vol. 22, No. 9, (2022), 3329. <https://doi.org/10.3390/s22093329>
4. Paul, L.C., Saha, H.K., Rani, T., Mahmud, M.Z., Roy, T.K. and Lee, W.-S., "An omni-directional wideband patch antenna with parasitic elements for sub-6 ghz band applications", *International Journal of Antennas and Propagation*, Vol. 2022, (2022). <https://doi.org/10.1155/2022/9645280>
5. Firdaus, F., Fadhillah, I., Ahmad, N. and Mohd Alic, A., "A light solution for device diversity problem in a wireless local area network fingerprint indoor positioning system", *International*

- Journal of Engineering, Transaction A: Basics*, Vol. 36, No. 4, (2023), 649-658. doi: 10.5829/IJE.2023.36.04A.05.
6. Sridher, T., Sarma, A. and Naveen Kumar, P., "Performance evaluation of onboard wi-fi module antennas in terms of orientation and position for iot applications", *International Journal of Engineering, Transaction A: Basics*, Vol. 35, No. 10, (2022), 1918-1928. doi: 10.5829/IJE.2022.35.10A.11.
 7. Ta, S.X., Choo, H. and Park, I., "Broadband printed-dipole antenna and its arrays for 5g applications", *IEEE Antennas and Wireless Propagation Letters*, Vol. 16, (2017), 2183-2186. doi: 10.1109/LAWP.2017.2703850.
 8. Saraereh, O.A., "A novel broadband antenna design for 5g applications", *CMC-Comput. Mater. Continua*, Vol. 67, No. 1, (2021), 1121-1136. <https://doi.org/10.32604/cmc.2021.015066>
 9. Patnaik, A. and Kartikeyan, M., "Compact dual and triple band antennas for 5g-iot applications", *International Journal of Microwave and Wireless Technologies*, Vol. 14, No. 1, (2022), 115-122. <https://doi.org/10.1017/S1759078721000301>
 10. Yazdani, R., Aliakbarian, H., Sahraei, A. and Vandenbosch, G.A., "A compact triple-band dipole array antenna for selected sub 1 ghz, 5g and wifi access point applications", *IET Microwaves, Antennas & Propagation*, Vol. 15, No. 15, (2021), 1866-1876. <https://doi.org/10.1049/mia2.12200>
 11. Abolade, J.O., Konditi, D.B., Mpele, P.M., Orimogunje, A.M. and Oguntoye, J.P., "Miniaturized dual-band antenna for gsm1800, wlan, and sub-6 ghz 5g portable mobile devices", *Journal of Electrical and Computer Engineering*, Vol. 2022, (2022). doi: 10.1155/2022/5455915.
 12. Cai, J., Zhang, J., Xi, S., Huang, J. and Liu, G., "A wideband eight-element antenna with high isolation for 5g new-radio applications", *Applied Sciences*, Vol. 13, No. 1, (2022), 137. <https://doi.org/10.3390/app13010137>
 13. Saleh, C.M., Almajali, E., Jarndal, A., Yousaf, J., Alja' Afreh, S.S. and Amaya, R.E., "Wideband 5g antenna gain enhancement using a compact single-layer millimeter wave metamaterial lens", *IEEE Access*, Vol. 11, (2023), 14928-14942. doi: 10.1109/JSAC.1987.1146527.
 14. Ghobadi, C. and Majidzadeh, M., "Multi attribute analysis of a novel compact uwb antenna with via-fed elements for dual band notch function", *International Journal of Engineering, Transactions A: Basics*, Vol. 27, No. 10, (2014), 1565-1572. doi: 10.5829/idosi.ije.2014.27.10a.10.
 15. Ding, K., Gao, C., Zhang, B., Wu, Y. and Qu, D., "A compact printed unidirectional broadband antenna with parasitic patch", *IEEE Antennas and Wireless Propagation Letters*, Vol. 16, (2017), 2341-2344. doi: 10.1109/LAWP.2017.2718000.
 16. Varamini, G., Keshtkar, A. and Naser-Moghadasi, M., "Compact and miniaturized microstrip antenna based on fractal and metamaterial loads with reconfigurable qualification", *AEU-International Journal of Electronics and Communications*, Vol. 83, (2018), 213-221. doi: 10.1016/j.aeue.2017.08.057.
 17. Samsuzzaman, M. and Islam, M.T., "Circularly polarized broadband printed antenna for wireless applications", *Sensors*, Vol. 18, No. 12, (2018), 4261. <https://doi.org/10.3390/s18124261>
 18. Balani, W., Sarvagya, M., Samasgikar, A., Ali, T. and Kumar, P., "Design and analysis of super wideband antenna for microwave applications", *Sensors*, Vol. 21, No. 2, (2021), 477. <https://doi.org/10.3390/s21020477>
 19. Qi, Z., Ding, X., Yang, W. and Chen, J., "A compact broadband planar inverted-f antenna with dual-resonant modes", *Applied Sciences*, Vol. 12, No. 17, (2022), 8915. <https://doi.org/10.3390/app12178915>
 20. Rana, S., Verma, J. and Gautam, A.K., "A wideband circularly polarized cpw-fed diamond shape microstrip antenna for wlan/wimax applications", *Progress In Electromagnetics Research C*, Vol. 131, (2023), 25-33. doi: 10.2528/PIERC22122106.
 21. Biswas, B., Ghatak, R. and Poddar, D., "A fern fractal leaf inspired wideband antipodal vivaldi antenna for microwave imaging system", *IEEE Transactions on Antennas and Propagation*, Vol. 65, No. 11, (2017), 6126-6129. doi: 10.1109/TAP.2017.2748361.
 22. Wang, J., Wong, H., Ji, Z. and Wu, Y., "Broadband cpw-fed aperture coupled metasurface antenna", *IEEE Antennas and Wireless Propagation Letters*, Vol. 18, No. 3, (2019), 517-520. doi: 10.1109/LAWP.2019.2895618.
 23. Asmeida, A., Abidin, Z.Z., Mohd Shah, S., Kamarudin, M.R., Malek, N.A. and Nebhen, J., "Wideband crescent-shaped slotted printed antenna with radiant circular polarisation", *International Journal of Antennas and Propagation*, Vol. 2021, (2021), 1-12. <https://doi.org/10.1155/2021/9975679>
 24. Hussain, M., Naqvi, S.I., Awan, W.A., Ali, W.A.E., Ali, E.M., Khan, S. and Alibakhshikenari, M., "Simple wideband extended aperture antenna-inspired circular patch for v-band communication systems", *AEU-International Journal of Electronics and Communications*, Vol. 144, (2022), 154061. <https://doi.org/10.1016/j.aeue.2021.154061>
 25. Koma'rudin, N., Zakaria, Z., Althwayb, A., Lago, H., Alsariera, H., Nornikman, H., Al-Gburi, A. and Soh, P., "Directional wideband wearable antenna with circular parasitic element for microwave imaging applications", (2022). <https://doi.org/10.32604/cmc.2022.024782>
 26. Studio, C., "Cst studio suite 3d em simulation and analysis software", *CST Studio Suite*, (2018).
 27. Balanis, C.A., "Antenna theory: Analysis and design, John wiley & sons, (2016).
 28. Collin, R.E., "Foundations for microwave engineering, John Wiley & Sons, (2007).
 29. Kumar, G. and Ray, K.P., "Broadband microstrip antennas, Artech house, (2002).

COPYRIGHTS

©2023 The author(s). This is an open access article distributed under the terms of the Creative Commons Attribution (CC BY 4.0), which permits unrestricted use, distribution, and reproduction in any medium, as long as the original authors and source are cited. No permission is required from the authors or the publishers.



Persian Abstract

چکیده

طراحی یک آنتن الگوی دو طرفه باند پهن، که با ادغام یک پیچ دایره‌ای، هلال‌ها به‌عنوان عناصر انگلی، احاطه‌شده توسط یک حلقه دایره‌ای مجاور سطح زمین، برای کار بر روی برنامه‌های باند متوسط G5 زیر 6 گیگاهرتز، انجام می‌شود. با مسی که بر روی بستر FR4 با گذردهی نسبی 4.3 و ارتفاع 1.6 میلی‌متر طراحی و ساخته شده است. آنتن پیشنهادی توسط یک موج بر همسطح 50 اهم تغذیه می‌شود که در همان سمت وصله دایره‌ای تابشی چاپ شده است. یک مدل آنتن مختصر با ابعاد $45 \times 45 \times 0.7$ میلی‌متر مکعب ساخته شد و برای تأیید نتایج شبیه‌سازی مورد بررسی قرار گرفت. سازگاری خوب بین نتایج تجربی و شبیه‌سازی تأیید شد. آنتن پیشنهادی از مزایای الگوی دو طرفه با بهره‌خوب 5.24 dBi و پوشش پهنای باند گسترده 111.4٪ (1.81-6.36 گیگاهرتز) برخوردار است - این یکی از پیشنهادهای خوب برای کاربرد تابش جدید G5 به ویژه برای محیط داخلی، باریک و طولانی است. منطقه خدمات مسیر مانند راهرو، تونل و ایستگاه قطار و غیره.



Effect of nGO on Morphology, Mechanical Properties and Thermal Behavior of PLA/nGO Sheets Before and After Thermoforming: An Experimental Study

S. Honarmandnia^{a,b}, H. Shahrajabian^{*a,b}

^a Department of Mechanical Engineering, Najafabad branch, Islamic Azad University, Najafabad, Iran

^b Modern Manufacturing Technologies Research Center, Najafabad Branch, Islamic Azad University, Najafabad, Iran

PAPER INFO

Paper history:

Received 01 July 2023

Received in revised form 23 July 2023

Accepted 25 July 2023

Keywords:

Poly Lactic Acid

Graphene Oxide Nanoparticles

Thermoforming Process

Tensile Test

Thickness Distribution

Differential Scanning Calorimetry Thermal

Test

ABSTRACT

Today, contrary to the benefits and advantages that the use of polymer materials has had for humans, the use of these materials has caused environmental problems for human life due to their non-degradability in nature. Therefore, the use of biodegradable polymers such as polylactic acid (PLA) is increasing. One of the main applications of plastic materials is the production of disposable containers. In this research, the thermoforming process of PLA sheets reinforced with graphene oxide nanoparticles (nGO) (0.4 and 1 wt.%) was investigated. Scanning electron microscopy (SEM) and X-ray diffraction (XRD) were used to study the morphology of the samples before and after thermoforming. The mechanical properties before and after the thermoforming process were investigated by tensile test. The results showed that after the thermoforming process, the tensile strength of the sheets significantly increased, so that for the sample containing 1wt.% of nGO, the tensile strength increased by about 70%. The results of the thickness distribution investigation showed that the lowest amount of thickness reduction, approximately 68%, is related to the sample containing 1 wt. % of nGO. The results of the DSC thermal test showed that the degree of crystallinity of the samples significantly decreased after thermoforming.

doi: 10.5829/ije.2023.36.09c.14

NOMENCLATURE

χ_c	Degree of crystallinity	ΔH_m^c	The heat of diffusion
ΔH_m	The melting enthalpy		

1. INTRODUCTION

Plastics based on petroleum materials such as polypropylene, polyethylene, polystyrene, and polyethylene terephthalate are strong, easy to process, durable, and relatively cheap. However, due to non-biodegradability, it creates problems when sending these materials to the waste stream. Biodegradable polymers have the potential to be a solution to the problem of plastic waste along with decreasing availability of landfills, global warming caused by increasing amounts of carbon dioxide in the atmosphere, and efforts to find sustainable or renewable raw materials. One of the most widely used biodegradable plastics is polylactic acid

(PLA) [1]. Polylactic acid is a popular biodegradable and biocompatible polyester obtained from the condensation of lactic acid extracted from renewable sources such as corn, sugarcane, and sugar beet pomace [2]. Recent advances in the polymerization industry of PLA, which have led to a reduction in the price of this polymer material, have made PLA able to compete with oil-based industrial polymers in terms of price [3]. Although this polymer has advantages such as environmental compatibility, high strength, and modulus, and a cost comparable to petroleum-based polymers, its inherent fragility, low hydrophilicity, and gas permeability limit its use. Adding nano fillers in low content such as nano-clay [4, 5], cellulose nanofiber /Ag [6], carbon nanotube

*Corresponding Author Institutional Email:

h.shahrajabian@pmc.iaun.ac.ir (H. Shahrajabian)

Please cite this article as: S. Honarmandnia, H. Shahrajabian, Effect of nGO on Morphology, Mechanical Properties and Thermal Behavior of PLA/nGO Sheets Before and After Thermoforming: An Experimental Study, *International Journal of Engineering, Transactions C: Aspects*, Vol. 36, No. 09, (2023), 1695-1703

[7], silica [8], silicon carbide [9], and titanium oxide [10] increases the mechanical, thermal, electrical and antibacterial properties of the polymer matrix.

Recent researches have been shown that nano graphene oxide (nGO) is a suitable alternative for nano-clay in polymer matrix due to low density, high thermal conductivity, and high mechanical properties [11-14]. One of the attractive features of nGO is good interaction and compatibility with polymer matrices due to the polar structures of GO (containing carbonyls, hydroxyls, and epoxides groups) [15]. Sharifiana and Shahrajabian [16] increased the elastic modulus and strength of the PLA matrix by 32% and 18%, respectively, by incorporating nGO in content of 0.4 wt.%. Fredi et al. [17] improved strain at the break point of PLA from 5.3% to 10.0% by adding nGO in content of 0.25 phr. Khammassi et al. [18] added GO and Ag nanoparticles into the PLA matrix and observed that the crystallization temperature increased from 105.8 °C to 122.54 °C, and the indentation load (in the nanoindentation test) enhanced by 28%.

Thermoforming is the most common method for producing disposable polymer containers [19]. Various polymer products, from electronic devices to medical products with materials of HDPE, ABS, PP, PS, and PLA, are produced by thermoforming method [20, 21]. In this process, a thermoplastic film or sheet which heated up to softening point of polymer (above glass transition temperature and lower melting point) is stretched into a female or male die by vacuum (vacuum assisted) or punch force (plug assisted) [22-24]. Various studies were done to investigate variables of the thermoforming process, such as viscoelastic behavior of sheet polymer, vacuum pressure, sheet temperature, heating time, and plug rate on product quality by experiments or finite element simulation [25-28]. They concluded that there are many independent variables which influence each other, and it is difficult to highlight an effective parameter.

PLA, due to its biodegradability, is a favorite polymer in packing industries [29], and therefore some research focused on thermoforming of PLA [30, 31]. Although a lot of research has been conducted on PLA thermoforming, little research has been done on the thermoforming process of PLA reinforced by nanofillers. Barletta and Puopolo [32] added calcium carbonate nanoparticles into PLA/PBS matrix, and studied the processability of the nanocomposite sheets by a thermoforming process. Considering the little research done on the thermoforming process of PLA nanocomposites, this research tries to investigate the thermoforming process of PLA nanocomposite sheets. The effect of nGO content on the thickness distribution of the sheets after forming was investigated. The influence of nGO on the morphology, mechanical properties, and thermal behavior of the sheet before and after thermoforming was examined.

2. MATERIALS AND METHODS

2. 1. Materials polylactic acid (PLA) granules (Bioflex®F 6510 grade) of melting point 160°C, with a molecular weight of 198000 g/mol, a density of 1.3 g/cm³ procured from Fkur GmbH, Germany. nGO in thickness of 3.2-4.5 µm was used as reinforcement in PLA matrix, and prepared from NANOSANY Co., Iran. Chloroform was used as the solvent of PLA, and obtained from Merck (Darmstadt, Germany).

2. 2. Preparation PLA and nGO were dried in a vacuum oven at 90 °C for 10h before processing. The nanocomposite films were prepared by a solvent casting technique. PLA granules weighing 5 g were dissolved on 110 ml of chloroform and mixed by a magnetic mixer for 5h to solve PLA granules completely. In the next step, nGO with a certain amount was dispersed in 15 ml of acetone solvent by ultrasonic homogenizer for 15 min. Then, nGO solution was added into PLA solution and stirred for 15 min by an ultrasonic homogenizer. Finally, the solution was poured into a glass container and was kept at ambient temperature for 24h to remove solvent and dry the sheets. To remove the solvent completely, the sheets were placed in a vacuum oven at 45 °C for 4 days. The composition of the prepared samples are stated in Table 1.

2. 3. Thermoforming All steps of the process, consisting of sheet preparation and thermoforming process, are presented in Figure 1. After preparing the nanocomposite sheets, the thermoforming process was done. The thermoforming was done by vacuum-assisted thermoforming technique. The product dimensions are shown in Figure 2. The polymer sheets were heated by a heater, which was placed on top of the sheets and followed by a vacuum process. A vacuum is applied when the temperature of the sheets reaches about 110 °C. The temperature of the sheets was measured by a thermometer. Figure 3 shows thermoformed sheets.

2. 4. Characterization The morphology and structures of the PLA and PLA/nGO sheets were investigated by field emission scanning electron microscopy (FE-SEM) and X-ray diffraction (XRD). X-ray diffraction pattern was obtained by a PHILIPS 1050 with Cu- α lines. Scanning was between 10° to 30° (2 θ) by

TABLE 1. The composition of the samples

Sample	nGO (wt.%)	PLA (wt.%)
PLA	-	100
PLG0.4	0.4	99.6
PLG1	1	99

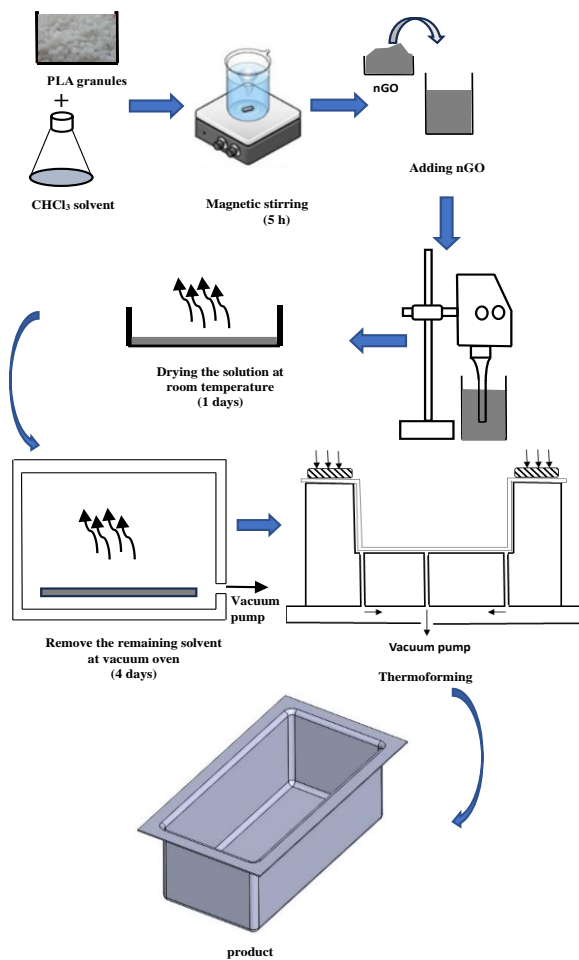


Figure 1. Schematic view of the process

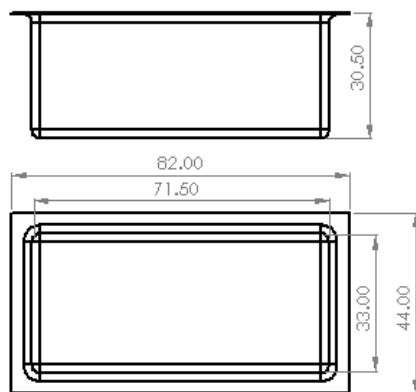


Figure 2. Product dimensions

step of 0.05° and scanning rate of $0.5/\text{min}$. The mechanical properties of the unformed sheets and formed sheets were evaluated by tensile test. Tensile test was done at room temperature by HOUNFFIELD machine test model of H25KS at a feed rate of $1 \text{ mm}/\text{min}$ according to ASTM D638 to measure tensile strength and elastic modulus

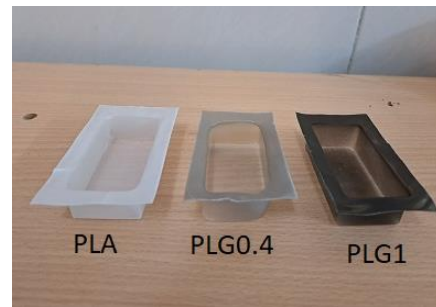
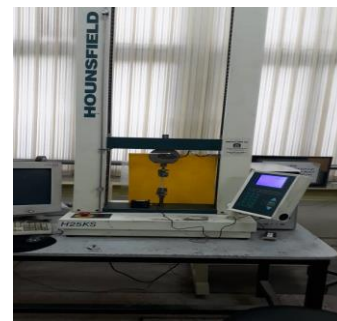


Figure 3. Thermoformed sheets

(Figure 4). The thermal behavior of the PLA and nanocomposite sheets was studied by differential scanning calorimetry (DSC) test. A SANAF DSC analyzer (Iran) in a temperature range of 20°C to 210°C by a heating rate of $10^\circ\text{C}/\text{min}$ was used to determine the melting point (T_m), glass transition temperature (T_g), and melting enthalpy. The thickness variation (distribution) of the formed sheet was measured along cross-section on halved samples by a dial caliper with a resolution of 0.01 mm . The measurements were done in 8 points in the cut section. Figure 5 shows a schematic view of the section in which thickness variations were measured.

3. RESULTS

3.1. Morphology Figure 4 shows the dispersion of nGO through the PLA matrix in the sample containing 1



(a)



(b)

Figure 4. Tensile test set-up

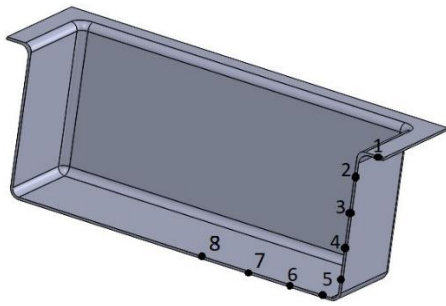
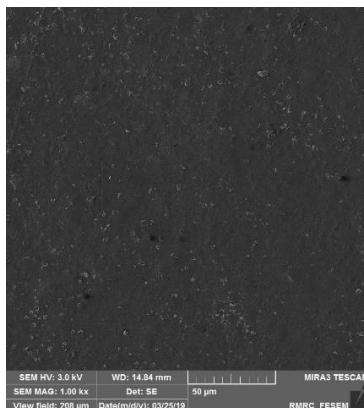
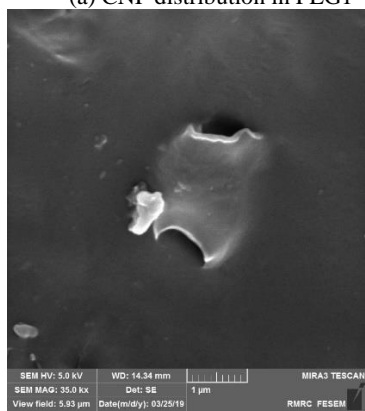


Figure 5. Points of thickness measurement

wt.% of nGO in two different magnifications by FE-SEM. As shown in Figure 4(a), GO nanoparticles have been dispersed in polymer matrix uniformly. Figure 4(b) shows the dispersion in higher magnification. In this figure, the uniform dispersion of nGO particles is more clearly visible, so that a nGO nanoparticle with an approximate length of 2 μm can be clearly seen in this figure. With a closer look, it can be seen the good adhesion of the nanoparticle to the polymer matrix. As shown in Figure 6, the nanoparticles the particles are well distributed on a nanoscale.



(a) CNF distribution in PLG1



(b) GO nanoparticle in PLG1

Figure 6. FE-SEM images of the samples

3. 2. X-ray Diffraction The X-ray diffraction pattern of PLA and nanocomposite sheets before the thermoforming process is shown in Figure 7. A broad peak can be seen between $2\theta=10^\circ$ to $2\theta=30^\circ$ for neat PLA sheet. This broad peak indicates the amorphous nature of the PLA crystal structure or has small crystals. The solution casting method can be the reason for the amorphous crystal structure, while PLA is a semi-crystalline polymer when it is produced by melting method. In the samples of PLG0.4 and PLG1, two peaks in $2\theta=16.7^\circ$ and $2\theta=19.3^\circ$ are observed. These two peaks represent planes of (200/110) and (203) in α type PLA with orthorhombic crystal structure, respectively. The presence of these two peaks in samples PLG0.4 and PLG1 indicates that adding nGO has caused the formation of the crystalline structure or an increase in the PLA crystalline percentage. GO nanoparticles have been able to act as nucleation sites for crystal formation and increase the crystalline rate of the PLA matrix. By observing the figure more closely, it can be seen that the peak intensity is higher for the samples of PLG0.4 and PLG1; as a result, the crystallization rate in this sample can be higher. The X-ray diffraction pattern of PLA and nanocomposite sheets after thermoforming process is shown in Figure 8. After the thermal forming process, the peaks at 16.7° and 19.3° have disappeared, and a new small peak has formed at 21.5° , which corresponds to the (015) plane. The disappearance of the peaks after the thermoforming process shows that the severe deformation caused by the thermal forming process destroyed most of the crystals and changed other parts. By comparing Figures 7 and 8, it can be found that the application of severe thermal deformation can reduce the crystallization of the PLA matrix.

3. 3. Thickness distribution PLA and nanocomposite sheets were produced in the form of cubic

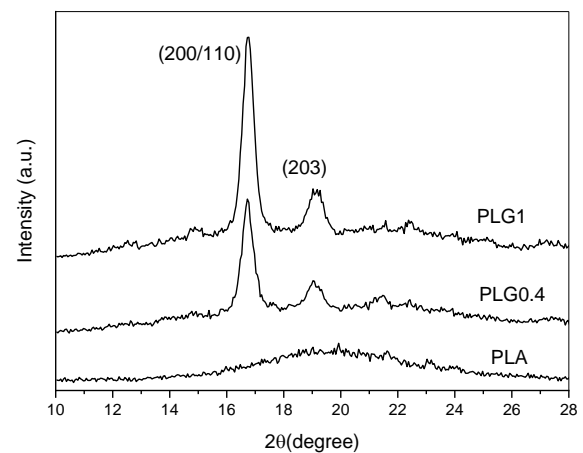


Figure 7. X-ray pattern of the sheets before thermoforming

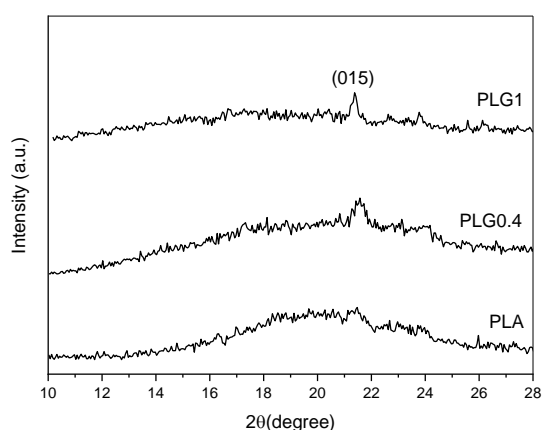


Figure 8. X-ray pattern of the sheets after thermoforming

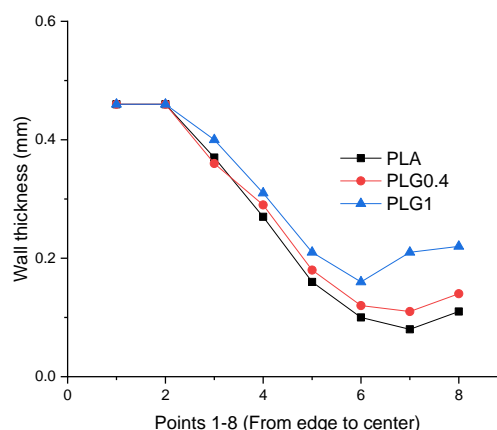


Figure 9. Thickness distribution of the samples

containers after thermoforming in female die. After the thermal forming process, the containers were cut, and the thickness of the sheets was measured at several points. The thickness distribution results for three samples of neat PLA, PLG0.4, and PLG1, are shown in Figure 9. As shown in this figure, the thickness of the edges of the sheets that have not been subjected to tension is almost equal to the thickness of the produced sheets (approximately 0.5 mm). By moving away from the edge and in the wall section of the containers, the thickness has decreased due to the tension. The decrease in thickness is increased by increasing the height from the edge of the container. On the side of the bottom of the container, this decrease in thickness continued until approaching the center of the bottom of the container; due to less tension, the thickness of the wall slightly increased. By comparing the samples, it can be observed that the reduction in wall thickness was lower for the samples containing graphene oxide nanoparticles. By increasing the percentage of graphene oxide nanoparticles from 0.4 to 1 wt.%, the thickness reduction is less. The maximum thickness reduction for neat PLA is 80%, while for PLG0.4 sample is 76%, and for PLG1 sample is 68%. This reduction in thickness changes for samples containing graphene oxide nanoparticles can be due to the higher strength of nanocomposite sheets because of the higher percentage of polylactic acid crystallization and the presence of graphene oxide nanoparticles.

3. 4. Mechanical Properties The mechanical properties of the sheets before and after thermoforming were evaluated by tensile test, and the stress-strain curves of the sheets before and after thermoforming are shown in Figures 10 and 11, respectively. The obtained data from stress-strain curves containing tensile strength, tensile modulus, and strain at break point (elongation) are presented in Tables 2 and 3. By adding graphene nano-oxide up to 1 wt.%, the elastic modulus increased from 2630 MPa to 3670 MPa, which shows an increase in

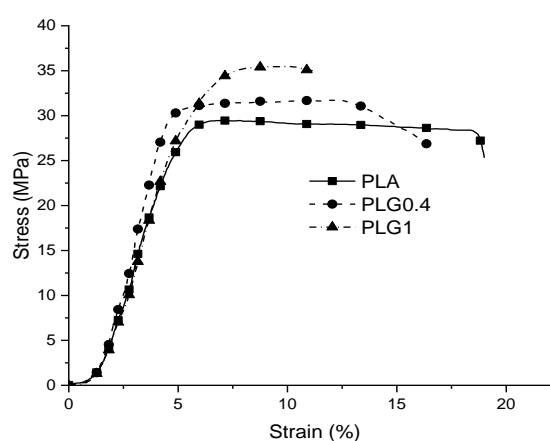


Figure 10. Stress-strain curve of the sheets before thermoforming

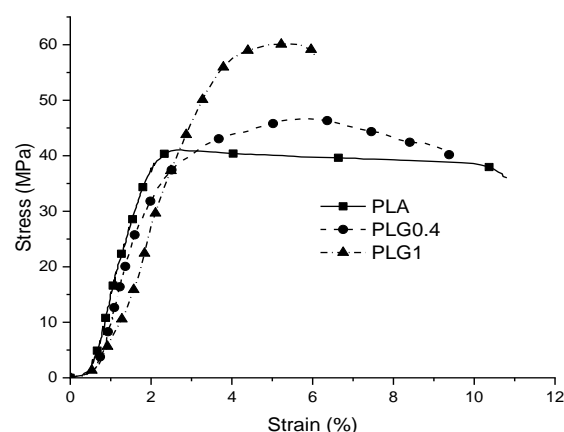


Figure 11. Stress-strain curve of the sheets after thermoforming

about 40%. The tensile strength also increased continuously from 28 MPa to 37 MPa by addition of graphene oxide nanoparticles up to 1 wt.%, which shows

TABLE 2. Obtained data from stress-strain curve of the samples before thermoforming

Sample	Young's modulus (MPa)	Tensile strength (MPa)	Elongation (%)
PLA	2630±130	28±3	21±1.5
PLG0.4	3452±170	32±4.5	17±1.25
PLG1	3670±150	37±6	12±2

TABLE 3. Obtained data from stress-strain curve of the samples after thermoforming

Sample	Young's modulus (MPa)	Tensile strength (MPa)	Elongation (%)
PLA	5210±160	42±4.5	11.5±1.85
PLG0.4	5310±150	46±6.5	10.2±1.65
PLG1	5430±170	63±8	6.8±1.42

a 32% increase in tensile strength. Unlike the elastic modulus and tensile strength, adding nGO into PLA has reduced the strain at the break point. The elongation for PLA is 21%, and by adding 1 wt.% of nGO, it has decreased to 12%. The results showed that adding nanoparticles has a significant positive effect on strength and elastic modulus. The reason for that can be considered to be an increase in the crystallinity of the PLA matrix, and the other is that the nanoparticles were able to support a part of the applied stress to the polymer matrix. After the sheets were subjected to thermoforming process and produced as plastic containers, tensile test samples were prepared from the bottom of the containers and subjected to tensile test to compare the mechanical properties of polymer and nanocomposite sheets before and after the thermoforming process to be compared, to determine the effect of the stretching process during thermoforming on the mechanical properties of the samples. Figure 11 shows the stress-strain curve of the samples after thermoforming. According to this curve, the elastic modulus of all three samples is almost the same and is about 5.3 GPa. By comparing this modulus with the elastic modulus of the samples before thermoforming process, it can be seen that the elastic modulus has significantly increased, so that for neat PLA, the modulus increased from 2630 MPa to 5210 MPa, which shows an increase of about 100%. The tensile strength for neat PLA is 42 MPa, and for the sample containing 1 wt.% of nGO increased to 63 MPa. By comparing the tensile strength of the samples before and after the thermoforming process, it can be understood that the strength had also increased significantly, so that for the sample containing 1 wt.% nGO, the tensile strength from 37 MPa before the thermoforming increased up to 63 MPa after thermoforming, which shows an increase of about 70%. The values of strain at the break point for all three samples after thermoforming

show a significant decrease in compared to before thermoforming. Almost for all three samples, the strain has decreased by about 50%. From the tensile test results, it can be concluded that the strength and rigidity of polymer sheets after the thermoforming process increased and their flexibility decreased.

3. 5. Thermal Properties In order to investigate the thermal behavior and degree of crystallinity of PLA and nanocomposite sheets, a DSC test was performed. The melting scan for the sheets before the thermoforming process and after the thermoforming process are shown in Figures 12 and 13, respectively. Data related to DSC diagram, including glass transition temperature (T_g), melting temperature (T_m), heat of diffusion (ΔH_m), and crystallinity (χ) for the sheets before and after the thermoforming process, is given in Tables 4 and 5, respectively. The degree of crystallinity can be expressed by the following formula (1):

$$X_c (\%) = \frac{\Delta H_m}{\Delta H_m^c} \times 100 \quad (1)$$

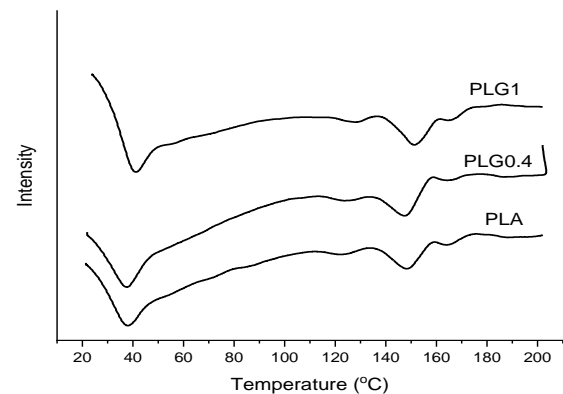
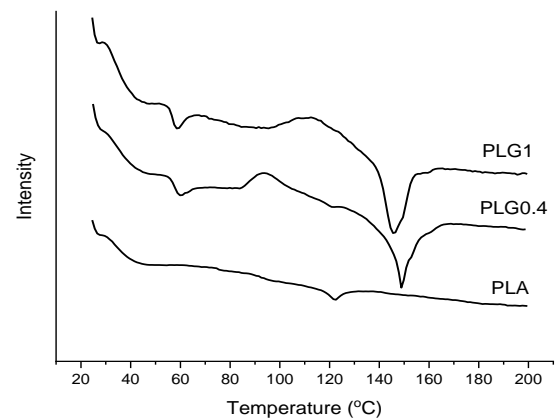
**Figure 12.** DSC melting scans of the sheets before thermoforming**Figure 13.** DSC melting scans of the sheets after thermoforming

TABLE 4. The DSC data of the sheets before thermoforming

Sample	T _g (°C)	T _m (°C)	ΔH _m (Jg ⁻¹)	χ (%)
PLA	37.7	147.8	5.4	5.7
PCNF	37.5	146.9	10.31	11.4
PCNFAG1	41.8	151.5	12.35	13.2

TABLE 5. The DSC data of the sheets after thermoforming

Sample	T _g (°C)	T _m (°C)	ΔH _m (Jg ⁻¹)	χ (%)
PLA	45	122.3	3.3	3.5
PCNF	60.2	149	6.05	6.5
PCNFAG1	59.2	146.7	8.52	10.98

where ΔH_m^c with value of 93 J/g is the heat of diffusion for 100% crystallite PLA.

Based on the data in Table 4, by adding nGO up to 1 wt.% to PLA, T_g has increased from 37.7 °C to 41.8 °C. An increase in T_g showed that the presence of nGO reduced the mobility of polymer chains and prevented them from moving. Melting temperature data showed that the melting temperature has increased from 147.8 °C to 151.5 °C. This increase in the melting point is due to an increase in the crystallinity and thickness of the lamellae. According to the crystallinity data obtained from the DSC scan, the degree of crystallinity in PLA has increased from 5.7 to 13.2% by adding nGO up to 1 wt.%. Crystallization results are also confirmed by x-ray test.

The DSC curve of the samples after thermoforming is given in Figure 13. By looking at this curve, it can be seen that the melting peak has become very small for neat PLA, which shows that the structure of this sheet has almost become amorphous after thermoforming. By comparing the data in Tables 4 and 5, it can be concluded that after the thermoforming process, T_g has significantly increased. For neat PLA, this temperature increased from 37.7 °C to 45 °C, and for the PLG0.4 sample, it increased from 37.5 to 60.2, which is a significant increase. This increase in T_g is caused by the stretching of the polymer chains and their entanglement, which limits their mobility. The comparison of melting temperature data for samples containing nGO shows that the melting temperature before and after thermoforming has not changed significantly. But for neat PLA, it can be seen that the melting temperature decreased from 147.8 °C to 122.3 °C, which shows a significant decrease. This is due to a considerable reduction in the crystallinity of the neat PLA. The data on the degree of crystallinity of the samples before and after thermoforming showed that the crystallinity has decreased for all samples.

4. CONCLUSION

In this research, thermoforming process of PLA/nGO nanocomposite sheets carried out. The x-ray diffraction

patterns after thermoforming showed that the peaks in 16.7° and 19.3° disappeared, and a new small peak is formed at 21.5°, which corresponds to the plane (015). According to the results of the thickness distribution of the samples after thermoforming, the decrease in wall thickness was lower for the samples containing graphene oxide nanoparticles. After thermoforming process, tensile strength of the samples significantly increased, so that for the sample containing 1 wt.% of nGO, the tensile strength increased from 37 MPa before the thermoforming to 63 MPa after the thermoforming process. By comparing the DSC thermal test data before and after thermoforming, it can be understood that the T_g has significantly increased after the thermal forming process. For neat PLA, this temperature increased from 37.7 °C to 45 °C, and for the PLG0.4, it increased from 37.5 °C to 60.2 °C. For all samples, the degree crystallinity decreased.

5. REFERENCES

1. Raquez, J.-M., Habibi, Y., Murariu, M. and Dubois, P., "Polylactide (pla)-based nanocomposites", *Progress in Polymer Science*, Vol. 38, No. 10-11, (2013), 1504-1542. <https://doi.org/10.1016/j.progpolymsci.2013.05.014>
2. Armentano, I., Dottori, M., Fortunati, E., Mattioli, S. and Kenny, J., "Biodegradable polymer matrix nanocomposites for tissue engineering: A review", *Polymer Degradation and Stability*, Vol. 95, No. 11, (2010), 2126-2146. <https://doi.org/10.1016/j.polymdegradstab.2010.06.007>
3. Liu, H. and Zhang, J., "Research progress in toughening modification of poly (lactic acid)", *Journal of Polymer Science Part B: Polymer Physics*, Vol. 49, No. 15, (2011), 1051-1083. <https://doi.org/10.1002/polb.22283>
4. Stloukal, P., Pekařová, S., Kalendova, A., Mattausch, H., Laske, S., Holzer, C., Chitu, L., Bodner, S., Maier, G. and Slouf, M., "Kinetics and mechanism of the biodegradation of pla/clay nanocomposites during thermophilic phase of composting process", *Waste Management*, Vol. 42, (2015), 31-40. <https://doi.org/10.1016/j.wasman.2015.04.006>
5. Jadidi, H., Shahrajabian, H. and Moghri, M., "Using the mass method to produce pvc/clay nanocomposite foams: The effect of nano-clay and foaming conditions on density and cell size", *Journal of Inorganic and Organometallic Polymers and Materials*, Vol. 26, (2016), 881-888. <https://doi.org/10.1007/s10904-016-0386-7>
6. Sheikh, K. and Shahrajabian, H., "Experimental study on mechanical, thermal and antibacterial properties of hybrid nanocomposites of pla/cnf/ag", *International Journal of Engineering, Transactions B: Applications*, Vol. 34, No. 2, (2021), 500-507. doi: 10.5829/IJE.2021.34.02B.23.
7. Nian, L., Wang, M., Sun, X., Zeng, Y., Xie, Y., Cheng, S. and Cao, C., "Biodegradable active packaging: Components, preparation, and applications in the preservation of postharvest perishable fruits and vegetables", *Critical Reviews in Food Science and Nutrition*, (2022), 1-36. <https://doi.org/10.1080/10408398.2022.2122924>
8. Vishal, K., Rajkumar, K., Sabarinathan, P. and Dhinakaran, V., "Mechanical and wear characteristics investigation on 3d printed silicon filled poly (lactic acid) biopolymer composite fabricated by fused deposition modeling", *Silicon*, Vol. 14, No. 15, (2022), 9379-9391. <https://doi.org/10.1007/s12633-022-01712-9>

9. Stukhlyak, P., Buketov, A., Panin, S., Maruschak, P., Moroz, K., Poltaranin, M., Vukherer, T., Kornienko, L. and Lyukshin, B., "Structural fracture scales in shock-loaded epoxy composites", *Physical Mesomechanics*, Vol. 18, (2015), 58-74. <https://doi.org/10.1134/S1029959915010075>
10. Mosalman, S., Rashahmadi, S. and Hasanzadeh, R., "The effect of tio2 nanoparticles on mechanical properties of poly methyl methacrylate nanocomposites (research note)", *International Journal of Engineering, Transactions B: Applications*, Vol. 30, No. 5, (2017), 807-813. doi: 10.5829/idosi.ije.2017.30.05b.22.
11. Mohammadnia, M., Derakhshani, E. and Naghizadeh, A., "Defluoridation of aqueous solution by graphene and graphene oxide nanoparticles: Thermodynamic and isotherm studies", *Iranian Journal of Chemistry and Chemical Engineering*, Vol. 39, No. 1, (2020), 67-77. doi: 10.30492/IJCCE.2020.33341.
12. Keshavarz, M.R. and Hassanajili, S., "Effect of graphene oxide reduction with l-ascorbic acid on electrical conductivity and mechanical properties of graphene oxide-epoxy nanocomposites", *Iranian Journal of Chemistry and Chemical Engineering*, Vol. 40, No. 3, (2021), 731-742. doi: 10.30492/IJCCE.2020.38254.
13. Liu, L., Zhang, J., Zhao, J. and Liu, F., "Mechanical properties of graphene oxides", *Nanoscale*, Vol. 4, No. 19, (2012), 5910-5916. <https://doi.org/10.1039/C2NR31164J>
14. Moslehi Niasar, M., Molaei, M. and Aghaei, A., "Electromagnetic wave absorption properties of barium ferrite/reduced graphene oxide nanocomposites", *International Journal of Engineering, Transactions C: Aspects*, Vol. 34, No. 6, (2021), 1503-1511. doi: 10.5829/IJE.2021.34.06C.14.
15. Gao, W., "The chemistry of graphene oxide", *Graphene oxide: Reduction Recipes, Spectroscopy, and Applications*, Vol., No., (2015), 61-95. https://doi.org/10.1007/978-3-319-15500-5_3
16. Sharifiana, M. and Shahrajabian, H., "The study of mechanical, thermal, and antibacterial properties of pla/graphene oxide/tio2 hybrid nanocomposites", *Iranian Journal of Chemistry and Chemical Engineering*, Vol. 41, No. 3, (2022), 799-807. doi: 10.30492/IJCCE.2021.128785.4173.
17. Fredi, G., Karimi Jafari, M., Dorigato, A., Bikiaris, D.N. and Pegoretti, A., "Improving the thermomechanical properties of poly (lactic acid) via reduced graphene oxide and bioderived poly (decamethylene 2, 5-furandicarboxylate)", *Materials*, Vol. 15, No. 4, (2022), 1316. <https://doi.org/10.3390/ma15041316>
18. Khammassi, S., Tarfaoui, M., Škrlová, K., Měřínská, D., Plachá, D. and Erchiqui, F., "Poly (lactic acid)(pla)-based nanocomposites: Impact of vermiculite, silver, and graphene oxide on thermal stability, isothermal crystallization, and local mechanical behavior", *Journal of Composites Science*, Vol. 6, No. 4, (2022), 112. <https://doi.org/10.3390/jcs6040112>
19. Banús, N., Boada, I., Xiberta, P., Toldrà, P. and Bustins, N., "Deep learning for the quality control of thermoforming food packages", *Scientific Reports*, Vol. 11, No. 1, (2021), 21887. <https://doi.org/10.1038/s41598-021-01254-x>
20. Ghorbani, S. and Matochi, A., "Thermoforming and its applications, a review", *Basparesh*, Vol. 10, No. 2, (2020), 37-47. doi: 10.22063/BASPARESH.2020.2539.1483.
21. Choi, J., Han, C., Cho, S., Kim, K., Ahn, J., Del Orbe, D., Cho, I., Zhao, Z.-J., Oh, Y.S. and Hong, H., "Customizable, conformal, and stretchable 3d electronics via pre-distorted pattern generation and thermoforming", *Science Advances*, Vol. 7, No. 42, (2021), eabj0694. doi: 10.1126/sciadv.abj0694.
22. Wittmann, L.-M. and Drummer, D., "Multilayer sheets for thermoforming non thermoformable polymers", *Journal of Plastic Film & Sheeting*, Vol. 38, No. 2, (2022), 225-244. <https://doi.org/10.1177/87560879211037387>
23. Albilali, A.T., Baras, B.H. and Aldosari, M.A., "Evaluation of mechanical properties of different thermoplastic orthodontic retainer materials after thermoforming and thermocycling", *Polymers*, Vol. 15, No. 7, (2023), 1610. <https://doi.org/10.3390/polym15071610>
24. Atmani, O., Abbès, F., Li, Y., Batkam, S. and Abbès, B., "Experimental and numerical investigation of the effects of sheet material, plug-assist tool material, and process conditions on the mechanical pre-stretching stage of plug-assist thermoforming", *The International Journal of Advanced Manufacturing Technology*, Vol. 122, No. 7-8, (2022), 3217-3234. <https://doi.org/10.1007/s00170-022-10125-2>
25. Wei, H., "Optimisation on thermoforming of biodegradable poly (lactic acid)(pla) by numerical modelling", *Polymers*, Vol. 13, No. 4, (2021), 654. <https://doi.org/10.3390/polym13040654>
26. O'Connor, C., Menary, G., Martin, P. and McConville, E., "Finite element analysis of the thermoforming of polypropylene", *International Journal of Material Forming*, Vol. 1, No. Suppl 1, (2008), 779-782. <https://doi.org/10.1007/s12289-008-0291-x>
27. Ghobadnam, M., Mosaddegh, P., Rezaei Rejani, M., Amirabadi, H. and Ghaei, A., "Numerical and experimental analysis of hips sheets in thermoforming process", *The International Journal of Advanced Manufacturing Technology*, Vol. 76, (2015), 1079-1089. <https://doi.org/10.1007/s00170-014-6329-y>
28. Turan, E., Konuşkan, Y., Yıldırım, N., Tuncalp, D., Inan, M., Yasin, O., Turan, B. and Kerimoğlu, V., "Digital twin modelling for optimizing the material consumption: A case study on sustainability improvement of thermoforming process", *Sustainable Computing: Informatics and Systems*, Vol. 35, (2022), 100655. <https://doi.org/10.1016/j.suscom.2022.100655>
29. Gonon, H., Srisa, A., Promhuad, K., Chonhenchob, V., Bumbudsanpharoke, N., Jarupan, L. and Harnkarnsujarit, N., "Pla thermoformed trays incorporated with cinnamaldehyde and carvacrol as active biodegradable bakery packaging", *Food Packaging and Shelf Life*, Vol. 38, (2023), 101123. <https://doi.org/10.1016/j.fpsl.2023.101123>
30. Sorimpuk, N., Choong, W. and Chua, B., "Design of thermoformable three dimensional-printed pla cast for fractured wrist", in IOP Conference Series: Materials Science and Engineering, IOP Publishing. Vol. 1217, (2022), 012002.
31. Swetha, T.A., Bora, A., Mohanrasu, K., Balaji, P., Raja, R., Ponnuchamy, K., Muthusamy, G. and Arun, A., "A comprehensive review on polylactic acid (pla)-synthesis, processing and application in food packaging", *International Journal of Biological Macromolecules*, (2023), 123715. <https://doi.org/10.1016/j.ijbiomac.2023.123715>
32. Barletta, M. and Puopolo, M., "Thermoforming of compostable pla/pbs blends reinforced with highly hygroscopic calcium carbonate", *Journal of Manufacturing Processes*, Vol. 56, (2020), 1185-1192. <https://doi.org/10.1016/j.jmapro.2020.06.008>

COPYRIGHTS

©2023 The author(s). This is an open access article distributed under the terms of the Creative Commons Attribution (CC BY 4.0), which permits unrestricted use, distribution, and reproduction in any medium, as long as the original authors and source are cited. No permission is required from the authors or the publishers.



Persian Abstract

چکیده

امروزه درمقابل مزایایی که استفاده از مواد پلیمری برای انسان دارند، استفاده از این مواد به دلیل عدم سازگاری با محیط زیست باعث مشکلاتی برای محیط زیست شده است. بنابراین استفاده از پلیمرهای زیست تخریب پذیر مانند پلی لاکتیک اسید (PLA) رو به افزایش است. یکی از کاربردهای مهم مواد پلاستیکی برای تولید ظروف یکبار مصرف است. در این تحقیق فرآیند شکل دهی حرارتی ورق PLA تقویت شده با نانوذرات اکسید گرافن (nGO) به مقدار ۰/۴ و ۱ درصد وزنی بررسی شد. از میکروسکوپ الکترونی روبشی و تفرق اشعه ایکس برای مطالعه مورفولوژی نمونه‌ها قبل و بعد از شکل دهی حرارتی استفاده شد. خواص مکانیکی نمونه‌ها توسط آزمون کشش بررسی شد. نتایج آزمون کشش نشان داد که بعد از شکل دهی حرارتی استحکام کششی نمونه‌ها افزایش قابل توجهی می‌یابد، بطوریکه استحکام کششی نمونه حاوی ۱٪ وزنی nGO حدود ۷۰٪ افزایش یافت. نتایج توزیع ضخامت نشان داد کمترین میزان کاهش ضخامت به میزان ۶۸٪ مربوط به نمونه حاوی ۱٪ وزنی نانوذرات اکسید گرافن است. براساس نتایج آزمون حرارتی DSC، میزان تبلور همه نمونه‌ها پس از شکل دهی حرارتی کاهش می‌یابد.



Joint Sensing Times Detection Thresholds and Users Association Optimization in Multi-Channel Multi-Antenna Cognitive Radio Networks

M. Sadeghian Kerdabadi^a, R. Ghazizadeh^b, H. Farrokhi^b, M. Najimi^c

^a Department of Mechanic Engineering, Malek-e ashtar, University of Technology, Isfahan, Iran

^b Department of Electrical and Computer Engineering, University of Birjand, Birjand, Iran

^c Faculty of Electrical, University of Science and Technology of Mazandaran (USTM), Behshahr, Mazandaran, Iran

PAPER INFO

Paper history:

Received 06 March 2023

Received in revised form 16 March 2023

Accepted 19 March 2023

Keywords:

Cognitive Radio Network

Multi Channels

Multi Antennas

Throughput

Energy Consumption

ABSTRACT

Energy consumption and throughput optimization in cognitive radio networks (CRNs) are two critical issues that have attracted more attention in recent years. In this paper, we consider maximization of the energy efficiency and improvement of the throughput as optimization metrics for jointly optimizing sensing times and energy detection thresholds in each sub-channel and selecting the spectrum sensing (SS) and data transmitting multi-antenna secondary users (SUs) in multi-channel multi-antenna CRN under constraints on the probabilities of false alarm and detection. The considered problem is solved based on the convex optimization method and the algorithm having less computational complexity compared to baseline approaches is proposed to achieve the optimal parameters and goals of the problem. The performance of the proposed scheme is evaluated by simulations and compared with the other methods. The results indicate that the proposed approach can achieve less energy consumption while the minimum required throughput is guaranteed.

doi: 10.5829/ije.2023.36.09c.15

1. INTRODUCTION

Cognitive Radio (CR) has emerged as a practical approach to enhance spectrum efficiency (SE) by allocating the sensed bands as idle of the licensed users (primary users, PUs) to the unlicensed users (secondary users, SUs) [1]. Therefore, SS becomes a fundamental task in CR to quickly and reliably detect the presence of the PUs [2]. Energy detection is the most common technique for SS due to its simple implementation. In addition, it does not need prior knowledge of the PU's signal. However, reliable SS is not always guaranteed because of multipath fading and shadowing. Cooperative SS (CSS) approaches have been proposed to overcome these problems. CSS combines the local sensing decisions of multiple SUs or antennas in a fusion center (FC) for making a more reliable final decision on the absence/presence of the PU by achieving the advantage of the spatial diversity in wireless channels [3]. A lot of

work has been done on sensing-throughput tradeoff and finding the optimum SS parameters such as detection threshold value for energy detection, SS time and power for data transmitting to guarantee the best performance on the probability of false alarm, P_f , the probability of detection, P_d , and as well as the throughput of CRN [4-13]. A sum-rate maximization strategy was proposed by Salari and Francois [14] to jointly obtain the optimal Energy Harvesting (EH) time allocation factor and distributed beamforming coefficients that achieve the best system performance for the secondary network under the individual EH power constraints at relays and an interference power constraint at the primary receiver. The sum throughput of SUs was maximized by Hameed et al. [15], while managing the interference constraint. For this goal, the uplink and downlink phase shift matrices of the IRS elements with optimal time slots for wireless energy transfer (WET) on downlink and wireless information transfer on uplink were optimized.

*Corresponding Author Email: mohammad.sadeghian@birjand.ac.ir
(M. Sadeghian)

Most early research on SS has been primarily performed on sensing a single-band. However, multi-channel (multi-band) spectrum access has recently developed where multiple bands used by more than one PU are sensed and accessed to enhance the throughput and reduce data transmission interruptions due to the activities of the PUs. Many approaches have been presented to achieve the maximum throughput of the multi-channel CRN by optimizing the different sensing and transmission parameters [16-23].

The above-mentioned works only consider single-antenna CRNs. However, multi-antenna systems can provide many benefits for CRN such as multiplexing gain and diversity [24, 25]. In multi-antenna CSS, diversity leads to behave SUs virtually the same as systems having multiple sensing SUs. These benefits can be exploited to enhance the sensing and transmission capabilities of CRN that overcomes the fading problem and hence, increases the SUs' throughput. The optimal values of the SS times, sensing thresholds and transmit power were obtained for increasing the throughput in multi-antenna CRNs subject to constraints on transmit power, P_d and P_f [26]. In a cooperative multiple-input single-output (MISO) CR system was proposed by Liu et al. [27], some of the antennas are used to transmit the SU's data and the rest antennas for transmitting the PU's data. Kumar et al. [28] enhanced the SE by using multi antennas CSS and minimizing the spectrum sensing error. The problem of a joint robust transmission, reflection and reception strategy design at an active reconfigurable intelligent surface (RIS)-assisted underlay MIMO CRNs is solved in which a secondary transmitter serves multiple secondary receivers, simultaneously [29]. The energy and matched filter detectors were employed by Rauniyar and Shin [30] as cascades in each antenna of the multi-antenna CRN. Then the local sensing results of all antennas were combined to enhance the detection performance. A SS algorithm based on sample variance was proposed that significantly reduces the number of sampling points in MIMO schemes to achieve the optimum detection performance [31]. An energy harvesting-based multi-antenna CR scheme presented by Liu et al. [32] for powering SUs by harvesting energy from radio frequency (RF) signal of the PU and the noise. The performance of SS and throughput can be enhanced by using more cooperative SUs in the network. Nonetheless, this enhancement is at the cost of increasing the consumed energy and communication overhead of CRN [33]. Therefore, the selection of Sensing and data Transmitting SUs (SSUs & TSUs) has a significant impact on the throughput and energy consumption of CRN. Moreover, the frame structure of the opportunistic spectrum access CR networks consists of a spectrum sensing time slot (duration τ) and a data transmission time slot (duration $T - \tau$), as shown in Figure 1. The longer sensing time increases the probability of detection

and PU protection but decreases the transmission opportunity of the CR. Hence, the achievable throughput of the SUs is reduced. Therefore, a fundamental tradeoff exists between the duration of spectrum sensing and data transmission. Also, the more or less sensing times lead to more energy consumption because it takes more time for sensing and data transmitting, respectively.

The interplay between the above-mentioned components calls for jointly optimizing the sensing and data transmission parameters of CRN, which is the major issue of this paper. The aim is to share the advantages of multi-antenna and multi-channel CRN.

We solve the joint optimization problem of the detection thresholds, SS times, and the selection of multi-antenna SSUs and TSUs for each sub-channel to minimize the energy consumption and improvement of the throughput of CRN.

The main contributions of this paper are outlined as follows:

- Most of work done so far on CRNs just optimizes either the achieved throughput or consumed energy of CRN, but in this paper, we consider minimization of the energy consumption and enhancement of the throughput, simultaneously.
- We have considered the optimization problem of the sensing times, detection thresholds, and the selection of the multi-antenna SSUs and TSUs for each sub-channel of the multi-channel multi-antenna CRN jointly to improve the throughput and minimization of the consumed energy over all the sub-channels under constraints on the global P_d and P_f whereas most of the past done studies formulated an optimization problem without taking the joint optimization of the above-mentioned parameters for multi-channel multi-antenna CRN into consideration.
- The presence of the PU signal is detected by the multi-antenna CSS, in which each antenna employs energy detection to sense the PU signal. As a result, the sensing results of all the sensing antennas are combined to make the global decision with the goal of incrementing the CR throughput and improving the detection capability by obtaining the sensing diversity gain that overcomes the multi-path fading problem.
- We provide mathematical proofs for the proposed model. Then, convex optimization methods and Karush–Kuhn–Tucker (KKT) conditions are used

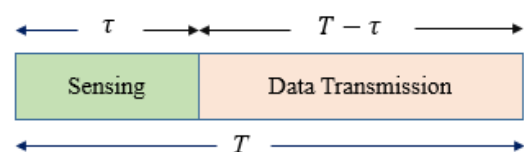


Figure 1. The time frame structure of the model

to solve our mix-variable optimization problem. Moreover, by using a convex-based iterative algorithm having less computational complexity compared to baseline approaches, the optimum sensing times and detection thresholds are achieved in each sub-channel. We also specify the sensing and data transmitting multi-antenna SUs on each sub-channel. Using the proposed algorithm, the sensing and data transmitting multi-antenna SUs for each suitable sub-channel are selected based on parameters such as detection probability, residual energy, and SNR such that the consumed energy is minimized and the constraints on the detection performance and the minimum required throughput are satisfied.

- Through simulations, we demonstrate that proposed scheme can significantly enhance the throughput and energy consumption of CRN when compared to structures using same sensing times or thresholds in all sub-channels or schemes, in which all single-antenna SUs are participated in SS and data transmitting.

The remainder of this paper is organized as follows. Section 2 describes the proposed system model. The problem formulation and analytical solution are also developed in this section. Section 3 provides the simulation results. The future prospect of the proposed approach are presented in section 4. Finally, conclusions are drawn in section 5.

2. SYSTEM MODEL AND PROBLEM FORMULATION

We consider a cooperative CRN comprised of FC, K PUs indexed by the set $\mathcal{K}=\{1,2,\dots,K\}$ and M SUs indexed by the set $\mathcal{M}=\{1,2,\dots,M\}$ distributed uniformly and equipped with L antennas as shown in Figure 2. The frequency band is assumed to be divided into K non-overlapping channels. Every PU can use only one of the bands. Each SU receives the PUs' signal with an instant signal-to-noise ratio (SNR) within a particular time interval. Some channels might not be used by the PUs and are available for opportunistic spectrum access. We use energy detection as the SS method in proposed CR system. Let f_s be the sampling frequency, τ_i and ε_i the sensing time and detection threshold for the i th sub-channel, respectively. It is assumed the sensing time for all sensing SUs in one sub-channel is the same.

We assume two hypotheses $H_{0,i}$ and $H_{1,i}$ for receiving the signals in each antenna, which refer to the inactive and active state of the PU on i th sub-channel, respectively. Let $Y_{ijl}(k)$ denote the k th sample in the i th sub-channel (the i th PU signal) received by l th antenna of j th SU, $s_i(k)$ is the k th sample of the transmitted signal from the i th PU, $w_{jl}(k)$ is the independent

identically distributed (i.i.d.) Gaussian random process with zero mean and the variance $\sigma_{n,j}^2$ received by l th antenna of j th SU. We assume a Rayleigh fading channel with gain h_{ijl} between the i th PU and l th antenna of j th SU defined as:

$$h_{ijl} = 10^{-\frac{L_{ijl}}{20}} \cdot g_{ijl} \quad (1)$$

where g_{ijl} is a random process with complex Gaussian distribution having zero mean and unit variance [34]. L_{ijl} has two components which are described as Equation (2): the first component is the path loss according to the free-space path loss model, and the second component expresses a real Gaussian random variable with zero mean and standard deviation of 3 based on large scale log-normal shadowing.

$$L_{ijl} = 20 \log \left(\frac{d_{ps_{ijl}}^{4\pi f_c}}{v} \right) + n_{jl} \quad (2)$$

where $d_{ps_{ijl}}$ expresses the distance of l th antenna of j th SU and i th PU. f_c denotes the working frequency, and v is the speed of light. Therefore, mathematically, the k th sample of the received signal of l th antenna of j th SU at the i th sub-channel, $y_{ijl}(k)$, can be written as two following hypotheses.

$$y_{ijl}(k) = \begin{cases} w_{jl}(k) & H_{0,i}: \text{PU is absent} \\ h_{ijl}s_i(k) + w_{jl}(k) & H_{1,i}: \text{PU is present} \end{cases} \quad (3)$$

$k = 1, 2, \dots, \tau_i f_s$

Therefore, the test statistic for l th antenna of j th SU on i th sub-channel is expressed as follows:

$$V_{ijl} = \frac{1}{\tau_i f_s} \sum_{k=1}^{\tau_i f_s} |y_{ijl}(k)|^2 \quad (4)$$

where $\tau_i f_s$ is the number of samples. By using the MRC technique as the diversity approach for combining the antenna's signal in j th SU, the test statistic of all antennas is accumulated to achieve the total received energy as follows [35]:

$$V_{ij} = \frac{1}{L\tau_i f_s} \sum_{k=1}^{\tau_i f_s} \left| \sum_{l=1}^L y_{ijl}(k) \cdot h_{ijl}^* \right|^2 \quad (5)$$

As a result, the following binary test is used to decide by the j th SU about the presence or absence of the PU in the i th sub-channel.

$$\text{Decide} = \begin{cases} H_{0,i} & \text{if } V_{ij} < \varepsilon_i \\ H_{1,i} & \text{if } V_{ij} > \varepsilon_i \end{cases} \quad (6)$$

The global P_d and P_f in j th SU for i th sub-channel can be expressed as follows:

$$P_{d_{ij}} = P(V_{ij} \geq \varepsilon_i | H_{1,i}) = Q_{L\tau_i f_s} \left(\sqrt{2} \gamma_{ij, \text{MRC}}, \frac{\sqrt{\varepsilon_i}}{\sigma_{\text{MRC}}} \right) \quad (7)$$

$$P_{f_{ij}} = P(V_{ij} \geq \varepsilon_i | H_{0,i}) = \frac{\Gamma(L\tau_i f_s, \frac{\varepsilon_i}{2\sigma_{\text{MRC}}^2})}{\Gamma(L\tau_i f_s)} \quad (8)$$

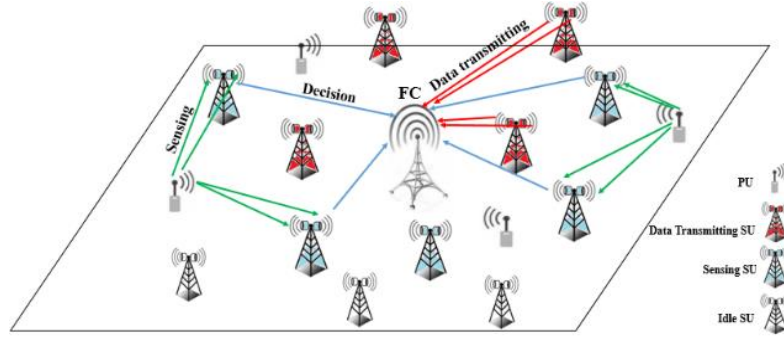


Figure 2. The multi-channel multi antenna CRN model

where $Q_m(a, b)$ denotes the generalized Marcum Q-function. $\Gamma(a)$ and $\gamma(a, b)$ express the gamma and incomplete gamma functions, respectively. $\gamma_{ij, MRC}$ is the average SNR of L antennas in j th SU and are defined as

$$\gamma_{ij, MRC} = \frac{(\sum_{l=1}^L |h_{ijl}|^2)^2 \cdot P_t}{\sigma_{MRC}^2} \quad \text{where } P_t \text{ denotes the transmit power of the PUs and } \sigma_{MRC}^2 \text{ is the variance of effective noise defined as } \sigma_{MRC}^2 = \sum_{l=1}^L |h_{ijl}|^2 \sigma_n^2.$$

It was shown that simultaneous participation of all SUs for sensing causes more energy consumption and higher P_f while the P_d will not increase significantly [22]. Therefore, we can select some SUs with the better P_d for SS in i th sub-channel while some others are selected to send their data to the FC through i th sub-channel, and the rest are considered idle to enhance the consumed energy and throughput. OR fusion rule is employed in FC to fuse the local decisions of the SUs. Therefore, the global P_d and P_f for i th sub-channel are expressed as follows:

$$P_{d_i} = 1 - \prod_{j=1}^M (1 - \rho_{ij} P_{d_{ij}}) \quad (9)$$

$$P_{f_i} = 1 - \prod_{j=1}^M (1 - \rho_{ij} P_{f_{ij}}) \quad (10)$$

where $\rho_{ij} \in \{0, 1\}$ is "1" if i th sub-channel is sensed by j th SU otherwise, it is considered as "0". Therefore, it should specify which SUs sense the i th sub-channel and which SUs transmit their data through i th sub-channel. If the SUs select transmitting the data on the i th sub-channel, the average throughput of the proposed CRN on all K channels is given below:

$$C = \sum_{i=1}^K \frac{T_f - \tau_i}{T_f} (\sum_{j=1}^M (P(H_{0,i})(1 - P_{f_i})\varphi_{ij} \log(1 + (SNR)_{ij}) + P(H_{1,i})(1 - P_{d_i})\varphi_{ij} \log(1 + (SINR)_{ij}))) \quad (11)$$

where $(SNR)_{ij} = \sum_{l=1}^L \frac{|h_{FSjl}|^2 \cdot P_{tij}}{\sigma_n^2}$ and $(SINR)_{ij} = \sum_{l=1}^L \frac{|h_{FSjl}|^2 \cdot P_{tij}}{p_{p,i}|h_{FPi}|^2 + \sigma_n^2}$. h_{FSjl} represents the channel gain

between FC and l th antenna of j th SU and h_{FPi} is the channel gain between FC and i th PU. P_{tij} and $p_{p,i}$ represent the transmitting power of the j th SU and i th PU on the i th sub-channel, respectively. The assignment index $\varphi_{ij} \in \{0, 1\}$ is "1" if the j th SU is selected for transmitting the data on the i th sub-channel otherwise it is considered as "0". We assume that $P(H_{0,i})$ and $P(H_{1,i})$ denote the probabilities that the i th sub-channel is idle and busy, respectively. T_f is the frame duration. The energy consumption of the proposed CRN is calculated by extending the considered model by Maleki et al. [36]. Therefore, the energy consumption of j th SU in each sub-channel at the sensing process can be written as follows:

$$E_{t_j} = \sum_{l=1}^L E_{s_{j,l}} + E_{t,dj} \quad (12)$$

where $E_{s_{j,l}}$ denotes the energy consumption by l th antenna of j th SU for sensing i th sub-channel. $E_{t,dj}$ represents the consumed energy for transmitting one decision bit from j th SU to the FC and is calculated as follows:

$$E_{t,dj} = E_{t-elec} + e_{amp} d_{FSj}^2 \quad (13)$$

where E_{t-elec} is the required energy for transmitter electronics and e_{amp} denotes the required amplification such that a specified receiver sensitivity level is satisfied. d_{FSj} represents the distance between FC and j th SU. With respect to the selection of the SUs for sensing, data transmitting, or being idle, the total consumed energy can be expressed as follows:

$$E_T = \sum_{i=1}^K \sum_{j=1}^M [\rho_{ij} [\sum_{l=1}^L E_{s_{j,l}} + E_{t,dj}] + \varphi_{ij} E_{td_{ij}}] \quad (14)$$

where $E_{td_{ij}}$ denotes the consumed energy by j th SU to send one data bit to the FC through i th sub-channel. Assuming that $E_{s_{j,l}}$ is the same for all antennas and the SUs denoted as E_s , we have:

$$E_T = \sum_{i=1}^K \sum_{j=1}^M [\rho_{ij} [L E_s + E_{t,dj}] + \varphi_{ij} E_{td_{ij}}] \quad (15)$$

Now, we assume that α and β denote the upper and lower

bounds of P_d and P_f in each sub-channel, respectively, to have more opportunity for using the idle channels and satisfy the PU's signal protection requirements from the interference.

By increasing the number of SUs for data transmitting in the CR network, the energy consumption and the total throughput are increased. However, the main goal is to achieve the minimum energy consumption of CRN while keeping throughput above a certain value, C_{th} , and interference to the PUs below a certain threshold. In other words, our goal is to find the number of SUs and specify the SUs for each sub-channel that minimizes the energy consumption, and also satisfies the minimum required total throughput of the CR. Therefore, all SUs do not need to cooperate for data transmission. Thus, the selection of the data transmitting SUs is considered for minimization of the energy consumption of the network and satisfaction of the required throughput of SUs.

Therefore, we can achieve the minimum energy consumption by solving the following optimization problem.

$$\min_{\rho_{ij}, \varphi_{ij}, \tau_i, \varepsilon_i} E_T \quad (16)$$

$$\text{s.t. } P_{d_i} \geq \beta \quad \forall i \in \mathcal{K} \quad (16.a)$$

$$P_{f_i} \leq \alpha \quad \forall i \in \mathcal{K} \quad (16.b)$$

$$C \geq C_{th} \quad (16.c)$$

$$\sum_{i=1}^K \rho_{ij} \leq 1 \quad \forall j \in \mathcal{M} \quad (16.d)$$

$$\sum_{j=1}^M \varphi_{ij} \leq 1 \quad \forall i \in \mathcal{K} \quad (16.e)$$

$$\rho_{ij} \varphi_{ij} = 0 \quad \forall i \in \mathcal{K}, j \in \mathcal{M} \quad (16.f)$$

$$\rho_{ij} \in \{0,1\} \quad \forall i \in \mathcal{K}, j \in \mathcal{M} \quad (16.g)$$

$$\varphi_{ij} \in \{0,1\} \quad \forall i \in \mathcal{K}, j \in \mathcal{M} \quad (16.h)$$

The constraint (16.d) indicates that each SU can only sense one channel in the sensing time slot. The constraint (16.e) indicates that each channel should be allocated to maximum of one SU for data transmitting in the transmitting duration. The constraint (16.f) expresses that sensing and transmitting cannot be accomplished by j th SU on i th sub-channel, simultaneously. Using constraint (16.b) and Equation (10), $n_i \leq \frac{\ln(1-\alpha)}{\ln\left(1 - \frac{r(L\tau_i f_s \frac{\varepsilon_i}{2\sigma_{MRC}^2})}{r(L\tau_i f_s)}\right)} = M_i$

where $n_i = \sum_{j=1}^M \rho_{ij}$ and M_i represents the number of sensing SUs and maximum number of sensing SUs in the i th channel, respectively. Due to the discrete nature of ρ_{ij} and φ_{ij} the problem is a non-deterministic polynomial time (NP) problem, and the general solution will be the

exhaustive search algorithm. Thus, all n_i sensing candidates and $M-n_i$ transmitting candidates in the i th sub-channel should be examined such that it achieves the minimum energy consumption and the constraints on the required detection performance for each sub-channel is satisfied. This algorithm has a high exponential complexity in the order of $O((M!)^K)$ for large M . Therefore, to reduce the complexity of the solution, ρ_{ij} and φ_{ij} are assumed as continuous parameters so that $\rho_{ij} \in [0,1]$ and $\varphi_{ij} \in [0,1]$. After solving our problem, ρ_{ij} and φ_{ij} are matched to discrete space again. As a result, the optimization problem can be reformulated as follows:

$$\min_{\rho_{ij}, \varphi_{ij}, \tau_i, \varepsilon_i} E_T = \sum_{i=1}^K \sum_{j=1}^M \rho_{ij} [L\tau_i P_s + E_{t,dj}] + \varphi_{ij} (T_f - \tau_i) P_{tij} \quad (17)$$

$$\text{s.t. } P_{d_i} \geq \beta \quad \forall i \in \mathcal{K} \quad (17.a)$$

$$\sum_{j=1}^M \rho_{ij} \leq M_i \quad \forall i \in \mathcal{K} \quad (17.b)$$

$$C \geq C_{th} \quad (17.c)$$

$$\sum_{i=1}^K \rho_{ij} \leq 1 \quad \forall j \in \mathcal{M} \quad (17.d)$$

$$\sum_{j=1}^M \varphi_{ij} \leq 1 \quad \forall i \in \mathcal{K} \quad (17.e)$$

$$\rho_{ij} \varphi_{ij} = 0 \quad \forall i \in \mathcal{K}, j \in \mathcal{M} \quad (17.f)$$

$$\rho_{ij} \in [0,1] \quad \forall i \in \mathcal{K}, j \in \mathcal{M} \quad (17.g)$$

$$\varphi_{ij} \in [0,1] \quad \forall i \in \mathcal{K}, j \in \mathcal{M} \quad (17.h)$$

where P_s is the sensing power of the SUs assumed to be the same for all SUs. P_{tij} represents the power for transmitting the data of j th SU on i th sub-channel. The above problem is not a standard convex optimization problem. However, the convex optimization approach can be employed to achieve a local solution instead of a global. For this purpose, the convex method based on the Lagrangian multiplier is used to solve the problem. We use Karush–Kuhn–Tucker (KKT) conditions to prioritize the SUs for SS and data transmitting in each sub-channel. Thus, the Lagrangian function is given by:

$$L(\varphi_{ij}, \rho_{ij}, \zeta, Y, \phi_i, \psi_i, \chi_i, \omega_j) = \sum_{i=1}^K \sum_{j=1}^M \rho_{ij} [L\tau_i P_s + E_{t,dj}] + \varphi_{ij} (T_f - \tau_i) P_{tij} + \zeta(C_{th} - C) + \sum_{i=1}^K \phi_i (\beta - P_{d_i}) + Y \rho_{ij} \varphi_{ij} + \sum_{i=1}^K \psi_i (\sum_{j=1}^M \rho_{ij} - M_i) + \sum_{i=1}^K \chi_i (\sum_{j=1}^M \varphi_{ij} - 1) + \sum_{j=1}^M \omega_j (\sum_{i=1}^K \rho_{ij} - 1) \quad (18)$$

where ζ , Y , ϕ_i , ψ_i , χ_i and ω_j represent the Lagrangian multipliers. Therefore, we have:

$$\frac{\partial L}{\partial \rho_{ij}} = L\tau_i P_s + E_{t,dj} - \phi_i (P_{d_{in}}) \prod_{n \neq j} (1 - \rho_{in} P_{d_{in}}) + \psi_i + \omega_j = 0 \quad \forall i \in \mathcal{K} \text{ and } \forall j \in \mathcal{M} \quad (19)$$

$$\begin{aligned} \frac{\partial L}{\partial \varphi_{ij}} = & (T_f - \tau_i)P_{tij} - \zeta \frac{T_f - \tau_i}{T_f} \left[P(H_{0,i}) \left(1 - \right. \right. \\ & P_{f_i}(\tau_i, \varepsilon_i) \left. \right) \log(1 + (SNR)_{ij}) + P(H_{1,i}) \left(1 - \right. \\ & P_{d_i}(\tau_i, \varepsilon_i) \left. \right) \log(1 + (SINR)_{ij}) \left. \right] + \chi_i = 0 \end{aligned} \quad (20)$$

For notation simplicity, we assume that $C_{ij}^0 = P(H_{0,i}) \log(1 + (SNR)_{ij})$ and $C_{ij}^1 = P(H_{1,i}) \log(1 + (SNR)_{ij})$. Therefore, we rewrite Equation (20) as:

$$\begin{aligned} \frac{\partial L}{\partial \varphi_{ij}} = & (T_f - \tau_i)P_{tij} - \zeta \frac{T_f - \tau_i}{T_f} \left((1 - \right. \\ & P_{f_i}(\tau_i, \varepsilon_i) \left. \right) C_{ij}^0 + \left(1 - P_{d_i}(\tau_i, \varepsilon_i) \right) C_{ij}^1 \left. \right) + \chi_i = 0 \end{aligned} \quad (21)$$

The goal is to prioritize the selection of the SUs as sensing or data transmitting in each sub-channel. Thus, the quantity of ρ_{ij} s and φ_{ij} s for the i th sub-channel is not essential. Instead, we compare the ratio of ρ_{ij}/ρ_{ik} for any pair of SUs. As a result, the SUs are prioritized for sensing and data transmitting on i th sub-channel by using the cost functions Equations (22) and (23) in which the SUs with smaller cost functions are selected as sensing and transmitting SUs, respectively.

$$\text{cost}(i, j) = L\tau_i P_s + E_{t,d_j} - \phi_i (P_{d_{ij}}) + \psi_i + \omega_j \quad (22)$$

We assume ψ_i and ω_j are identical for all SUs in all sub-channels. Therefore,

$$\text{cost}(i, j) = L\tau_i P_s + E_{t,d_j} - \phi_i (P_{d_{ij}}) \quad (23)$$

and for data transmitting SUs, we have:

$$\begin{aligned} \text{cost}(i, j) = & E_{td_{ij}} - \zeta \frac{T_f - \tau_i}{T_f} (C_{ij}^0 \prod_{j=1}^M (1 - \\ & \rho_{ij} P_{f_j}) + C_{ij}^1 \prod_{j=1}^M (1 - \rho_{ij} P_{d_j})) \end{aligned} \quad (24)$$

We use the complimentary slackness conditions to specify the optimum Lagrangian multipliers as follows:

$$\sum_{i=1}^K \phi_i (P_{d_i} - \beta) = 0 \rightarrow \begin{cases} \phi_i = 0, P_{d_i} > \beta \\ \phi_i \neq 0, P_{d_i} = \beta \end{cases} \text{ or} \quad (25-1)$$

$$(25-2)$$

$$\sum_{i=1}^K \psi_i (\sum_{j=1}^M \rho_{ij} - M_i) = 0 \rightarrow \begin{cases} \psi_i = 0, \sum_{j=1}^M \rho_{ij} < M_i \\ \psi_i \neq 0, \sum_{j=1}^M \rho_{ij} = M_i \end{cases} \text{ or} \quad (25-3)$$

$$(25-4)$$

$$\zeta (C - C_{th}) = 0 \rightarrow \begin{cases} \zeta = 0, C > C_{th} \\ \zeta \neq 0, C = C_{th} \end{cases} \text{ or} \quad (25-5)$$

$$(25-6)$$

$$\sum_{i=1}^K \chi_i (\sum_{j=1}^M \varphi_{ij} - 1) = 0 \rightarrow \begin{cases} \chi_i = 0, \sum_{j=1}^M \varphi_{ij} \neq 1 \\ \chi_i \neq 0, \sum_{j=1}^M \varphi_{ij} = 1 \end{cases} \text{ or} \quad (25-7)$$

$$(25-8)$$

$$\sum_{j=1}^M \omega_j (\sum_{i=1}^K \rho_{ij} - 1) = 0 \rightarrow \begin{cases} \omega_j = 0, \sum_{i=1}^K \rho_{ij} < 1 \\ \omega_j \neq 0, \sum_{i=1}^K \rho_{ij} = 1 \end{cases} \text{ or} \quad (25-9)$$

$$(25-10)$$

$$Y \rho_{ij} \varphi_{ij} = 0 \rightarrow \begin{cases} Y = 0, \rho_{ij} \varphi_{ij} \neq 0 \\ Y \neq 0, \rho_{ij} \varphi_{ij} = 0 \end{cases} \text{ or} \quad (25-11)$$

$$(25-12)$$

We note that P_{d_i} , P_{f_i} , and E_T are the increasing functions of ρ_{ij} s for the i th sub-channel. Therefore, we can decrease ρ_{ij} so that $P_{d_i} = \beta$ is satisfied for i th sub-channel. As a result, we can achieve smaller P_{f_i} and E_T . Therefore, $\phi_i \neq 0$ is considered a true condition. If the detection performance on i th sub-channel is satisfied by less sensing SUs, condition (25-3) will be optimal otherwise, (25-4) will be true. In other words, conditions (25-3) and (25-4) determine the maximum number of sensing SUs in each sub-channel. We consider $C = C_{th}$ as the optimal condition because E_T is an increasing function of ρ_{ij} s. Therefore, we can achieve less energy consumption when ρ_{ij} s decreases while satisfying the constraint on the minimum required throughput. Since the SUs cannot use more than one channel for transmitting their data and thus condition (25-8) is considered optimum. Conditions (25-9) and (25-10) indicate that the SUs can sense up to one sub-channel in the sensing duration. The last condition expresses that the data transmitting and sensing cannot be performed by one SU, simultaneously, so $\rho_{ij} \varphi_{ij} = 0$ is a true condition. To achieve the optimum SS time and detection threshold in each sub-channel and select the suitable SSUs and TSUs, an iterative algorithm as shown in the following flow chart, based on the bisection method [37] called STDTST, is proposed. First, we determine the priority of the sub-channels by computing the average SNR of the SUs over each sub-channel and sorting them in ascending order. Then, we select the sub-channels having the highest priority, $i = 0$. In the next step, P_d and P_f are computed for all SUs in i th sub-channel. At each iteration in which ϕ , ζ , τ , and ε are updated by the bisection algorithm, the cost function in Equation (23) for all SUs over selected sub-channel is computed and sorted in ascending order, then the SUs with the lowest cost are considered to be participate in SS until the global $P_{d_i} \geq \beta$ on the i th sub-channel is met, and the maximum number of selected SUs on i th sub-channel becomes less than M_i . Then, the cost function (24) is calculated for the remaining SUs on i th sub-channel and sorted in ascending order. We select the SUs having the lower cost for data transmitting on i th sub-channel while guaranteeing the required throughput. The values τ , ε , ϕ and ζ are updated by using bisection search approach according to the following rule. If $P_{d_i} \geq \beta$, τ is decreased; otherwise is increased. As a result, we can achieve the optimum τ by this algorithm. The same approach is employed simultaneously to obtain the optimum ζ , ϕ . Now, for finding the optimum ε , we employ the same algorithm to the one used to obtain the optimum τ . However, the difference lies in updating, where ε increases if $P_{d_i} \geq \beta$ and vice versa. The condition for stopping the algorithm is that its accuracy becomes less than a small predetermined threshold. The complexity of our proposed algorithm to find the

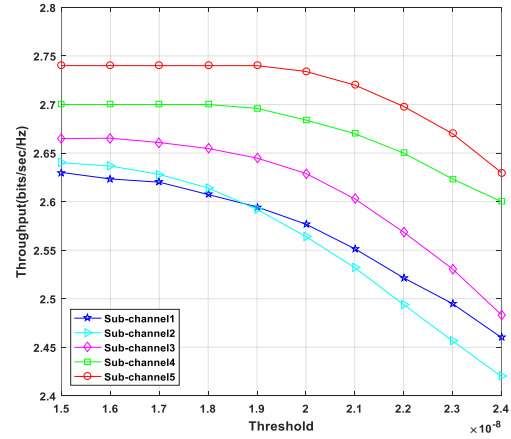
solutions is linear in the order of $O(MK)$, since, only the cost functions should be computed for all SUs over the sub-channel in each iteration which is much less than the computational complexity of the exhaustive search algorithm.

3. SIMULATION RESULTS

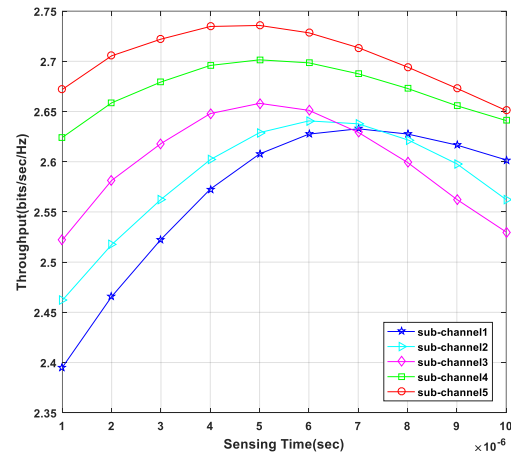
For simulations, we consider a cooperative CRN consisting of the SUs and PUs located randomly with a uniform distribution in the square area with a variable length between 100 m to 500 m in which FC is located in the center of the square. The 2.4 GHz IEEE 802.15.4/ZigBee is used as the communication technology in the network. We assume that the channel model from the PUs to the FC and each SU to the FC, is as Equation (1) [38]. We employed MATLAB 2015a for simulations and each point in the results is obtained by averaging over 10000 independent random experiments. The simulation parameters are listed in Table 1. Let us first analyze the optimality of average achievable throughput versus the sensing time and detection threshold over the five sub-channels, as shown in Figure 3. We would like to maximize the throughput over the five sub-channels.

TABLE 1. The simulation parameters

Parameter	Value
The number of SU (M)	50 ~500
The number of PU (K)	5
The number of antenna (L)	2 ~ 4
α	0.1
β	0.9
f_c	2.4 MHz
$P(H_0)$	0.6
$P(H_1)$	0.4
T_f	100 ms
f_s	1 MHz
v	3×10^8 m/s
E_s	190 nJ
E_{t-elec}	80 nJ
e_{amp}	40.4 pJ/m ²
p_p	20 mW
C_{th}	10 bits/sec
Data rate	250 Kb/s
Receiver sensitivity	-90 dBm



(a)



(b)

Figure 3. The average throughput vs. (a) Detection threshold (b) Sensing times for different sub-channels when $K = 5$, $M = 100$ and $L=2$

It can be clearly seen that there is an optimal τ and ϵ for each sub-channel that maximizes the throughput. The throughput for each sub-channel is low in very short sensing time because the detection performance is low, and therefore, P_f is high while, in a long sensing time, the throughput is low because the data transmitting time is very short. Therefore, there is a tradeoff between the sensing time and throughput over each sub-channel. In Figure 4, the consumed energy in different sub-channels versus different sensing times and detection thresholds has been obtained. The energy consumption is high in small and large τ because, in small τ the more time is used for data transmitting, while in large τ more time is used for sensing. From Figures 3(a) and 4(a), we can also see that there are optimal detection thresholds for each sub-channel that maximizes the throughput and achieve the minimum energy consumption over each sub-channel.

The more significant thresholds achieve less throughput and more energy consumption.

In Figure 5(b), P_d in each sub-channel versus different sensing times is evaluated. We can see that increasing the sensing time leads to an increment in the global P_d in each sub-channel until it reaches to 1. Therefore, the signal quality of the PUs can be sufficiently maintained. We also can see that P_d for different sub-channels is almost identical and close to each other. That's due to the fact that the optimal selection of the SUs can compensate the low SNR or non-optimal sensing time or detection threshold for the different sub-channels. Although the average global P_d constraint for all sub-channels is maintained, however according to Figure 4, it increases energy consumption. By decreasing the detection threshold, the global P_d and P_f for each sub-channel increase, and the desired detection performance is obtained by using fewer SUs. Therefore, the consumed energy over the sub-channels is reduced.

Table 2 shows the average SNR, optimal sensing times, and detection thresholds obtained with Algorithm 1 for each sub-channels when $K = 5$, $M = 100$, and $L=2$. Since all K sub-channels can be used by CR users for transmission, thus the objective is to achieve the minimum sum of the energy consumption, and improve the sum of the throughput of all sub-channels by optimizing the sensing times, detection thresholds and the selection of the SSUs and TSUs in all frequency bands.

Note that in the multi-channel scenario, the global P_d and P_f requirements and the minimum required throughput of CRN in different sub-channels may differ.

Algorithm 1. The algorithm to find the optimum detection thresholds and sensing times and to select the SSUs and TSUs on each sub-channel for a multi-channel multi-antenna CRN.

Initialization:

τ_{max} = a large enough number
 τ_{min} = 0
 ε_{max} = a large enough number
 ε_{min} = 0
 ζ_{min} = 0
 ζ_{max} = a large enough number
 ϕ_{min} = 0
 ϕ_{max} = a large enough number
 $\varepsilon_1, \varepsilon_2, \varepsilon_3, \varepsilon_4$ are the small numbers
 Compute average SNR of all SUs on all sub-channel
 $i=0$ % index of sub-channel

Sort all SNR_i in an ascending order so SNR_0 has maximum value

WHILE ($i < K$ % number of sub-channel) **do**

WHILE ($|\tau_{max} - \tau_{min}| > \varepsilon_1$) **do**

$\tau_i = (\tau_{max} + \tau_{min})/2$

WHILE ($|\varepsilon_{max} - \varepsilon_{min}| > \varepsilon_2$) **do**

$\varepsilon_i = (\varepsilon_{max} + \varepsilon_{min})/2$

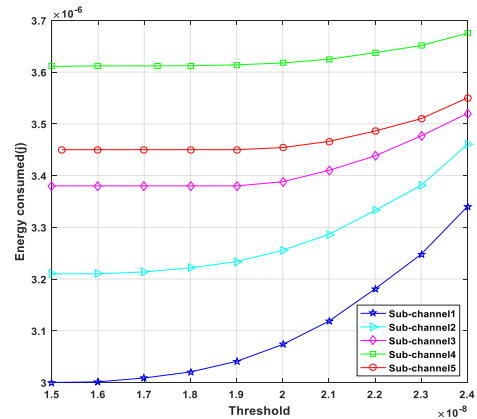
 Compute $P_{d_{ij}}$ and $P_{f_{ij}}$ for all SU

WHILE ($|\phi_{max} - \phi_{min}| > \varepsilon_3$) **do**

$\phi_i = (\phi_{max} + \phi_{min})/2$
WHILE ($|\zeta_{max} - \zeta_{min}| > \varepsilon_4$) **do**
 $\zeta = (\zeta_{max} + \zeta_{min})/2$
 Compute $cost(i, j) = L\tau_i P_s + E_{t,d_j} - \phi_i (P_{d_{ij}})$ for all SUs
 Sort cost functions (23) in an ascending order
 $m=0$ % The number of SSUs with higher priority
 Compute M_i (maximum number of SU for sensing)
WHILE ($m < M_i$) **do**
 Compute $P_{d_i} = 1 - \prod_{j=1}^m (1 - P_{d_{ij}})$
 IF $P_{d_i} > \beta$ **THEN BREAK**
 ELSE $m = m + 1$
 END IF
END WHILE
 Compute E_T according to (15)
 $N_t = M - m$ % The remaining SUs which can be selected as TSU
 Compute cost function (24) for all SUs
 Sort cost functions (24) in an ascending order
 $t = 0$ % The number of selected TSUs
WHILE ($t < N_t$)
 Compute C % total throughput
 IF $C \geq C_{th}$ **THEN BREAK**
 ELSE $t = t + 1$
 END IF
END WHILE
IF $P_{d_i} > \beta$ **THEN** $\zeta_{max} = \zeta$
ELSE $\zeta_{min} = \zeta$
END IF
END WHILE
IF $P_{d_i} > \beta$ **THEN** $\phi_{max} = \phi_i$
ELSE $\phi_{min} = \phi_i$
END IF
END WHILE
IF $P_{d_i} > \beta$ **THEN** $\varepsilon_{min} = \varepsilon$
ELSE $\varepsilon_{max} = \varepsilon$
END IF
END WHILE
IF $P_{d_i} > \beta$ **THEN** $\tau_{max} = \tau$
ELSE $\tau_{min} = \tau$
END IF
END WHILE
 $i = i + 1$

END WHILE

Output: The optimal τ , ε , TSUs, SSUs for each sub-channel and optimum energy efficiency and throughput



(a)

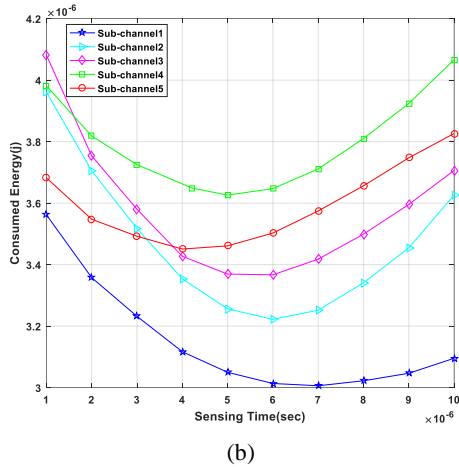


Figure 4. The consumed energy vs. (a) Detection threshold (b) Sensing times for different sub-channels

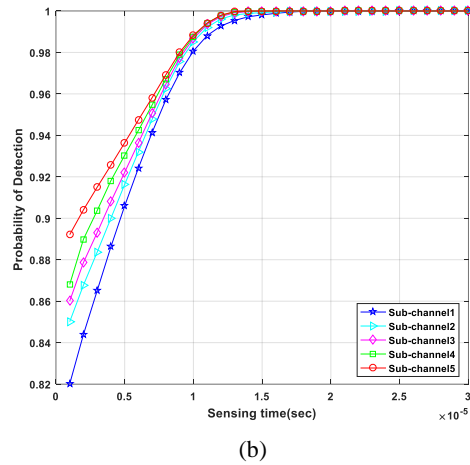
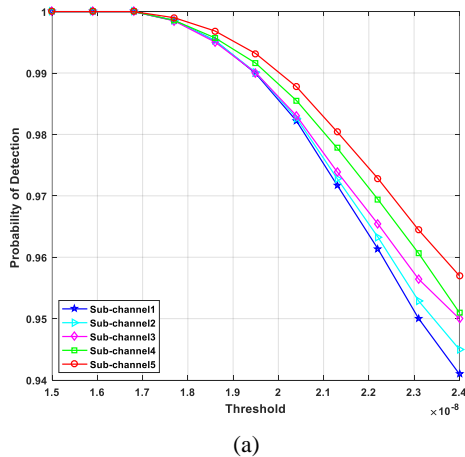


Figure 5. The probability of detection vs. (a) Detection thresholds and (b) Sensing times in each sub-channel

However, we consider the sum of the throughput over all sub-channels. Now, we compare the proposed algorithm with the following schemes in the simulations.

1. Joint optimization scheme of the Sensing Time and Detection Threshold and selection of SSUs and TSUs called STDTS: This scheme is similar to STDTS, the difference is that the TSUs over each sub-channel are selected based on Equation (24) so that the energy consumption and the throughput constraints are satisfied then, according to Equation (23) the SSUs over each sub-channel are determined while satisfying the constraints on the maximum number of SSUs and P_{d_i} .
2. Random Selection of the SUs scheme (RSMA): In this algorithm, TSUs and SSUs are randomly selected over each sub-channel until the constraints on the P_{d_i} is satisfied. In this approach, none of the sensing times and detection thresholds for sub-channels are optimized.



(a)

TABLE 2. Average SNR, optimal sensing times and detection thresholds for a multi antenna multi-channel CR network with 5 sub-channels, 100 SUs with 2 antennas

Sub-Channel	Average SNR	Optimum sensing time (s)	Optimum threshold
Sub-channel1	6.4134	0.7116e-5	0.1524e-7
Sub-channel2	6.5876	0.6153e-5	0.1587e-7
Sub-channel3	6.6943	0.5059e-5	0.1623e-7
Sub-channel4	7.5441	0.4960e-5	0.1788e-7
Sub-channel5	7.7238	0.4235e-5	0.1865e-7

3. Joint optimization scheme of the Detection Threshold, the selection of SSUs and TSUs (DTST): The SSUs and TSUs are selected similar to the STDTS algorithm while the sensing times are considered the same and predetermined for all sub-channels.
4. Joint optimization scheme of the Sensing Time and the selection of SSUs and TSUs (STST): In this method, after determining the priority of sub-channels based on their average SNR for each sub-channel, the cost function in Equation (23) is computed and sorted in ascending order. Then, the SUs with the lowest cost is considered to participate in SS until the global $P_{d_i} \geq \beta$ on the i th sub-channel is met, and the constraint on the maximum number of selected SSUs is satisfied. After that, from the remaining SUs, the SUs with the lowest cost in Equation (24) are selected for data transmitting so that the minimum required total throughput is satisfied. The values of the sensing times are updated for each sub-channel by using the following rule: If the $P_{d_i} \geq \beta$, the sensing time will decrease otherwise, it will increase. This algorithm

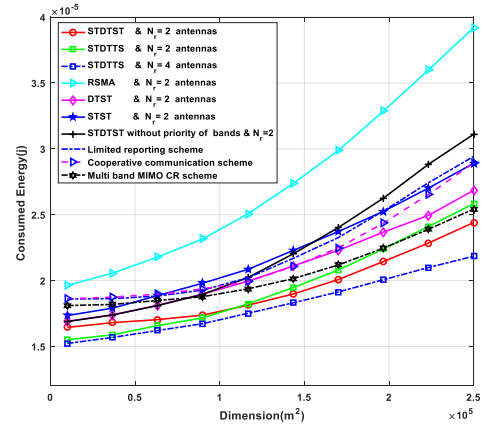
allocates equal detection thresholds to all sub-channels.

5. STDST without priority of bands: This scheme is similar to STDST the difference is that the prioritization of sub-channels is not performed.
6. The limited reporting scheme [22].
7. The cooperative communication scheme between CRN and the primary network [24].
8. The presented multi-band MIMO CR scheme reported by Moghimi et al. [26].

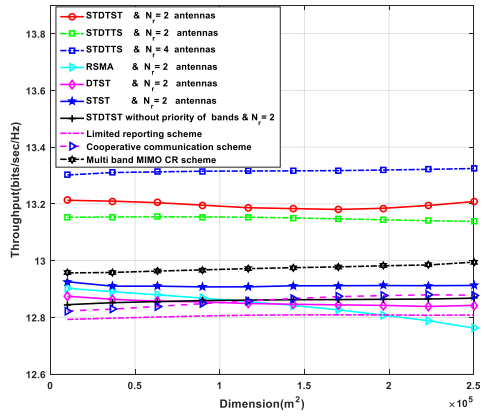
We consider a CRN with 5 PUs and 100 SUs equipped with 2 or 4 antennas. The detection threshold levels and the sensing times are set according to Table 2 for each sub-channel. The total throughput threshold is fixed at 10. The sampling time ratio and the reporting time ratio for the limited reporting scheme are set to $0.15e^{-4}$ and $0.4e^{-4}$, respectively. We consider a multi-band 4×4 MIMO CR system for the presented scheme by Moghimi et al. [26]. In Figure 6, the average throughput and consumed energy of all the schemes are compared in different dimensions of the network. It can be seen that all algorithms satisfy the constraint on the minimum required throughput in different dimensions. It is clear that in large dimensions, the difference between the throughput of STDTTs with 4 antennas and other algorithms becomes greater, which is due to the enhancement of the diversity gain. It can be seen that the prioritization of sub-channels leads to the increment of throughput and reduction of the energy consumption of CRN, especially in large dimensions. Moreover, because of the random selection of the SSUs and TSUs over each sub-channel, RSMA scheme has more energy consumption and less throughput in comparison to other schemes.

Figure 7 indicates P_d of different algorithms for the first sub-channel with the lowest SNR in different dimensions when the number of the SU is $M=100$ and the detection threshold for STST and RSMA algorithms is fixed to $0.18e^{-7}$. The sensing time for DTST and RSMA algorithms is set to $0.7e^{-5}$. The detection threshold and the sensing times for STDST and STDTTs schemes are set according to Table 1. It can be seen that increasing the dimension of the network decreases the P_d for all schemes because the network obtains higher chances to distribute more SUs far from the PUs. However, the minimum required P_d constraint for all algorithms, $P_{d_1} \geq \beta$, is satisfied. We can also see that selecting the non-optimal detection threshold for the first sub-channel would have a very negative effect on detection performance.

In Figure 8, we investigate the impact of the number of SUs on the total throughput and energy consumption of CRN when the dimensions of the network are set to $100 \text{ m} \times 100 \text{ m}$. We can see STDTTs with 4 antennas has more throughput and less energy consumption than other schemes. We also see that, compared with STDTTs



(a)



(b)

Figure 6. The impact of the dimension of the network on the (a) Consumed energy (b) Total throughput of CRN

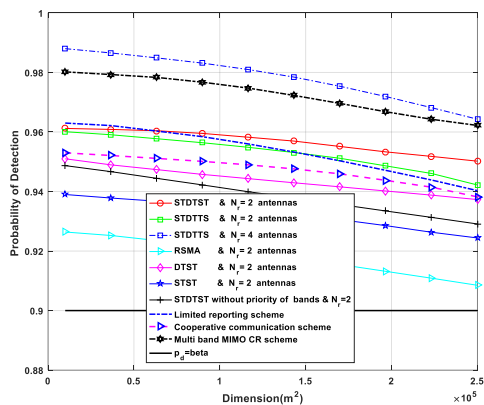


Figure 7. P_d versus dimension of the network for first sub-channel

with 2 antennas, the 4×4 multi-band MIMO CR approach achieve more throughput. Figure 9 depicts P_d versus the number of SUs for different algorithms in

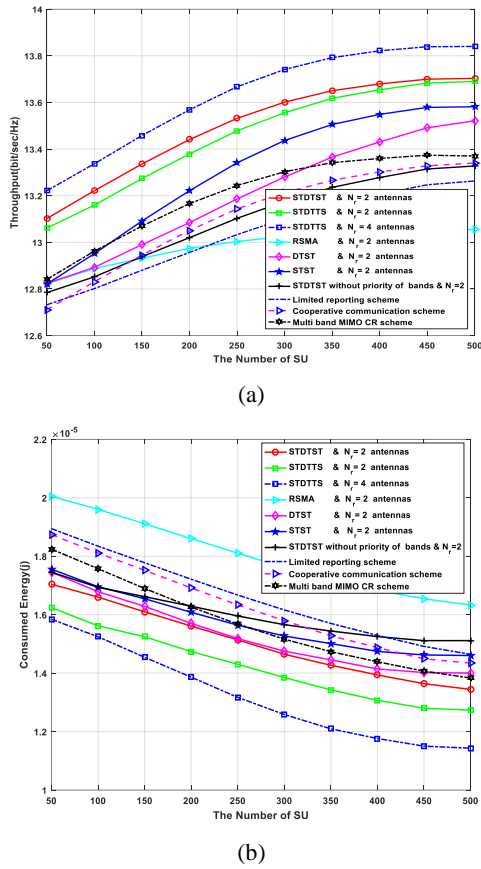


Figure 8. (a) The total throughput (b) Energy consumption of CRN vs the number of the SU

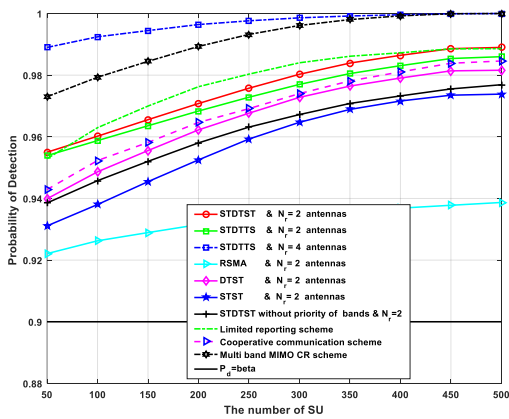


Figure 9. The impact of the number of the SU on P_d in first sub-channel

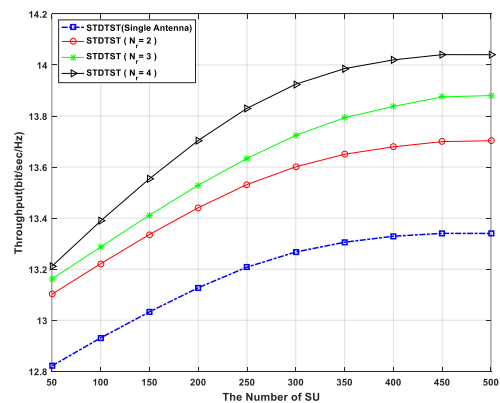
the first sub-channel. It can be observed that the P_d of all schemes increases by increasing the number of SUs until reaches to the maximum value. Thus, when the number of the SUs is large enough, it has little effect on the detection performance. Considering Figure 8 and the

results illustrated in Figure 9, it can be concluded that the increment of the number of antennas increases P_d especially when the dimensions are small. For example, when the dimensions of the network are 100 m x 100 m and the desired P_d for the first sub-channel using the STDTTS scheme is considered as 0.99, at least 250 SUs with 2 antennas must be distributed in the network while the above detection performance can be satisfied by 80 SUs with 4 antennas. We can also see that the STDTTS scheme can achieve approximately 13.4 bits/s/Hz total throughput by 125 SUs with 4 antennas or 205 SUs with 2 antennas in 100 m x 100 m network dimensions. Therefore, when the minimum total throughput can be achieved by SUs having the fewer numbers of antenna, it is more appropriate to exclude employing more antennas since it will be useless and has more cost. However, it is possible to consume more energy because the more SUs must be applied to achieve the minimum required total throughput.

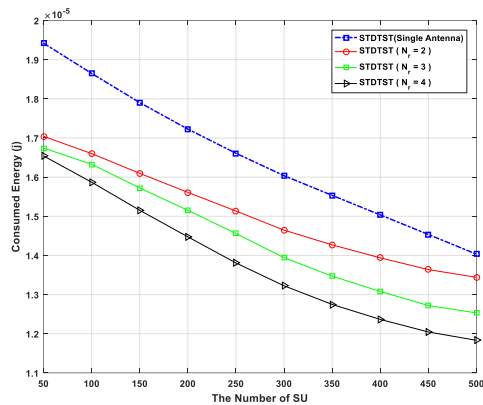
As a result, the final decision about the number of antennas should be obtained based on the tradeoff between implementation cost and consumed energy.

In Figure 10, the impact of the number of SUs having different numbers of antenna on the total throughput and consumed energy is evaluated when the STDTST algorithm is used. The SUs with 1, 2, 3, and 4 antennas are considered, while the dimensions of the network are 100 m x 100 m. From Figure 10(b), we can see that the STDTST with more antennas consumes less energy than other cases. Therefore, the number of antenna used for the implementation cost depends on the difference in the implementation cost and complexity between adding antennas and adding SUs with less antennas for energy saving.

Finally, the convergence of the STDTST algorithm is analyzed in Figure 11, when M=100, K=5, L=2 and the dimensions of the network are 100 m x 100 m. The energy consumption decreases in each iteration and converges to a fixed and minimum point in the 69th iteration.



(a)



(b)

Figure 10. (a) The joint influence of the number of the SU and number of antennas on the (a) throughput (b) energy consumption

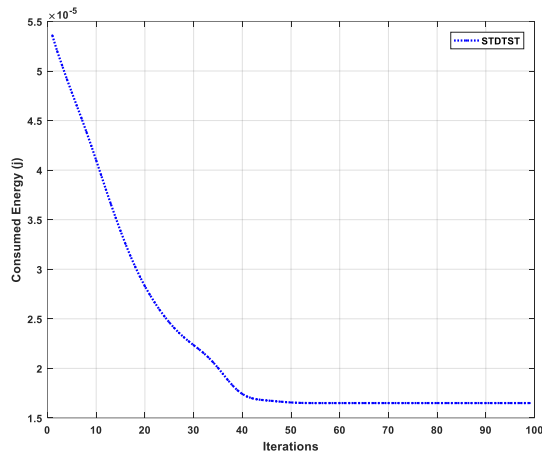


Figure 11. The convergence performance of STDTST algorithm for different iterations

3. 1. Results Analysis In Figures 3(a), 4(a) and 5(a) we investigated the impact of detection threshold on the average throughput, energy consumption and probability of detection for different sub-channels in the multi-antenna multi-channel CR network, respectively. It can be seen that when the threshold is less than a unique optimal value the average throughput can attain almost the maximum and constant value for each sub-channel while more threshold leads to less throughput. Figure 4(a) shows that as the threshold increases, the energy consumption increases. That's due to the fact that as the threshold increases, the probability of detection for each SU in each sub-channel decreases and the selection of more SUs is required to satisfy detection performances. Figures 3(b), 4(b) and 5(b) show the influence of the sensing time on the throughput, energy consumption and probability of detection for different sub-channels,

respectively. We can see, the probability of detection increases with the increasing of the sensing time until it reaches to 1. In Figure 3(b), the achievable throughput for each sub-channel is less at a small or large sensing time, that's due to the fact that the small sensing time decreases the detection performance, whereas large sensing time reduces the data transmitting time and therefore, we see the tradeoff between the sensing time and achievable throughput of the CR network.

Form Figure 4(b), we can clearly see that there exist an optimal sensing time for minimizing the energy consumption over the five sub-channels. It can be seen that at the unique optimal sensing times for each subchannel, the energy consumption can attain almost the minimum value, while the more or less sensing times leads to more energy consumption because it gets more times for sensing and data transmitting, respectively.

Therefore, according to Figures 3 to 5, the minimum threshold and sensing time should be achieved, such that the throughput of the secondary network is maximized and the total energy consumption is minimized, while detection constraints can be satisfied. Thus, We see that P_{d_j} increase by increasing the time sensing and by decreasing the threshold. As a result, the fewer number of SUs participating in the spectrum sensing is required to satisfy the detection constrains and reduce the total energy consumption. Figure 6 shows the influence of dimensions of the network on the throughput and energy consumption of all the schemes. As can be observed, all schemes maintain the throughput threshold constraint for all dimensions. It can be seen when the dimension increases the more energy is consumed because the detection performance will be decreased by increasing the length of network as shown in Figure 7. Therefore, it should be selected more SUs for satisfying the detection performance and transmitting their data to the FC to satisfy the constraint (17.c). When the dimension of the network is small, the SUs will have a high density in the area. Therefore, the constraint on the detection performance can be satisfied by selecting less SUs. In addition, by increasing the dimension of the network the average distance from the PUs to the SUs and from the SUs to the FC increases. Thus, it consumes more energy to guarantee the minimum sensitivity of the receivers.

The influence of the number of SUs on the total throughput, energy consumption, and probability of detection of all the schemes is shown in Figures 8 and 9. We see that the average throughput increases monotonically by increasing the number of SUs, however it grows slowly when the quantity of SU is large until it reaches to the maximum value and then is fixed. It can be clearly seen from Figure 8(b) that the total consumed energy of CRN decreases with the increasing number of SUs. This can be expressed by the fact that as the number of SUs increases, there will be a greater chance for more SSUs or TSUs be near the PUs or FC. Therefore, the total

throughput and P_d increase while the located SUs near to FC leads to less energy consumption. It is also shown that the throughput enhances by increasing the number of antenna because of the enhancement of the diversity gain.

The impact of changing the number of antenna on the total throughput and consumed energy of STDTST scheme is shown in Figure 10. It can be observed that the multi-antennas strategy outperforms the one using single antenna. We analyzed the convergence of proposed algorithm in Figure 11. We can see that the algorithm correctly converges to the minimum value after several iterations.

4. FUTURE PROSPECT OF THE PROPOSED APPROACH

We anticipate that CR technology will soon emerge from early-stage laboratory trials and vertical applications to become a general-purpose programmable radio that will serve as a universal platform for wireless system development, much like microprocessors fulfill that role for computation. The evolution of CR toward CR networks is underway; the concept of CR networks is to intelligently organize a network of CRs. Applications of spectrum-sensing CR include emergency-network and WLAN higher throughput and transmission-distance extensions. The CR technology will be used commercially in the 5G and 6G cellular networks. 6G networks will be able to use higher end of the radio spectrum than 5G networks and provide substantially higher capacity and much lower latency. While reliable spectrum sensing techniques are pivotal, the CRN's throughput, energy efficiency, and channel maintenance are important considerations for the SUs. This has primarily motivated the employment of multi-channel multi-antenna CR paradigm. Multi-antenna SUs to sense and access multiple channels, simultaneously promised significant enhancements to the network's throughput and energy efficiency. In addition, it provides seamless handoff from band to band, which improves the link maintenance and Quality of Service (QoS) and reduces data transmission interruptions.

Moreover, cooperative networks were analyzed, and a possible extension to integrate such a powerful paradigm into multi-channel CRN was suggested. Particularly, cooperative multi-channel CR provided a desirable compromise between spatial diversity and sampling complexity. In addition, some of the most common performance measures that help evaluate the network's performance in terms of spectrum reliability and network's throughput have been presented.

However, there are fundamental limits and tradeoffs among several critical design parameters in multi-channel multi-antenna CRNs that must be carefully investigated. The most common considerations are the

sensing time, detection threshold, network throughput, data combination methods, detection reliability, number of cooperating SUs, power control, and channel assignment. Some of these cases, such as sensing time, and detection threshold were discussed in this paper. The rest will be explained in the following.

1. One of the key issues in cooperative communications is how to combine the collected information from the participating SUs. There are three main techniques, namely: hard combining, soft combining, and hybrid combining. 1) Hard Combining: In this technique, the SU merely sends its final one-bit decision to the other SUs. In this technique, the SU shares its original sensing information (or original statistics) with the other SUs without locally processing them. Hard combining requires less overhead compared to soft combining. However, since the statistics at each SU are reduced to one bit, there is an information loss that propagates to the other SUs. Therefore, the final decision is less reliable compared to soft combining. The soft combination techniques such as MRC, EGC, OC, SC, SLS, SLC, and hard combination methods consist of AND, OR and MAJORITY for CRs with and without multiple antenna. Therefore, the selection of the optimal combination technique is essential, which was not discussed in this paper, and it can be considered as an effective research case in future works when it is added to the proposed model of this paper.
2. Optimum power allocation is vital for improving the network's throughput and protecting PUs. It becomes even more important when the underlay scheme is used, since power adaptation becomes necessary. Therefore, our future works include adding transmit power and interference bounds as constraint functions.
3. While increasing the number of cooperating SUs improves the reliability of detection and reduces sensing time, it incurs a long delay due to the time required to collect the information from all the SUs. To tackle this issue, the SUs can simultaneously send their decisions on orthogonal frequency bands, yet this requires larger bandwidth. Thus, an effective scheme should be proposed to obtain the minimum number of SUs to maintain the desired performance, which was not considered in this paper, and can be investigated in future works.
4. One can presume that accessing all available bands would theoretically increase the throughput. However, when a SU accesses all these bands, there is a higher probability that a PU returns to at least one of them. Thus handoff becomes necessary, which consequently increases the network's overhead. Therefore, optimizing the number of sub-channels for spectrum access becomes essential. To

guarantee that each SU picks the best channels, frequent channel reselections become inevitable, and hence high overhead is incurred. To reduce the overhead, a proper approach is required where the SU selects a channel as long as it can support the least possible transmission rate. Otherwise, an alternative channel is randomly selected. This algorithm has a lower throughput, yet it reduces the frequency of channels' reselections. The future work advises using of adaptive bandwidth selection for the proposed multi-channel multi-antenna CRN to further maximize the network's throughput.

5. Recently, energy harvesting (EH) from ambient radio frequency (RF) signal sources has been proposed as a promising solution to address the energy shortage problem. In an Energy Harvesting Cognitive Radio (EHCR) network, a CR transmitter collects energy from RF signals by EH when a PU is present in the channel and employs it for data transmission when the spectrum is idle. Therefore, the SU should search for not only a vacant channel of PUs for its data transmission, but also an occupied channel for EH. In future works, we can use an energy harvesting-based multi-channel multi-antenna CR network to execute cooperative SS, data transmission, and RF energy harvesting by a secondary transmitter from PU's signal and the ambient noise, simultaneously.

5. CONCLUSION

In this paper, we studied the problem of designing the optimal sensing times and detection thresholds in each sub-channel and selecting the multi-antenna SSUs and TSUs in the multi-channel multi-antenna CRNs for improvement of both throughput and energy efficiency so that the constraints on the global P_d and P_f in each sub-channel are satisfied. Our problem formulated, and the priority of SUs for sensing and data transmitting in each sub-channel determined. We proposed the algorithm having less computational complexity than baseline approaches to achieve the optimal parameters and goals of the problem. Furthermore, simulation results have shown that the proposed structures and algorithms can consistently achieve an improvement on the throughput and energy consumption in comparison to the structures using the same sensing times or thresholds in all sub-channels or schemes in which all single-antenna SUs have participated in spectrum sensing and data transmitting on all sub-channels.

5. REFERENCES

1. Mergu, K. and Khan, H., "Mitigation of spectrum sensing data falsification attack in cognitive radio networks using trust based

- cooperative sensing", *International Journal of Engineering, Transactions C: Aspects*, Vol. 34, No. 6, (2021), 1468-1474. <https://doi.org/10.5829/IJE.2021.34.06C.10>
2. Asif, H.M., "F.: Spectrum sensing challenges & their solutions in cognitive radio based vehicular networks int", *J. Commun. Syst.(02)*, (2021), 23-25. <https://doi.org/10.1002/dac.4748>
3. Zhao, H., Tan, Y., Pan, G., Chen, Y. and Yang, N., "Secrecy outage on transmit antenna selection/maximal ratio combining in mimo cognitive radio networks", *IEEE Transactions on Vehicular Technology*, Vol. 65, No. 12, (2016), 10236-10242. <https://doi.org/10.1109/TVT.2016.2529704>
4. Kishore, R., Gurugopinath, S., Muhaidat, S., Sofotasios, P.C., Dobre, O.A. and Al-Dhahir, N., "Sensing-throughput tradeoff for superior selective reporting-based spectrum sensing in energy harvesting hcrrns", *IEEE Transactions on Cognitive Communications and Networking*, Vol. 5, No. 2, (2019), 330-341. <https://doi.org/10.1109/TCCN.2019.2906915>
5. Sarala, B., Devi, S.R. and Sheela, J.J.J., "Spectrum energy detection in cognitive radio networks based on a novel adaptive threshold energy detection method", *Computer Communications*, Vol. 152, (2020), 1-7. <https://doi.org/10.1016/j.comcom.2019.12.058>
6. Jiang, H., Yu, Z., Yang, J. and Kang, K., "Throughput-oriented full-duplex cognitive radio network parameter optimization", *International Journal of Antennas and Propagation*, Vol. 2022, (2022), 1-8. <https://doi.org/10.1155/2022/4056645>
7. Ahmed, A., Mishra, D., Prasad, G. and Baishnab, K.L., "Cognitive radio timing protocol for interference-constrained throughput maximization", *IEEE Transactions on Cognitive Communications and Networking*, Vol. 8, No. 2, (2021), 989-1004. <https://doi.org/10.1155/2022/4056645>
8. Kumar, A., Thakur, P., Pandit, S. and Singh, G., "Hsa-spc: Hybrid spectrum access with spectrum prediction and cooperation for performance enhancement of multiuser cognitive radio network", *Computer Networks*, Vol. 203, (2022), 108596. <https://doi.org/10.1016/j.comnet.2021.108596>
9. Liu, X. and Tan, X., "Optimization algorithm of periodical cooperative spectrum sensing in cognitive radio", *International Journal of Communication Systems*, Vol. 27, No. 5, (2014), 705-720. <https://doi.org/10.1002/dac.2377>
10. Sadeghian Kerdabadi, M., Ghazizadeh, R., Farrokhi, H. and Najimi, M., "Energy consumption minimization and throughput improvement in cognitive radio networks by joint optimization of detection threshold, sensing time and user selection", *Wireless Networks*, Vol. 25, (2019), 2065-2079. <https://doi.org/10.1007/s11276-018-1797-x>
11. Liu, X., Xu, B., Wang, X., Zheng, K., Chi, K. and Tian, X., "Impacts of sensing energy and data availability on throughput of energy harvesting cognitive radio networks", *IEEE Transactions on Vehicular Technology*, Vol. 72, No. 1, (2022), 747-759. <https://doi.org/10.1109/TVT.2022.3204310>
12. Das, D., Khadanga, R.K. and Rout, D.K., "A matching game framework for users clustering and resource allocation with wireless power transfer in a cr-noma network", *International Journal of Communication Systems*, Vol. 36, No. 2, (2023), e5376. <https://doi.org/10.1002/dac.5376>
13. Bokobza, Y., Dabora, R. and Cohen, K., "Deep reinforcement learning for simultaneous sensing and channel access in cognitive networks", *IEEE Transactions on Wireless Communications*, (2023). <https://doi.org/10.1109/TWC.2022.3230872>
14. Salari, S. and Chan, F., "Maximizing the sum-rate of secondary cognitive radio networks by jointly optimizing beamforming and energy harvesting time", *IEEE Transactions on Vehicular Technology*, (2023). <https://doi.org/10.1109/TVT.2023.3238347>
15. Hameed, I., Camana, M.R., Tuan, P.V. and Koo, I., "Intelligent reflecting surfaces for sum-rate maximization in cognitive radio

- enabled wireless powered communication network", *IEEE Access*, Vol. 11, (2023), 16021-16031. <https://doi.org/10.1109/ACCESS.2023.3243848>
16. Singh, J.S.P., "Apc: Adaptive power control technique for multi-radio multi-channel cognitive radio networks", *Wireless Personal Communications*, Vol. 122, No. 4, (2022), 3603-3632. <https://doi.org/10.1007/s11277-021-09103-w>
 17. Gutierrez del Arroyo, J.A., Borghetti, B.J. and Temple, M.A., "Considerations for radio frequency fingerprinting across multiple frequency channels", *Sensors*, Vol. 22, No. 6, (2022), 2111. <https://doi.org/10.3390/s22062111>
 18. Huang, X.-L., Tang, X.-W. and Hu, F., "Dynamic spectrum access for multimedia transmission over multi-user, multi-channel cognitive radio networks", *IEEE Transactions on Multimedia*, Vol. 22, No. 1, (2019), 201-214. <https://doi.org/10.1109/TMM.2019.2925960>
 19. Tamaddondar, M. and Noori, N., "Hybrid massive mimo channel model based on edge detection of interacting objects and cluster concept", *International Journal of Engineering, Transactions B: Applications*, Vol. 35, No. 2, (2022), 471-480. <https://doi.org/10.5829/IJE.2022.35.02B.23>
 20. Thanh, P.D., Hoan, T.N.K. and Koo, I., "Joint resource allocation and transmission mode selection using a pomdp-based hybrid half-duplex/full-duplex scheme for secrecy rate maximization in multi-channel cognitive radio networks", *IEEE Sensors Journal*, Vol. 20, No. 7, (2019), 3930-3945. <https://doi.org/10.1109/JSEN.2019.2958966>
 21. Gharib, A., Ejaz, W. and Ibnkahla, M., "Enhanced multiband multiuser cooperative spectrum sensing for distributed crns", *IEEE Transactions on Cognitive Communications and Networking*, Vol. 6, No. 1, (2019), 256-270. <https://doi.org/10.1109/TCCN.2019.2953661>
 22. So, J. and Kwon, T., "Limited reporting-based cooperative spectrum sensing for multiband cognitive radio networks", *AEU-International Journal of Electronics and Communications*, Vol. 70, No. 4, (2016), 386-397. <https://doi.org/10.1016/j.aeue.2015.12.017>
 23. Alhamad, R., "Nonorthogonal multiple access with adaptive transmit power and energy harvesting using intelligent reflecting surfaces for cognitive radio networks", *Signal, Image and Video Processing*, Vol. 17, No. 1, (2023), 83-89. <https://doi.org/10.1007/s11760-022-02206-2>
 24. Liu, X., "A new sensing-throughput tradeoff scheme in cooperative multiband cognitive radio network", *International Journal of Network Management*, Vol. 24, No. 3, (2014), 200-217. <https://doi.org/10.1002/nem.1859>
 25. Contreras, A., "Objective functions for the optimization of an ultra wideband antenna", *International Journal of Engineering, Transactions A: Basics*, Vol. 34, No. 7, (2021), 1743-1749. <https://doi.org/10.5829/IJE.2021.34.07A.19>
 26. Moghimi, F., Mallik, R.K. and Schober, R., "Sensing time and power optimization in mimo cognitive radio networks", *IEEE Transactions on Wireless Communications*, Vol. 11, No. 9, (2012), 3398-3408. <https://doi.org/10.1109/TWC.2012.081312.112278>
 27. Liu, X., Jing, Q., Jia, Y., Zhong, W. and Guan, Y.L., "Sensing-throughput tradeoff for cooperative multiple-input single-output cognitive radio", *International Journal of Communication Systems*, Vol. 28, No. 5, (2015), 848-860. <https://doi.org/10.1002/dac.2709>
 28. Kumar, A., Pandit, S., Thakur, P. and Singh, G., "Optimization of fusion center parameters with threshold selection in multiple antenna and censoring-based cognitive radio network", *IEEE Sensors Journal*, Vol. 22, No. 5, (2022), 4709-4721. <https://doi.org/10.1109/JSEN.2022.3142197>
 29. Allu, R., Taghizadeh, O., Singh, S.K., Singh, K. and Li, C.-P., "Robust beamformer design in active ris-assisted multiuser mimo cognitive radio networks", *IEEE Transactions on Cognitive Communications and Networking*, Vol. 9, No. 2, (2023), 398-413. <https://doi.org/10.1109/TCCN.2023.3235788>
 30. Rauniyar, A. and Shin, S.Y., "Multiple antenna-aided cascaded energy and matched filter detector for cognitive radio networks", *International Journal of Distributed Sensor Networks*, Vol. 11, No. 9, (2015), 175943. <https://doi.org/10.1155/2015/175943>
 31. Ren, X. and Chen, C., "Spectrum sensing algorithm based on sample variance in multi-antenna cognitive radio systems", *AEU-International Journal of Electronics and Communications*, Vol. 70, No. 12, (2016), 1601-1609. <https://doi.org/10.1016/j.aeue.2016.09.013>
 32. Liu, X., Li, B. and Liu, G., "Simultaneous cooperative spectrum sensing and energy harvesting in multi-antenna cognitive radio", *Mobile Networks and Applications*, Vol. 23, (2018), 263-271. <https://doi.org/10.1007/s11036-017-0946-2>
 33. Vahedian, B. and Mahmoudi-Nasr, P., "Toward energy-efficient communication protocol in wban: A dynamic scheduling policy approach", *International Journal of Engineering, Transactions A: Basics*, Vol. 35, No. 1, (2022), 191-200. <https://doi.org/10.5829/IJE.2022.35.01A.18>
 34. Ebrahimzadeh, A., Najimi, M., Andargoli, S.M.H. and Fallahi, A., "Sensor selection and optimal energy detection threshold for efficient cooperative spectrum sensing", *IEEE Transactions on Vehicular Technology*, Vol. 64, No. 4, (2014), 1565-1577. <https://doi.org/10.1109/TVT.2014.2331681>
 35. Song, Z., Zhang, Z., Liu, X., Liu, Y. and Fan, L., "Simultaneous cooperative spectrum sensing and wireless power transfer in multi-antenna cognitive radio", *Physical Communication*, Vol. 29, (2018), 78-85. <https://doi.org/10.1016/j.phycom.2018.04.022>
 36. Maleki, S., Pandharipande, A. and Leus, G., "Energy-efficient distributed spectrum sensing for cognitive sensor networks", *IEEE Sensors Journal*, Vol. 11, No. 3, (2010), 565-573. <https://doi.org/10.1109/JSEN.2010.2051327>
 37. Monemian, M., Mahdavi, M. and Omid, M.J., "Optimum sensor selection based on energy constraints in cooperative spectrum sensing for cognitive radio sensor networks", *IEEE Sensors Journal*, Vol. 16, No. 6, (2015), 1829-1841. <https://doi.org/10.1109/JSEN.2015.2503324>
 38. Hojjati, S.H., Ebrahimzadeh, A., Najimi, M. and Reihanian, A., "Sensor selection for cooperative spectrum sensing in multiantenna sensor networks based on convex optimization and genetic algorithm", *IEEE Sensors Journal*, Vol. 16, No. 10, (2016), 3486-3487. <https://doi.org/10.1109/JSEN.2016.2535862>

COPYRIGHTS

©2023 The author(s). This is an open access article distributed under the terms of the Creative Commons Attribution (CC BY 4.0), which permits unrestricted use, distribution, and reproduction in any medium, as long as the original authors and source are cited. No permission is required from the authors or the publishers.



Persian Abstract

چکیده

بهینه‌سازی مصرف انرژی و گذردهی در شبکه‌های رادیوشناختگر (CRN) دو موضوع مهمی است که در سال‌های اخیر توجه زیادی را به خود جلب کرده است. در این مقاله، بهینه‌سازی توام زمان‌های طیف‌سنجی و آستانه‌های آشکارساز انرژی در هر زیرکانال و انتخاب کاربران ثانویه چندآنتنه طیف‌سنج و ارسال‌کننده داده با هدف بهینه‌سازی بازده انرژی و بهبود گذردهی در CRN چندآنتنه چندکاناله و تحت محدودیت احتمالات هشدار غلط و آشکارسازی در نظر گرفته می‌شود. مسئله تعریف شده مبتنی بر مدل پیشنهادی، بر اساس روش بهینه‌سازی محدب حل شده و الگوریتمی با پیچیدگی محاسباتی کمتر در مقایسه با رویکردهای مینا پیشنهاد شده است. عملکرد طرح پیشنهادی با شبیه‌سازی‌ها ارزیابی و با سایر طرح‌ها مقایسه می‌شود. نتایج نشان می‌دهد که روش پیشنهادی می‌تواند به مصرف انرژی کمتری دست یابد در حالی که حداقل گذردهی مورد نیاز تضمین شده است.

AIMS AND SCOPE

The objective of the International Journal of Engineering is to provide a forum for communication of information among the world's scientific and technological community and Iranian scientists and engineers. This journal intends to be of interest and utility to researchers and practitioners in the academic, industrial and governmental sectors. All original research contributions of significant value focused on basics, applications and aspects areas of engineering discipline are welcome.

This journal is published in three quarterly transactions: Transactions A (Basics) deal with the engineering fundamentals, Transactions B (Applications) are concerned with the application of the engineering knowledge in the daily life of the human being and Transactions C (Aspects) - starting from January 2012 - emphasize on the main engineering aspects whose elaboration can yield knowledge and expertise that can equally serve all branches of engineering discipline.

This journal will publish authoritative papers on theoretical and experimental researches and advanced applications embodying the results of extensive field, plant, laboratory or theoretical investigation or new interpretations of existing problems. It may also feature - when appropriate - research notes, technical notes, state-of-the-art survey type papers, short communications, letters to the editor, meeting schedules and conference announcements. The language of publication is English. Each paper should contain an abstract both in English and in Persian. However, for the authors who are not familiar with Persian, the publisher will prepare the latter. The abstracts should not exceed 250 words.

All manuscripts will be peer-reviewed by qualified reviewers. The material should be presented clearly and concisely:

- *Full papers* must be based on completed original works of significant novelty. The papers are not strictly limited in length. However, lengthy contributions may be delayed due to limited space. It is advised to keep papers limited to 7500 words.
- *Research notes* are considered as short items that include theoretical or experimental results of immediate current interest.
- *Technical notes* are also considered as short items of enough technical acceptability with more rapid publication appeal. The length of a research or technical note is recommended not to exceed 2500 words or 4 journal pages (including figures and tables).

Review papers are only considered from highly qualified well-known authors generally assigned by the editorial board or editor in chief. Short communications and letters to the editor should contain a text of about 1000 words and whatever figures and tables that may be required to support the text. They include discussion of full papers and short items and should contribute to the original article by providing confirmation or additional interpretation. Discussion of papers will be referred to author(s) for reply and will concurrently be published with reply of author(s).

INSTRUCTIONS FOR AUTHORS

Submission of a manuscript represents that it has neither been published nor submitted for publication elsewhere and is result of research carried out by author(s). Presentation in a conference and appearance in a symposium proceeding is not considered prior publication.

Authors are required to include a list describing all the symbols and abbreviations in the paper. Use of the international system of measurement units is mandatory.

- On-line submission of manuscripts results in faster publication process and is recommended. Instructions are given in the IJE web sites: www.ije.ir-www.ijeir.info
- Hardcopy submissions must include MS Word and jpg files.
- Manuscripts should be typewritten on one side of A4 paper, double-spaced, with adequate margins.
- References should be numbered in brackets and appear in sequence through the text. List of references should be given at the end of the paper.
- Figure captions are to be indicated under the illustrations. They should sufficiently explain the figures.
- Illustrations should appear in their appropriate places in the text.
- Tables and diagrams should be submitted in a form suitable for reproduction.
- Photographs should be of high quality saved as jpg files.
- Tables, Illustrations, Figures and Diagrams will be normally printed in single column width (8cm). Exceptionally large ones may be printed across two columns (17cm).

PAGE CHARGES AND REPRINTS

The papers are strictly limited in length, maximum 8 journal pages (including figures and tables). For the additional to 8 journal pages, there will be page charges. It is advised to keep papers limited to 3500 words.

Page Charges for Papers More Than 8 Pages (Including Abstract)

For International Author ***	\$55 / per page
For Local Author	100,000 Toman / per page

AUTHOR CHECKLIST

- Author(s), bio-data including affiliation(s) and mail and e-mail addresses).
- Manuscript including abstracts, key words, illustrations, tables, figures with figure captions and list of references.
- MS Word files of the paper.



THOMSON REUTERS
WEB OF SCIENCE



Scopus®



CAS®
A DIVISION OF THE
AMERICAN CHEMICAL SOCIETY



Scientific Indexing Services

Google
Scholar